OXIDATION BEHAVIOR OF VERY HIGH TEMPERATURE REACTOR (VHTR)

CANDIDATE MATERIALS: 316L STAINLESS STEEL,

ALLOY 617, AND INCOLOY-800H

_____

A Dissertation

presented to

the Faculty of the Graduate School

at the University of Missouri

_____

In Partial Fulfillment

of the Requirements for the Degree

Doctor of Philosophy

_____

by

HAKAN US

Tushar K. Ghosh and Sudarshan K. Loyalka. Dissertation Supervisor

DECEMBER 2016

The undersigned, appointed by the Dean of the Graduate School, have examined the dissertation entitled

OXIDATION BEHAVIOR OF VERY HIGH TEMPERATURE REACTOR (VHTR)
CANDIDATE MATERIALS: 316L STAINLESS STEEL,
ALLOY 617, AND INCOLOY 800-H

Presented by Hakan Us

A candidate for the degree of doctor of philosophy

and hereby certify that, in their opinion, it is worthy of acceptance

---

TUSHAR K. GHOSH

SUDARSHAN K. LOYALKA

MARK A. PRELAS

ROBERT V. TOMPSON, JR

DABIR S. VISWANATH

DEDICATION

I would like to dedicate this dissertation to my family and my parents. I would like to express my deep thanks to my father, Ahmet Us, and to my mother, Fatma Us, for all of their support throughout my whole life.

I am also thankful to my friends for their help and support. I am thankful for everyone who was a part of my dream and for helping me to make my dream come true.

ACKNOWLEDGEMENTS

TABLE OF CONTENTS

LIST OF FIGURES

xiii

LIST OF TABLES

OXIDATION BEHAVIOR OF VERY HIGH TEMPERATURE REACTOR (VHTR)
CANDIDATE MATERIALS: 316L STAINLESS STEEL,
ALLOY 617, AND INCOLOY 800-H

Hakan Us

Dr. Tushar K. Ghosh and Dr. Sudarshan K. Loyalka, Dissertation Supervisors

ABSTRACT

High temperature nuclear reactors require alloys to perform well at temperatures around 1000 to 1400 K. The oxidation behavior of three high temperature reactor candidate materials, 316 L stainless steel, alloy 617, and Incoloy 800-H under different conditions were investigated in the present work. For molybdenum-based 316 L stainless steel, the tests were performed isothermally at temperatures between 773 K and 1,273 K (in steps of 100 K) for 24 hours in controlled air environments. The oxidation behavior followed the parabolic oxidation kinetic rate law. The activation energy was 149.21 kJ/mol at 873 K to 1273 K. At 773 K, a thin external oxide layer was observed, while at higher temperatures a continuous and relatively irregular and inwardly protruded external oxide layer was observed. The external layer width and composition depended on increasing temperatures. At 1073 K a Cr_2O_3 layer was detected. After 1273 K, a Fe_2O_3 sub-layer formed in addition to the Cr_2O_3 layer. Continuous larger external oxide scales and grain boundary ridges were also observed with increasing temperatures. The oxide morphology and structure of 316L stainless steel were strongly affected by the controlled air environments. The best oxidation resistance of 316L stainless steel was observed at 1073 K with the highest Cr content value. At 1273 K, mass gain was related to iron oxidation. Increasing oxidation temperatures were attributed to the formation of pores, voids, and grain boundaries.

Alloy 617 tests were performed isothermally at temperatures between 1073 K to 1473 K (in steps of 100 K) for 24 hours in controlled air environments. The oxidation behavior followed the parabolic oxidation kinetic rate law. The activation energy was found to be 233.46 kJ/mol for 1073 K to 1473 K. At 1073 K to 1473 K, a thin external oxide layer was identified as an NiO Cr_2O_3 double layer. The external layer had Cr_2O_3, and the inner layer was a NiO layer. Meanwhile, a continuous and relatively irregular and inwardly protruded external oxide layer was observed with an external layer width dependent on increasing temperatures. Besides the NiO-Cr_2O_3 layer, Al_2O_3 areas were also detected. Figures sequentially showed a continuous growth of external oxide scales and grain boundary ridges with temperatures. The oxide morphology and structure of alloy 617 were strongly affected by environments. At 1473 K, the increasing mass gain was related to Ti oxidation. The oxidation depth increased as the temperature increased. Increasing oxidation temperatures is attributed to the formation of pores, voids, and grain boundaries.

Incoloy 800H tests were performed isothermally at temperatures between 1073 K to 1473 K (in steps of 100 K) for 24 hours in controlled air environments. The activation energy was found to be 266.8 kJ/mol for 1073 K to 1473 K Results showed that the oxidation followed a parabolic oxidation kinetic law. Spallation occurred as a result of oxidation after 1373 K. At 1473 K, the increasing mass gain was related to Ti oxidation. As revealed by SEM, a triple layered external oxide scale was formed.

A thermogravimetric analyzer, scanning electron microscopy/energy dispersive X-ray spectroscopy, and X-Ray diffraction were among the analytical techniques used.

CHAPTER 1. INTRODUCTION

1.1. Very High Temperature Reactors (VHTRs)

A very high-temperature reactor (VHTR) is a helium-cooled, graphite-moderated reactor with a ceramic core and tristructural-isotropic (TRISO)-coated fuel particles[1]. Coolant outlet temperatures of 1273 K (1000 °C) or above are expected (eventually slated to reach 1773 K (1500 °C)). High temperature allows for more efficient electrical generation and better thermal conditions for process heat applications.

Two reactor design concepts are being studied for VHTRs: the prismatic reactor and the pebble bed reactor. VHTR uses an annular core configuration. In a prismatic core, the hexagonal moderator and fuel blocks are arranged to form an inner graphite reflector, a center active fuel core (rings 6 –8), and an outer replaceable graphite reflector. The active core is approximately 26 ft in height and consists of 102 fuel columns, each of which is a stack of ten fuel blocks (1020 fuel blocks total). In addition to the replaceable graphite components, the prismatic core also includes a permanent side graphite reflector, vessel coolant channels, and the core barrel[1].

The main challenge to VHTR is the availability of structural and other materials that can perform well under high temperatures and neutron fluxes. Radiation, diffusion, and chemical reactions can all affect the microstructure of the material properties.

The experience with very high temperature reactor technology derives from eight previously constructed reactors that vary in size, outlet temperature, primary fluid, and purpose: Dragon (Prismatic Reactor; United Kingdom), Arbeitsgemeinschaft Versuchsreaktor (AVR; Pebble Bed Reactor; Germany), Thorium Hochtemperatur

Reaktor (THTR; Pebble Bed Reactor; Germany), High Temperature Test Reactor
(HTTR; Prismatic Reactor; Japan), High Temperature Reactor-10 (HTR-10; Pebble Bed
Reactor; People's Republic of China), Peach Bottom 1 (Prismatic Reactor; United
States), and Fort St. Vrain (FSV; Prismatic Reactor; United States).

1.2. Candidate Materials and Challenges

The key out-of-core structures in VHTRs include the reactor pressure vessel
(RPV, made of 2¼ Cr bainitic steel or 9 Cr martensitic steel), the cross-vessel
component, and the intermediate heat exchangers (IHXs) that divert heat from the
primary side of the reactor to a hydrogen production plant. Such components place great
demands on their materials of construction. Thin sheets endure heat from 850 °C to
950 °C and must sustain a differential pressure of 6 to 7 MPa during off-normal events.
Therefore, mechanical strength, creep resistance and corrosion resistance are required for
their extended lifetime (approximately 20 years). Such temperatures demand the use of
Ni-base alloys rich in chromium (about 22 mass%) and are strengthened by additions of
molybdenum, cobalt and tungsten. Examples include Inconel 617 (Ni-22Cr- 12Co-8Mo-
0.1C) and Haynes 230 (Ni-22Cr-14W-2Mo-0.1C)[2].

Materials were subjected to higher temperatures and irradiation in the VHTR than
in past designs. Larger amounts of irradiation caused more displacements and
transmutations than in current nuclear service conditions. Higher temperatures increase
the atomic diffusion rates and chemical reaction rates at the surface of and within the
VHTR materials, which affects the microstructure and material properties. Long-term
chemical processes such as corrosion are expected to become more like direct and
(relatively) instantaneous chemical reactions[1].

Candidate materials considered for this VHTR research are noted in the Table 1, and the issues/requirements are noted in Table 2 below.

Table 1. VHTR candidate materials

Fuel and cladding	Coolant / Moderator	Control	Pressure vessel	Piping/Internals	IHX/Steam generator
UCO UO$_2$ Pyrolytic Carbon* Silicon carbide* IG-110 or IG-430	Helium Graphite Nitrogen Molten Salt	Cf/C,SiCf/SiC (Clad) Alloy 800H	Modified 9Cr1Mo-V Steel P91 SA508 Gr.3 Class 1,2 SA533 Gr.B 2.25Cr-Mo steel	Alloys 617 X, XR, 230, 602CA, 800H Carbon fiber reinforced carbon Cf / C SiCf / SiC	Ni base Alloys (Alloy 617 Alloy 230) Hastelloy XR

*3–6

Table 2. Candidate VHTR materials in different nations [2]

Nation	Candidate materials
Republic of Korea	• F/M (Mod.9Cr1Mo) or low alloy steel for the reactor vessel; • high-temperature nickel alloys (Hastelloy X, IN 617 or Haynes 230) for gas ducts and intermediate heat exchanger; • C/C, SiC/SiC composites or austenitic stainless steels (16Cr-16Ni-2Mo- 1Nb or 800H) for control rods;
United States	• low alloy steel (SA-508) or Grade 91 steel for the pressure vessel; • high alloy stainless steels (alloy 800H), graphite and SiC/SiC or C/C composites for reactor internals; • nickel alloys (Haynes 230, Alloy 800H, Inconel 617, Hastelloy X) or ceramics for heat transfer system and heat exchangers.
Japan	• graphite or SiC/SiC composites for the core and reflector; • 2.25Cr-Mo steel for pressure vessel and high-temperature coaxial tubes, with possible use of 9Cr F/M steel for extended lifetimes; • Hastelloy XR for high-temperature coaxial tube liner and IHX heat-pipe; • Alloy 800H for control rod sleeve in the HTTR and also in VHTR (either, but below 900°C for 5 years). C/C and SiC/SiC composites are also considered

Switzerland	• Materials of interest are conventional RPV steels, grade 91, IN617, IN800H and others; • ODS steels, TiAl or fibre reinforced ceramics for high-temperature options.
France	• 9%Cr F/M steels (and improved versions) for the pressure vessel; • C/C or SiC/SiC composites for control rods; • nickel-based alloys (Inconel 617, Haynes 230) or ODS alloys for intermediate heat exchangers; • nickel-based alloys (Haynes 230, Inconel 617) for the primary cooling circuit; • graphite for the core; • SiC, SiC/SiC composites (as well as other carbides and nitrides) for cladding materials.

The issues addressed in this dissertation include:

• Creep fatigue, embrittlement, thermal expansion, thermal fatigue, crack resistance, oxidation resistance, carburization resistance and thermal conductivity;

• High-temperature creep (950 °C-1223 K) for nickel alloys;

• Corrosion resistance in impure He and in air or nickel alloys;

• Flexural strength for composites;

• Oxidation resistance in impure He and in air for composites.

1.2. Objectives and Scope of This Research

The objective of the present research was to investigate the oxidation behavior of three candidate VHTR materials. A systematic and comprehensive investigation of the thermal oxidation of three alloys under varying oxidation conditions was carried out. The investigation contains studies of the developing oxide phases, the oxide microstructure, the oxidation kinetics and the oxidation behavior of the alloys as a function of the oxidation conditions (temperature, time, and atmosphere).

1.3. Dissertation Organization

This dissertation is organized as follows:

Chapter I provides a short background on VHTRs and a summary of the objectives of this research work and the organization of this thesis.

Chapter II, presents background information on oxidation theory at high temperatures, the principle of oxidation kinetics, and the basic theory for growth of oxides.

Chapter III describes of the experimental methods and the various techniques used in this study, such as:

- identification of oxides formed on the surface by X-ray diffraction,
- observation of the surface morphology and microstructure of the layers by scanning electron microscopy/energy dispersive X-ray spectroscopy (SEM/EDS) and
- measure mass change rate by thermogravimetric analyzer (TGA).

Chapter IV, V, and VI form the main parts if this dissertation. Each chapter is devoted to the study of oxidation of candidate materials; SS-316L, Alloy 617, and Incoloy 800H. The chapters include literature reviews, experimental results, discussions and conclusions for each candidate material, separately.

CHAPTER 2. OXIDATION AT HIGH-TEMPERATURE THEORY

2.1. Theory of Oxidation

Every metal and alloy reacts with air at elevated temperatures. Oxidation increases with temperature. Oxidation is an electrochemical process. The chemical process of metal oxidation is not simply.

$$M + \tfrac{1}{2} O_2 \rightarrow \quad MO \qquad\qquad (1)$$

It actually consists of two partial reactions;

$$M \rightarrow M^{2+} + 2e^- \text{ (metal oxidation at metal scale interface)} \qquad (2)$$

And $\qquad\qquad \tfrac{1}{2} O_2 + 2e^- \rightarrow O_2$ (Oxidant reduction at scale gas interface) $\qquad$ (3)

and generally $\qquad\qquad xM + (1/2) yO_2 \rightarrow M_xO_y \qquad\qquad (4)$
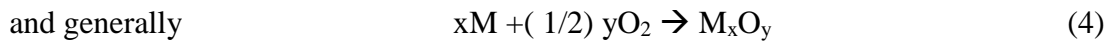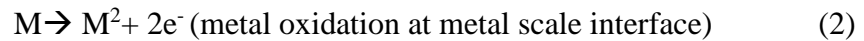
Figure 1 shows that the oxide layer processing in an ionic conductor (electrolyte), an electronic conductor, and an electrode at which oxygen is reduced. The diffusion

barrier through which electrons and ions must migrate to lattice defect sites (Vm and Vo).
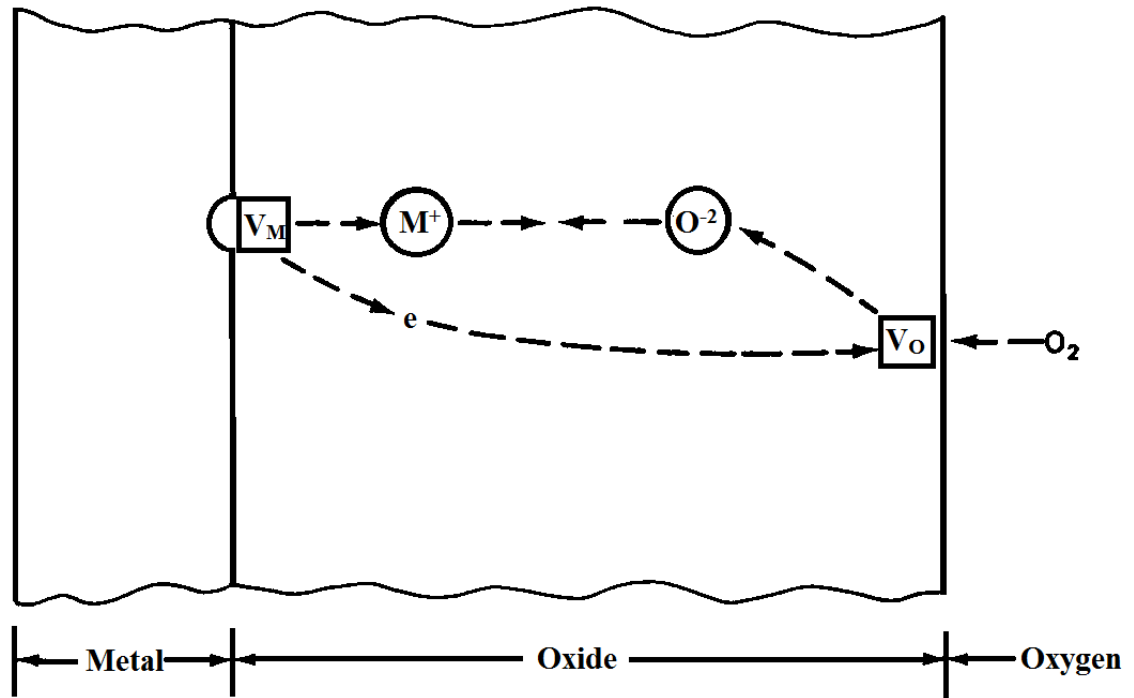
Figure 1. Schematic Illustration of electrochemical processes occurring during gaseous oxidation.

A metal surface reacts with oxygen at high temperature by initial adsorption of oxygen. Once the chemical reaction is initiated, oxygen starts to dissolve to form the surface oxide through oxide nucleation, and then forms a continuous film, that may protect the underlying metal. The film may also thicken into a non-protective scale with various defects including cavities, microcracks, and porosity, as shown in Figure 2.

The chemical and physical properties are of importance in determining the rate of oxidation and the life of equipment exposed to high-temperature oxidizing environments.
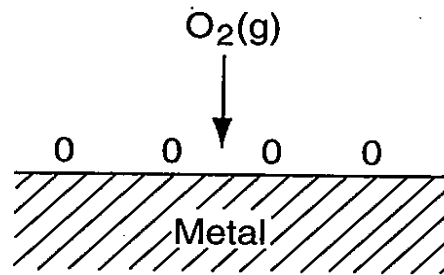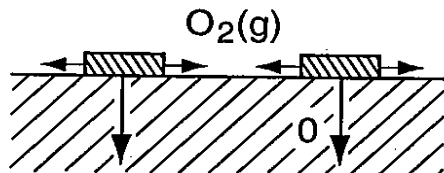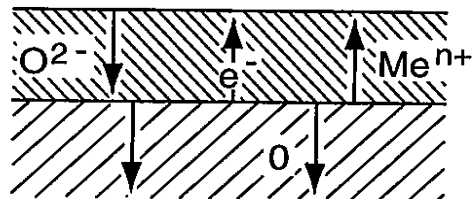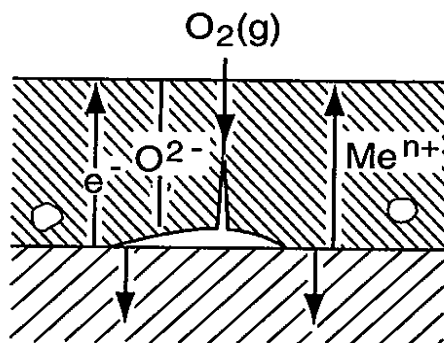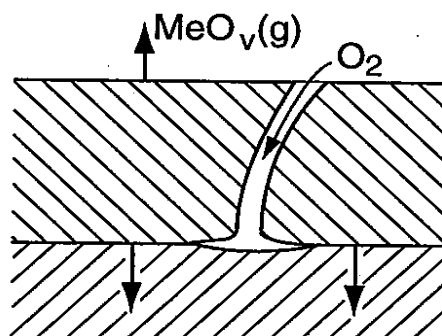
Figure 2. Film and scale formation on metal at high temperature oxidation.

2.2. High Temperature Oxidation

2.2.1. Thermodynamic of High Temperature Oxidation

The thermodynamics of oxidation of a metallic material can be described by the energy that is lost or gained in heating as the metal reacts with other compounds. Two points are important, first, the more the energy released when forming the compound, such as an oxide, the more stable the compound is. Second, as the temperature is raised, more of the oxidizing species is required to maintain the oxide.

Metal is characterized thermodynamically by a standard free energy change (Gibbs energy change) ΔG which must be negative for the reaction to proceed, all reactants and products being at the standard state. The second law of thermodynamics describes the reaction of metal oxidizing. Second law describes standard (Gibbs) free energy change(ΔG)[7] as

$$\Delta G = \Delta H - T\Delta S \qquad (5)$$

where, H is enthalpy, T is the absolute temperature, and S is the entropy. No reaction will proceed unless ΔG is negative. Under these conditions the second law states[7,8]:

When $\Delta G < 0$, spontaneous reaction is expected. Thus, $\Delta G = 0$ represents equilibrium, and $\Delta G > 0$ represents a thermodynamically impossible process.

For a chemical process, based on one mole of O_2, the reaction will be:

$$(2x/y)\ M + O_2 = (2/y)\ M_xO_y \qquad (6)$$

For this reaction, reactants and products give a free-energy change, ΔG_{2MO}, which can be expressed as

$$\Delta G \Delta G_{O_2/MO} = \Delta G^o_{O_2/MO} + RT \ln \frac{a_{M_xO_y^{2/y}}}{(a_M^{\frac{2x}{y}})(a_{O_2,MO})}, \qquad (7)$$

where R is the gas constant and T is absolute temperature. Because activities of pure solids in the stable form are defined as unity at all temperatures and pressure, this equation reduces to

$$\Delta G^o_{O_2/MO} = RT \ln p_{O_2/MO}, \qquad (8)$$

where $\Delta G^o_{O_2/MO} = 0$ at equilibrium and $p_{O_2/MO} = a_{O_2/MO}$ This equation describes the relationship between the standard state free energy change, $\Delta G^o_{O_2/MO}$, for formation of pure oxide, MO, on the base metal, M, and the characteristic equilibrium oxygen pressure, $p_{O_2/MO}$ and oxide at any temperature, T. The nonstandard state oxygen dissociation pressures leading to oxide formation or reduction on pure metals can be found from the Ellingham/ Richardson[9] diagram (Figure 3). But note that this diagram cannot predict the rate of oxidation.
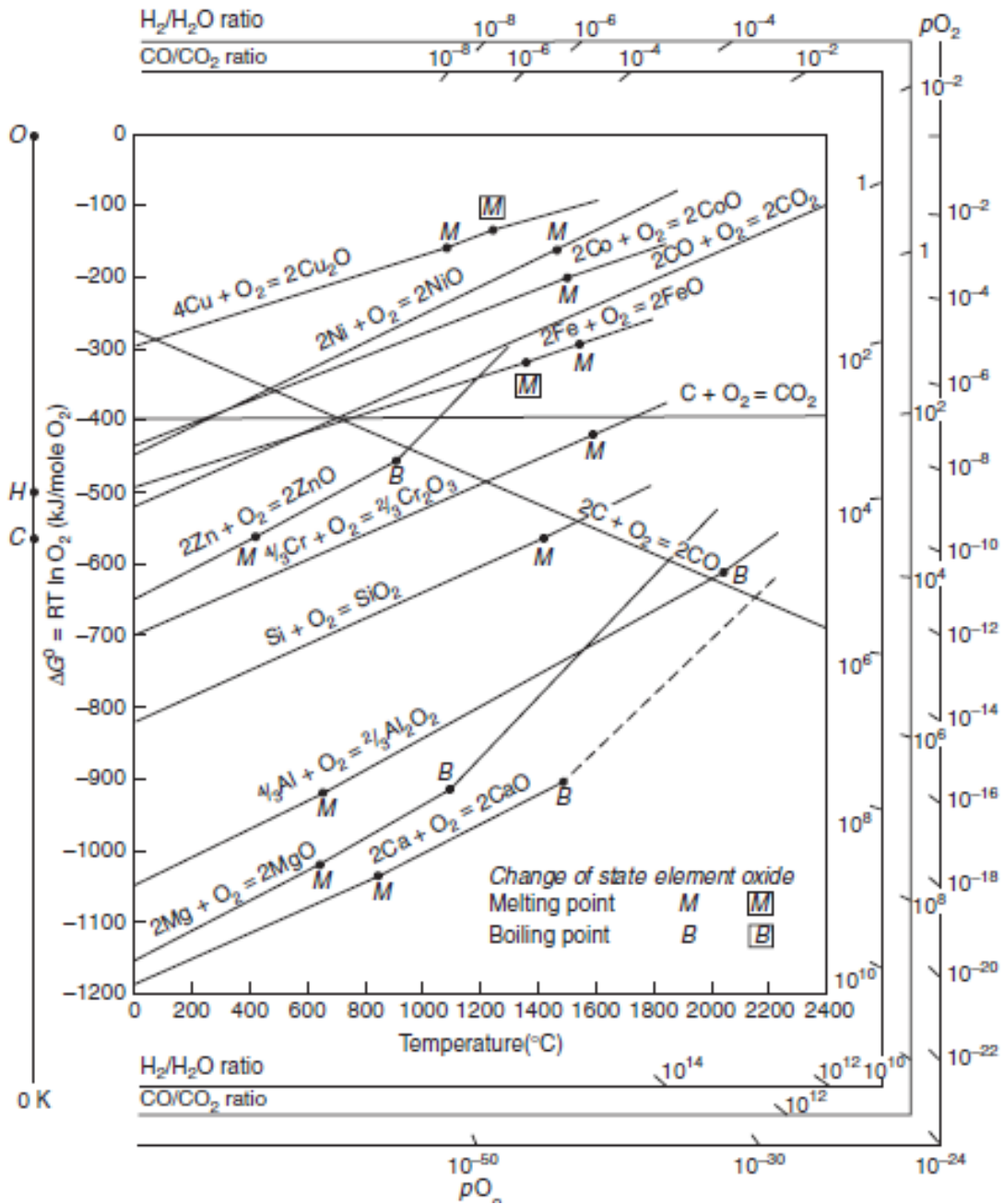
Figure 3. Ellingham diagram of free energy versus temperature for oxidation of metals[9].

2.2.2. Pilling- Bedworth Ratio

The volume of the oxide formed, relative to the volume of the metal consumed, is

an important parameter in predicting the degree of protection provided by the oxide scale.

If the oxide volume is relatively low, tensile stresses will tend to crack the oxide layers. If the oxide volume is very high, stresses will tend to lead to a break in the adhesion between the metal and oxide. For a high degree of protection, the oxide formed should be similar to that of the metal being oxidized[9]. This argument is the basis for the Pilling-Bedworth ratio.

The Pilling- Bedworth ratio is given by

$$\text{PB ratio} = \frac{\text{volume of oxide produced}}{\text{volume of metal consumed}} = \frac{Wd}{nDw} \tag{9}$$

where W is the molecular weight of oxide, and D the density of the oxide, d is the density of metal, w is the atomic weight of the pure metal, and n is the number of metal atoms in the oxide molecule[10].

If a volume ratio of less than 1 produces insufficient oxide to cover the metal and are non-protective, and if that ratio is around or greater than 2, the oxide stress affects the poor oxidation resistance of the metal due to cracking and spalling. The ideal ratio, would be close to 1. To be protective to oxidation, the oxide must possess a coefficient of expansion nearly equal to that of the metal substrate. It must also have good adherence, a high melting point, a low vapor pressure, good high temperature plasticity to resist fracture, a low electrical conductivity or low diffusion coefficient for metal ions and oxygen, and a volume ratio to 1[7,11].

2.2.3. Oxidation Kinetics

The oxidation kinetics laws—linear, parabolic, logarithmic, and cubic—describe the oxidation rates. The oxidation rate can be described by measuring weight gain per

unit area and thickness. Various forms of the rate as a function of time are shown in Figure 4:
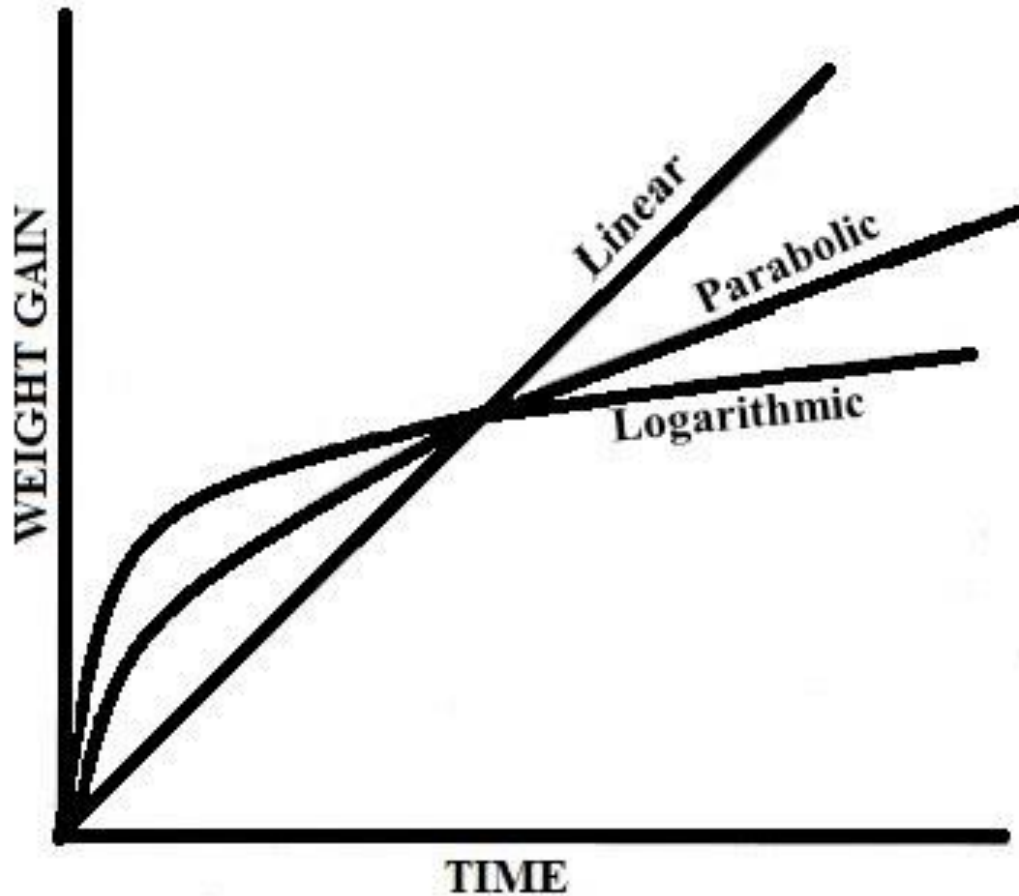
Figure 4. Weight gain versus time for the kinetics laws

2.2.3.1. Linear Kinetics

Linear oxidation is characteristic of metals which form a porous or cracked scale such that the scale does not represent a diffusion barrier between the two reactants. Linear rate law is usually observed under conditions where a phase boundary process is the rate determining step for the reaction, although other steps in the mechanism of oxidation can lead to the same result.

The simplest empirical relationship of scale growth with time is:

13

$$(\Delta m/a) = k_l t + C \qquad (10)$$

where, $(\Delta m/a)$ is the weight change per unit area, t is oxidation time, k_l is linear rate constant, C is a constant, and $g.cm^2s^{-1}$ are units in term of mass gain measurements.

2.2.3.2. Parabolic Kinetics

When the rate controlling step in the oxidation process is diffusion of ions through a compact oxide scale, with chemical potential gradient as the driving force, the parabolic rate law is usually observed. It is defined by the equation;

$$(\Delta m/a)^2 = k_p t + C \qquad (11)$$

where, $(\Delta m/a)$ is weight gain per unit area, t is exposure time, k_p is parabolic rate constant, C is a constant and units in term of mass gain measurements $g.cm^2s^{-1}$.

2.2.3.3. Logarithmic Kinetics

During the oxidation of several metals at low temperature, (below 673 K) the reaction is initially quite rapid and then drops off to low or negligible values. This behavior can often be described by the logarithmic rate equations, which include direct logarithmic and inverse logarithmic rate equations

$$\text{Direct Logarithmic } x = k_{log} \log t \qquad (12)$$

$$\text{Inverse logarithmic } 1/x = B - k_{il} \log t \qquad (13)$$

where, x=oxide thickness or weight gain, t is the exposure time, k_{log}, k_{il} and B represent the constants at constant temperatures.

2.2.3.4. Cubic Kinetics

Cubic kinetics is an intermediate stage between logarithmic and parabolic kinetics. Under specific conditions, some metals oxidize according to cubic law.

14

$$(\Delta m/a)^3 = k_c t + C \tag{14}$$

where $(\Delta m/a)$ is mass gain per unit area, t is exposure time, k_c is cubic rate constant, and C is a constant.

2.2.4. Activation Energy

Experimental studies have shown that the oxidation rate constant, k, of various rate equations can be described by an Arrhenius equation. Activation energies can be derived from an analysis of the resulting plots, which aid in defining oxidation behavior. The equations that lead to the determination of activation energy are discussed below.

The rate constant, k, is normally found to depend upon temperature according to the Arrhenius equation

$$k = A \exp(-Q/RT) \tag{15}$$

where the pre-exponential constant A is called the frequency factor, Q is the activation energy of the reaction, and T is temperature (K). Taking logarithms

$$\text{Log } k = \text{Log } A - (Q/2.3030R)(1/T) \tag{16}$$

enables a graph to be made in which log k is plotted against 1/T to form the slope of –Q in plot. Note: R is the gas constant (8.31 J/mol K).

2.2.5. High temperatures materials
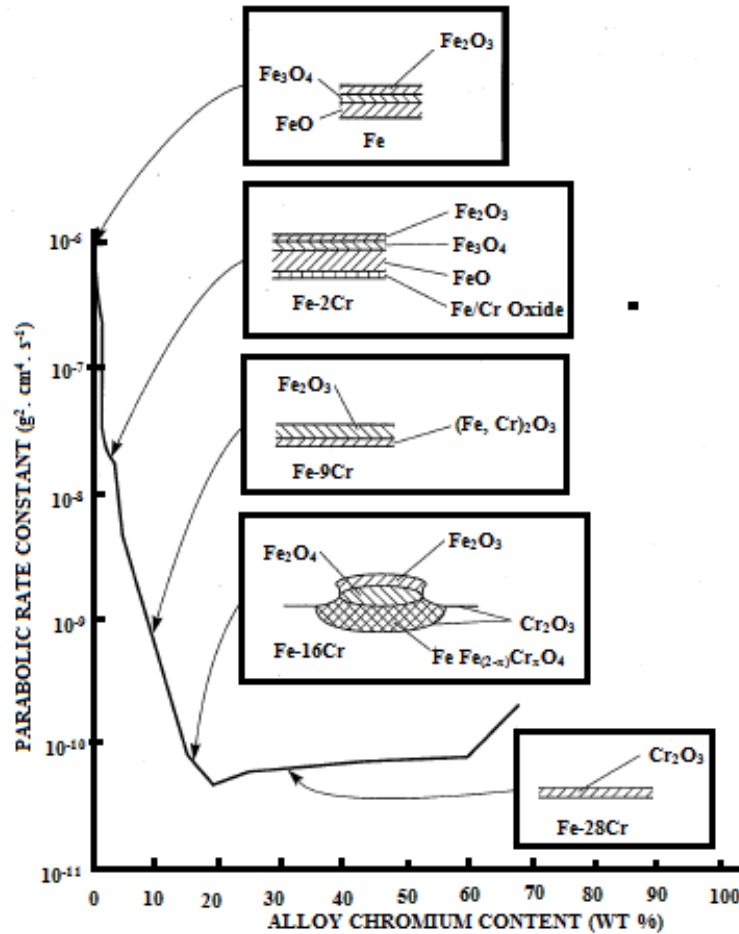
Figure 5. Effect of chromium content on the corrosion resistance and oxide morphology of iron-chromium alloys at 1273 K.

Individual elements in an alloy lead to differing structural strengths as well as high temperature oxidation resistance; thus, most alloys designed for high temperature oxidation resistance contain chromium. Figure 5 shows the effect of increasing chromium content on the oxidation resistance and oxide morphology if Fe-Cr alloys are oxidized at 1273 K. Oxidation rates decrease sharply as Cr is increased to 20%, and chromium oxide

formation increases until they predominate in the oxide film. Similar effects are also seen in nickel and cobalt containing alloys.

Nickel, with chromium, improves the high temperature oxidation resistance of the stainless steels, just as it does aqueous corrosion resistance at lower temperatures. Alone, nickel has little effect on the oxidation resistance of iron. Nickel stabilizes the austenitic face centered cubic phase, which is more creep resistant than ferrite at high temperature.

Adding silicon to alloys leads to adherent resistance films alone and in conjunction with chromium. Silicon is added at 2 to 3% levels to many iron and nickel-based chromium bearing alloys to improve corrosion resistance, especially at lower temperatures.

Adding aluminum leads to protective oxides but at a lower rate than chromium. Also, aluminum forms brittle intermetallic phases with iron, restricting allowable alloy concentrations. Thus, efforts to replace strategic chromium with aluminum have been unsuccessful, because aluminum oxides do not form fast additions to repair mechanical damage during oxidation. Nevertheless, aluminum additions of a few percent are used frequently to enhance the oxidation resistance of iron and nickel based chromium bearing alloys.

Molybdenum, tungsten, and niobium provide little improvement in oxidation resistance but are often added to enhance mechanical properties at high temperature.

2.2.5.1. Oxidation and Alloy Contents Effects on Alloy

Oxidation is generally described as a form of high-temperature corrosion. On the other hand, oxidation is not always damaging to alloys. Most corrosion on heat resistant

alloys leads to oxide film and protection of the alloy surface. Chromium oxide (Cr_2O_3) is the most common of such films. High-temperature corrosion mechanisms cause material degradation when contaminants (sulfur, chlorine, vanadium, etc.) are present in the atmosphere.

The operating temperature assumes a critical role in determining the oxidation rate. As temperature is increased, the rate of oxidation also increases. In lower allowable operating temperatures for some alloys such as austenitic stainless steels, increased chromium content is the most common way of improving oxidation resistance. Also. increasing the nickel content of the austenitic stainless steels up to about 30% can have a strong beneficial synergistic effect when used with chromium, which also improves oxidation resistance.

Most alloys tend to have increasing penetration rates with increasing temperature for all oxygen concentrations. Some exceptions are alloys with 1 to 4% Al. These alloys require higher temperatures to form Al_2O_3 as the dominant surface oxide, which grows more slowly than the Cr_2O_3 that dominates at lower temperatures.

The alloy structure can affect metal penetration, which occurs by subsurface oxidation along grain boundaries and within the alloy grains, as shown in Fig. 6. Most of the heat-resistant alloys are based upon combinations of Fe-Ni-Cr. These alloys show about 80 to 95% of the total penetration as subsurface oxidation. Some alloys vary in how much of the total penetration occurs by subsurface oxidation as time passes, until long-term behavior is established; this can happen even though the corrosion product morphologies may remain constant. Alloys vary greatly in the extent of surface scaling and subsurface oxidation[9].

18
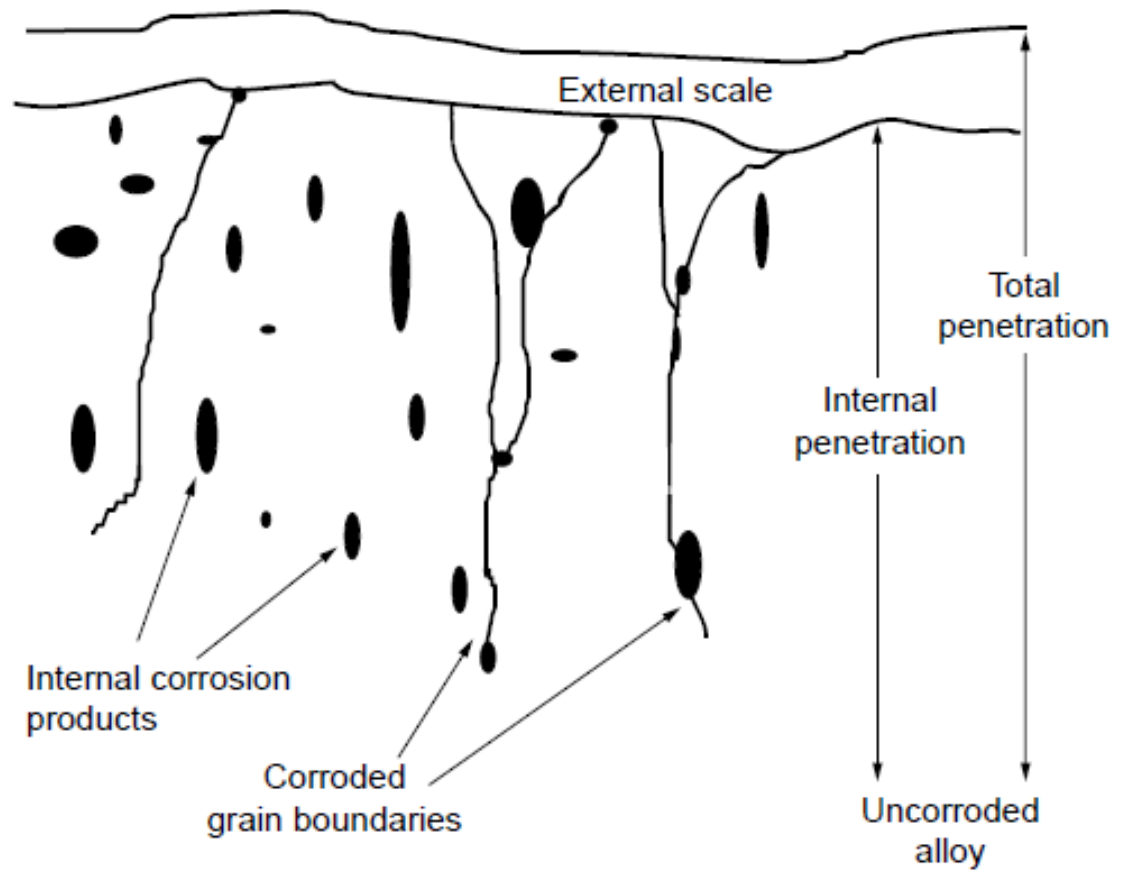
Figure 6. Schematic view of total penetration measurement for a typical corrosion product morphology[9].

CHAPTER 3. MATERIALS AND METHODS

3.1. Materials

3.1.1. 316L Stainless Steel

Type 316 L stainless steel is being considered for core barrel assemblies and other metallic reactor internal components that would experience temperatures up to 893 K[12].

Type 316L is an extra-low carbon version of Type 316. Table 3 shows the properties of interest for oxidation studies.

Table 3. Properties of SS-316L [13,14]

Density	7.99 g/cm^3
Melting Range	1644 K-1672 K
Composition (%)	Ni (12), Cr (17), Mo (2.5), Fe (65), Si (1), Mn (2), C (0.03), P (0.045), S (0.03)
UNS Number	S31603

As received SS-316L (nuclear grade UNS S31603) strips were first cut into test samples with approximate dimensions of 12 mm × 11 mm × 0.4 mm (each sample was measured separately for calculation of the oxidation rate constant). This is the ideal geometry to fit the sample bucket used in thermal gravimetric analysis (TGA). Sample surfaces were reground with 400 grit silicon-carbide paper to simulate the surface roughness of actual components.

3.1.2. Alloy 617

Alloy 617 (UNS N06617) is one of the leading candidates to meet the structural material requirements of the very high temperature reactors. It is a solid-solution

strengthened, nickel-chromium-cobalt-molybdenum-aluminum alloy having an exceptional creep strength and oxidation resistance. Nickel, chromium, and aluminum provide good cyclic oxidation and carburization resistance at high temperatures, while cobalt and molybdenum provide solid-solution strengthening. Its excellent creep-rupture strength even at elevated temperatures and its ability to retain toughness after long-time exposure at elevated temperatures makes it a potential candidate material for construction of the IHX for the VHTR. This alloy exhibits good metallurgical stability and good hot workability[15]. Alloy 617 is an Ni base alloy. Table 4 shows the properties of interest for oxidation studies.

Table 4. Properties of 617 Alloy. [16]

Density	8.36 g/cm^3
Melting Range	1603 K-1648 K
Composition (%)	Ni (54), Cr (22), Co (12.5), Mo (9), Fe (1), Ti (0.3), Mn (2), C (0.07),
UNS Number	N06617

As received Alloy 617 strips was first cut into test samples with dimensions approximately they are 15 mm x 12.8 mm x 0.4 mm, and each sample was measured separately for calculation of the oxidation rate constant. Sample surfaces were reground by 400 grit silicon-carbide paper to simulate the surface roughness of actual components.

3.1.3. Incoloy 800-H

Alloy 800-H is an iron-base solid-solution strengthened alloy with large additions of nickel (30–35 wt. %) and chromium (19–23 wt. %). While nickel and chromium ensure good oxidation and carburization resistance, carbon imparts high temperature strength and resistance to creep and rupture. Alloy 800-H is currently approved under

ASME BPVC-III NH for use up to 1033 K. For the pebble bed reactor design, Alloy 800H is a candidate material for control rod sheath materials for VHTR.

Table 5. Properties of Incoloy 800-H. [17]

Density	7.94 g/cm^3
Melting Range	1630 K-1658 K
Composition (%)	Ni (30-35), Cr (19-23), Al (0.15-0.60), Fe (39.5 min), C (0.05-0.10),
UNS Number	N08810

As received Incoloy 800-H strips were first cut into test samples with dimensions that are approximately 2.86 cm x 1.1 cm x 0.15 cm, and each sample was measured separately for calculation of oxidation rate constant. The samples' surfaces were reground using 400 grit silicon-carbide paper to simulate the surface roughness of actual components. Then, samples were cleaned with methanol and acetylene and dried for one hour with furnace tubes at 373 K. This procedure led to the ideal geometry needed to fit the sample bucket used in the thermal gravimetric apparatus.

3.2. Equipment and Methods

We used TGA to measure the oxidation rate isothermally. Then, we examined the oxide layer structure with SEM and XRD. Equipment, operating conditions and methods are covered in the following sections.

3.2.1. Thermogravimetric analyzer

A Thermax700 thermogravimetric analyzer from ThermoScientific was used to obtain the mass change vs. temperature data in real-time during oxidation of materials in air. The volume of the bucket was 35 m. The balance had a 100 g capacity and resolution of ±1.0 µg. Mixtures of dry medical-grade air in ultra-high purity research-grade helium

22

having a total flow rate of 50 mL/min were used in the experiment. Mass flow controllers were used to control the flow rates. The mass change was measured isothermally once the desired temperature was reached in the TGA. Mass change data was sent from the TGA to a computer using automated data collection software. Figure 7 is a schematic of the experimental setup. Figure 8 contains some photos of the setup.
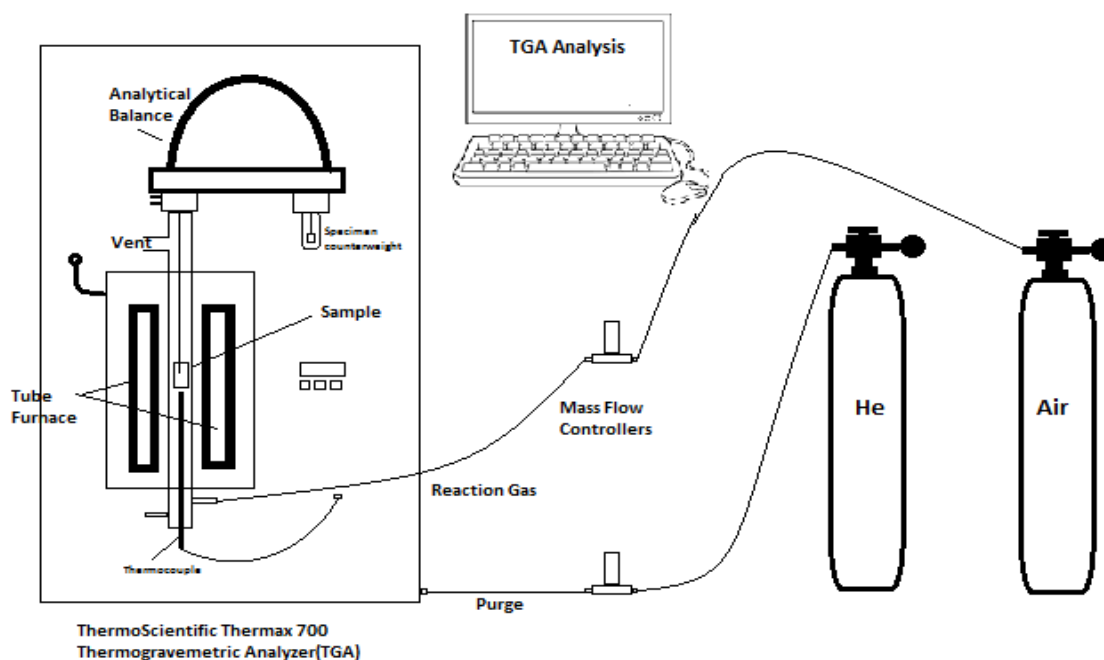
Figure 7. A schematic of the experimental system for studying oxidation of steel.

Figure 8. Photos of the experimental system for oxidation studies using TGA.

Samples were first heated in ultra-high purity helium at a constant rate of about 5 K/min until the desired oxidation temperature was reached, at which point the flow was switched to a 100% dry air environment. The 316L samples were oxidized at 773, 873, 973, 1073, 1173, and 1273 K for a duration of 24 h. The Alloy 617 samples were oxidized at 1073, 1173, 1273, 1373 and 1473 K for a duration of 24 h. The Incoloy 800-H samples were oxidized at 1073, 1173, 1273, 1373 and 1473 K for a duration of 24 h.

3.2.2. Scanning Electron Microscopy/Energy Dispersive X-Ray Spectroscopy

SEM and EDS analyses were obtained with FEI Quanta 600 FEG and the EDS detector was the Bruker XFlash® 6|30. The backscatter detector was used on all the images that had BSED indicated along the bottom. In addition, a low vacuum mode was used at 40 Pa for most of the images to reduce charging.

Additionally, high resolution images of pure samples were obtained using a Pioneer SEM/EDS in a secondary electron mode. It had multiple scanning modes, an accelerating voltage ranging 15, an image resolution of 512×440, an image pixel size of 0.17 µm, and a magnification of 1500 kV. Energy dispersive spectroscopy (EDS) quantitative surface elemental data was simultaneously available from Pioneer.

3.2.3. X-Ray Diffraction

XRD measurements were performed with PANalytical X'Pert Materials Research Diffractometer utilizing a Cu x-ray source. The XRD analysis was performed at room temperature at a scan speed of 0.4°/min and by varying the value of 2θ from 6.015° to 89.985°. The target was Cu, and a 1° slit was used for divergence and scattering.

CHAPTER 4. OXIDATION OF 316L STAINLESS STEEL AT HIGH TEMPERATURES IN AIR

4.1. Introduction

High-temperature oxidation of the nuclear reactor candidate material, molybdenum-based 316L stainless steel, was studied in different atmospheres. The tests were performed isothermally at temperatures between 773 K to 1273 K (in steps of 100 K) for 24 hours in controlled air environments. The oxidation behavior followed the parabolic oxidation kinetic rate law. The activation energy was found to be 149.21 kJ/mol for 873 K to 1273 K. At 773 K, a thin external oxide layer was observed, while at higher temperatures a continuous and relatively irregular and inwardly protruded external oxide layer was observed. The external layer width and composition depended on increasing temperatures. At 1073 K, a Cr_2O_3 layer was detected. After 1273 K, a Fe_2O_3 sub-layer formed in addition to the Cr_2O_3 layer. Continuous larger external oxide scales and grain boundary ridges were also observed with increasing temperatures. The oxide morphology and structure of 316L stainless steel were strongly affected by their environment.

The best oxidation resistance of 316L stainless steel was observed at 1073 K with the highest Cr content value. At 1273 K, mass gain was related to iron oxidation. Increasing oxidation temperatures were attributed to the formation of pores, voids, and grain boundaries. A thermogravimetric analyzer, scanning electron microscopy/energy dispersive x-ray spectroscopy, and x-ray diffraction were among the analytical techniques used.

Generation IV nuclear reactor systems pose significant challenges to materials selection and qualification. In these reactors, structural components will undergo varied service conditions such as (a) exposure to higher temperatures, (b) higher neutron doses, and (c) extremely corrosive environments[18]. These new challenges can affect the micro-structure of the materials and hence their properties[19]. Several Ni-based alloys are under serious consideration[20–22]. Ni-based alloys, such as Alloy 617, Haynes 230, are being considered for intermediate heat exchanger (IHX) and hot gas duct (HGD) due to excellent high temperature corrosion resistance, carburization, and decarburization conditions[23]. In these alloys, the formation of a protective external Cr oxide layer prevents the direct interaction between metal and environments. However, despite the excellent oxidation resistance, when the materials are exposed to high temperatures for prolonged period of operation, oxidation at the surface would be significant[23]. Then, oxidation would contribute to the mechanical property degradation of the alloys by metal loss, internal oxide formation, carburization, decarburization, and so forth.

Besides the above materials, austenitic stainless steels have been widely used as structural materials in nuclear power plants with excellent strength at high temperature and good oxidation/corrosion resistance[24]. The 316L stainless steel is an austenitic chromium-nickel-molybdenum steel. Grade SS-316L stainless steel (SS) is deemed suitable for some Generation IV reactor concepts. It is a candidate material for inner structural supports and radiation shielding in disposal waste packages[25].

Oxidation behavior depends on temperature, oxidative environment/surface, alloy composition, time, etc. Oxidation of austenitic stainless steel has already been studied by

several authors as a function of alloy composition[26–31], oxidative environment[32–35], temperature[24,29,31,33,36–46], and time[26,30]. These works show that such steels can form a stable, dense, continuous, adherent and protective oxide layer consisting of various oxides.

The oxidation resistance of stainless steel mainly depends on chromium content; thus, oxidation resistance increases with chromium content in steel composition[47]. The second factor is temperature. Heating and cooling can cause cracking and spalling of the steel surface. Alloy compositions have more Ni and Si, which increase resistance to oxidation; also, higher Ni and Mo content improve spalling resistance. 316L stainless steel is an austenitic chromium-nickel-molybdenum steel, which possesses superior strength and adequate resistance to oxidation at high temperatures. Oxidation at high temperature involves the oxidation of reactive elements, formation of oxide scales, and internal oxidation[48]. Chromium has been shown to be the key element to oxidation resistance[49]. 316L-SS contains greater than 17% Cr content. Chromium has a much greater affinity for oxygen relative to other elements in the alloy and preferentially forms chromium oxide, which gives an adherent, stable, and protective layer on the alloy surface that "protects" from further oxidation. The reaction kinetics and nature of the surface scales formed during oxidation are important for projecting the service life of alloys in reactor systems and also for evaluating degradation characteristics in high temperature applications[47]. Recent studies show that the oxidation kinetics of the austenitic stainless steel[50–52] and 316-SS[26,35] follows a parabolic law in the high temperatures.

The oxidation behavior of most stainless steels follow parabolic kinetics during high temperature oxidation. The thermal diffusion capability of the ionic areas through a compact oxide film and the driving force is the chemical potential gradient that develops across the film. The diffusion process is an outward diffusion of cations, an inward diffusion of anions, or both, and could possibly involve the transport of electrons across the oxide film[53].

Grade SS-316L has a particularly high resistance to pitting and crevice corrosion in chloride environments[54,55]. It also has excellent tolerance to radiation damage. Grade SS-316L is a low carbon version (> .03%) of Grade SS-316 and is immune from grain boundary carbide precipitation [56]. High-temperature corrosion studies of Grade SS-316L are lacking. Elevated temperatures tend to increase corrosion action, heat transfer may effect corrosivity, and thermal cycling can increase metal wasting through spallation on the metal surface.[57].

Corrosion of SS-316L as exposed to supercritical water[58,59], wet argon[60,61], and to Li_2BeF_4 [36] have been investigated earlier. Oxidation of coated SS-316L in air[33,62] has been investigated previously also, but the range of conditions studied was limited.

4.2. Results

4.2.1. Oxidation Kinetics

4.2.1.1. Oxidation Data 316L from TGA

Weight change of the samples was measured isothermally in the range of 773 K to 1273 K in 100% air. It was found that weight loss occurred at 773 K and at 873 K. However, at 973 K and above the samples gained weight. No spallation was observed in

the range of 773 K to 1073 K, although spallation was detected at 1173 K and 1273 K. The results are plotted in Fig. 9.
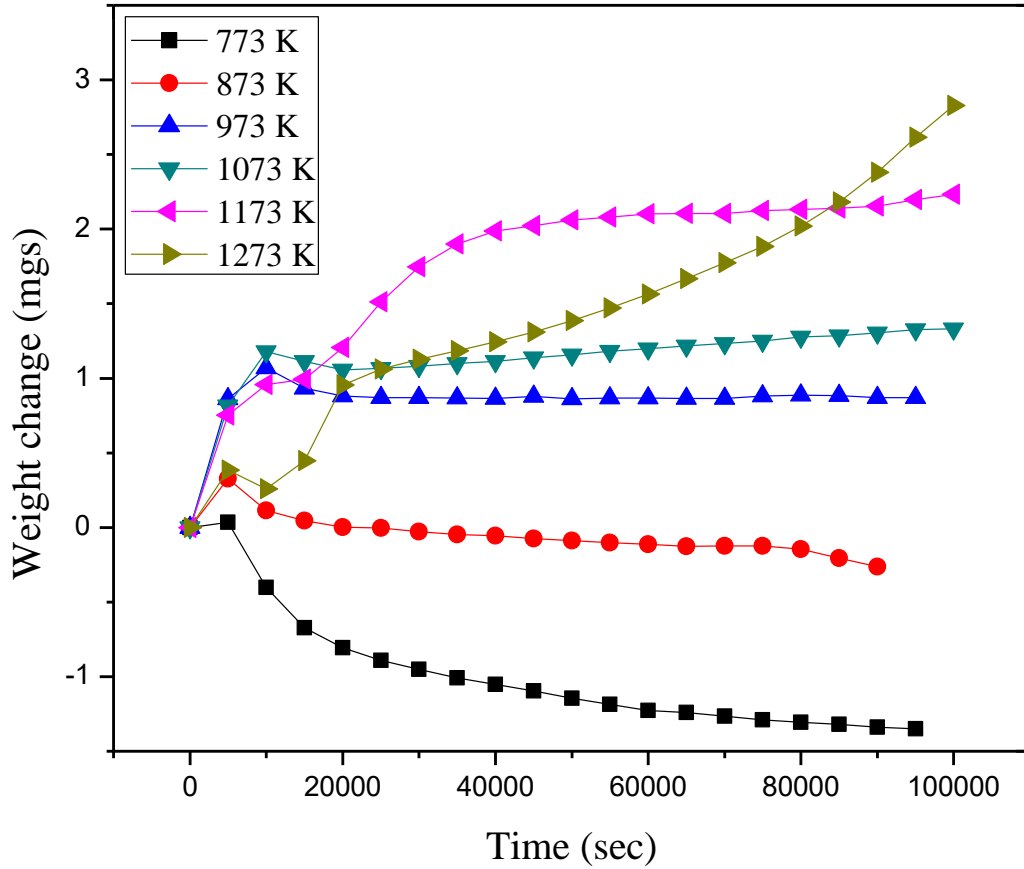
Figure 9. Oxidation of 316L SS in dry-medical grade air using TGA at 773 K to 1273 K.

Table 6 displays weight loss and weight gain data from TGA. Oxidation runs were performed more than twice to confirm the reliability and repeatability of the data.

Table 6. Total weight loss and weight gain after 24-hour air exposure.

Temperature (K)	Weight Loss (mg)	Weight Gain (mg)
773	-1.36	
873	-0.26	

973	0.87
1073	1.33
1173	2.23
1273	2.92

At 773 K and 873 K, weight loss was observed. At 773 K, the loss started after 100 min (600 sec) and continued for a duration of 24 hours. Surface morphology images show some dark grains. No spallation was observed. At 873 K, weight loss started after 400 min. The total weight loss is shown in Table 6. After 973 K weight gain was observed and the mass gain increased with increasing temperature. At 1173 K and 1273, scale spallation was detected.

4.2.1.2 Oxidation Kinetics

TGA plots of mass gain per unit area vs. time are shown in Fig. 10. Up to 1273 K the oxidation of SS-316L samples appears to follow parabolic kinetics.
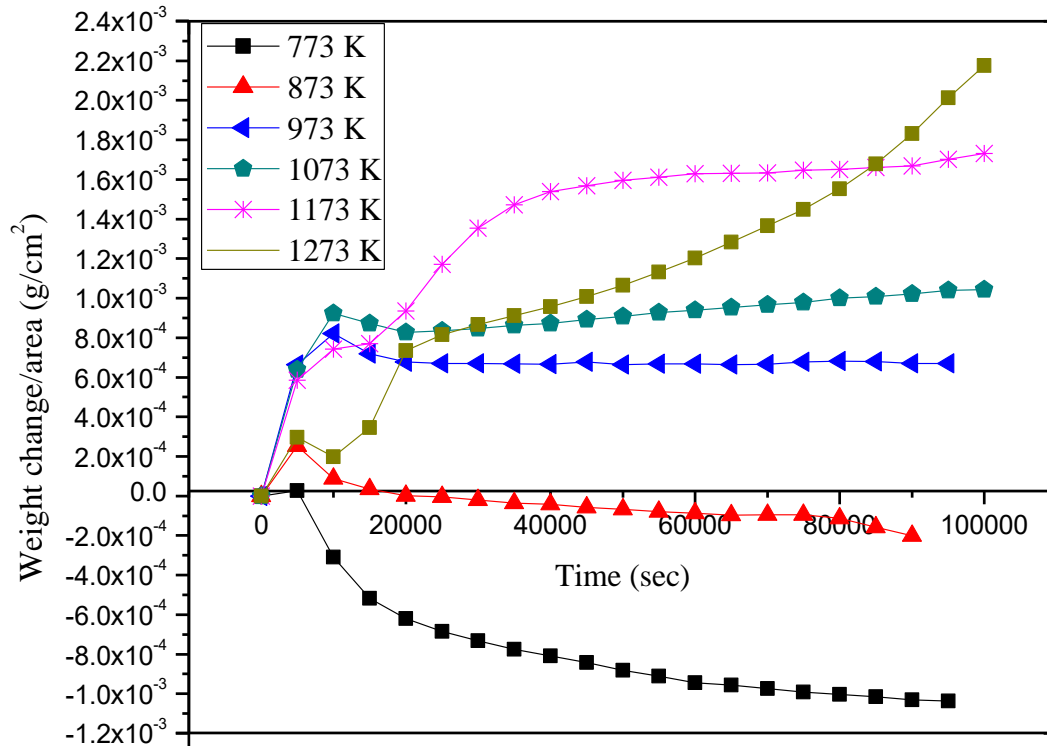
Figure 10. Oxidation kinetics for SS-316L plot of mass gain per unit area versus exposure time for temperatures in the range of 773 K ~1273 K. (t=0 concerted to the time when the sample reached set temperature).

Figure 11 shows the oxidation kinetics of 316L stainless steel as obtained by our measurements.

Equation	y = a + b*x				
Adj. R-Sq	0.9422	--	--	--	--
		Value	Standard Error	Value	Standard Error
773 K	Slope	2.096E-11	2.30622E-12	8.72627E-12	4.52694E-13
873 K	Slope	9.04385E-14	1.38448E-13	--	--
973 K	Slope	1.98967E-11	1.4331E-11	6.15181E-14	8.59251E-14
1073 K	Slope	3.44927E-11	1.54588E-11	5.36635E-12	8.03194E-14
1173 K	Slope	5.89769E-11	3.44456E-12	7.76408E-12	7.02543E-13
1273 K	Slope	2.54164E-11	1.22069E-12	8.74799E-11	7.92994E-12
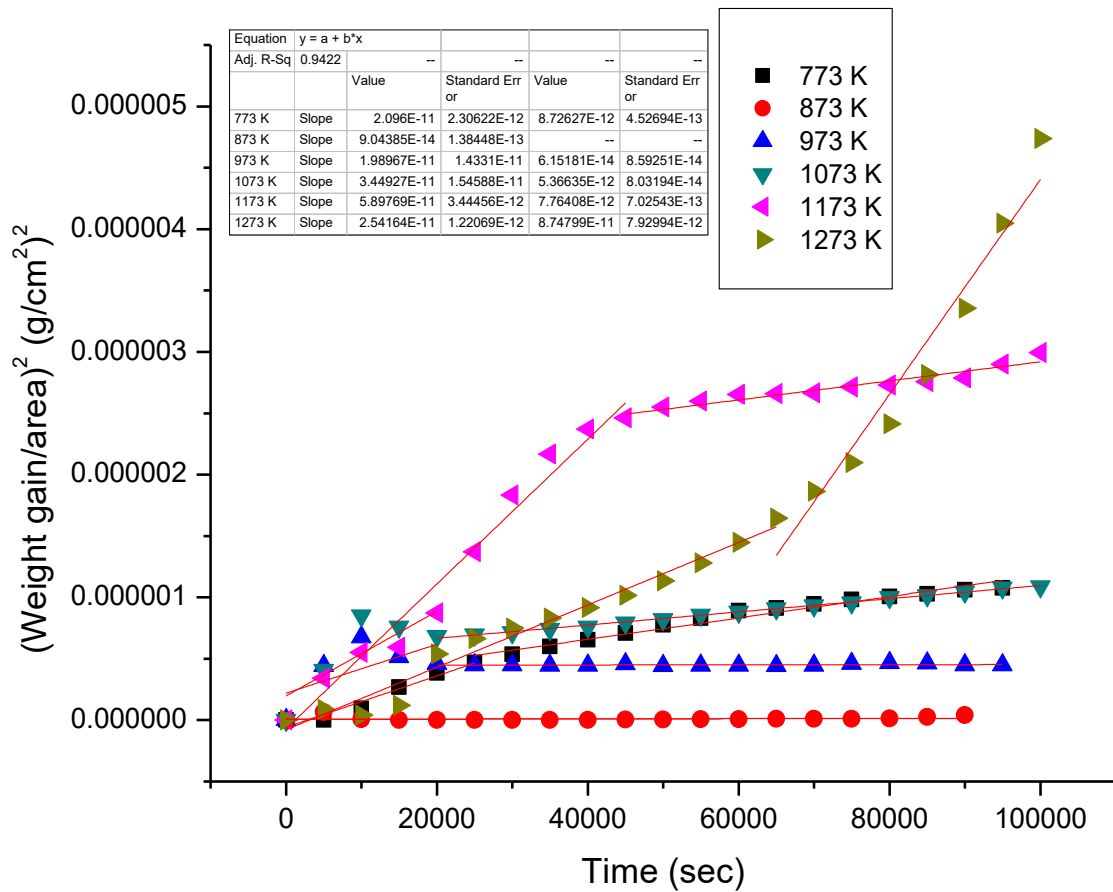
Figure 11. Oxidation kinetics for SS-316L plot of (mass gain per unit area) 2 versus exposure time for temperatures in the range of 773 K ~1273 K. (t = 0 converting to the time when the sample reached the set temperature).

Table 7. Experimental parabolic oxidation rate constant, kp of SS-316L.

Temperature (K)	k value (g^2m^{-4} sec^{-1})			
773 K	$2.096x10^{-11}$	t < 20000 sec	$8.72627x10^{-12}$	t > 20000 sec
873 K	$9.04385x10^{-14}$	-	-	-
973 K	$1.98967x10^{-11}$	t < 20000 sec	$6.15181x10^{-14}$	t > 20000 sec
1073 K	$3.44927x10^{-11}$	t < 20000 sec	$5.36635x10^{-12}$	t > 20000 sec
1173 K	$5.89769x10^{-11}$	t < 40000 sec	$7.76408x10^{-12}$	t > 40000 sec
1273 K	$2.54164x10^{-11}$	t < 65000 sec	$8.74799x10^{-11}$	t > 65000 sec

Table 7 shows the data on parabolic relationship where a best fitting line passed through the origin giving a k value of 773 K to 1273 K.

4.2.1.3. Activation Energy

The rate constant k normally depends upon temperature per the Arrhenius equation. Fig. 12 shows a graph in which ln k is plotted against 1/RT with a slope of –Q. The activation energy of oxidation reaction Q for a parabolic rate of oxidation SS-316L is 149.21 kJ/mol (873 K to 1273 K). In the literature, activation energy values ranging from 83 to 138 kJ mol^{-1} have been reported for the low-temperature regime in austenitic stainless steels and high Ni alloys[63–65].

	Value	Standard Error
Intercept	-8.7000	2.40133
Slope	-2.6593	2.352
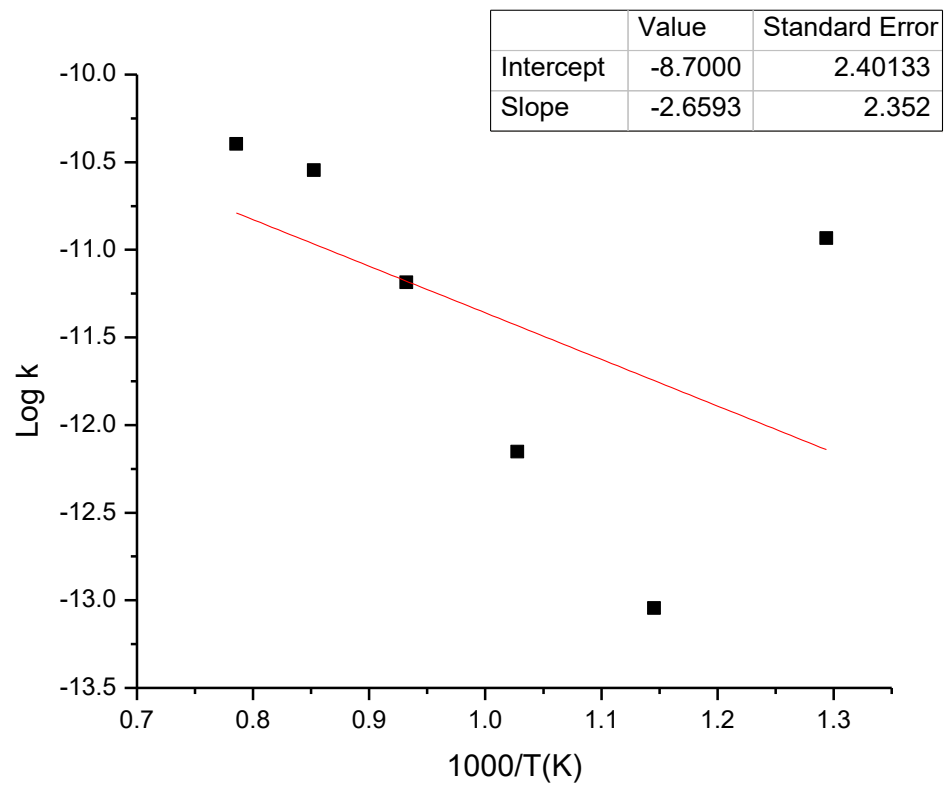
Figure 12. Arrhenius plot and exhibited activation energy (773 K-1273 K).

Equation	y = a + b*x		
Adj. R-Square	0.97396		
		Value	Standard Error
--	Intercept	-4.06818	0.60812
--	Slope	-7.79661	0.63533
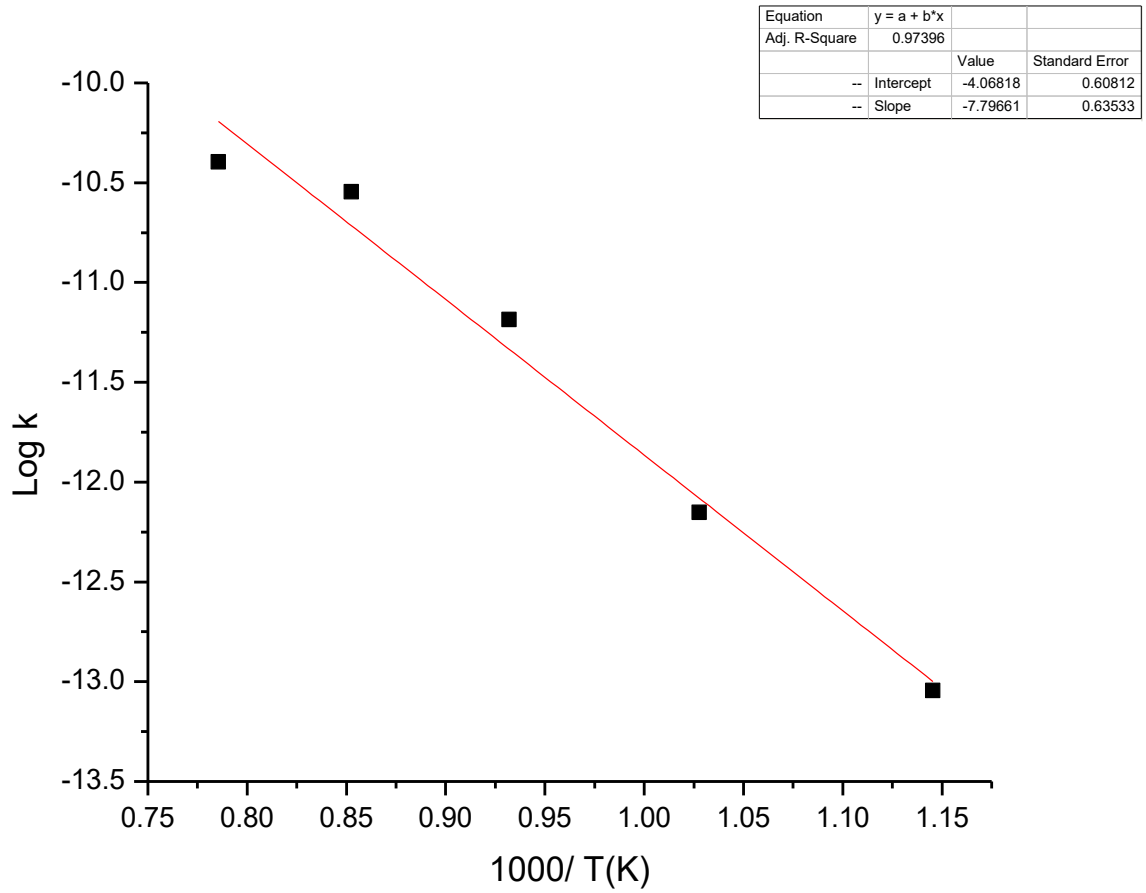
Figure 13. Arrhenius plot and exhibited activation energy (873 K to 1273 K).

4.2.2. Oxidation Microstructure (Surface Analysis) with Scanning electron microscopy/energy dispersive X-ray spectroscopy (SEM/EDS)

4.2.2.1. Room Temperature (297 K)

The SEM images of SS-316L exposed to air atmosphere at the temperature of 297 K are shown in Fig. 14. and the corresponding EDS figures are shown in Fig. 15. The scratches on the sample appeared after it was reground with 400 grit silicon-carbide paper.
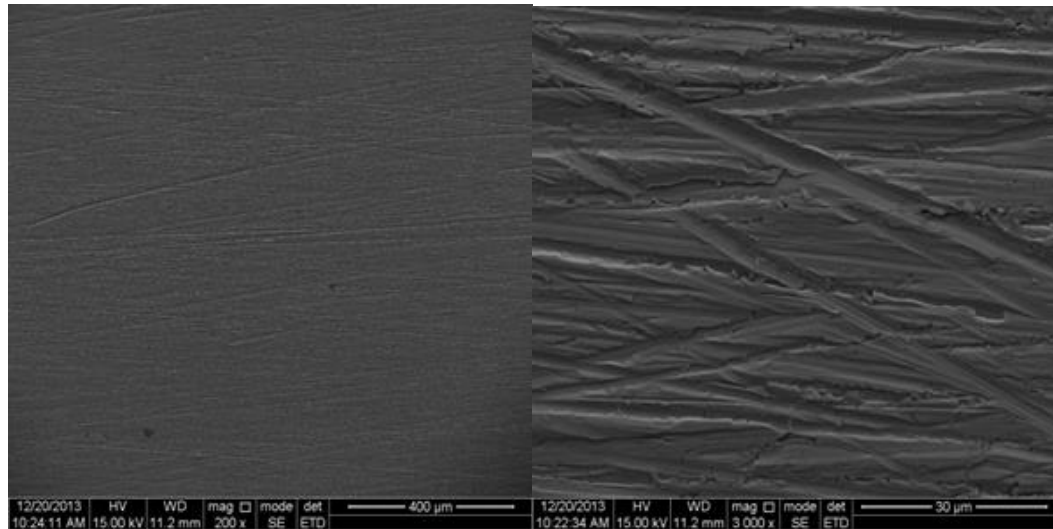
Figure 14. The SEM images of 316L SS sample exposed to air atmosphere at the 297 K
temperature are shown here as a) 400 µm and b) 30 µm.
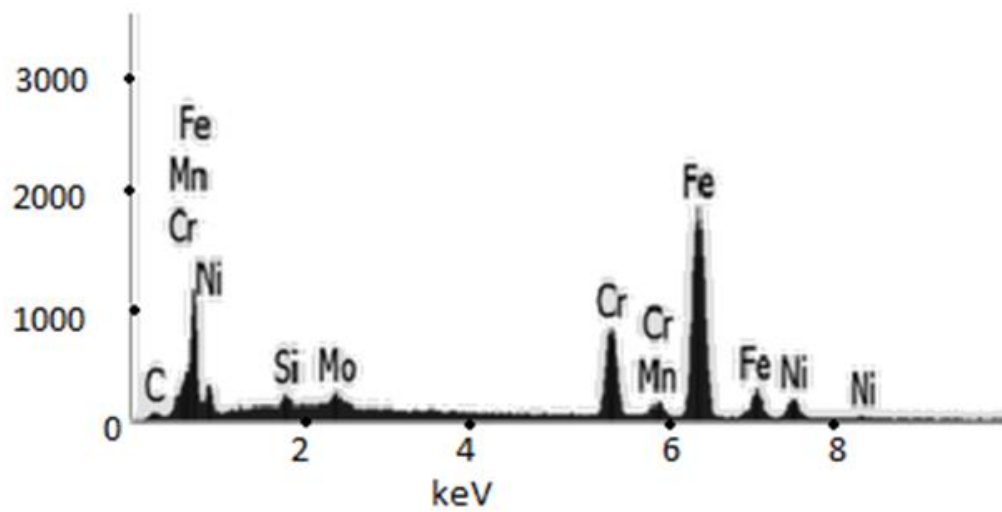
Figure 15. EDS spectrum of 316L SS sample at 297 K.

4.2.2.2. 773 K

The surface morphology of oxidized samples indicated deposits over the surface as seen in Fig. 16. Some of the deposits had less Cr, while the plain surface of the sample had high Cr content. This clearly indicates the selective outward diffusion of Cr.
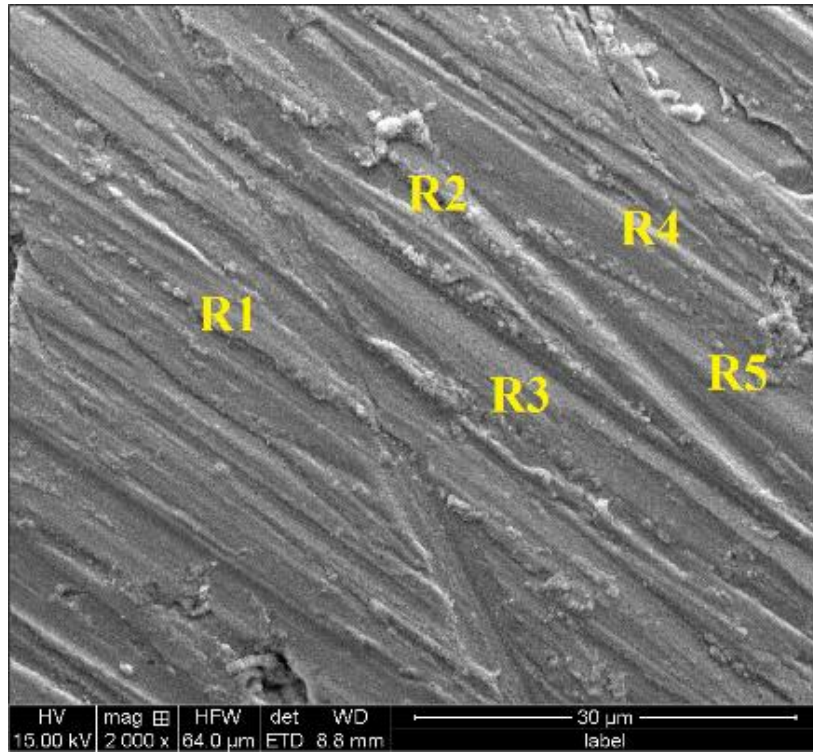
Figure 16. Surface morphology of 316L stainless steel at 773 K and EDS spectrum.
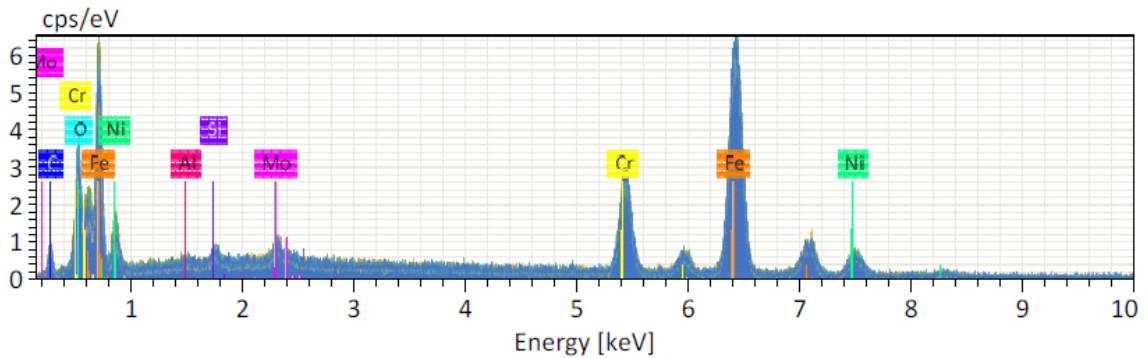
Figure 17. At 773K, EDS spectrum of 316L stainless steel

Tables 8-9 show the atomic and mass percent of different regions as analyzed by EDS. Table 8 shows that the sample is composed of mainly 52.87% Fe, 12.51% Cr, 7.33% Ni, and 11.37% C by atomic percent. According to Table 9, the sample contained 65.44% Fe, 14.41% Cr, 9.54% Ni, 3.03% C by mass percent.

Table 8. Surface morphology atomic percent analysis on the five different locations on the surface at 773 K

Element	C	O	Al	Si	Cr	Mn	Fe	Cu	Ni	Mo
R1	10.78	17.18	0.27	0.80	11.81	-	51.20	-	7.03	0.92
R2	15.32	10.55	0.25	0.76	11.97	-	52.51	-	7.67	0.97
R3	9.03	15.84	0.36	0.68	12.80	-	52.70	-	7.58	1.01
R4	10.51	12.82	0.19	0.91	13.06	-	54.14	-	7.49	0.90
R5	11.24	13.28	0.17	0.84	12.92	-	53.79	-	6.90	0.86
Mean (Absolute deviation)	11.37	13.94	0.25	0.80	12.51	-	52.87	-	7.33	0.93
Sigma (Standard deviation)	2.35	2.61	0.08	0.08	0.58	-	1.16	-	0.35	0.06

Table 9. Surface morphology mass percent analysis on the surface of steel at 773 K.

Element	C	O	Al	Si	Cr	Mn	Fe	Cu	Ni	Mo
R1	2.94	6.24	0.17	0.51	13.93	-	64.86	-	9.36	2.00
R2	4.11	3.77	0.15	0.48	13.89	-	65.47	-	10.05	2.08
R3	2.39	5.58	0.21	0.42	14.65	-	64.81	-	9.80	2.14
R4	2.75	4.47	0.11	0.56	14.79	-	65.88	-	9.58	1.87
R5	2.97	4.68	0.10	0.52	14.80	-	66.19	-	8.92	1.82
Mean (Absolute deviation)	3.03	4.95	0.15	0.50	14.41	-	65.44	-	9.54	1.98
Sigma (Standard deviation)	0.64	0.97	0.05	0.05	0.46	-	0.61	-	0.43	0.13
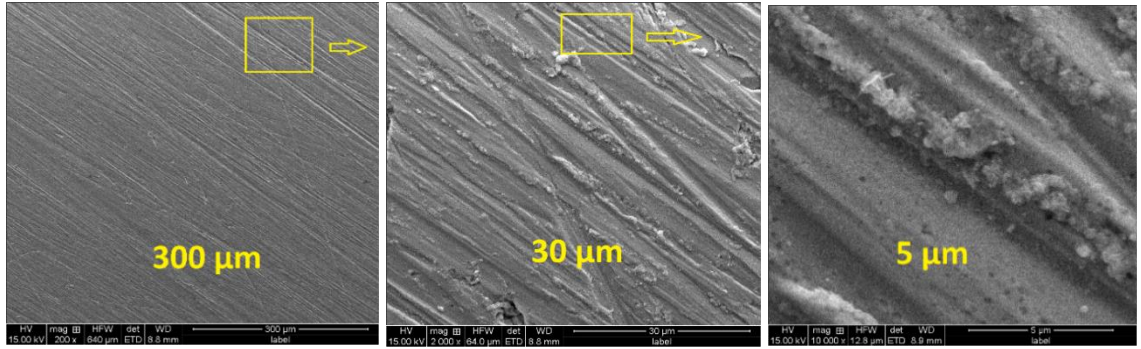
Figure 18. SEM images show surface morphology samples at 773 K, at 300 µm, 30 µm and 5 µm.

Figure 18 shows that at grain boundaries, high surface relief protrusions are present. Some grain boundaries leaning forward on adjacent grains are also observed. No scale spallation was observed.

4.2.2.3. 873 K

The SEM surface images and EDS intensity peaks corresponding to 873 K are shown in Figure 19. The EDS intensity peaks corresponding to the developed scale are dominated by Cr and Fe peaks (Figure 20).
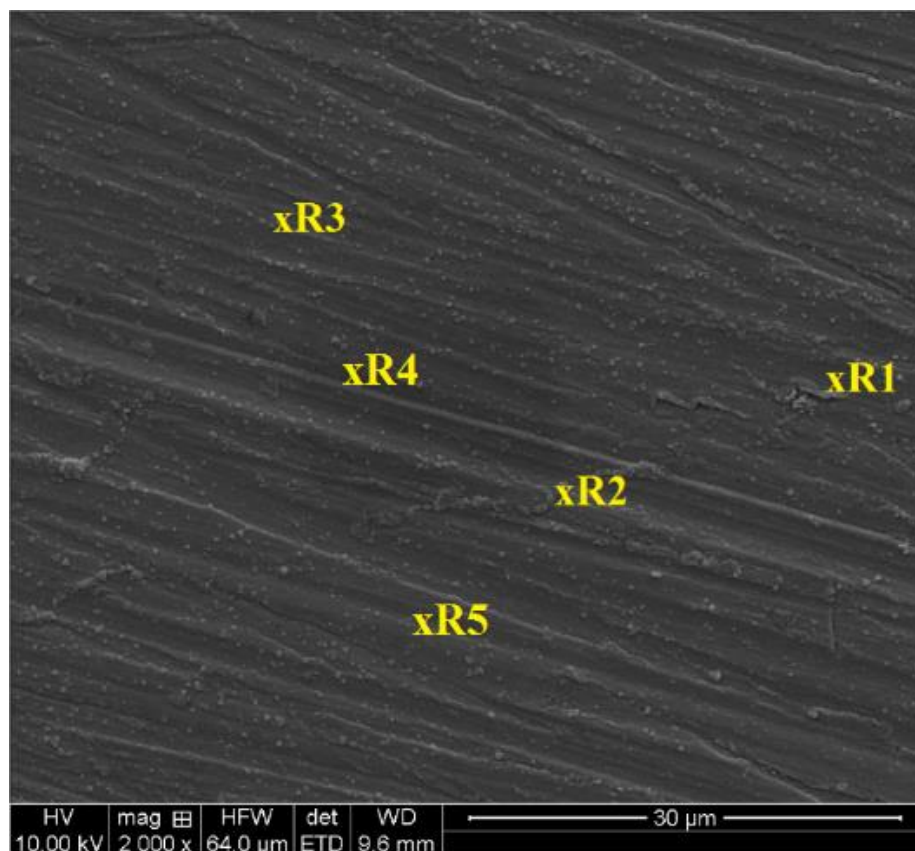
Figure 19. Surface morphology of 316L stainless steel at 873 K.
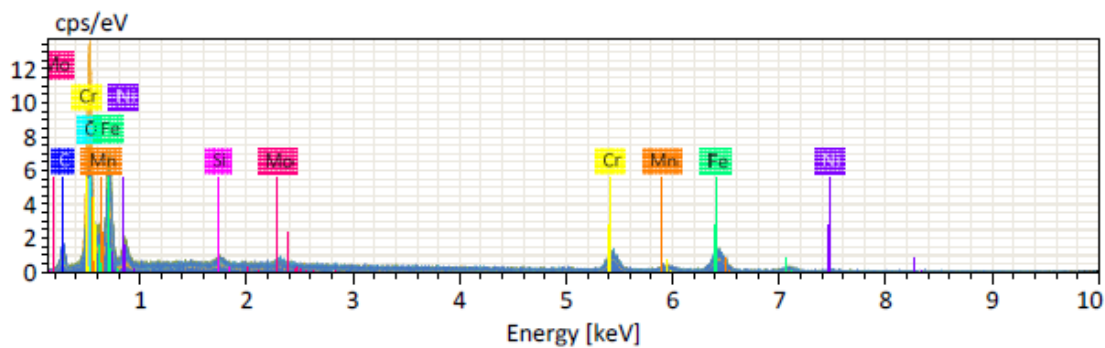
Figure 20. EDS results of 316L stainless steel at 873K.

EDS analyses performed on the surface are given in Figure 20 and Tables 10-11. Table 10 shows that the sample is composed of mainly 38.00% Fe, 14.94% Cr, 3.79% Ni, and 8.35% C by atomic percent. According to Table 11, the sample contains 3.11% Fe, 19.67% Cr, 5.48% Ni, and 2.57% C by mass percent.

Table 10. Elemental atomic percentages from EDS surface morphology analysis for five different locations on the surface at 873 K.

Element	C	O	Al	Si	Cr	Mn	Fe	Cu	Ni	Mo
R1	6.54	24.03	-	1.33	16.32	1.91	44.35	-	4.90	0.60
R2	3.61	52.79	-	0.82	11.50	2.54	27.78	-	0.63	0.33
R3	6.24	24.10	-	1.49	18.11	1.78	43.00	-	3.96	1.33
R4	8.64	26.66	-	1.33	15.14	2.39	39.72	-	5.58	0.53
R5	16.73	26.44	-	1.54	13.65	2.27	35.13	-	3.87	0.37
Mean (Absolute deviation)	8.35	30.80	-	1.30	14.94	2.18	38.00	-	3.79	0.63
Sigma (Standard deviation)	5.01	12.35	-	0.29	2.52	0.32	6.73	-	1.90	0.41

Table 11. Surface morphology mass percent analysis on the surface at 873 K.

Element	C	O	Al	Si	Cr	Mn	Fe	Cu	Ni	Mo
R1	1.84	8.99	-	0.88	19.85	2.45	57.92	-	6.73	1.35
R2	1.33	25.84	-	0.71	18.30	4.27	47.47	-	1.13	0.96
R3	1.74	8.96	-	0.97	21.88	2.27	55.82	-	5.40	2.96
R4	2.54	10.44	-	0.92	19.28	3.22	54.33	-	8.03	1.25
R5	5.39	11.35	-	1.16	19.05	3.35	52.65	-	6.10	0.95
Mean (Absolute deviation)	2.57	13.12	-	0.93	19.67	3.11	53.64	-	5.48	1.49
Sigma (Standard deviation)	1.64	7.18	-	0.17	1.36	0.80	3.95	-	2.61	0.84
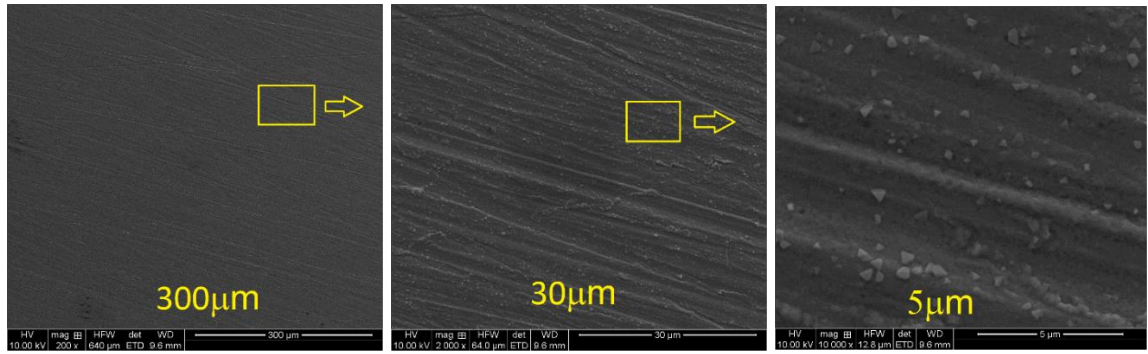
Figure 21. SEM surface morphology at 873 K, at 300 µm, 30 µm and 5 µm.

According to Fig. 21, oxide scale spallation was not observed on the surface in the SEM images. The surface was observed to have nodular grains. Grain regions are untidy and some grains are distantly relative to each other.

4.2.2.4. 973 K-1073 K

An oxide grained structure was found after 973 K and 1073 K. Figures 22 and 24 show a scale. At 973 K, the scale contained predominantly Cr and Mn peaks. At 1073 K, the scale contained predominantly Cr and Fe peaks (Figures 23 and 25).
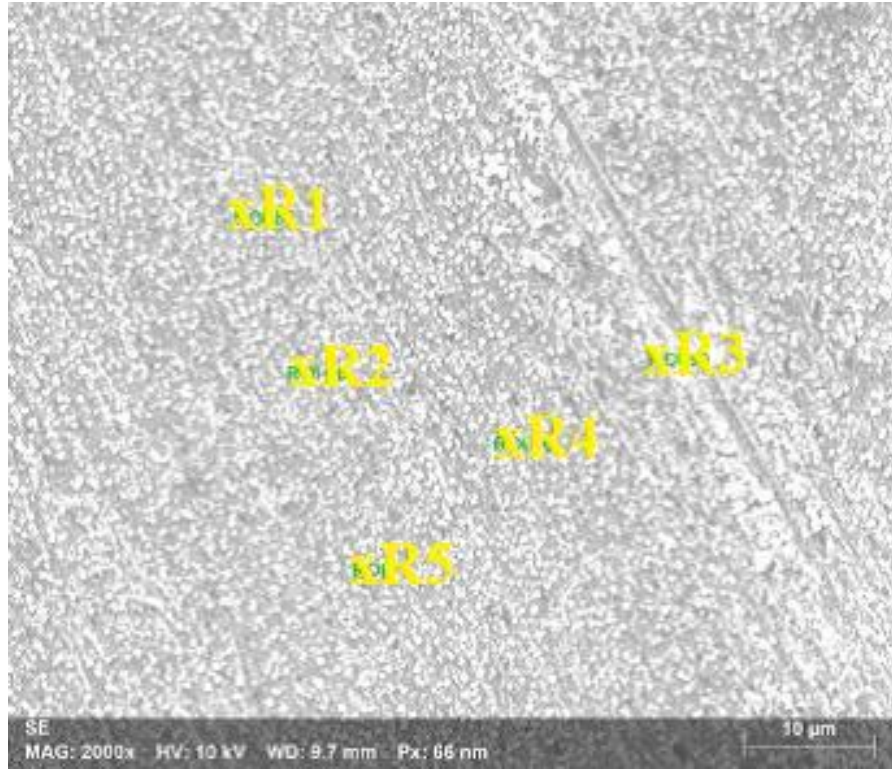
Figure 22. SEM surface morphology of 316L stainless steel at 973 K.
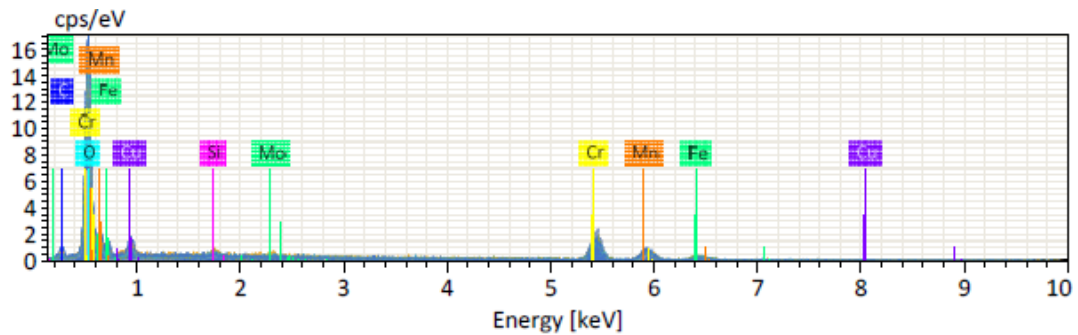
Figure 23. EDS Results of 316L stainless steel at 973K.

Table 12 shows that the sample is composed of mainly 26.95% Cr, 7.82% Mn, and 5.89% Fe by atomic percent. According to Table 13, the sample contains 43.16% Cr, 13.53% Mn, and 10.12% Fe by mass percent.

Table 12. Surface morphology atomic percent analysis in the five different locations on

the surface at 973 K.

Element	C	O	Al	Si	Cr	Mn	Fe	Cu	Ni	Mo
R1	1.32	55.00	-	1.14	24.51	10.35	5.45	2.10	-	0.13
R2	1.15	52.57	-	2.43	24.97	8.33	8.28	2.09	-	0.18
R3	0.31	50.30	-	1.09	41.56	0.00	6.47	0.03	-	0.24
R4	3.09	54.26	-	1.90	21.93	9.58	6.77	2.22	-	0.24
R5	4.72	55.78	-	0.99	21.76	10.86	2.47	3.38	-	0.05
Mean (Absolute deviation)	2.12	53.58	-	1.51	26.95	7.82	5.89	1.96	-	0.17
Sigma (Standard deviation)	1.77	2.19	-	0.63	8.30	4.48	2.17	1.21	-	0.08

Table 13. Surface morphology mass percent analysis on the surface at 973 K.

Element	C	O	Al	Si	Cr	Mn	Fe	Cu	Ni	Mo
R1	049	27.32	-	0.99	39.57	17.65	9.45	4.14	-	0.40
R2	0.42	25.55	-	2.07	39.45	13.90	14.05	4.04	-	0.53
R3	0.11	23.76	-	0.91	63.82	0.00	10.67	0.05	-	0.68
R4	1.17	27.40	-	1.68	36.00	16.62	11.94	4.45	-	0.74
R5	1.85	29.15	-	0.90	36.95	19.49	4.50	7.01	-	0.15
Mean (Absolute deviation)	0.81	36.64	-	1.31	43.16	13.53	10.12	3.94	-	0.50
Sigma (Standard deviation)	0.70	2.05	-	0.54	11.65	7.83	3.57	2.49	-	0.23
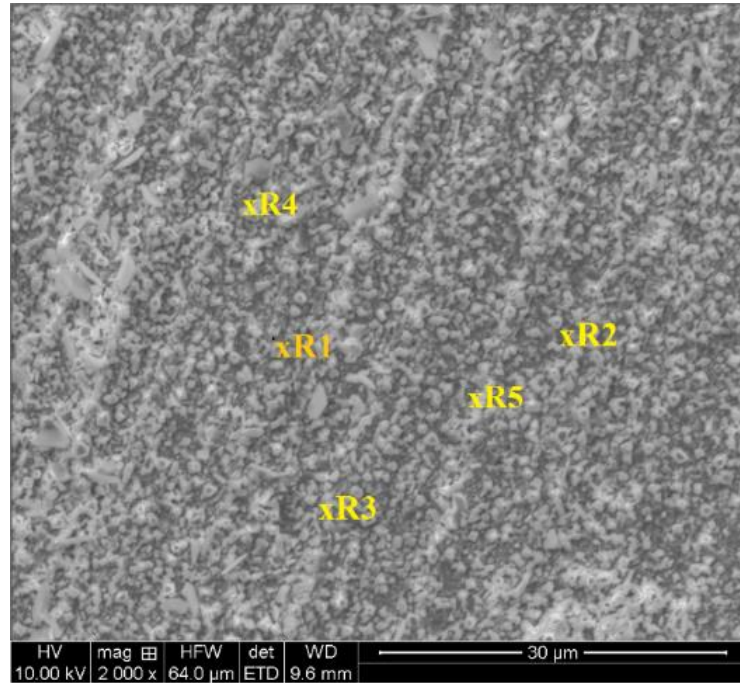
Figure 24. Surface morphology of 316L stainless steel at 1073 K.
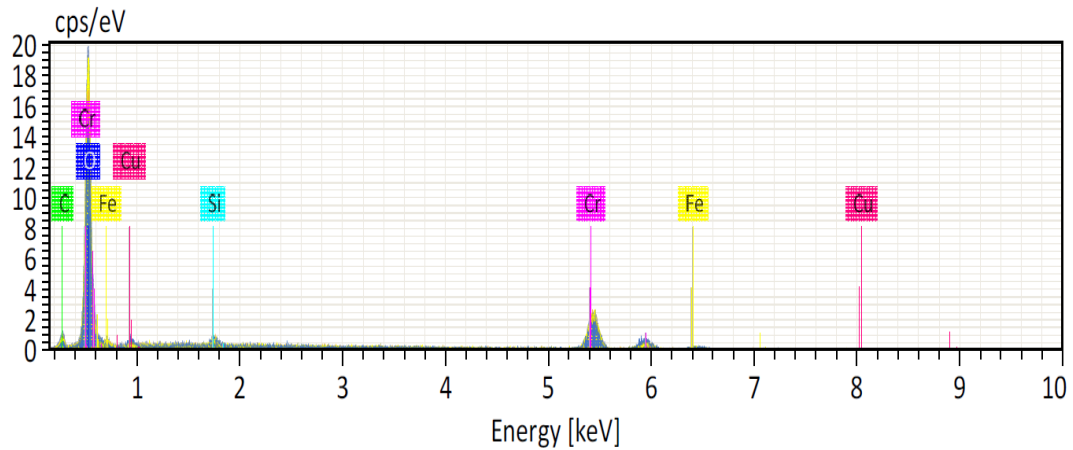
Figure 25. EDS results of 316L stainless steel at 1073K.

Table 14 shows that the sample is composed of mainly 31.52% Cr, 3.63% Fe, and 5.17% C.by atomic percent. According to Table 15, the sample contains 56.68% Cr, 7.00% Fe, and 2.15% C by mass percent.

Table 14. Surface morphology atomic percent analysis in the five different locations on the surface at 1073 K.

Element	C	O	Al	Si	Cr	Mn	Fe	Cu	Ni	Mo
R1	6.68	51.06	-	0.73	37.08	-	4.14	0.31	-	-
R2	5.84	60.41	-	1.37	30.00	-	2.33	0.05	-	-
R3	3.27	59.89	-	2.07	29.10	-	5.12	0.55	-	-
R4	3.97	60.99	-	1.22	30.08	-	3.67	0.08	-	-
R5	6.10	57.95	-	1.47	31.34	-	2.91	0.24	-	-
Mean (Absolute deviation)	5.17	58.06	-	1.37	31.52	-	3.63	0.25	-	-
Sigma (Standard deviation)	1.47	4.08	-	0.49	3.21	-	1.08	0.20	-	-

Table 15. Surface morphology mass percent analysis on the surface at 1073 K.

Element	C	O	Al	Si	Cr	Mn	Fe	Cu	Ni	Mo
R1	2.59	26.38	-	0.66	62.27	-	7.46	0.63	-	-
R2	2.53	34.92	-	1.39	56.35	-	4.69	0.12	-	-
R3	1.36	33.16	-	2.02	52.36	-	9.89	1.21	-	-
R4	1.68	34.46	-	1.21	55.23	-	7.24	0.17	-	-
R5	2.57	32.54	-	1.45	57.19	-	5.70	0.54	-	-
Mean (Absolute deviation)	2.15	32.29	-	1.35	56.68	-	7.00	0.53	-	-
Sigma (Standard deviation)	0.58	3.44	-	0.49	3.62	-	1.98	0.44	-	-
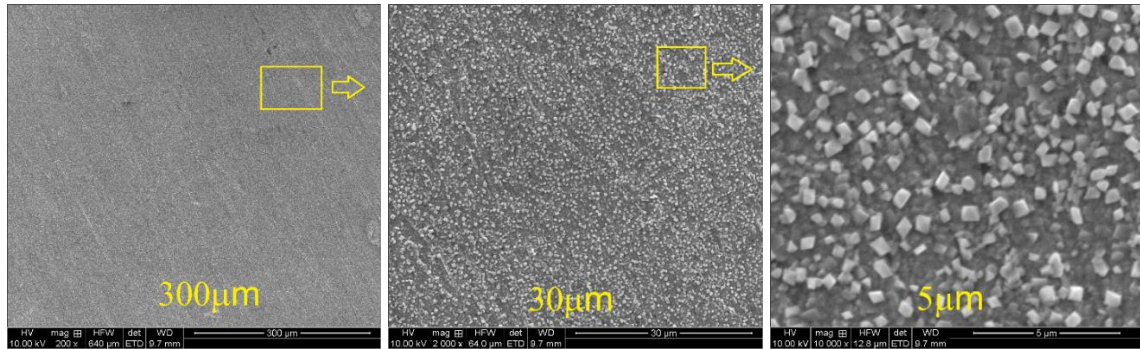
Figure 26. Surface morphology at 973 K, at 300 µm, 30 µm and 5µm.
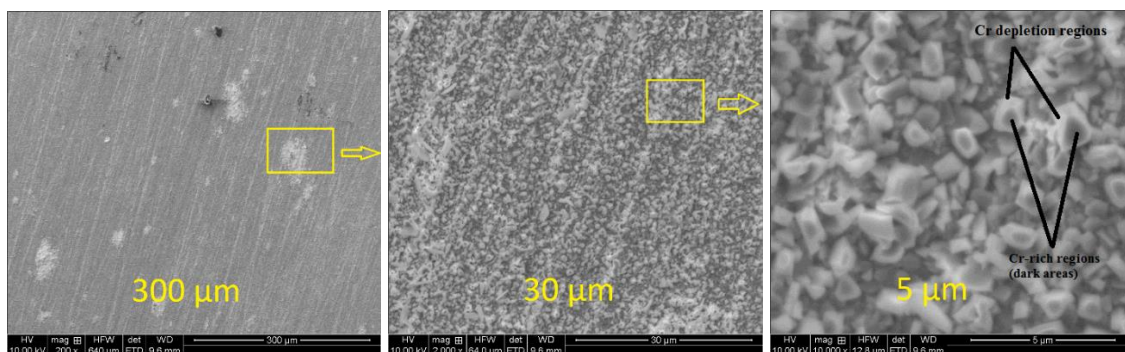
Figure 27. Surface morphology at 1073 K, at 300µm, 30µm and 5µm.

The SEM images of 973 K are shown in Fig. 26. Additionally, 1073 K are shown in Fig. 27. SEM images of the samples show the polishing lines all over the surface, in addition to Cr depletion and Cr-rich regions in Fig. 27.

A fine oxide-grained structure developed in the sample after exposure to air. The scale was found to be highly adherent as no spalling was observed on the sample (Fig. 27).

4.2.2.5. 1173 K-1273 K

The surface morphology of the scale formed at 1173 K is shown in Fig. 28 and at 1273 K is shown in Fig. 30. Scale spallation was observed at both temperatures. Interestingly, this scale exhibits large flat crystals and small grains at 1173 K. EDS analysis of the sample was performed at 1173 K as shown in Fig. 29. EDS analysis indicates that the sample contains mainly Cr and Fe and small amounts of Mn and C are also present.

SEM micrographs and corresponding EDS spectra come from five different random regions of one sample. The SEM micrograph shows five regions of faceted grains over porous, flaky oxidation products. The EDS spectrum of faceted grains shown in Figs. 29 and 30 are similar except for their Cr and Fe content. The composition of grains as analyzed by EDS have their atomic percentages listed in Tables 16 and 18, besides mass percentages, which are listed in Table 17 and 19.
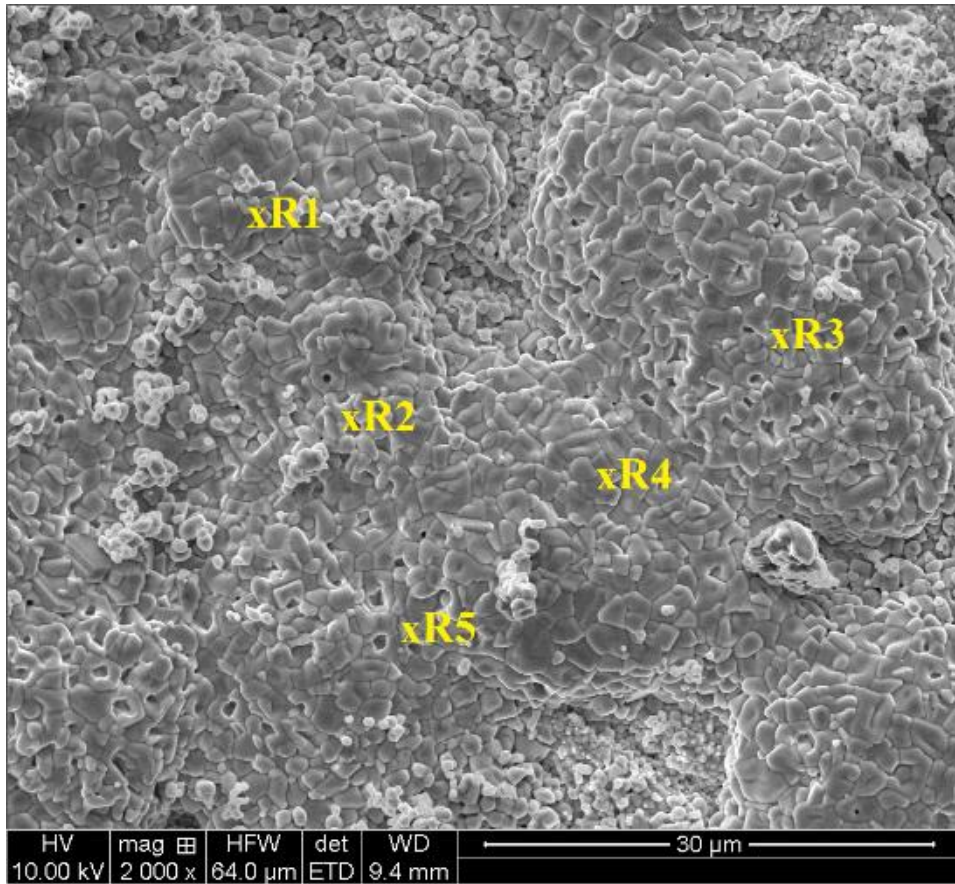
Figure 28. Surface morphology of 316L stainless steel sample at 1173 K
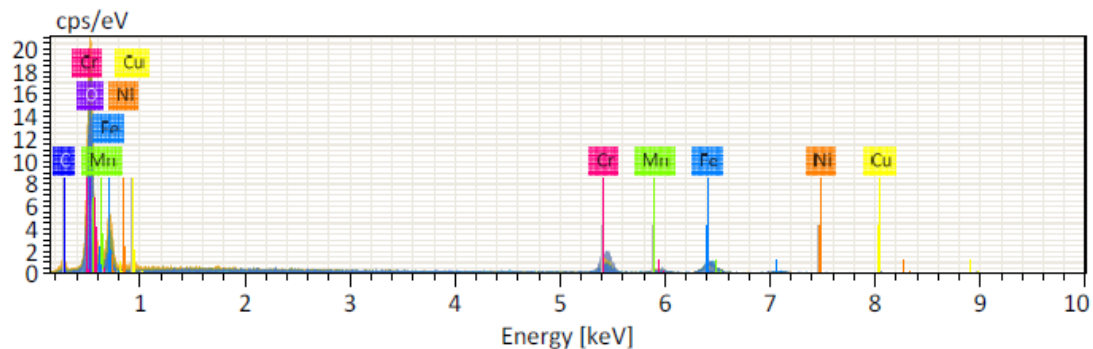
Figure 29. EDS spectrum of 316L stainless steel at 1173 K.

Table 16 shows that the sample is composed of mainly 26.29% Fe, 18.61% Cr, 1.98% C, and 1.85% Mn by atomic percent. According to Table 17, the sample contains 12.51% Fe, 27.57% Cr, 0.78% C, and 3.10% Mn by mass percent.

Table 16. Surface morphology atomic percent analysis in five different locations on sample surface at 1173 K.

Element	C	O	Al	Si	Cr	Mn	Fe	Cu	Ni	Mo
R1	1.12	33.31	-	-	16.82	2.60	45.91	0.12	0.12	-
R2	2.32	62.08	-	-	11.14	1.48	22.83	0.01	0.15	-
R3	0.52	39.14	-	-	41.44	0.52	18.29	0.09	0.00	-
R4	4.97	61.83	-	-	13.28	2.64	16.02	0.85	0.42	-
R5	0.97	58.12	-	-	10.40	2.02	28.39	0.00	0.10	-
Mean (Absolute deviation)	1.98	50.90	-	-	18.61	1.85	26.29	0.21	0.16	-
Sigma (Standard deviation)	1.80	13.64	-	-	13.00	0.88	11.95	0.36	0.16	-

Table 17. Surface morphology mass percent analysis on sample surface at 1173 K.

Element	C	O	Al	Si	Cr	Mn	Fe	Cu	Ni	Mo
R1	0.32	12.87	-	-	21.11	3.45	61.89	0.18	0.18	-
R2	0.94	33.49	-	-	19.53	2.75	42.99	0.01	0.29	-
R3	0.16	16.30	-	-	56.07	0.75	26.58	0.14	0.00	-
R4	2.09	34.62	-	-	24.16	5.08	31.30	1.88	0.87	-
R5	0.37	29.20	-	-	16.98	3.49	49.79	0.00	0.18	-
Mean (Absolute deviation)	0.78	25.29	-	-	27.57	3.10	12.51	0.44	0.30	-

| Sigma (Standard deviation) | 0.79 | 10.06 | - | - | 16.14 | 1.57 | 14.21 | 0.81 | 0.33 | - |
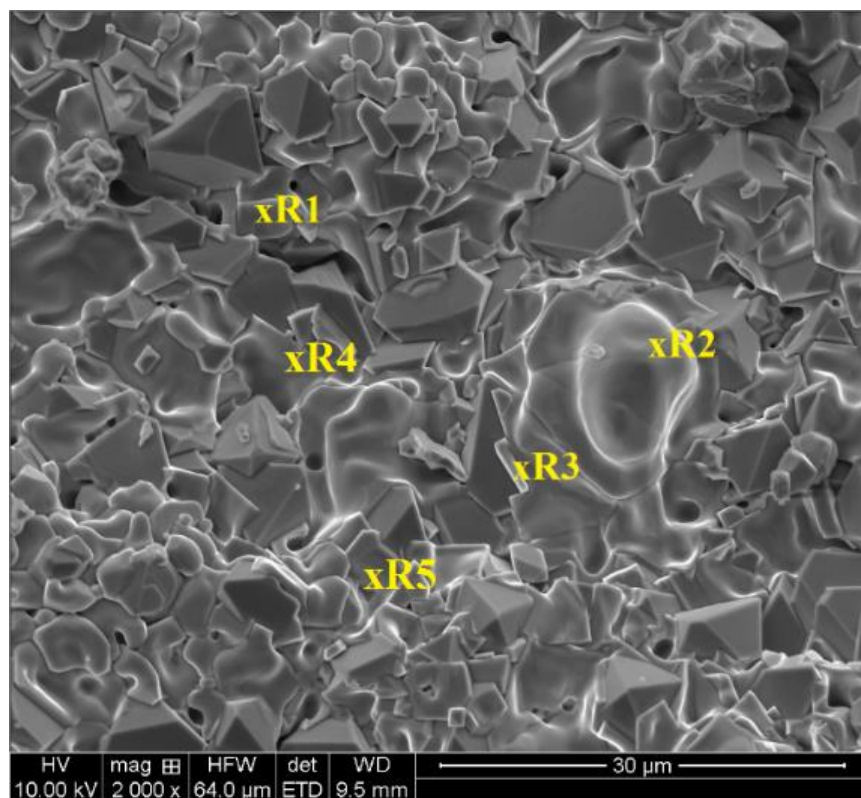
Figure 30. Surface morphology of 316L stainless steel sample at 1273K.
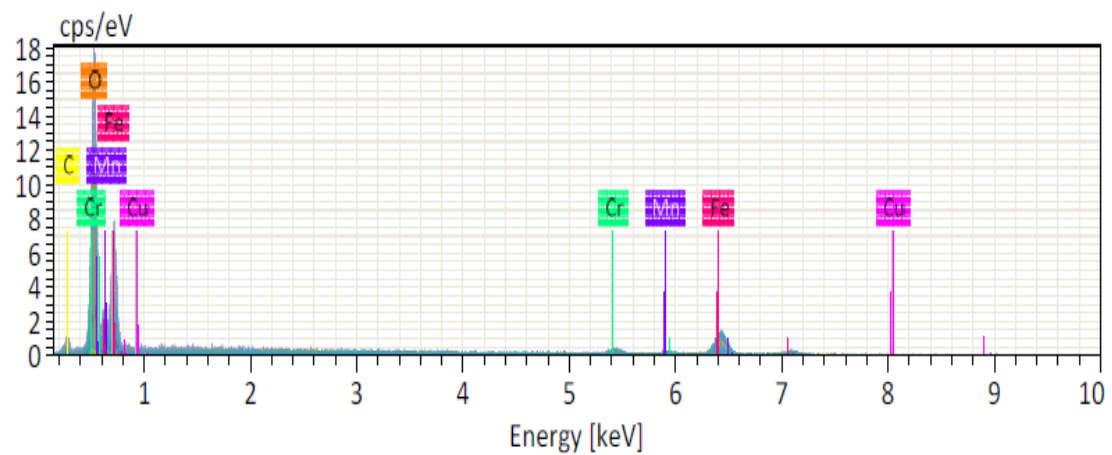
Figure 31. EDS spectrum of 316L stainless steel sample at 1273 K.

Table 18 shows that the sample is composed of mainly 54.11% Fe, 3.45%Cr, 3.41% Mn, and 2.75% C by atomic percent. However, Table 19, shows the sample containing 73.12% Fe, 4.28% Cr, 0.96% C, and 4.50% Mn by mass percent.

Table 18. Surface morphology atomic percent analysis in the five different locations on the 316L stainless steel sample surface at 1273 K.

Element	C	O	Al	Si	Cr	Mn	Fe	Cu	Ni	Mo
R1	2.68	46.29	-	-	3.08	2.54	45.22	0.22	-	-
R2	5.73	59.23	-	-	0.99	1.98	31.87	0.19	-	-
R3	0.88	2.97	-	-	4.17	5.54	86.44	0.00	-	-
R4	2.44	49.96	-	-	2.91	2.54	41.73	0.44	-	-
R5	2.03	22.03	-	-	6.08	4.44	65.28	0.15	-	-
Mean (Absolute deviation)	2.75	36.09	-	-	3.45	3.41	54.11	0.20	-	-
Sigma (Standard deviation)	1.80	23.05	-	-	1.87	1.51	21.77	0.16	-	-

Table 19. Surface morphology mass percent analysis on the 316L stainless steel sample surface at 1273 K.

Element	C	O	Al	Si	Cr	Mn	Fe	Cu	Ni	Mo
R1	0.89	20.49	-	-	4.44	3.86	69.93	0.38	-	-
R2	2.32	31.91	-	-	1.74	3.66	59.95	0.41	-	-
R3	0.19	0.88	-	-	4.01	5.63	89.28	0.00	-	-
R4	0.84	22.99	-	-	4.34	4.01	67.02	0.80	-	-
R5	0.53	7.68	-	-	6.89	5.31	79.39	0.20	-	-
Mean (Absolute deviation)	0.96	16.79	-	-	4.28	4.50	73.12	0.36	-	-
Sigma (Standard deviation)	0.81	12.42	-	-	1.83	0.91	11.42	0.30	-	-
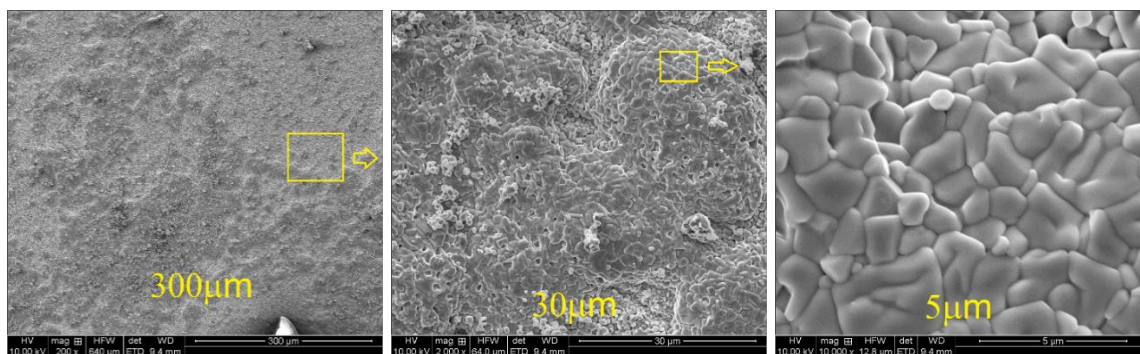
Figure 32. Surface morphology of 316L stainless steel sample at 1173 K of 300 µm, 30 µm and 5 µm.
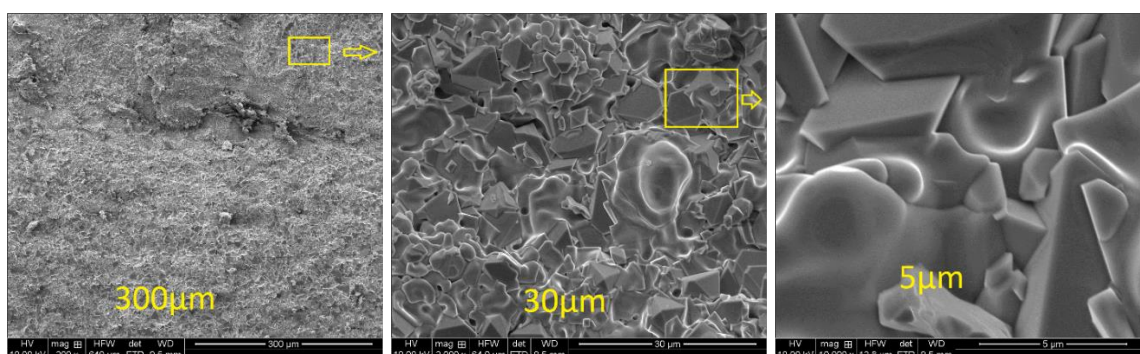
Figure 33. Surface morphology of 316L stainless steel sample at 1273 K of 300 µm, 30 µm and 5 µm.

Figures 32-33 display the SEM images capturing the surface morphology of the samples. Figures clearly show many crystals that are stacked together during the growth of the scale. The growing surface crystals are continuously distributed to form a dense polylithic scale. The images at 300 µm working distance reveal the areas that are severely affected by spallation.

The granular morphology of the samples can be seen in Figure 32-33. In Fig. 33 the particles with rounded shape and those with sharp-edged shape can be distinguished. On average, the sizes of particle grains are larger in the case of 1273 K samples as compared to those of 1173 K.

51

4.2.3. Oxidation Microstructure (Cross-Section Analysis) with Scanning electron microscopy/energy dispersive X-ray spectroscopy (SEM/EDS)

4.2.3.1. 773 K

At 773 K, no scale spallation was observed. This scale does not exhibit many flat crystals and grains for this particular testing condition. EDS analysis of the sample surface's scale composition was performed as shown in Table 20. SEM cross-section morphology micrograph reported the compositions in two regions. At 773 K, shown in Fig. 34, the first region (outer layer) focused on the white area. This area had mainly Si and O. The second region (inner layer) shows the presence of Cr, O, Ni and a significant amount of Fe. Our results also show that no pitting corrosion occurs during oxidation. We find that the oxide scale is crack free and still adherent after cooling to room temperature. Surface morphologies are shown in Fig. 34. Double layers were formed in the cross section of the sample. External layer (the top, or oxide layer) contained Si and O while the internal layer contained large amounts of Cr, Fe, and Ni.

The EDS analysis of the surface oxide and the microstructure below are shown in Fig. 35. At 773 K, the surface oxide was mostly Cr and iron rich oxide. Furthermore, small amounts of Ni were detected. Fig. 35 also shows an elemental map of a well-developed layer of silica at the alloy/oxide interface.

EDS analyses performed on the cross-section are given in Tables 20. The presence of silicon was noted at the internal interface and along the steel grain boundaries. It appears that silicon is mainly located close to the internal interface (Fig. 34-35).

As shown in Figs. 36 different regions were analyzed by EDS-SEM analysis. Fig. 36a shows Region 1 (outer layer) and Fig. 36b shows Region 2 (inner layer) on EDS graph.
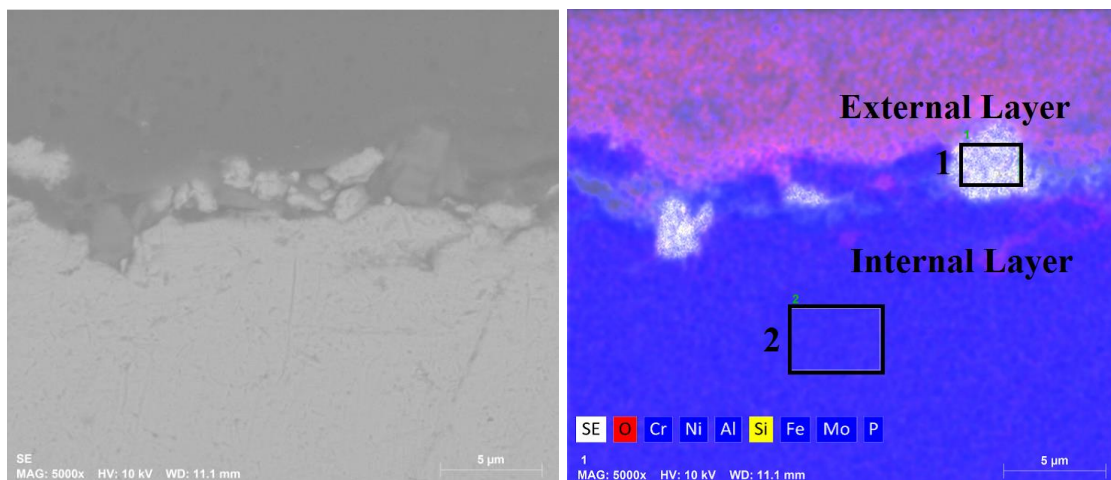
Figure 34. SEM images of the 316L stainless steel sample oxide cross-section after exposure to air at 773 K.
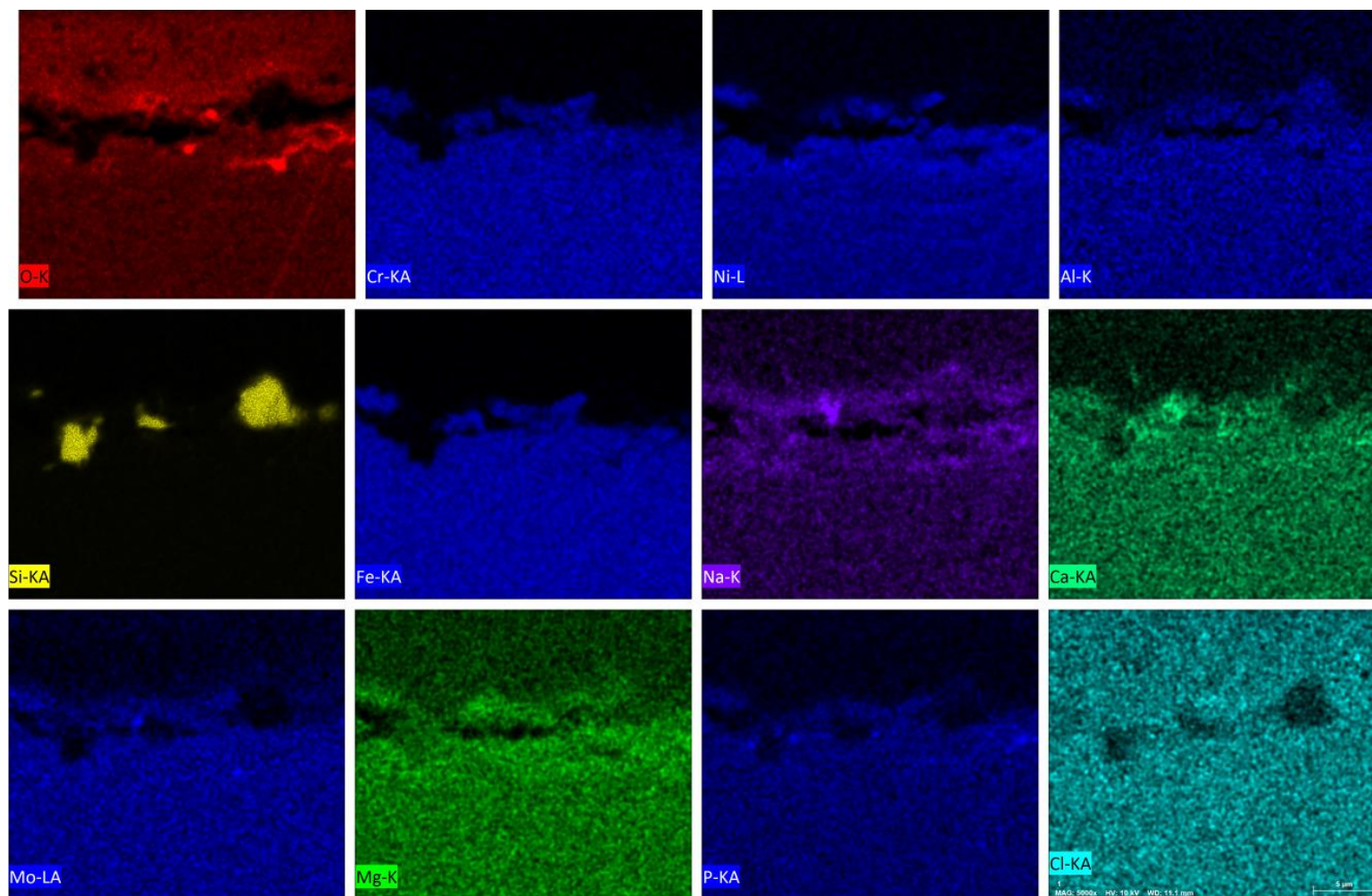
Figure 35. The elemental maps in a cross sectional area of the 316L stainless steel sample oxide film at 773 K.
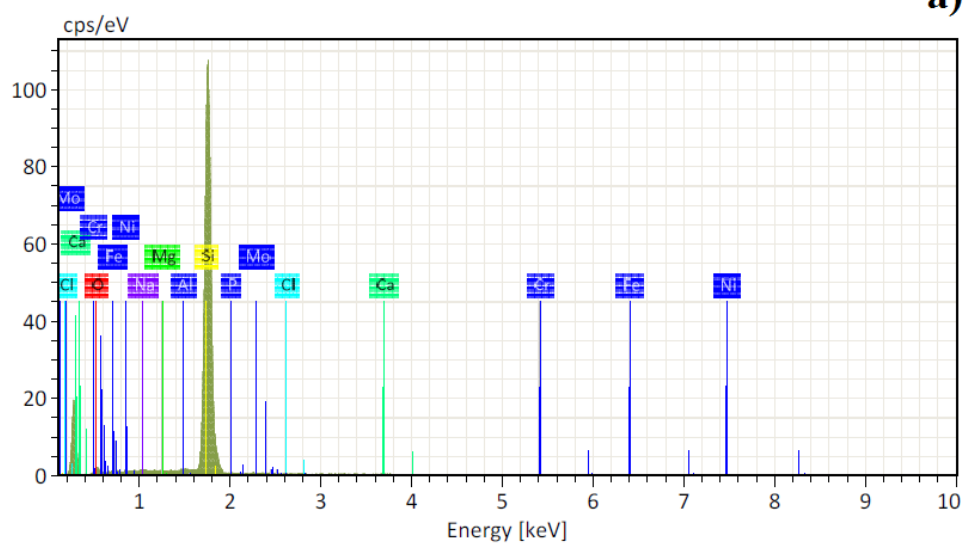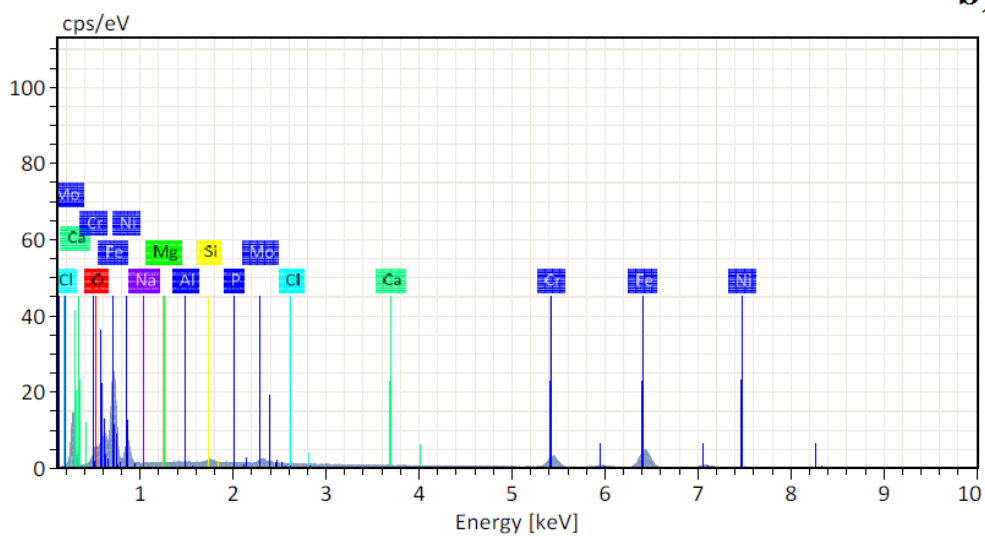
Figure 36. EDS graph of 316L stainless steel sample tested at 773 K for a) Section 1 (Region 1) and b) Section 2 (Region 2)

Table 20. Region 1 and Region 2 mass % and atomic % at 773 K.

Element	Region 1 (Section 1)		Region 2 (Section 2)	
	Mass (%)	Atomic (%)	Mass (%)	Atomic (%)
Oxygen	1.42	4.51	1.05	4.15
Sodium	0.18	0.39	0.00	0.00
Magnesium	0.00	0.00	0.00	0.00
Aluminum	0.18	0.34	0.05	0.12
Silicon	51.18	92.61	0.61	1.38
Phosphorus	0.00	0.00	0.00	0.00
Chlorine	0.09	0.12	0.04	0.08
Calcium	0.25	0.32	0.11	0.17
Chromium	0.89	0.87	14.32	17.41
Iron	0.57	0.52	57.79	67.91
Nickel	0.08	0.07	9.51	10.24
Molybdenum	0.47	0.25	1.61	1.06
Sum	55.30	100.00	85.09	100.00

4.2.3.2. 873 K

As shown in Fig. 37 the scale does not exhibit many flat crystals and grains for this particular testing condition. This project's SEM cross-section morphology micrograph reported on the composition of one random region of the oxidized sample as shown in Fig. 37. The oxidation layer was very thin since mainly silicon and oxygen peaks were detected there. The tested region shows the presence of Cr, O, Ni and a significant amount of Fe. Our results also show that no pitting corrosion occurred during oxidation at 873 K for SS-316L. In addition, the oxide scale was crack free and still adherent after cooling to room temperature. EDS analyses performed on the cross-section are given in Table 21.
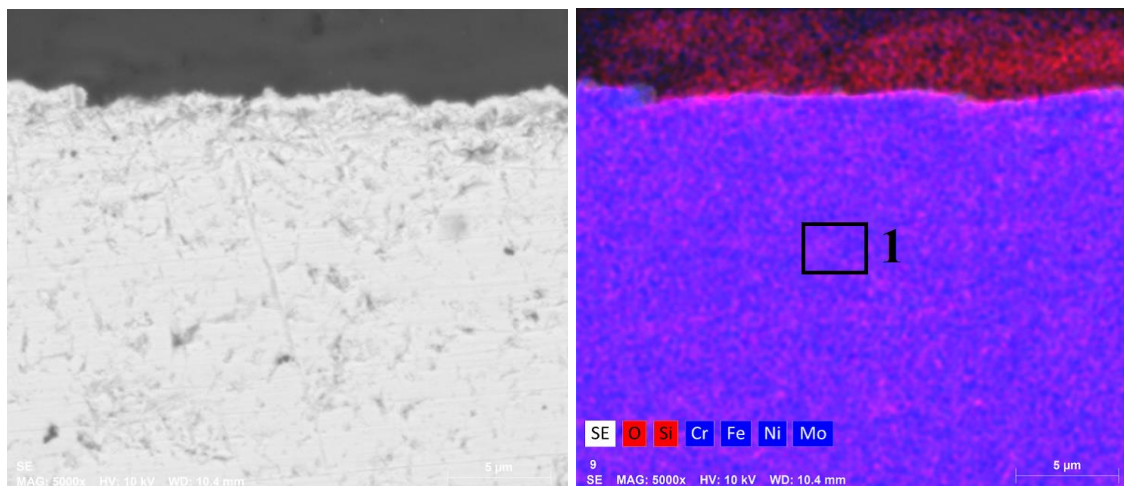
Figure 37. SEM images of 316L stainless steel sample cross-section showing effect of the

oxide after exposure to air at 873 K.
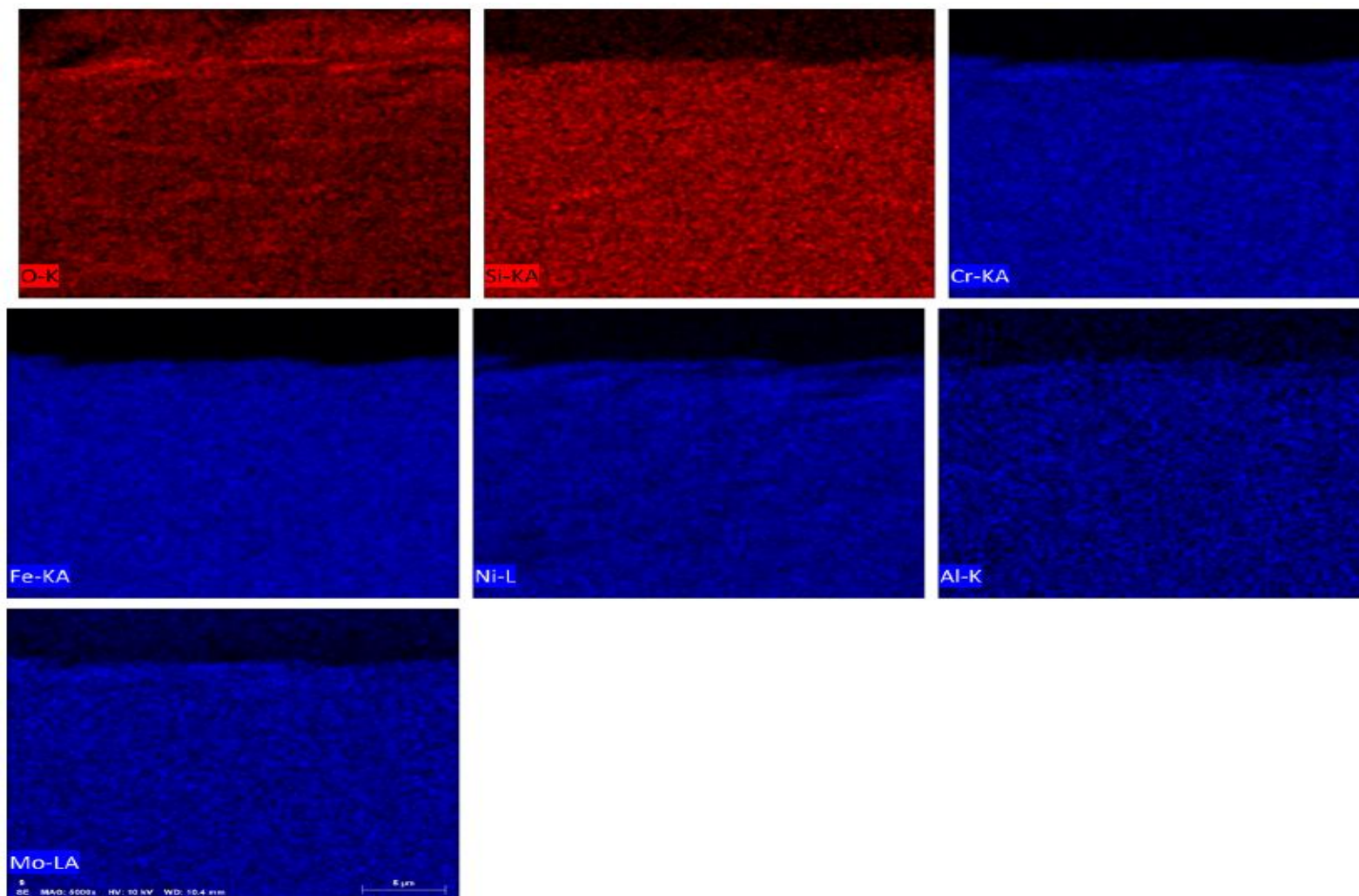
Figure 38. The elemental maps of 316L stainless steel sample in a cross sectional area of the oxide film at 873 K.
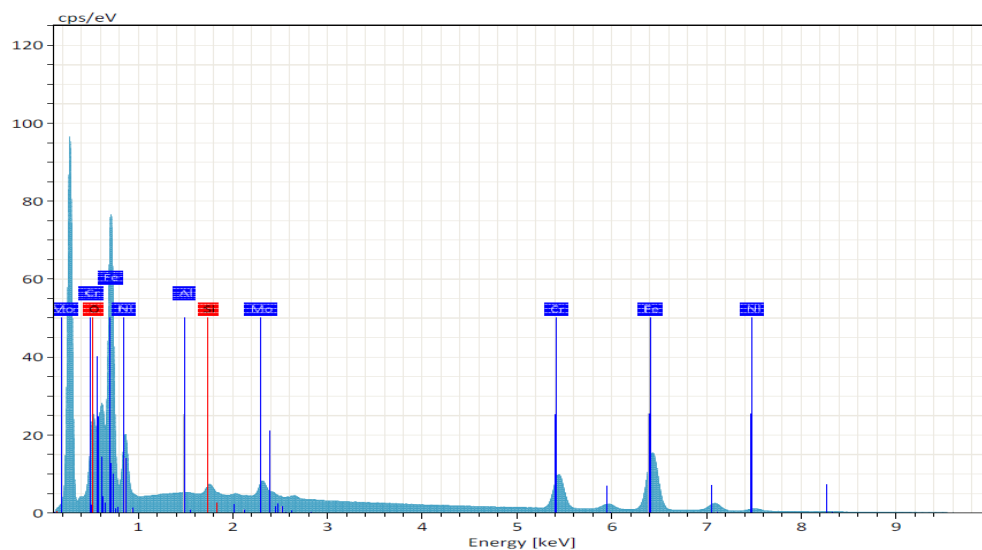
Figure 39. EDS spectrum of 316L stainless steel at 873 K.

Table 21. Mass % and atomic % at 873 K.

Element		Mass (%)	Atomic (%)
Oxygen		2.14	7.95
Aluminum		0.05	0.12
Silicon		0.59	1.25
Chromium		14.22	16.28
Iron		60.61	64.60
Nickel		8.59	8.71
molybdenum		1.76	1.09
	Sum	87.96	100.00

4.2.3.3. 973 K
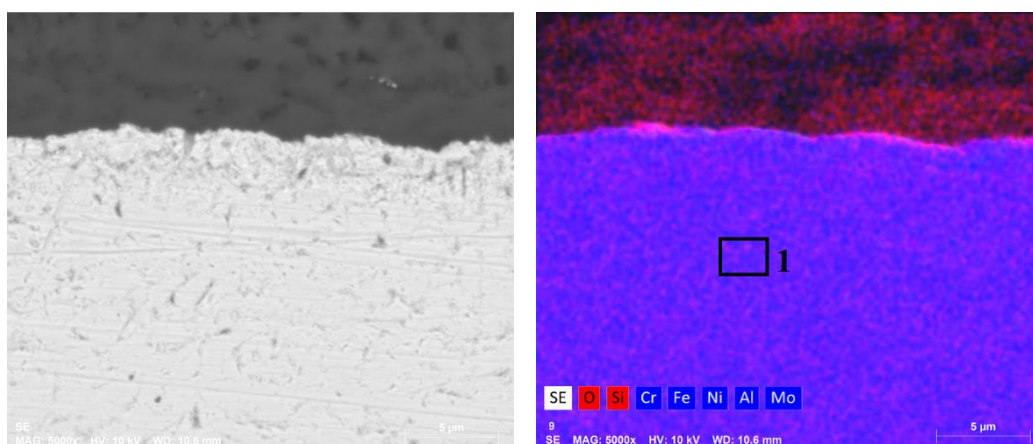
Figure 40. SEM images of 316L stainless steel sample cross section oxide after exposure to air at 973 K.
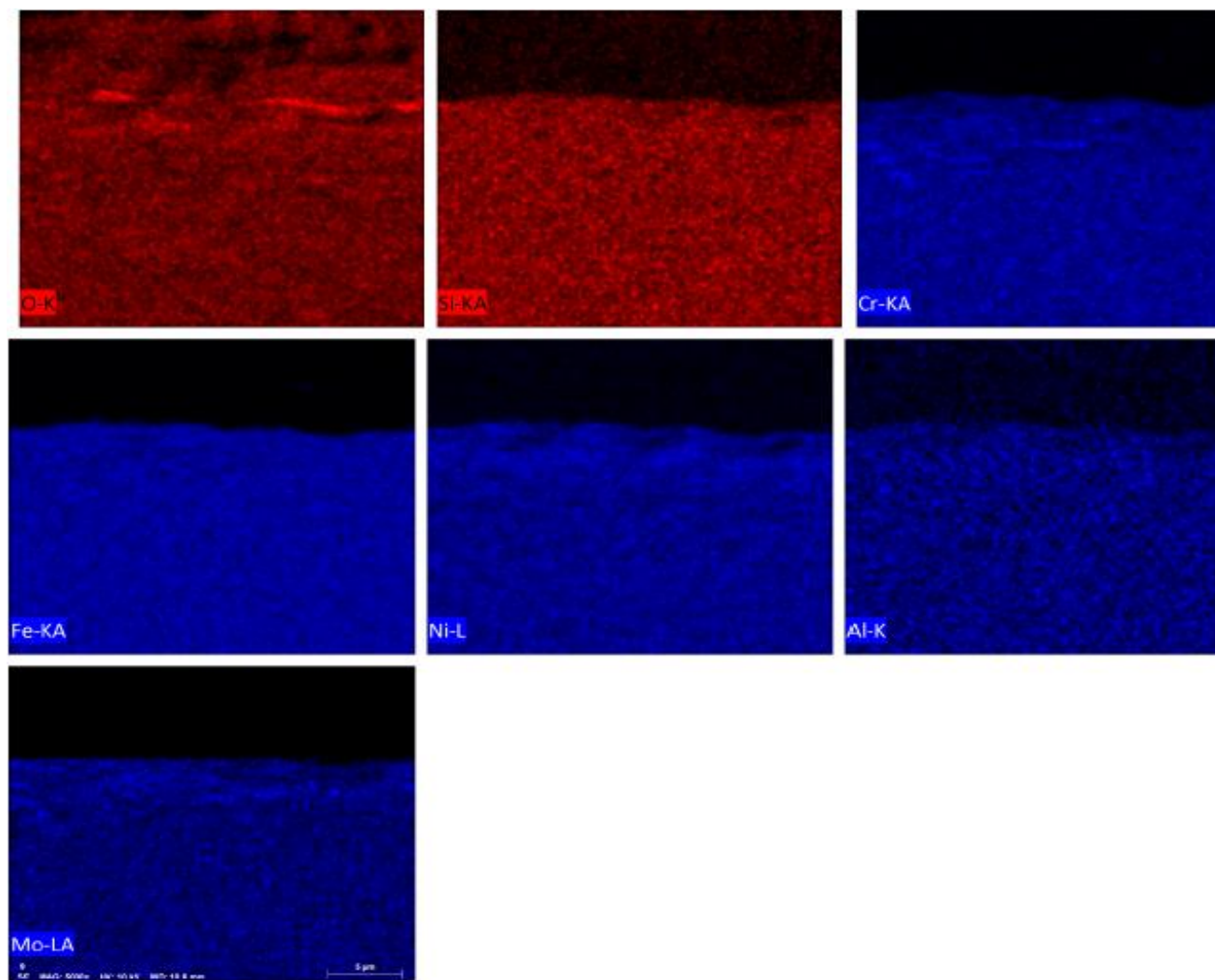
Figure 41. The elemental maps on the 316L stainless steel sample's cross sectional area of the oxide film at 973 K.
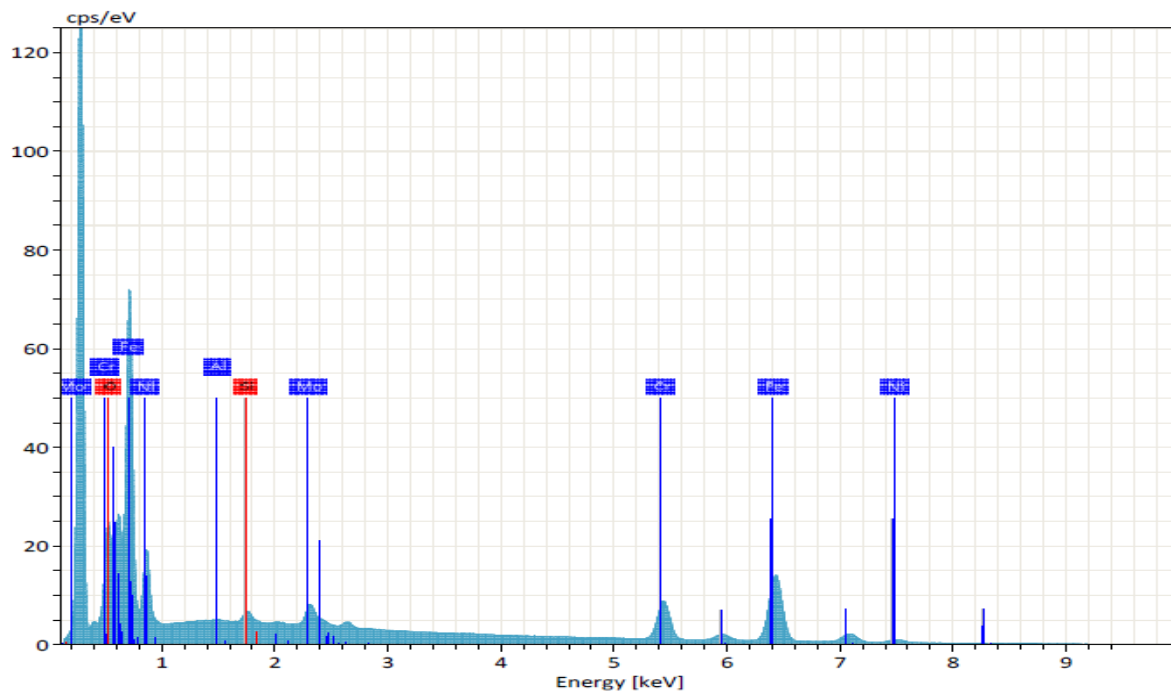
Figure 42. EDS graph at 973 K

Table 22. Mass % and atomic % at 973 K.

Element		Mass (%)	Atomic (%)
Oxygen		2.39	8.85
Aluminum		0.06	0.12
Silicon		0.57	1.19
Chromium		13.78	15.69
Iron		60.47	64.08
Nickel		8.80	8.87
molybdenum		1.94	1.19
	Sum	87.99	100.00

4.2.3.4. 1073 K

SEM images depict two regions (Fig. 43). At 1073 K, the first region mainly contains O and Cr with a small amount of Si. The second region mainly consists of Fe and Cr, which also has Ni, Mo, and O.

61
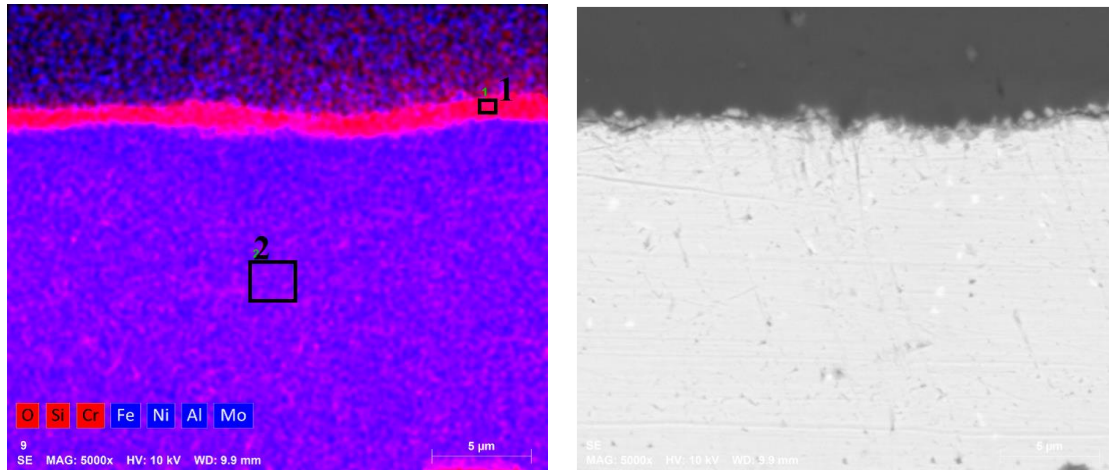
Figure 43. SEM images of the 316L stainless steel sample oxide cross-section after exposure to air at 1073 K.

At 1073 K, flat crystals were observed at the external interface. The compact chromia (chromic oxide) part of the scale exhibited some internal oxidation with small pegs penetrating into the steel.

Fig. 44 displays the SEM images that show the presence of a well-developed layer of Si and Cr at the alloy/oxide interface.
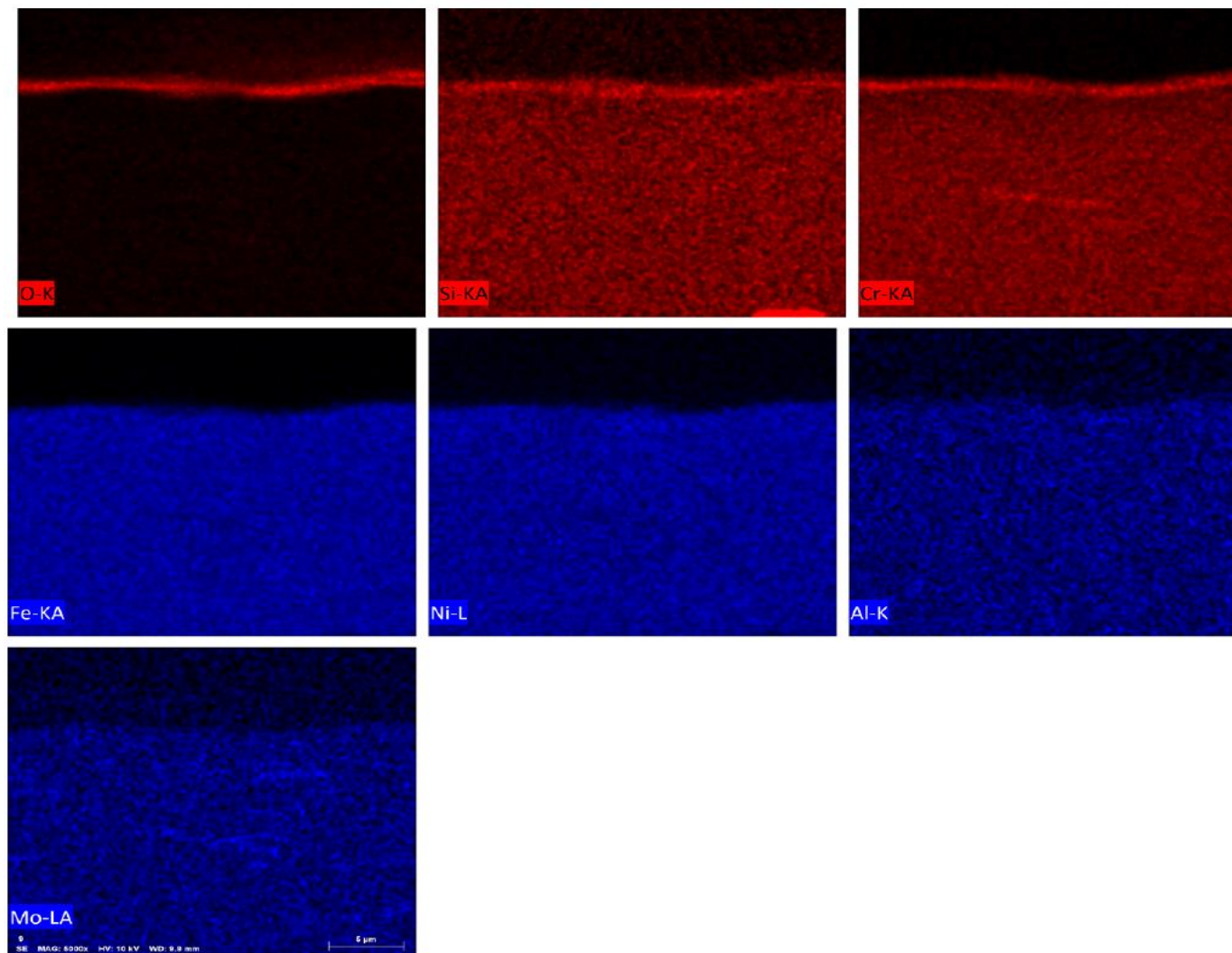
Figure 44. The 316L stainless steel sample elemental maps in a cross sectional area of the oxide film at 1073 K.
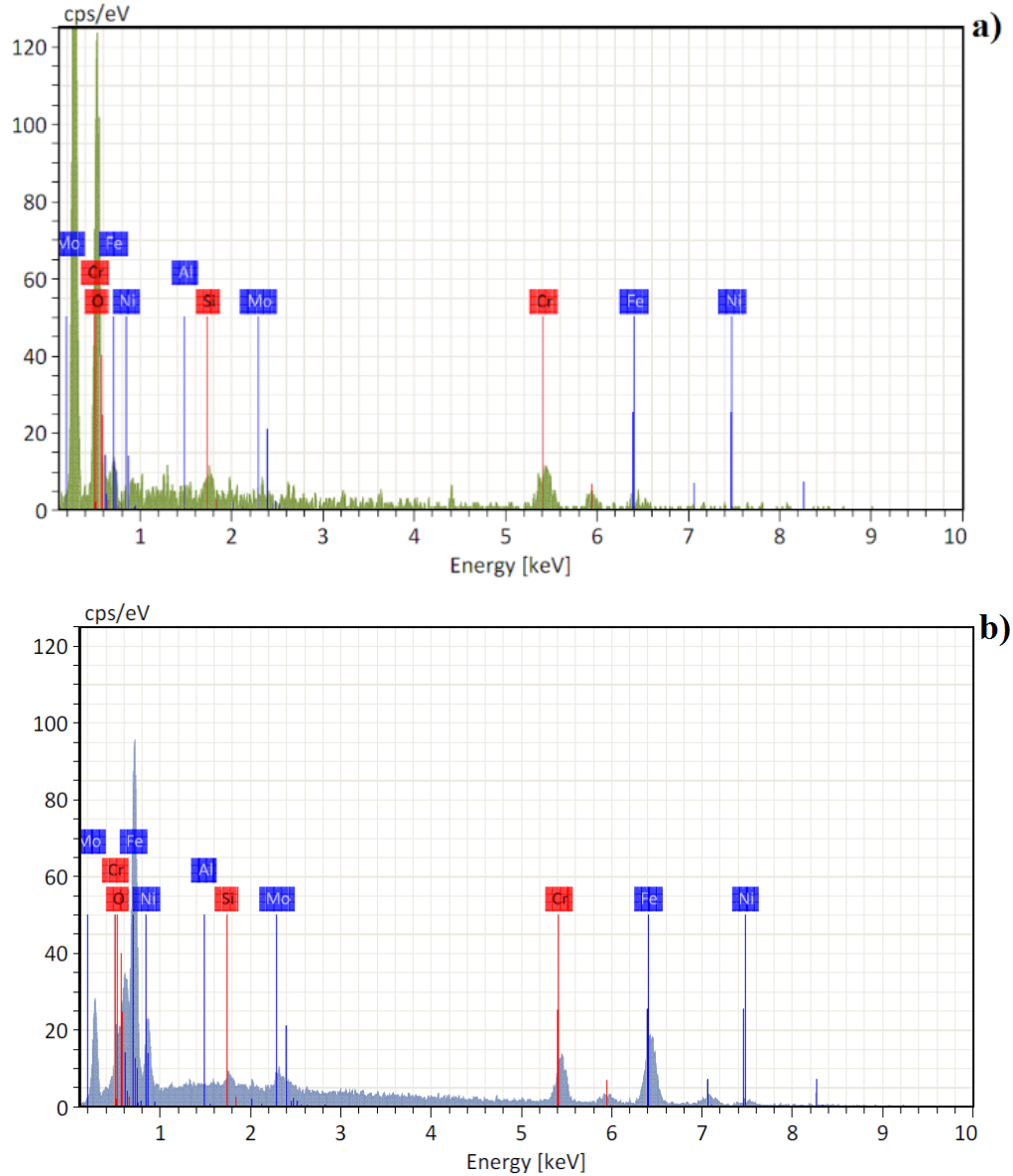
Figure 45. EDS graph at 1073 K for a) Section 1 (Region 1) and b) Section 2 (Region 2).

The results of EDS analyses performed on the cross-section are given in Tables 23 and Fig. 45. EDS analysis showed that a small amount of iron containing oxides were found in the oxide scale. The scale cross-section also revealed that the oxide scale was

adherent to the substrate. Silicon and molybdenum were found at the metal/oxide

interface.

Table 23. Region 1 and Region 2 mass % and atomic % of oxidized steel at 1073 K.

Element	Region 1		Region 2	
	Mass (%)	Atomic (%)	Mass (%)	Atomic (%)
Oxygen	16.89	66.25	0.84	3.14
Aluminum	0.22	0.52	0.33	0.06
Silicon	0.68	1.51	0.37	0.78
Chromium	23.22	28.03	16.67	19.06
Iron	2.92	3.29	63.48	67.58
Nickel	0.00	0.00	7.94	8.04
molybdenum	0.62	0.41	2.18	1.35
Sum	44.55	100.00	91.50	100.00

4.2.3.5. 1173K

Fig. 46 shows the EDS analysis results of the surface oxide and the

microstructure. At 1173 K, the surface oxide was mostly Cr, Fe and Si-rich oxide.

Furthermore, Ni was slightly enriched
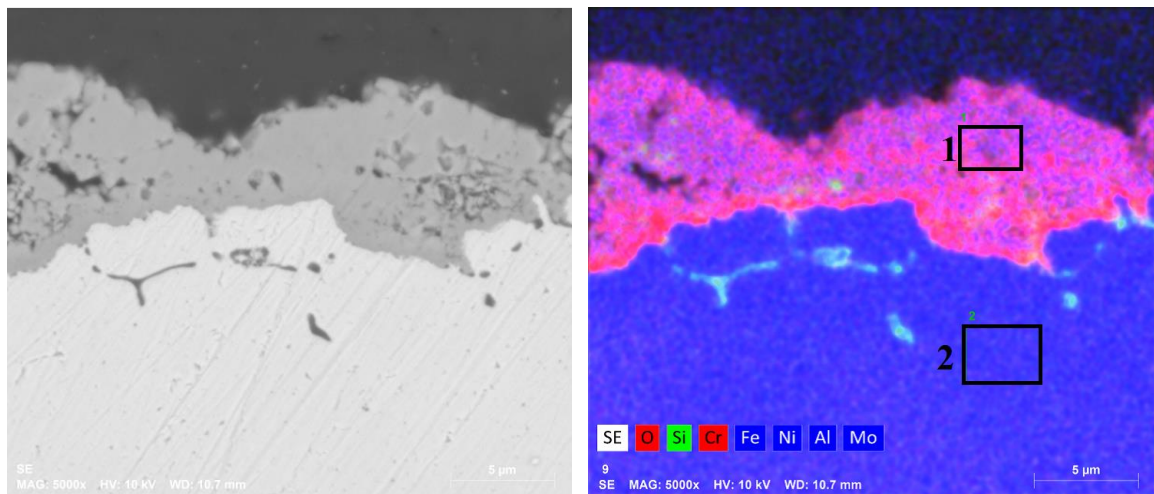
Figure 46. SEM images of the cross-section of the oxide after exposure to air at 1173 K.
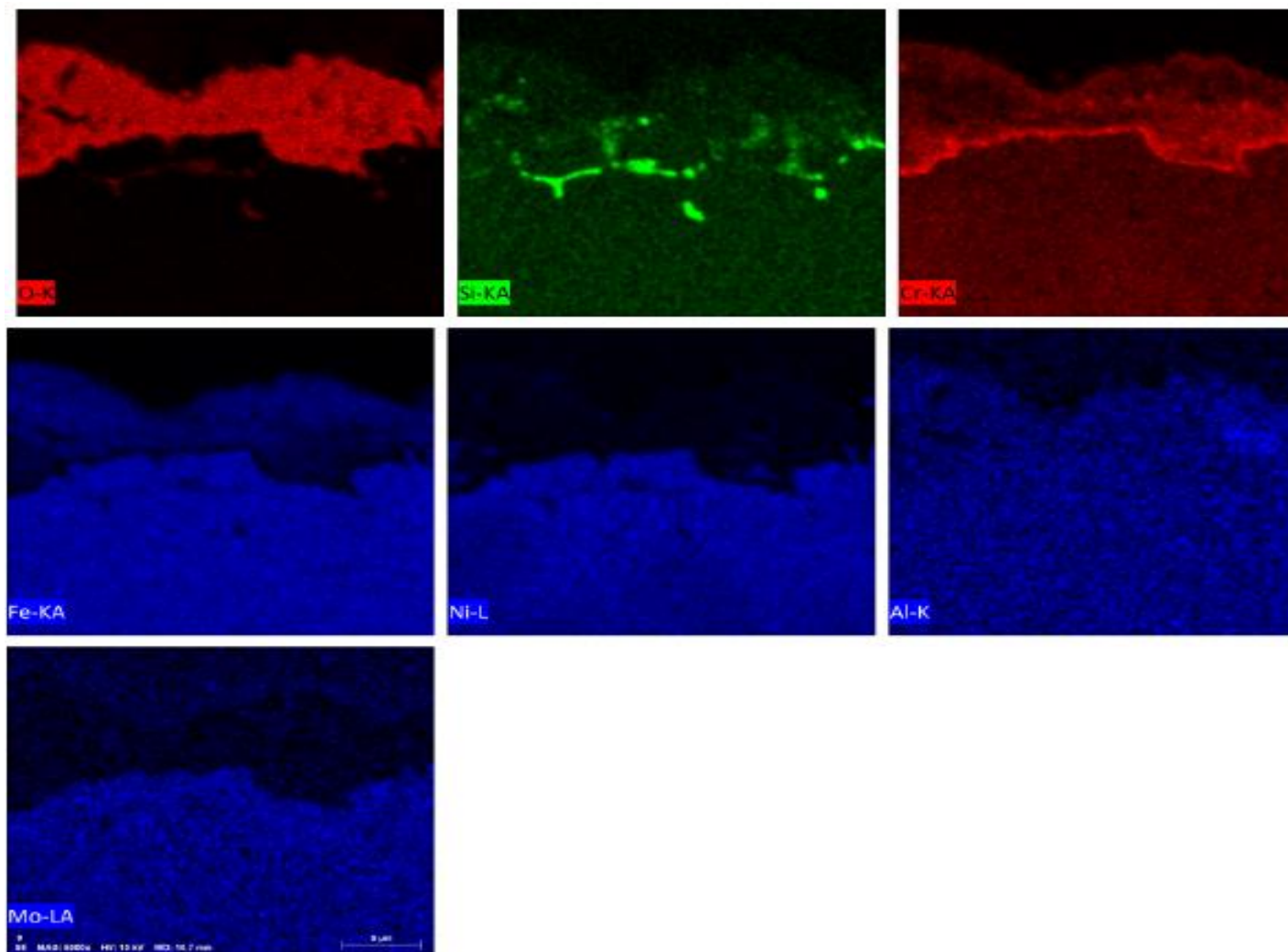
Figure 47. The elemental maps in a cross sectional area of the oxide film at 1173 K
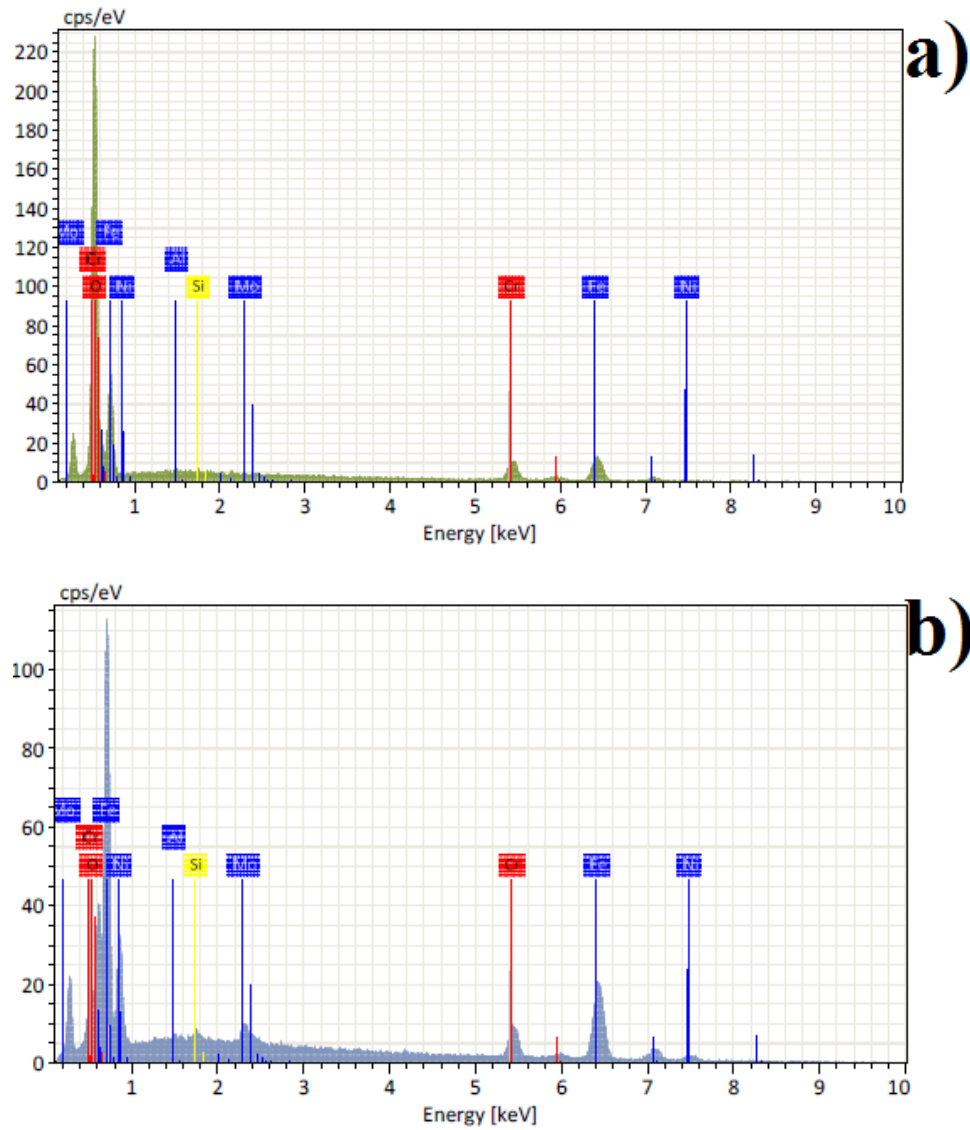
Figure 48. EDS graph at 1173 K a) Section 1 (Region 1) and b). Section 2 (Region 2).

Table 24. Region 1 and Region 2 mass % and atomic % for oxidized steel at 1173 K.

Element	Region 1		Region 2	
	Mass (%)	Atomic (%)	Mass (%)	Atomic (%)
Oxygen	25.87	60.91	0.46	1.81
Aluminum	0.15	0.21	0.04	0.09
Silicon	0.11	0.14	0.28	0.62
Chromium	14.81	10.73	10.69	12.97
Iron	41.11	49.80	63.54	71.80
Nickel	0.36	0.23	10.55	11.34
molybdenum	0.13	0.05	2.06	1.36
Sum	82.54	100.00	87.62	100.00

4.2.3.6. 1273 K

SEM images are given for two regions (Fig. 49). The first region (outer layer) mainly contains Cr and Mo oxide content with a small amount of Si. The second region (inner layer), mainly consists of Fe with a small amount of Ni, Mo and O. As shown in Fig. 49, the external oxide layer was observed as untidy and showed crack free areas, mostly consisting of Si and Mo at the alloy/oxide interface region.

Fig. 51 shows the EDS analysis of the surface oxide effect on the microstructure for two regions.
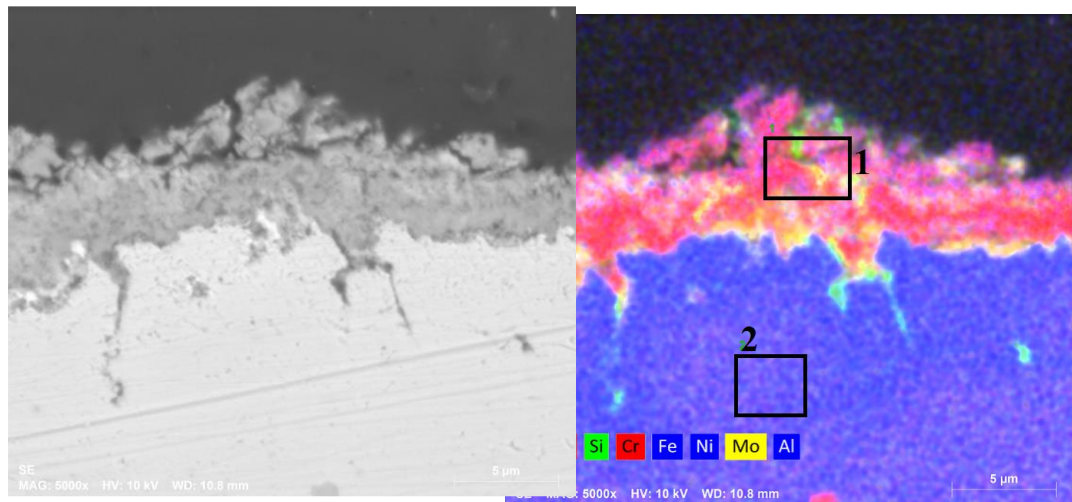
Figure 49. SEM images of the oxide affected cross section in Regions 1 and 2 (shown in figure on right) after exposure to air at 1273 K

Figure 50 shows elemental maps designating the presence of a well-developed layer of Si, Mo, and Cr-rich oxide layers at the alloy interface.
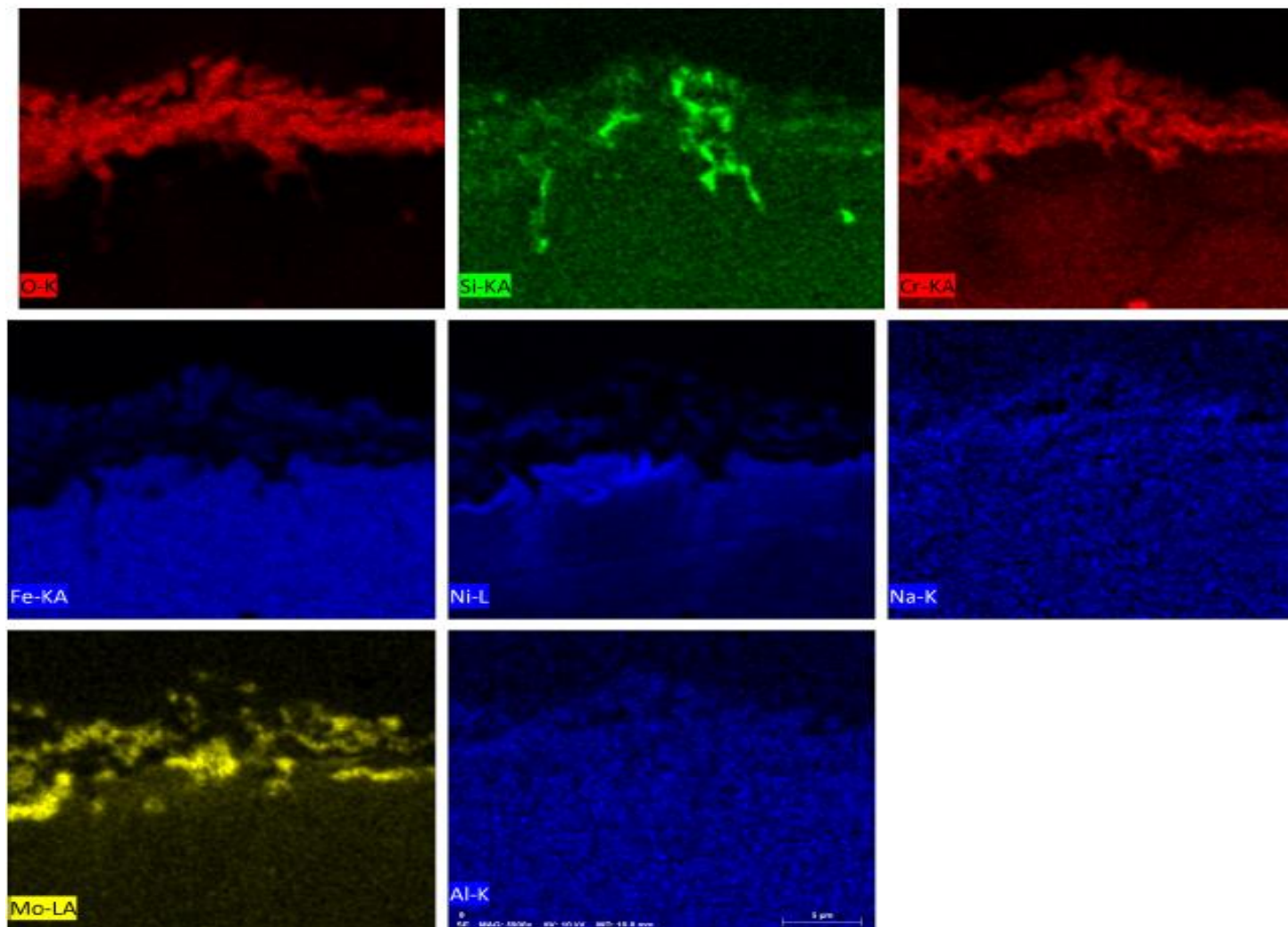
Figure 50. The elemental maps in a cross sectional area of the oxide film at 1273
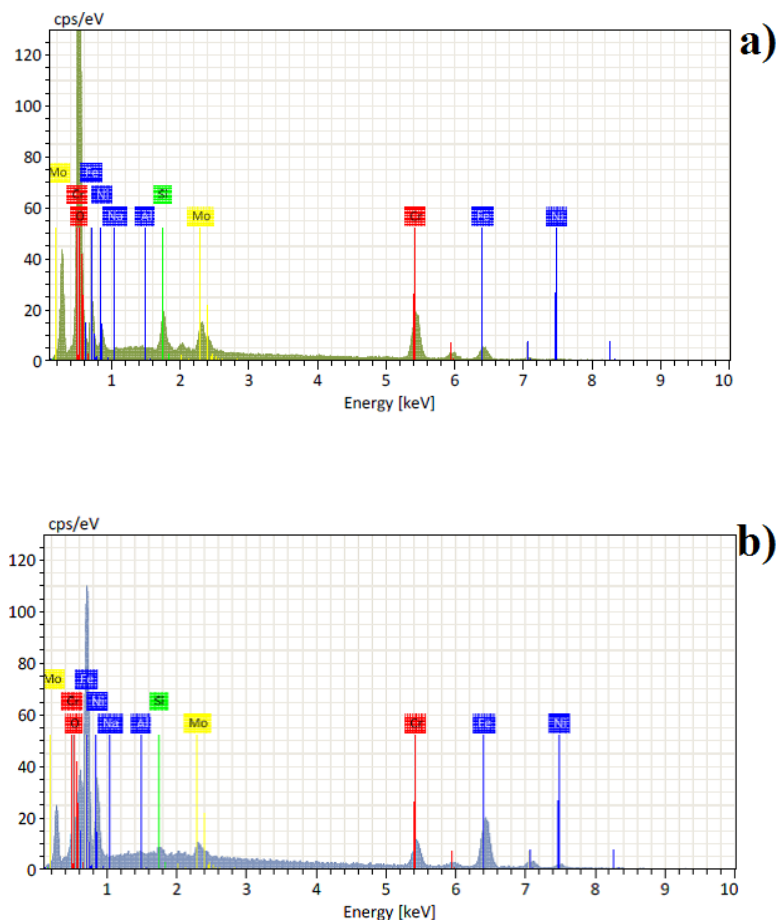
Figure 51. EDS graph at 1273 K for a) Region 1 and b) Region 2.

Table 25 shows different regions that were analyzed by EDS-SEM analysis. Fig. 51a shows Region 1 (outer layer) and Fig. 51b shows Region 2 (inner layer) EDS atomic and mass percentage.

Table 25. Region 1 and Region 2 mass % and atomic % at 1273 K.

		Region 1		Region 2	
Element		Mass (%)	Atomic (%)	Mass (%)	Atomic (%)
Oxygen		26.78	61.63	0.67	2.64
Aluminum		0.00	0.00	0.04	0.09
Silicon		2.43	3.19	0.60	1.36
Chromium		29.31	20.76	12.74	15.47
Iron		16.68	11.00	59.45	67.20
Nickel		2.97	1.87	11.25	12.10
molybdenum		4.03	1.55	1.73	1.14
	Sum	82.21	100.00	86.49	100.00

4.2.4. Characterization of the oxidized Layer with X-Ray Diffraction

The XRD results for oxidized SS-316 samples at 873, 1073 and 1273 K are shown in Fig. 52. The x-ray diffraction pattern of the air exposed samples at 773 K, 873 K and 1073 K show that they are composed of Fe-Cr (JCPDS file No. 34-0396), $Cr_{0.19}$ $Fe_{0.7}$ $Ni_{0.11}$ (JCPDS file No. 33-0397) and Fe_2O_3 (JCPDS file No. 84-0311). $Cr_{0.19}$ $Fe_{0.7}$ $Ni_{0.11}$ appears to have the strongest peak intensity among these oxides at 773 K and 873 K, while Fe_2O_3 and Fe-Cr have the strongest peak intensities among these oxides at 1073 K. This result was expected because at 1073 K the oxidation mechanism changes to inner oxidation of the alloy. At 973 K and 1173 K, x-ray diffraction pattern of air exposed samples was composed of $Cr_{0.19}$ $Fe_{0.7}$ $Ni_{0.11}$ (JCPDS file No. 33-0397) and Fe_2O_3 (JCPDS file No. 84-0311 $Cr_{0.19}$ $Fe_{0.7}$ $Ni_{0.11}$ appears to have the strongest peak intensity among these oxides at 973 K while Fe_2O_3 and Fe-Cr have the strongest peaks intensity among these oxides at 1173 K.

At 1273 K, a scale formed and was composed of Fe_2O_3 (JCPDS file No. 86-2368) and $Fe_{2.942}O_4$ (JCPDS file No. 86-1355) while Fe_2O_3 peaks were the strongest peaks.
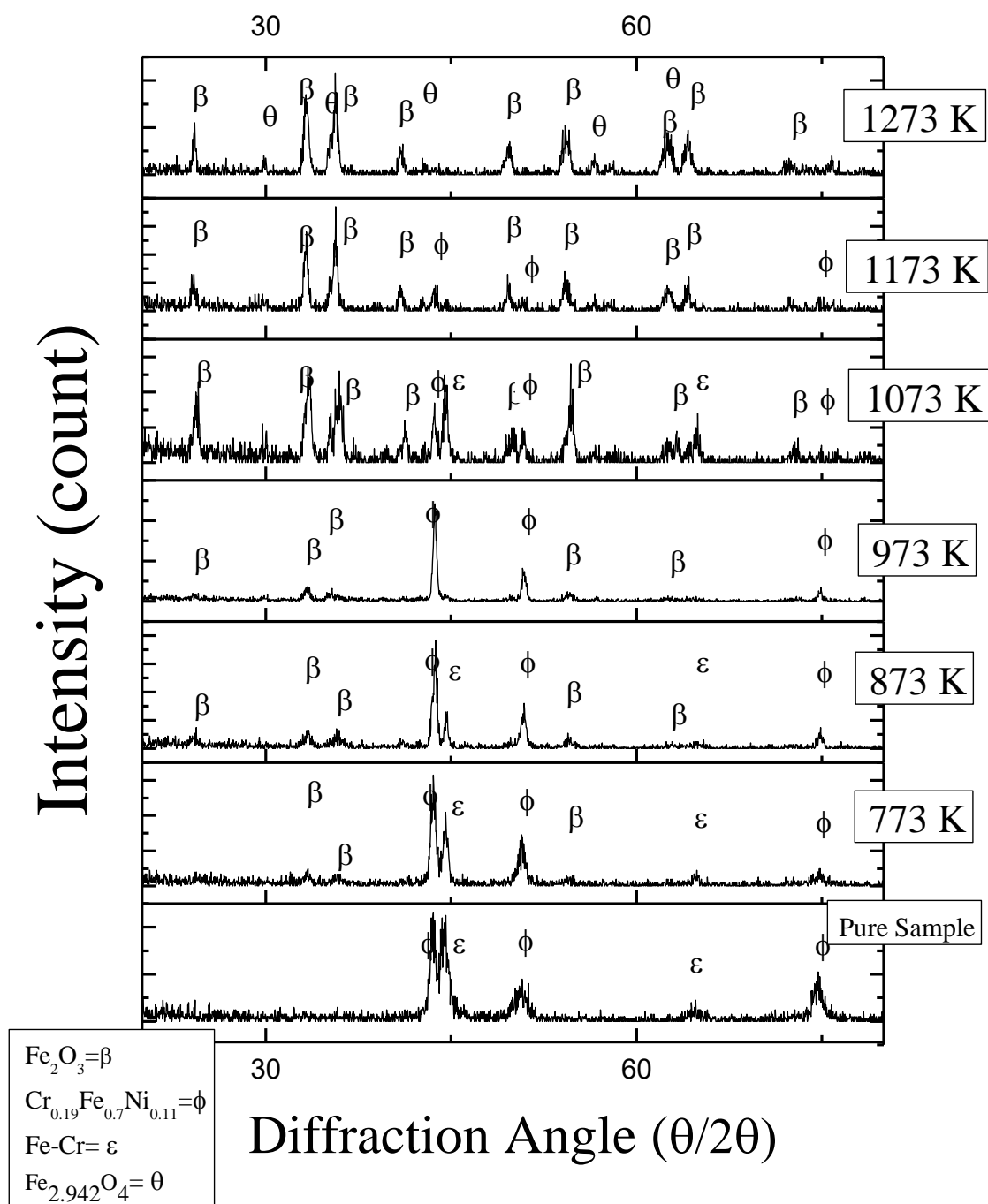
Figure 52. X-Ray diffraction of 316L stainless steel pure sample at 773 K to 1273 K.

4.3. Discussion

Fig. 16 shows the SEM analysis under 773 K where grain boundaries with high relief measurements can lean forward on adjacent grains. We also observed samples tested under 773 K to have dissolution with depletion of Cr and corrosion products with relatively less Cr and more O.

After a 24-hour air exposure, samples developed layers of oxides formed on the cross section of the SS-316L, as shown in Fig. 34. The external layer had extensive SiO, and the inner layer had a significant Cr, Ni, and Fe layer, which correlated well with the XRD results for $Cr_{0.19}$ Fe_{07} $Ni_{0.11}$. The SEM elemental map in Fig. 35 shows that the outer-oxidation layer contained significant amounts of Si and O. However, the inner layer contained less Si and Fe, Cr and Ni content.

The results using elemental maps indicated that the eternal oxide was composed of an Fe and Cr-rich oxide, which was supported by XRD analysis. On the other hand, the internal oxide layer was composed of Cr, Fe and Ni-rich oxide.

Li and Gleeson [28] compared and analyzed the oxidation behavior of Ni-base alloys with and without approximately 2.7 wt.% Si addition. Si addition was found to improve oxidation resistance by forming a continuous SiO_2 layer at the alloy scale interface, which resulted in decreased oxidation kinetics (see Fig. 34).

At 873 K under air atmosphere, the samples exhibited uniform dissolution with high amounts of Cr, Fe, and Ni products. High temperatures accelerated the outward diffusion of Cr to the surface resulting in higher Cr content than at 773 K as shown in Tables 10–11. At 873 K, enhanced dissolution with Cr depletion and formation of oxidation

products with high Cr, Fe and O content were observed. There were more Cr rich regions when samples were exposed to air. A comparison of Cr, Fe, and O contents and the corresponding EDS values as given in Tables 10-11 reveal that at 873 K, Cr had depleted in the air environment and oxidation products were visible in some regions. Changes in the Cr and Fe content over the surface and in the deposits were probably due to the high affinity of Cr and Fe towards O. This indicates that high temperature and oxygen rich atmosphere enhanced the oxidation of samples.

For the temperature range of 973 K to 1073 K, samples studied under air atmosphere exhibited the formation of oxide over the entire surface, which could be the reason for the increase in weight during TGA experiments. Depletion of Cr and formation of corrosion products with high Cr content at high temperatures and air atmosphere is evident in Tables 12 and 13. In air atmosphere, oxidation product formation with Cr depletion was observed in some areas on the surface as marked in Fig. 22. Figure 24 shows depleted Cr in regions with corrosion product morphology. The SEM images of Cr-Mo steel studied in air atmosphere revealed severely attacked regions. Porous regions with high Cr and Mo and regions with thick corrosion product morphology with depleted Cr and Mo were found. Depletion of Cr in some regions could be due to the formation of soluble Cr compounds. The SEM images clearly showed that Cr-Mo steel oxidation is higher at 1073 K (Figs. 22-24).

The porous morphology of Cr and Mo being severely depleted or attacked to the preferential leaching of elements from the surface and formation of corrosion products can be easily seen in the SEM elemental map (Fig. 41 and Fig 44). The chemical composition

as analyzed using EDS for air exposed samples for 24 h are Fe, Cr, Ni and Mo. Cr and Fe oxidation was observed after 24 h exposure as analyzed by EDS (Fig. 42 and 45).

After 24 hours in air at 1073 K, the sample formed a thin layer of oxides on the cross section, as shown in Fig. 43. The external layer containing Cr_2O_3 was extensive, while the internal layer was largely composed of iron oxide (Fe_2O_3). Cr and Ni were also detected.

The amount of Cr in a stainless steel alloy is regarded as the main factor for increasing its resistance to corrosion[66]. However at higher temperatures, the oxidation resistance was frequently lost due to oxide scale failure and formation of iron oxide[67]. After 1073 K, the amount of chromium observed in the samples decreased while iron particles increased. Our results are in good comparison with related articles.

After 1173 K, chromium atomic percent was about 18.65% and Fe atomic percent was about 26.29% at the surface. At 1273 K, the oxide layer was observed and some cracks were also observed extending from the outside going inside. Layers of oxides formed on the cross section of samples, as shown in Fig. 47. The outer layer scale is generally comprised of Cr_2O_3 and Fe_2O_3. We also detected an inner layer comprised of Fe_2O_3. The iron content was significant, but we also observed Cr, Ni, and a small amount Si and Mo.

At 773 K, Si was detected at the metal/oxide interface (Fig. 34). Some studies have discussed the role of molybdenum and silicon on the oxidation behavior of Ni-based alloys. Molybdenum is added into 316L steel as a solid solution strengthener[26]. Although a large amount of silicon can have a detrimental effect on alloy mechanical properties[26], Silicon

can also protect against iron oxidation[32,37]. Our results show the opposite behavior for the amount of silicon and iron content found in the samples.

Kinetic results concerning the samples are reported in Table 6. Weight loss and weight gain curves obtained at 773 K to 1273 K are parabolic. Under temperatures of 773 K and 873 K, weight loss occurred during oxidation. After reaching and surpassing 973 K, a weight gain occurred during oxidation. In all cases, the parabolic parts, as shown in Fig. 11, of the kinetic curves correspond to a growing chromia scale. Our results at 1073 K to 1273 K are comparable to the Lopez paper[33]. In the Evans paper [27] the parabolic rate constant was minimal with an intermediate alloy silicon content where an interlayer of silica was formed between the outer oxide and the metal. Our results at 773 K are comparable with Evans et al. [27].

In most of the heat-treated surfaces, a drop in Cr content was recorded at 1173 K and at 1273 K. This is thought to be due to Cr volatilization from the surface during heat treatment. Many years ago, workers observed significant losses of Cr due to volatilization during the oxidation of Fe-Cr alloys at temperatures above 1173 K, e.g. [67,68]. These losses were also noted in flowing dry oxygen at temperatures between 1373 K and 1473 K. Our study observed significant losses of Cr content at 1173 K[67,68].

4.4. Conclusions

- SEM and EDS figures sequentially showed a continuous growth of external oxide scales and grain boundary ridges with increasing temperature.

- The amount of chromium in a stainless-steel alloy is regarded as the main factor to increase corrosion resistance. The best corrosion resistance was observed at 1073 K.

- At 773 K, a thin external oxide layer was observed, while a continuous and relatively irregular and inwardly protruding external oxide layer was observed in the external layer with increasing temperature. At 1073 K, a Cr_2O_3 layer was observed. After 1273 K, a Fe_2O_3 sub-layer formed beside the Cr_2O_3 layer.

- The oxide morphology and structure of SS-316L were strongly affected by the oxidation environments.

- At 1273 K, the weight gain in samples was attributed to iron oxidation.

- The oxidation depth increased as the temperature increased due to the formation of pores, voids, and grain boundaries subjected to exposure in high temperatures.

- The oxidation behavior of SS-316L followed Wagner's parabolic oxidation kinetic rate law. The activation energy is 144.1 kJ/mol for temperatures ranging from 873 K to 1273 K.

CHAPTER 5. OXIDATION OF ALLOY 617 AT HIGH

TEMPERATURES IN AIR

5.1. Introduction

High temperature oxidation of nuclear reactor candidate material INCONTEL[®] alloy 617, referred to throughout this dissertation as alloy 617, was studied at different temperatures. The tests were performed isothermally at temperatures between 1073 K and 1473 K (in steps of 100 K) for 24 hours in controlled air environments. The oxidation behavior followed the parabolic oxidation kinetic rate law. The activation energy was found to be 233.46 kJ/mol for 1073 K to 1473 K. At 1073 K to 1473 K, a thin external oxide layer was observed as a NiO-Cr_2O_3 double layer, in which the inner layer was NiO and the external layer was Cr_2O_3. During the process, a continuous and relatively irregular and inwardly protruding external oxide layer was observed with its thickness dependent on increasing temperatures. In addition to the NiO-Cr_2O_3 layer, we also found areas of Al_2O_3. Figures show the sequentially continuous growth of external oxide scales and grain boundary ridges related to temperatures. The oxide morphology and structure of alloy 617 were strongly affected by their environments. At 1473 K, the increasing mass gain was related to Ti oxidation. The oxidation depth increased as the temperature increased. Exposure to high temperatures contributed to the formation of pores, voids, and grain boundaries. A thermogravimetric analyzer, scanning electron microscopy/energy dispersive x-ray spectroscopy, and x-ray diffraction were used to complete analyses.

A very high temperature reactor (VHTR) is one of the Generation IV reactors used for producing electricity and hydrogen production. A variety of materials were reviewed as the ideal candidate to exploit the Generation IV reactor concept, especially VHTR. Several Ni-based alloys were seriously considered. The materials for high temperature structural[69–71] Ni-base alloys are important candidate materials for VHTR, especially since they are used in many high temperature reactors. This is because of their high temperature creep strength, oxidation resistance , excellent material properties, namely, phase stability, and high efficiency system[21,22,72]. Currently, Ni-based alloys, Alloy 617 and other Ni base alloys are considered for use with an intermediate heat exchanger (IHX) and hot gas duct (HGD). This is due to their excellent high temperature corrosion resistance against various environments such as oxidation, carburization, and decarburization conditions[22,73,74]. In these materials, the protective external Cr oxide prevents the direct interaction between metal and their environment[23]. Chromium (Cr) and aluminum (Al) are allowed to form a surface oxide layer to protect against duration at high temperatures[75–77] .

Among the variety of materials reviewed, several nickel base alloys were seriously considered as suitable materials for these high-temperature components[21–23]. However, oxidation and the high-temperature corrosion resistance of these alloys became a concern because they can affect the degradation property of super alloys by metal loss, decarburization, and internal oxidation[78,79]. Alloy 617 is a solid-solution, strengthened, nickel-chromium-cobalt-molybdenum alloy with an exceptional combination of high temperature strength and oxidation resistance[16,78,80]. Therefore, to understand the oxidation behavior and the stability of oxides, several researchers have investigated the high-temperature oxidation of alloys in air atmosphere[81–85] and in various helium

environments[23,78,85–90] . The corrosion damage in a simulated VHTR atmosphere has been studied by Bates[91], Christ et al.[92,93], Jang[94] and was recently investigated by Cabet et al[69,95–97]. Research on short-term and long-term corrosion in high-temperature helium and air was reported by Kim[79], Jang[85], and Wright [98]. However, the evolution of oxides and the microstructural changes of Alloy 617 during high-temperature oxidation had not been clearly identified at the time of this writing. This dissertation addresses this information gap.

5.2. Results

5.2.1. Oxidation Kinetics and Oxidation Data Alloy 617 from TGA

Weight change of the samples was measured isothermally in the range of 1073 K to 1473 K in 100% air. Results are plotted in Fig. 53.
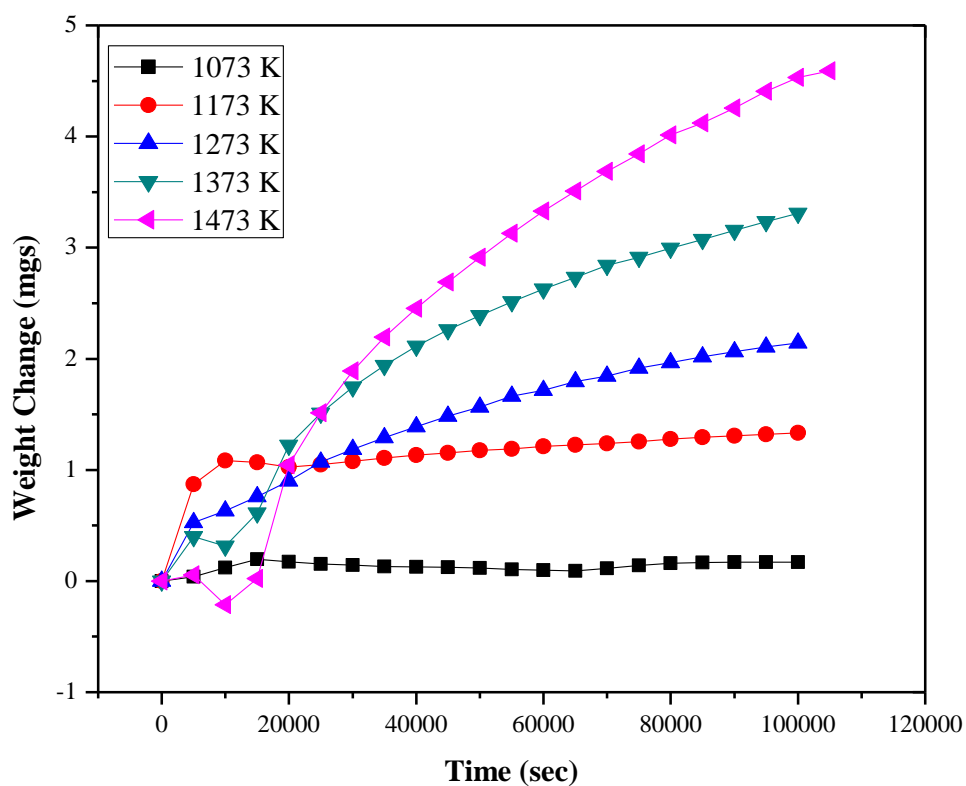
Figure 53. Oxidation of alloy 617 in dry-medical grade air using TGA at temperatures ranging from 1073 K to 1473 K.

Table 26 displays weight gain data from TGA. Oxidation runs were performed more than twice to confirm the reliability and repeatability of the data.

Table 26. Total weight gains at each temperature (K) after 24-hour air exposure.

Temperature (K)	Weight Gain (mg)
1073	0.57
1173	1.33
1273	2.14
1373	3.31
1473	4.59

The total weight gain is shown in Table 26. Weight gain was observed and the mass gain increased with increasing temperature. The first 20000 seconds obtained variable weight gains because first 20000 secs represent the heating temperature interval.

5.2.1.2 Oxidation Kinetics/ Rate Constant

Oxidation kinetics of alloy 617 were quantified through measurement of their mass gain per unit area (Δm/a) as a function of time at temperatures of 1073 K, 1173 K, 1273 K, 1373 K, and 1473 K in air by using thermogravimetric analysis (TGA). Plots of mass gain per unit area vs. time for the oxidation of alloy 617 at temperatures from 1073 K to 1473 K are illustrated in Fig. 54.
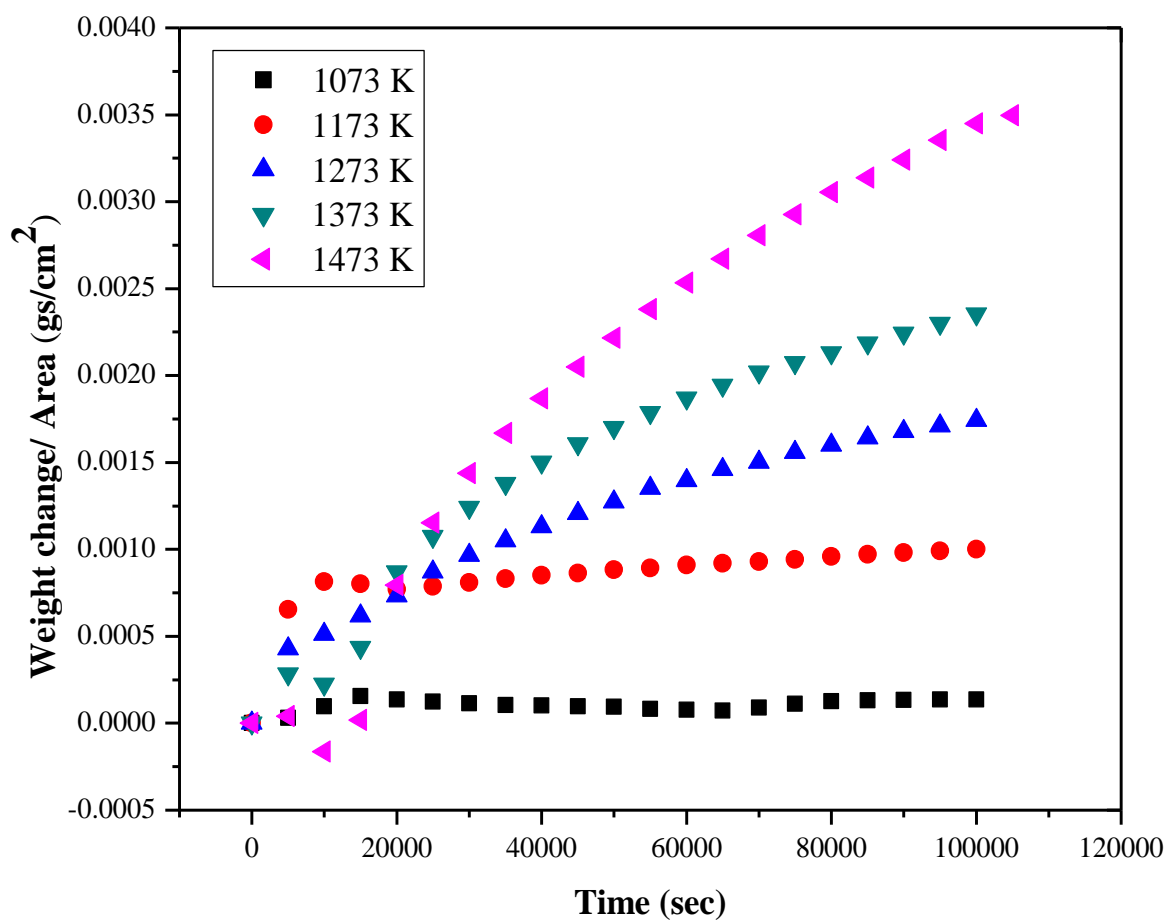
Figure 54. Oxidation kinetics for 617 alloy plot of mass gain per unit area versus oxidation time for temperatures in the range 1073 K–1473 K. (t = 0 refers to the time when the sample reached set temperature)

Figure 55 shows the oxidation kinetics of alloy 617 as obtained by our measurements.

Equation	y = a + b*x		
Adj. R-Square	0.09409	0.74532	0.99622
		Value	Standard Error
1073 K	Slope	7.48728E-14	4.2682E-14
1173 K	Slope	6.33249E-12	8.20747E-13
1273 K	Slope	3.17579E-11	4.37371E-13
1373 K	Slope	6.01786E-11	1.30555E-12
1473 K	Slope	1.3084E-10	3.14007E-12
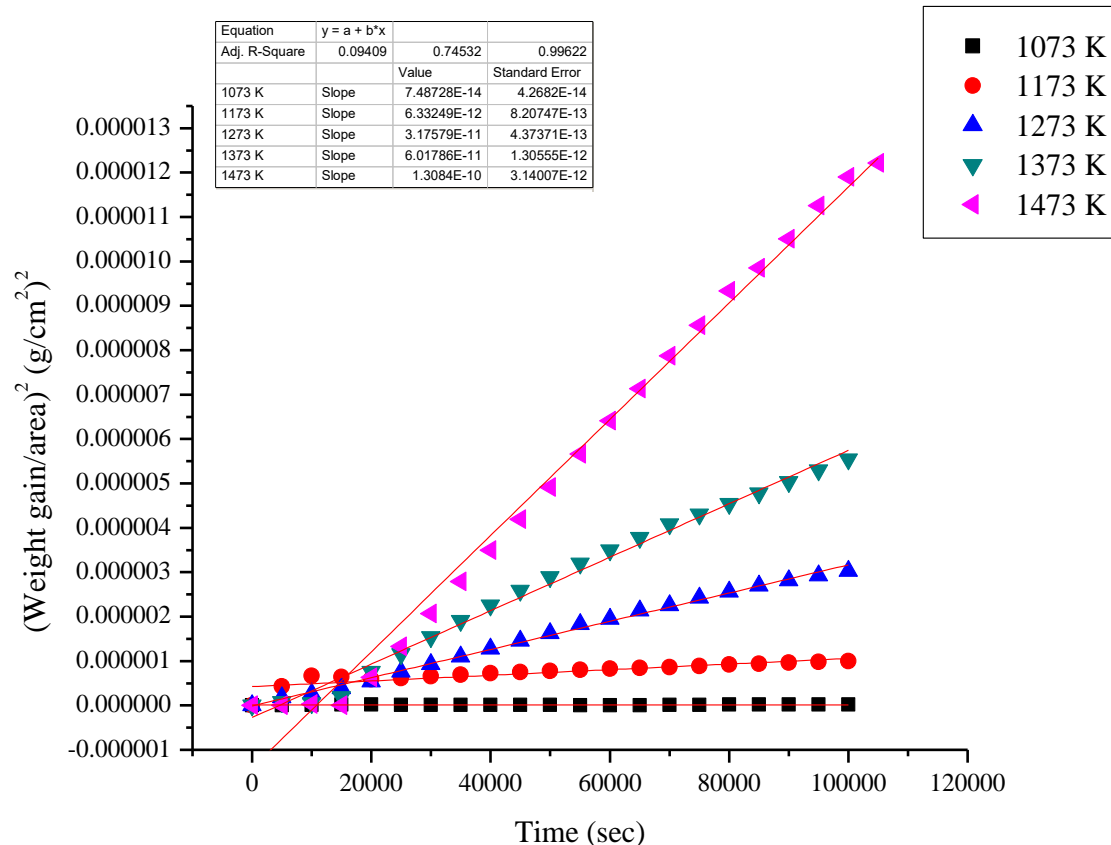
Figure 55. Oxidation kinetics for alloy 617 plot of (mass gain per unit area) 2 versus oxidation time for temperatures in the range 1073 K–1473 K. (t = 0 refers to the time when the sample reached set temperature)

As shown in Figure 55, the weight changes in the air conditions were similar to those found when subjected to temperature of 1073 K to 1473 K. The parabolic rate constants were identified by fitting oxidation data sets to linear lines, and the results are listed in Table 27.

Table 27. Experimental parabolic oxidation rate constant, kp value of alloy 617.

Temperature (K)	k_p value $(g^2 cm^{-4} sec^{-1})$
1073 K	7.487×10^{-14}
1173 K	6.332×10^{-12}
1273 K	3.176×10^{-11}
1373 K	6.018×10^{-11}
1473 K	1.308×10^{-10}

5.2.1.3 Activation Energy

The graph in which log k is plotted against 1/T will have a slope of – Q in Fig. 56. The activation energy of the oxidation coating reaction Q for a parabolic rate of oxidation for the 617 alloy is 233.46 kJ/mol.

Equation	y = a + b*x		
Adj. R-Square	0.86025		
		Value	Standard Error
B	Intercept	-1.28162	1.92911
B	Slope	-12.19889	2.40996
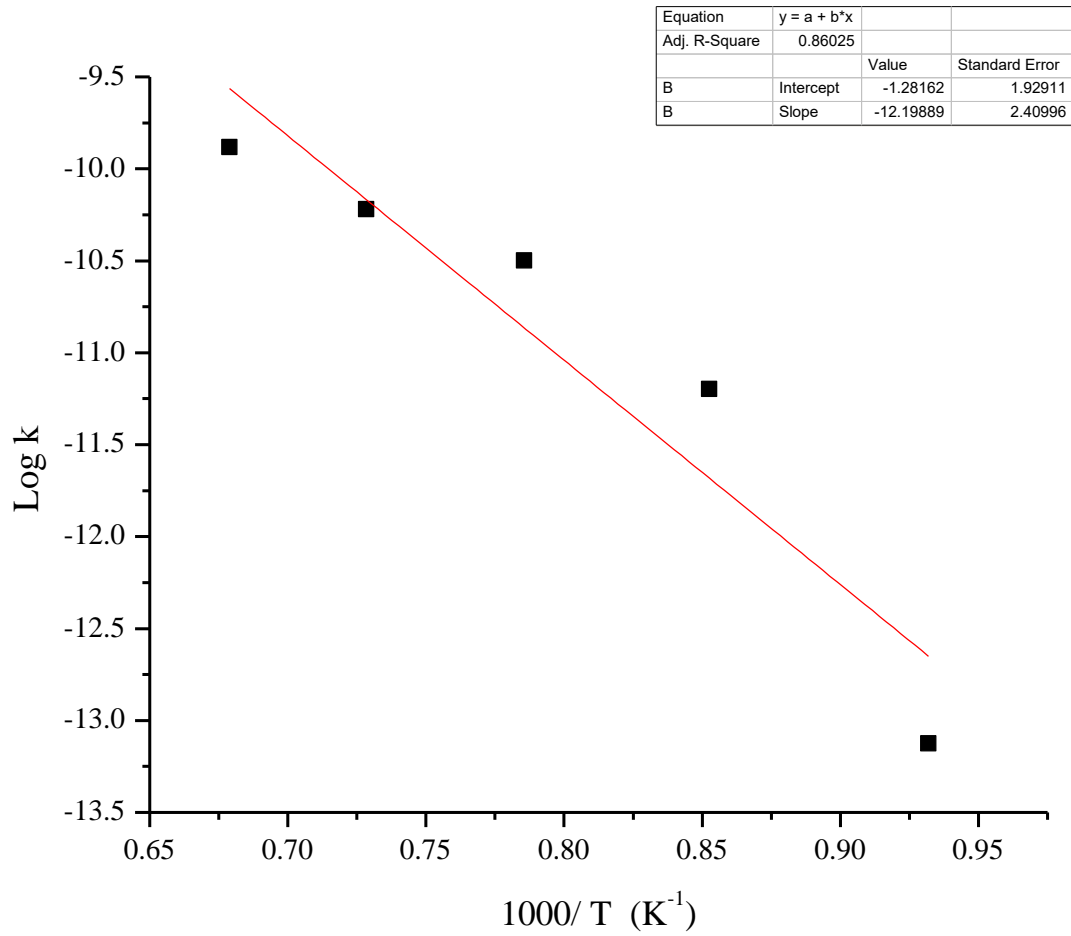
Figure 56. Arrhenius plot and exhibited activation energy for alloy 617 at 1073 K to 1473 K.

5.2.2. Oxidation Microstructure (Surface Analysis) with Scanning electron microscopy/energy dispersive X-ray spectroscopy (SEM/EDS)

This section will discuss the effects of oxidation on the alloy 617 surface under different temperatures. The microstructure will be examined using SEM/EDS,

5.2.2.1. Room Temperature (Pure Sample)

The SEM images of alloy 617 at the room temperature pure sample are shown in Fig. 57 and the corresponding EDS figures are shown in Fig.58. The scratches appear as the sample was reground with 400 grit silicon-carbide paper.
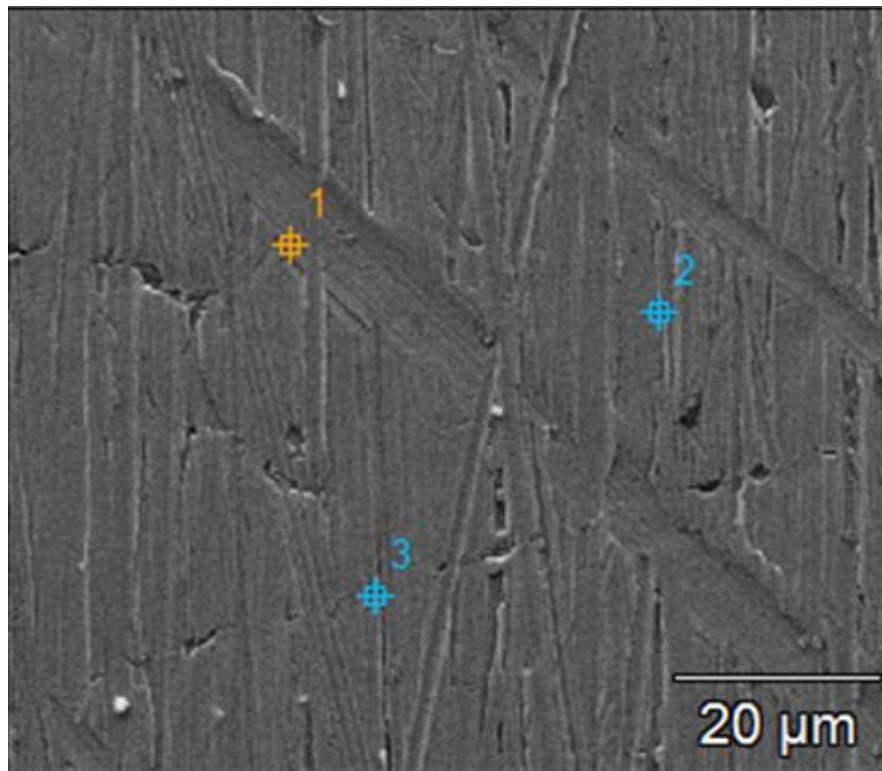
Figure 57. SEM surface morphology of Alloy 617.
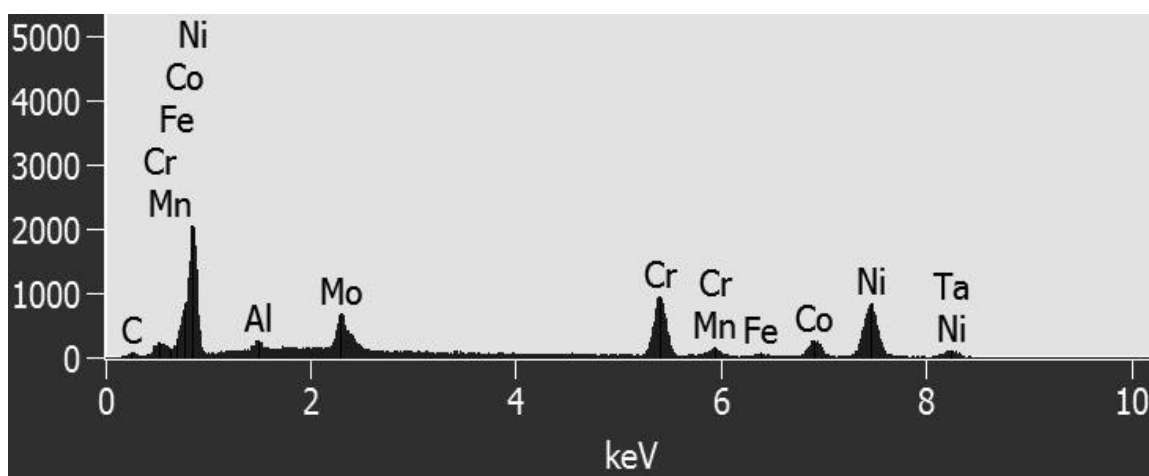
Figure 58. EDS spectrum of alloy 617

As shown in Table 28, atomic and mass percent means of three different randomly selected regions were analyzed by EDS revealing their absolute deviation.

Table 28. Surface morphology mass percent analysis on alloy surface for pure sample.

Element	C	Al	Si	Ti	Cr	Mn	Fe	Co	Ni	Mo	Ta
Mass percent Mean (Absolute deviation)	6.08	0.96	0.28	0.29	20.32	0.06	1.28	22.61	51.28	7.89	0.48
Atomic percent Mean (Absolute deviation)	23.7	1.68	0.47	0.29	18.48	0.05	1.09	9.08	61.83	3.89	0.13

5.2.2.2. 1073 K

As shown in Figures 59 and 60 as well as Tables 29 –30, Cr_2O_3 was the predominant formation on the alloy surface. Table 29 shows that the alloy surface contained Ni, Mo, and Co as well as barely detectable amounts of Al, Si, Ti, and Fe. In Fig. 59, R2 and R4 are near protruding white lines or ridges made up of particles

containing mostly Cr . At 1073 K, nodular type structures, but not large nodules and platelets were observed as shown in Figure 59, and based on the surface oxide scales captured by the EDS spectrum (Figure 60), the nodules and platelets oxides were mostly composed of Cr, Ni, and Mo.
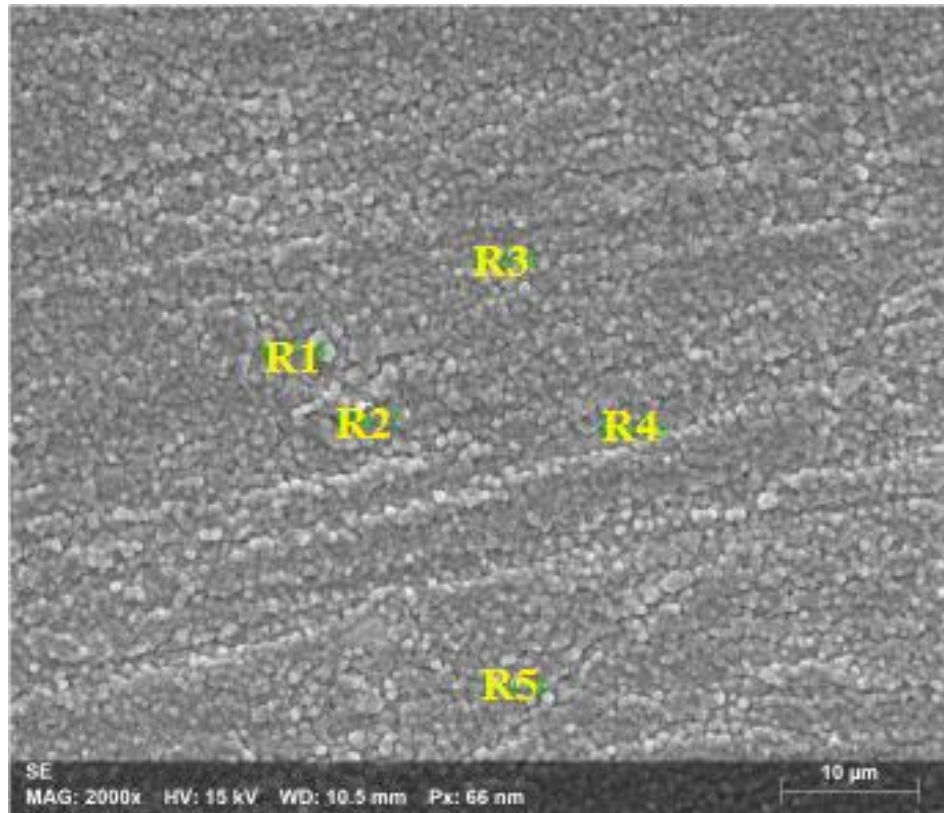
Figure 59. Surface morphology of alloy 617 in air for 24 h at 1073 K.

As shown in Tables 29 and 30, atomic and mass percent of different regions were analyzed by EDS. Table 29 shows that the sample was composed mainly of 58.57% O, 24.38% Cr, and 7.21% Ni by atomic percent. Table 30 shows the alloy 617 sample contained 42.25% Cr, 31.25% O, and 13.84% Ni by mass percent.

Table 29. Surface morphology atomic percent analysis in the five different locations on the surface of alloy 617 in air for 24 h at 1073 K.

Spectrum	C	O	Al	Si	Ti	Cr	Fe	Co	Ni	Mo
R1	2.84	59.86	0.80	-	1.76	26.94	0.278	0.95	4.98	1.60
R2	4.10	61.67	0.14	-	1.96	25.83	0.12	0.93	4.48	0.77
R3	4.91	53.45	0.36	-	1.10	23.11	0.33	3.02	12.24	1.49
R4	7.19	59.44	0.53	-	1.16	23.63	0.09	1.42	5.55	0.99
R5	3.27	58.42	0.36	-	2.91	22.40	0.27	2.09	8.79	1.49
Mean	4.46	58.57	0.44	-	1.78	24.38	0.22	1.68	7.21	1.27
Sigma	1.72	3.09	0.25	-	0.74	1.92	0.11	0.88	3.28	0.36

Table 30. Surface morphology mass percent analysis in the five different locations on the surface of alloy 617 in air for 24 h at 1073 K.

Spectrum	C	O	Al	Si	Ti	Cr	Fe	Co	Ni	Mo
R1	1.13	31.77	0.71	-	46.47	46.47	0.50	1.85	9.70	5.08
R2	1.71	34.32	0.13	-	3.26	46.71	0.23	1.91	9.14	2.58
R3	1.82	26.44	0.30	-	1.62	37.15	0.57	5.50	22.20	4.41
R4	3.04	33.42	0.51	-	1.94	43.18	0.17	2.94	11.45	3.35
R5	1.27	30.30	0.32	-	4.52	37.75	0.49	3.99	16.71	4.63
Mean	1.80	31.25	0.39	-	2.83	42.25	0.39	3.24	13.84	4.01
Sigma	0.75	3.10	0.22	-	1.15	4.60	0.18	1.54	5.55	1.02
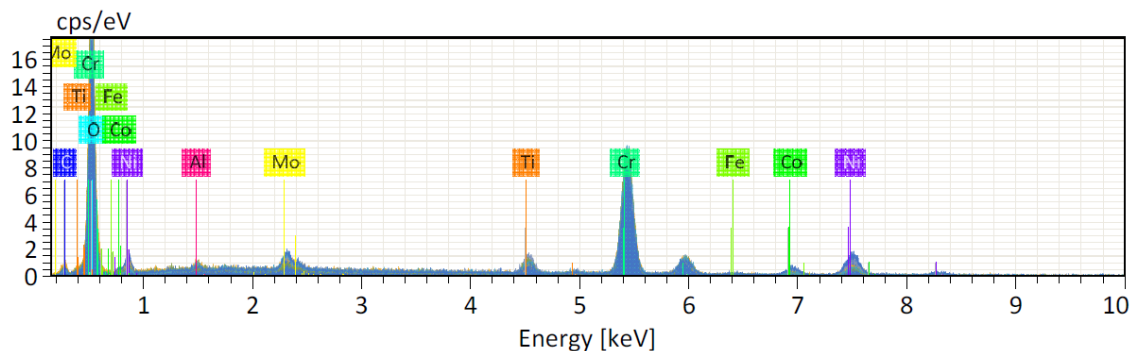
Figure 60. EDS spectrum of alloy 617 at 1073 K.
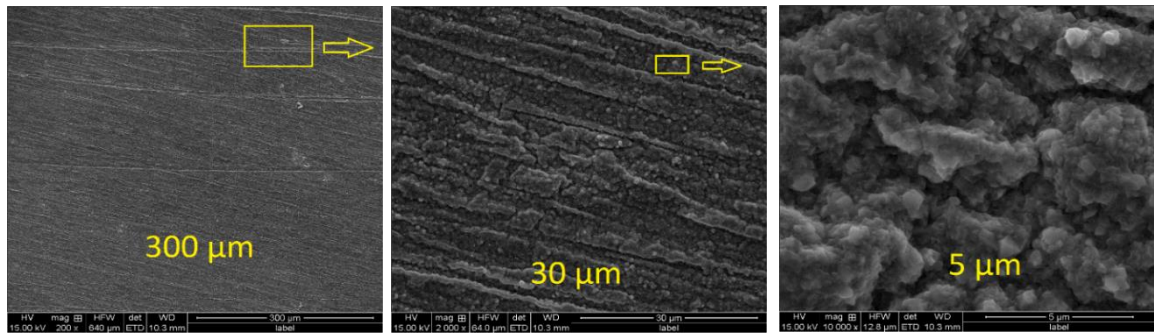
Figure 61. Surface morphology of alloy 617 in air for 24 h at 1173 K, at 300 µm, 30 µm and 5 µm.

5.2.2.3. 1173 K

At 1173 K, the alloy surface is mostly covered with a nodular shape structure and grain boundaries ridges were formed as shown in Figure 62, which shows chromium rich oxide has grown on the INCONEL® alloy 617 surface at 1173 K. The oxide appears to be constituted by small nodules (see Figure 62) made up of titanium, aluminum, nickel, and molybdenum above the alloy grain boundaries as shown in Figure 63. Finally, Cr and Mo rich carbides are also observed in the alloy matrix.
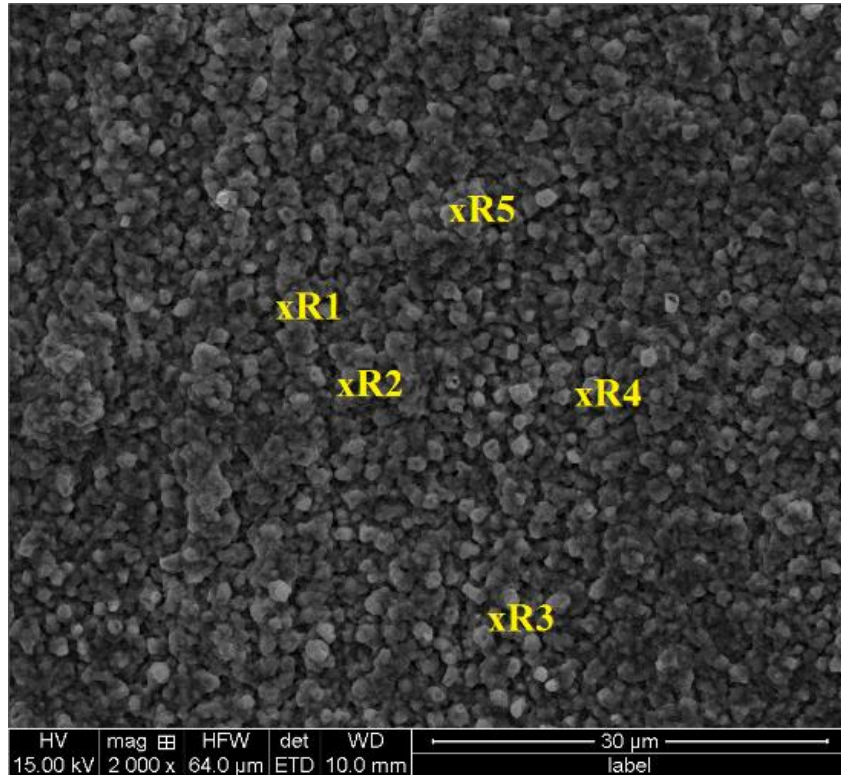
Figure 62. Surface morphology of alloy 617 in air for 24 h at 1173 K.
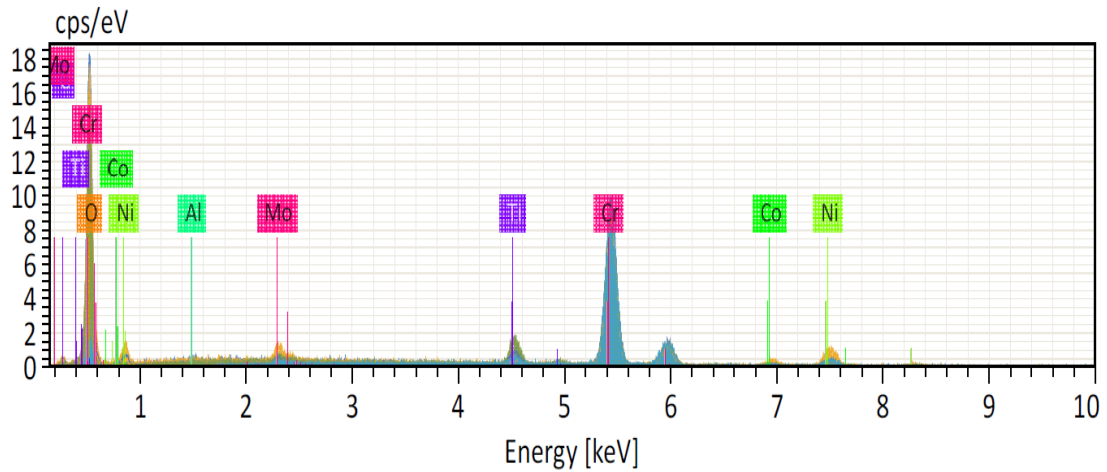
Figure 63. EDS spectrum of alloy 617 at 1173K.

As shown in Tables 31-32 atomic and mass percent of different regions were analyzed by EDS. Table 31 shows that the sample is composed of mainly 48.08% Cr,

40.33% O, and 5.22% Ni by atomic percent. According to Table 32, the sample contained

64.20% Cr, 19.65% O, and 8.31% Ni by mass percent.

Table 31. Surface morphology atomic percent analysis in the five different locations on the surface of alloy 617 in air for 24 h at 1173 K.

Spectrum	C	O	Al	Si	Ti	Cr	Fe	Co	Ni	Mo
R1	0.22	13.93	0.23	-	2.14	73.45	-	1.21	7.45	1.37
R2	1.96	56.44	0.28	-	4.08	33.23	-	0.55	2.66	0.80
R3	0.98	18.95	0.33	-	1.49	72.56	-	0.80	4.17	0.73
R4	4.18	54.22	0.07	-	0.60	28.98	-	2.14	8.64	1.18
R5	3.26	58.09	0.36	-	1.83	32.20	-	0.63	3.17	0.46
Mean	2.12	40.33	0.25	-	2.03	48.08	-	1.07	5.22	0.91
Sigma	1.62	21.92	0.11	-	1.29	22.81	-	0.65	2.67	0.36

Table 32. Surface morphology mass percent analysis in the five different locations on the surface of alloy 617 in air for 24 h at 1173 K.

Spectrum	C	O	Al	Si	Ti	Cr	Fe	Co	Ni	Mo
R1	0.05	4.65	0.13	-	2.13	79.67	-	1.49	9.12	2.75
R2	0.75	28.92	0.25	-	6.26	55.33	-	1.04	5.00	2.45
R3	0.26	6.69	0.19	-	1.57	83.30	-	1.04	5.41	1.54
R4	1.57	27.10	0.06	-	0.89	47.07	-	3.93	15.84	3.53
R5	1.30	30.90	0.32	-	2.91	55.66	-	1.24	6.19	1.48
Mean	0.79	19.65	0.19	-	2.75	64.20	-	1.75	8.31	2.35
Sigma	0.65	12.85	0.10	-	2.10	16.19	-	1.24	4.51	0.86
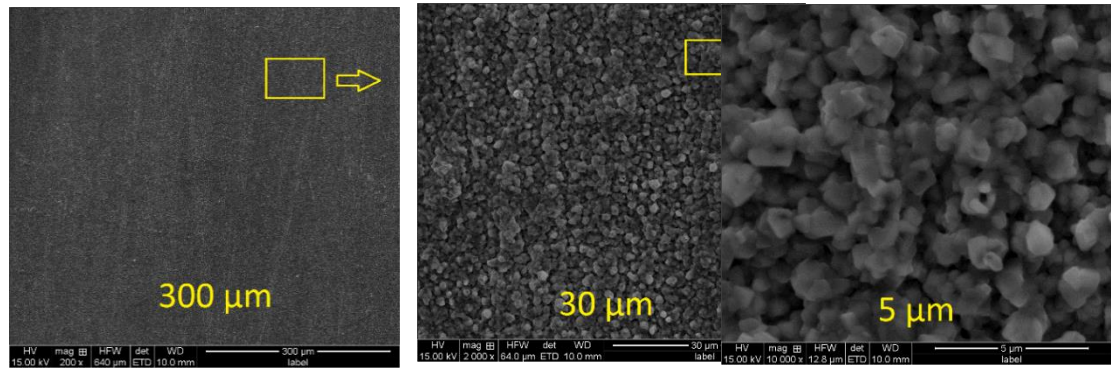
Figure 64. Surface morphology of alloy 617 in air for 24 h at 1173 K, at 300 µm, 30 µm and 5 µm film thickness.

5.2.2.4. 1273 K

Figure 65 illustrates surface oxidation on the INCONEL® alloy 617 surface after 1273 K, characterized by an alloy 617 oxide. The comparison of 1073 K (Figure 59) and 1173 K (Figure 62) temperatures and their effect on the alloy 617 oxide as shown in suggests that the nodules are more numerous at 1073 K. At 1273 K, coalesced nodules were detected as shown in Fig. 65 in the bright-surface region where enriched chromium oxidation was detected.
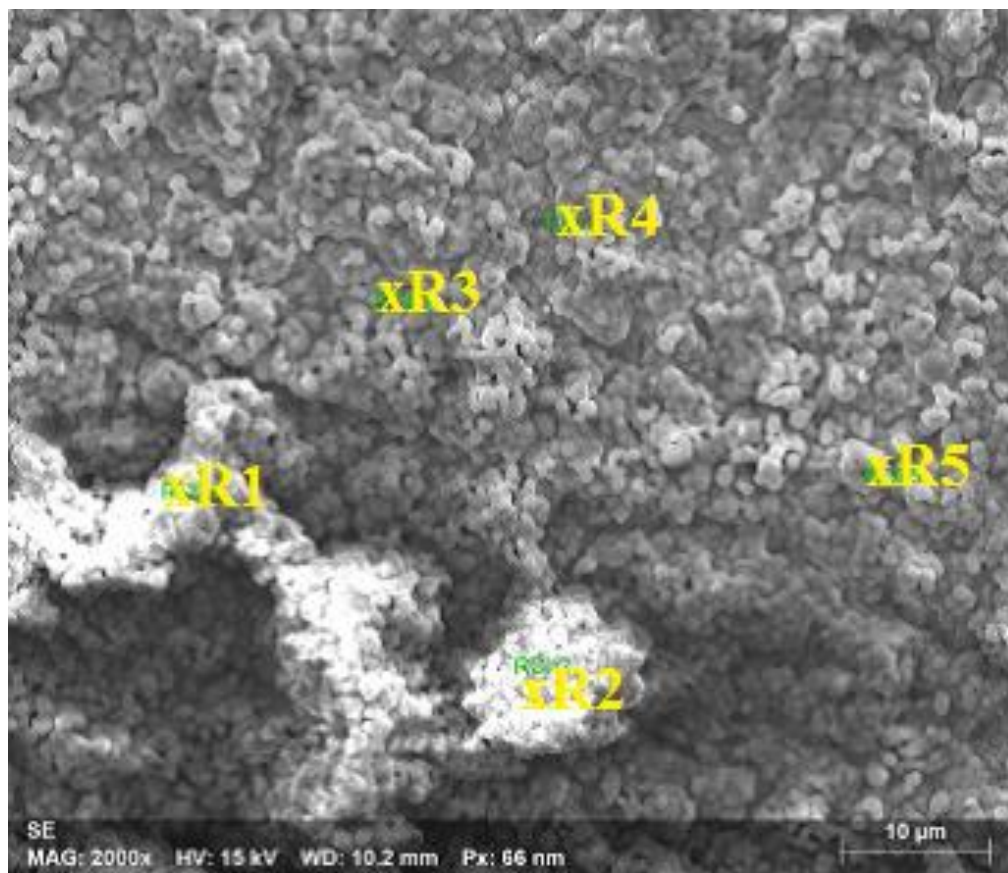
Figure 65. Surface morphology of alloy 617 in air for 24 h at 1273 K.
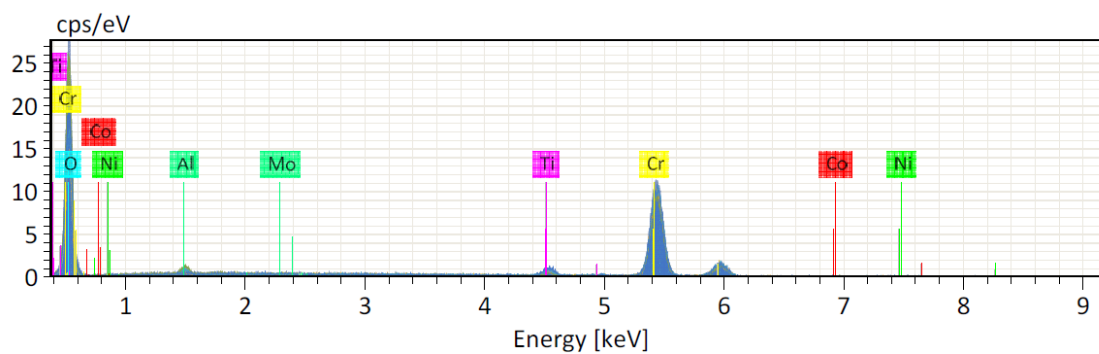
Figure 66. EDS spectrum of alloy 617 at 1273 K.

EDS analyses performed on the surface are given in Figure 66 and Tables 33 and 34. Table 33 shows that the sample is composed mainly of 34.98% Cr, 58.52% O, and

3.85% C by atomic percent. According to Table 34, the sample contains 61.93% Cr and 32.42% O by mass percent.

Table 33. Surface morphology atomic percent analysis in the five different locations on the surface of alloy 617 in air for 24 h at 1273 K

Spectrum	C	O	Al	Si	Ti	Cr	Fe	Co	Ni	Mo
R1	3.48	54.98	1.32	-	1.68	37.64	-	0.21	0.66	0.03
R2	4.68	65.11	0.84	-	0.71	28.25	-	0.08	0.33	0.00
R3	5.82	62.29	0.47	-	0.84	30.29	-	0.12	0.14	0.02
R4	2.80	51.61	0.57	-	1.53	4291	-	0.06	0.48	0.04
R5	2.50	58.60	0.36	-	2.18	35.80	-	0.19	0.33	0.05
Mean	3.85	58.52	0.71	-	1.39	34.98	-	0.13	0.39	0.03
Sigma	1.38	5.43	0.38	-	0.61	5.87	-	0.06	0.19	0.02

Table 34. Surface morphology mass percent analysis in the five different locations on the surface of alloy 617 in air for 24 h at 1273 K.

Spectrum	C	O	Al	Si	Ti	Cr	Fe	Co	Ni	Mo
R1	1.37	28.85	1.17	-	2.64	64.20	-	0.40	1.26	0.10
R2	2.12	39.35	0.86	-	1.28	55.48	-	0.19	0.73	0.00
R3	2.58	36.75	0.47	-	1.49	58.07	-	0.27	0.30	0.07
R4	1.05	25.69	0.48	-	2.28	69.40	-	0.12	0.88	0.11
R5	1.01	31.48	0.32	-	3.51	62.50	-	0.37	0.65	0.16
Mean	1.62	32.42	0.66	-	2.24	61.93	-	0.27	0.76	0.09
Sigma	0.70	5.60	0.35	-	0.90	5.43	-	0.12	0.35	0.06
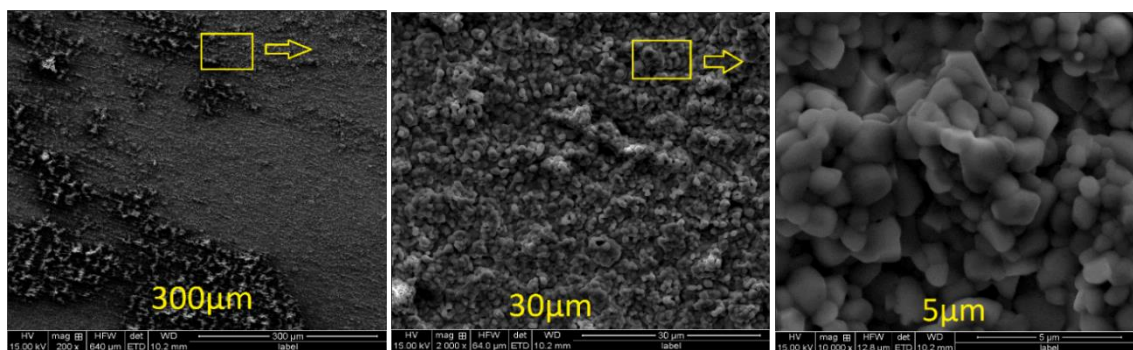
Figure 67. Surface morphology of alloy 617 in air for 24 h at 1273 K, at 300 µm, 30 µm and 5 µm

Fig 67 shows the surface morphology of the Cr_2O_3. It clearly shows that many Cr_2O_3 crystals that are stacked together during the growth of the scale. The growing surface crystals are not continuously distributed to form a dense monolithic scale. It is noteworthy that there are small openings or pores between the crystals as they grow, indicating that the interface where the crystals contact one another contains small pores. This implies that, as two crystallites with their own facets grow together, the interfacial regions are not continuous and provide an active pathway for Cr and O transport. These results suggest that the occurrence of Cr–O oxidation reaction may be beneath the scale/gas interface during the growth of the scale. It was also found that concentration gradients for elemental nickel and cobalt are present within the chromia.

5.2.2.5. 1373 K

At 1373 K, Fig 68 and Fig. 70, show a surface morphology where many nodules that are stacked together during the growth of the scale. From the EDS graph Fig. 69. and tables 35-36, we detected rich Cr and Ti oxide.
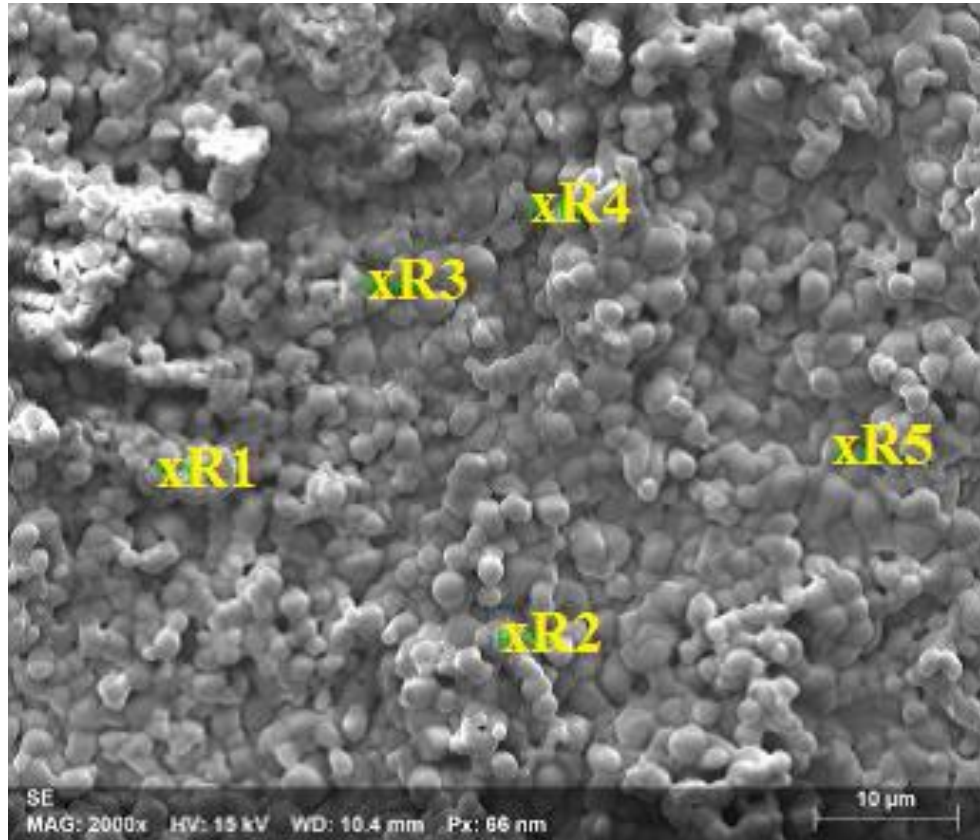
Figure 68. Surface morphology of alloy 617 in air for 24 h at 1373 K and EDS spectrum.
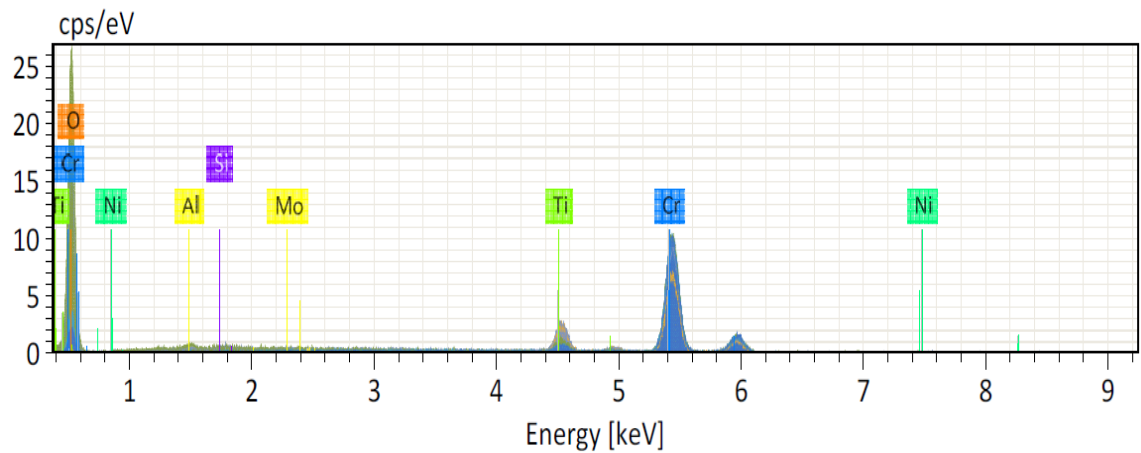
Figure 69. EDS spectrum of Alloy 617 at 1373K.

EDS analyses performed on the surface are given in Figure 69 and Tables 35-36. Table 35 shows that the sample is composed of mainly 53.65% Cr, 34.47% O, and 7.01 % Ti by atomic percent. According to Table 36, the sample contains 70.31% Cr, 17.89% O and 8.27% Ti by mass percent.

Table 35. Surface morphology atomic percent analysis in the five different locations on the surface of alloy 617 in air for 24 h at 1373 K.

Spectrum	C	O	Al	Si	Ti	Cr	Fe	Co	Ni	Mo
R1	1.96	24.38	1.35	0.39	2.68	68.81	-	-	0.43	0.00
R2	2.83	65.13	0.54	0.11	2.10	29.00	-	-	0.30	0.00
R3	2.37	61.44	0.33	0.19	6.46	28.70	-	-	0.35	0.16
R4	0.57	4.81	0.94	4.54	20.70	65.97	-	-	1.35	1.13
R5	1.81	16.60	1.59	0.46	3.12	75.75	-	-	0.31	0.36
Mean	1.91	34.47	0.95	1.14	7.01	53.65	-	-	0.55	0.33
Sigma	0.85	27.74	0.53	1.91	7.84	22.91	-	-	0.45	0.47

Table 36. Surface morphology mass percent analysis in the five different locations on the surface of alloy 617 in air for 24 h at 1373 K.

Spectrum	C	O	Al	Si	Ti	Cr	Fe	Co	Ni	Mo
R1	0.56	9.30	0.87	0.26	3.06	85.34	-	-	0.60	0.00
R2	1.25	38.32	0.54	0.11	3.69	55.44	-	-	0.65	0.00
R3	1.00	34.34	0.31	0.18	10.80	52.13	-	-	0.71	0.53
R4	0.14	1.59	0.52	2.63	20.46	70.80	-	-	1.63	2.23
R5	0.48	5.92	0.96	0.29	3.33	87.84	-	-	0.41	0.77
Mean	0.69	17.89	0.64	0.70	8.27	70.31	-	-	0.80	0.71
Sigma	0.44	17.11	0.27	1.09	7.54	16.47	-	-	0.48	0.92
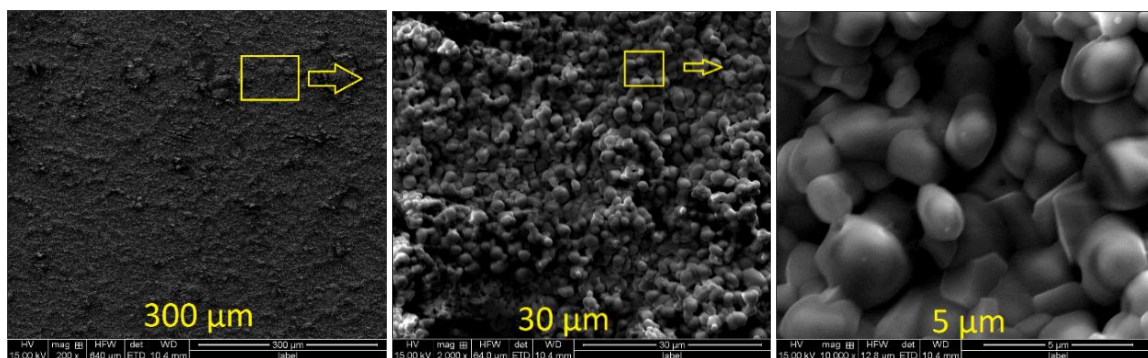
 Figure 70. Surface morphology of alloy 617 in air for 24 h at 1373 K, at 300 µm, 30 µm and 5 µm.

5.2.2.6. 1473 K

Spallation of the oxide scale may also contribute to the formation of a rugged oxide/metal substrate after 24 h at 1473 K. The spallation of the scale was mainly caused by the outer TiO_2 layer, as shown in Fig. 71 and Tables 37 and 38. Most of the TiO_2 layer was spalled due to the difference in the thermal expansion between inner Cr_2O_3 layer and outer TiO_2 layer. As shown in Figure 71 and Figure 73, Ti ions were concentrated within the surface oxide layer after 2 h. According to Sigler's oxidation tests[99], using Ti-modified Fe–20 Cr alloys, a small amount of Ti (0.46 wt.%) increased the weight gain significantly.
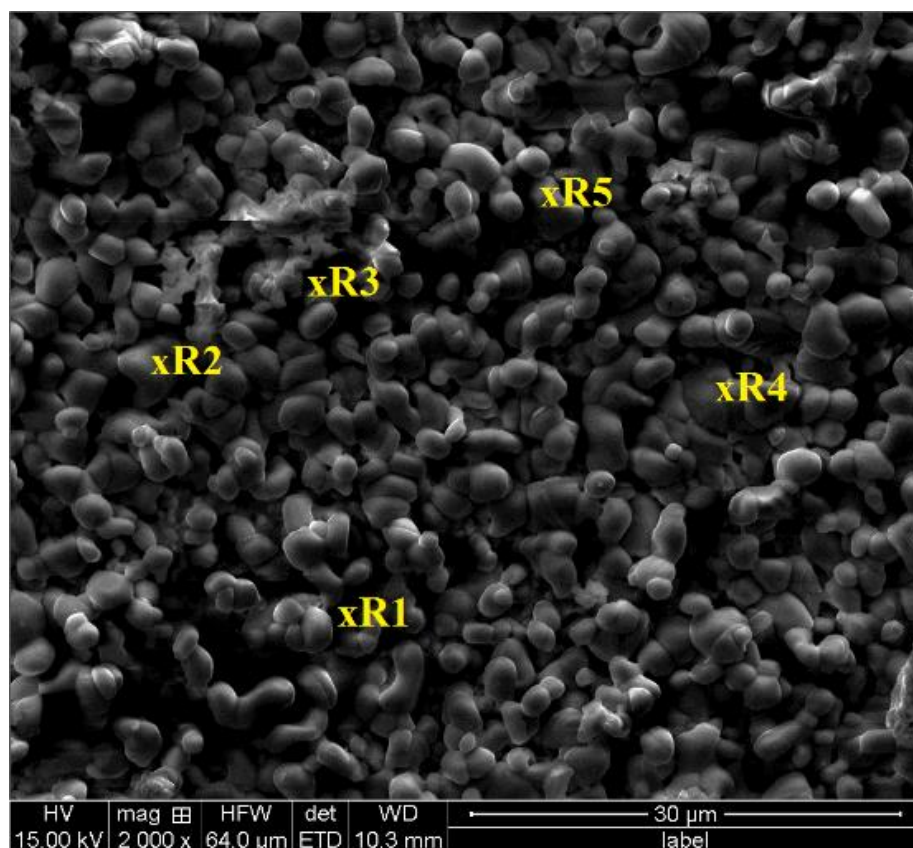
Figure 71. Surface morphology of alloy 617 in air for 24 h at 1473 K and EDS spectrum.
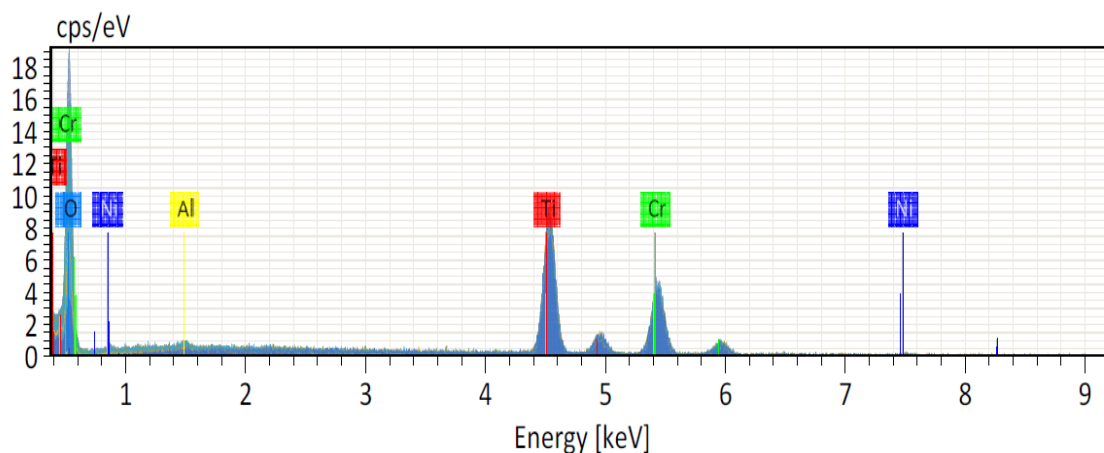
Figure 72. EDS spectrum of alloy 617 at 1473 K.

EDS analyses performed on the surface are given in Figure 70 and Tables 37 and 38. Table 37 shows that the sample is composed of mainly 64.51% O, 20.34% Ti and

10.28% Cr by atomic percent. According to Table 38, the sample contains 40.57% O, 35.88% Ti and 19.81% Cr by mass percent.

Table 37. Surface morphology atomic percent analysis in the five different locations on the surface of alloy 617 in air for 24 h at 1473 K.

Spectrum	C	O	Al	Si	Ti	Cr	Fe	Co	Ni	Mo
R1	4.45	71.29	0.96	-	14.98	8.04	-	-	0.27	-
R2	4.15	71.01	1.08	-	15.36	8.09	-	-	0.32	-
R3	3.44	73.65	0.95	-	14.11	7.41	-	-	0.44	-
R4	2.59	59.48	0.99	-	24.19	12.10	-	-	0.65	-
R5	1.58	47.13	1.78	-	33.07	15.74	-	-	0.69	-
Mean	3.24	64.51	1.15	-	20.34	10.28	-	-	0.47	-
Sigma	1.17	11.17	0.36	-	8.20	3.58	-	-	0.19	-

Table 38. Surface morphology mass percent analysis in the five different locations on the surface of alloy 617 in air for 24 h at 1473 K.

Spectrum	C	O	Al	Si	Ti	Cr	Fe	Co	Ni	Mo
R1	2.25	48.09	1.09	-	30.25	17.63	-	-	0.68	-
R2	2.08	47.54	1.21	-	30.78	17.61	-	-	0.77	-
R3	1.77	50.54	1.10	-	28.97	16.52	-	-	1.10	-
R4	1.10	33.57	0.95	-	40.86	22.19	-	-	1.34	-
R5	0.58	23.11	1.47	-	48.52	25.08	-	-	1.24	-
Mean	1.56	40.57	1.16	-	35.88	19.81	-	-	1.03	-
Sigma	0.70	11.82	0.20	-	8.51	3.67	-	-	0.29	-
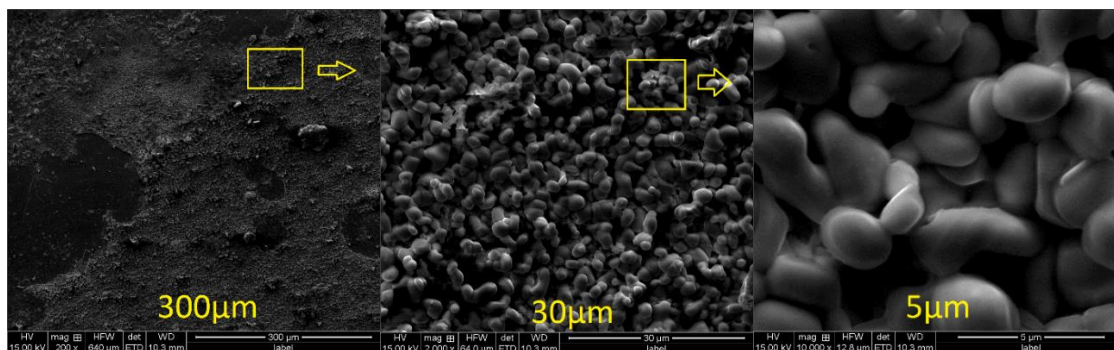
Figure 73. Surface morphology of alloy 617 in air for 24 h at 1473 K, at 300 µm, 30 µm and 5 µm.

5.2.3. Oxidation Microstructure (Cross-Section Analysis) with Scanning electron microscopy/energy dispersive X-ray spectroscopy (SEM/EDS)

5.2.3.1. 1073 K

At 1073 K, the SEM cross-section morphology micrograph reported the compositions of two regions. At 1073 K, as shown in Fig. 74, the first region (outer layer) mainly Cr and O. The Second region (inner layer) shows the presence of Al, Ni, and Cr. Surface morphologies are shown in Fig. 76. Double layers were formed in the cross section of the sample. External layer (the top, or oxide layer) contained a Cr–oxide layer, and the internal layer contained large amounts of Ni. We find that the oxide scale has small cracks. Small round shaped areas rich in chromium and molybdenum are shown with different colors in Figure 74.

The EDS analysis of the surface oxide and the microstructure are shown in Fig. 76. At 1073 K, the surface oxide was mostly Cr rich oxide. Fig. 75 also shows an elemental map of a well-developed layer alloy/oxide interface. In addition, an EDS analysis of the sample surface was performed as shown in Table 39.

As shown in Fig. 74 different regions were analyzed by EDS analysis. Figure 76 shows the Region 1 (outer layer) and Region 2 (inner layer) EDS graph.

EDS analyses performed on the cross-section are given in Table 39. The presence of chromium was noted at the external interface and nickel and aluminum was noted at the internal interface. It appears that aluminum is mainly located between external and internal layer (Fig. 74).
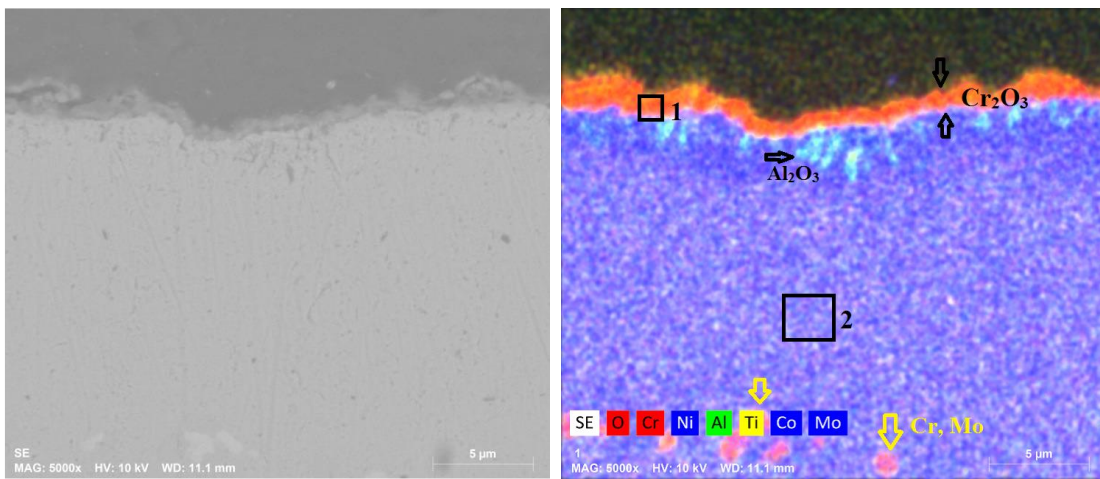
Figure 74. SEM images of the cross-section of the oxide after exposure to air at 1073 K
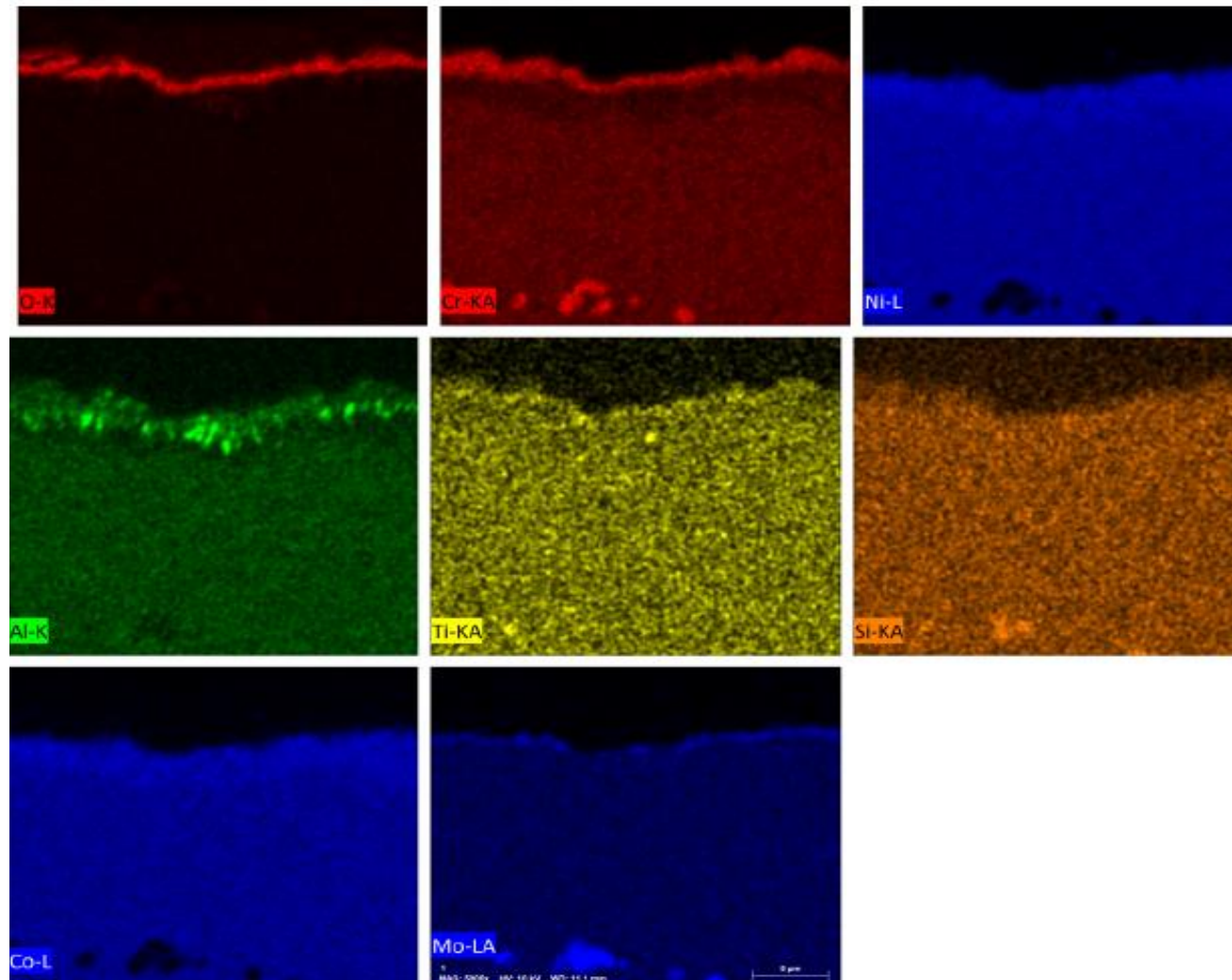
Figure 75. The elemental maps in a cross sectional area of the oxide film at 1073 K.
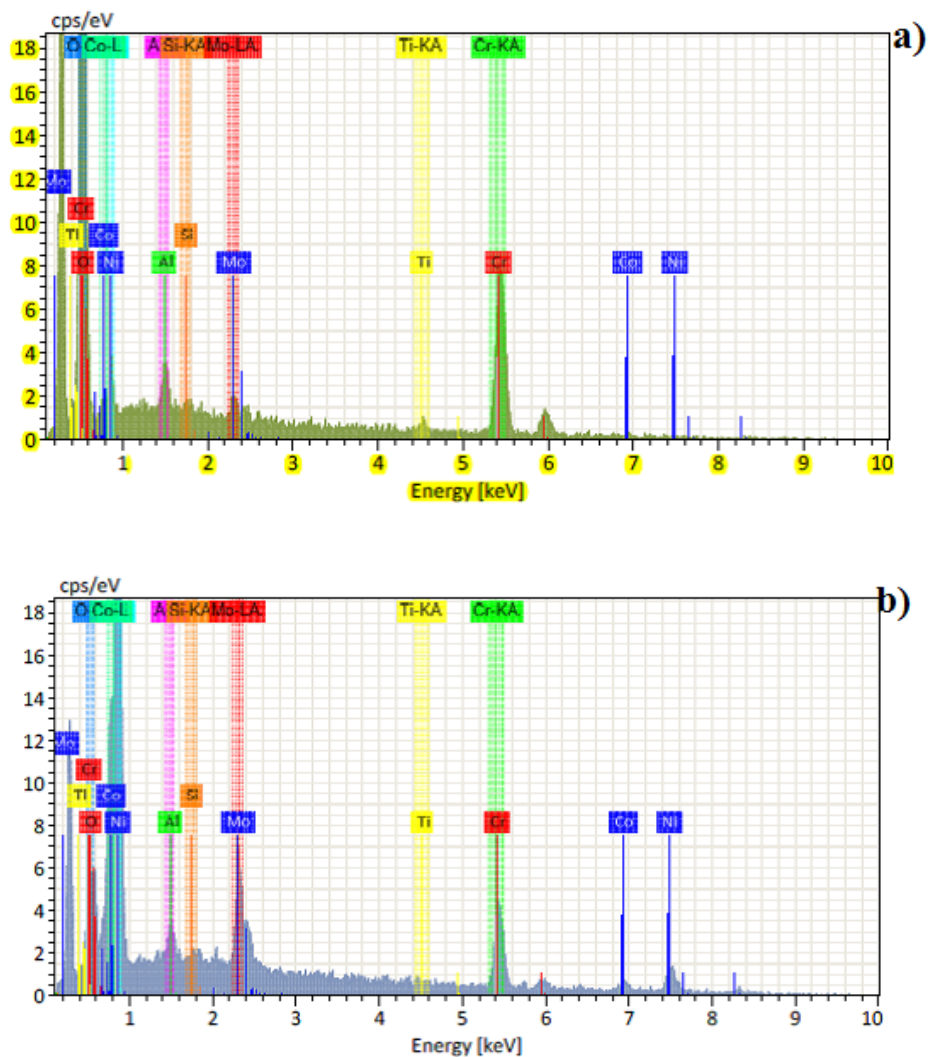
Figure 76. EDS graph at 1073 K a). Section 1 (Region 1) b). Section 2 (Region 2)

Table 39. Region 1 and Region 2 mass % and atomic % at 1073 K.

Element	Region 1 (section 1)		Region 2 (section 2)	
	Mass (%)	Atomic (%)	Mass (%)	Atomic (%)
Oxygen	22.46	57.11	0.53	2.37
Aluminum	0.47	0.70	0.64	1.71
Silicon	0.12	0.17	0.14	0.34
Titanium	1.30	1.11	0.42	0.63
Chromium	46.85	36.66	21.58	29.68
Cobalt	0.98	0.68	5.95	7.22
Nickel	4.11	2.85	43.20	52.64
Molybdenum	1.71	0.73	7.27	5.42
Sum	77.99	100.00	79.72	100.00

5.2.3.2. 1173 K

SEM images depict two regions as shown in Figure 77. At 1173 K, the first region mainly contains O and Cr, and also a small amount of Al and Ti. The second region mainly consists of Al and Ni, and also has Mo, Ni, Cr and Co.

The results of EDS analyses performed on the cross-section are given in Tables 40 and Fig. 79. Elements were detected by the SEM element map in Fig. 78, which clearly shows a relatively thick and continuous chromium layer beneath the Ni-containing layers. Therefore, two distinct oxide morphologies were observed as steady-state as shown in Fig. 77. Oxide morphology is mostly a double layer consisting of an inner NiO layer and outer Cr_2O_3 layer with one medium region in the second region; thus, the Al_2O_3 region, as shown in Figure 77 and elemental map Figure 78.

Fig. 79 shows the EDS analysis results of the surface oxide and the microstructure. At 1173 K, the surface oxide was mostly Cr-rich oxide. Fig. 77 displays the SEM images that show the presence of a well-developed layer of Cr at the alloy/oxide interface.
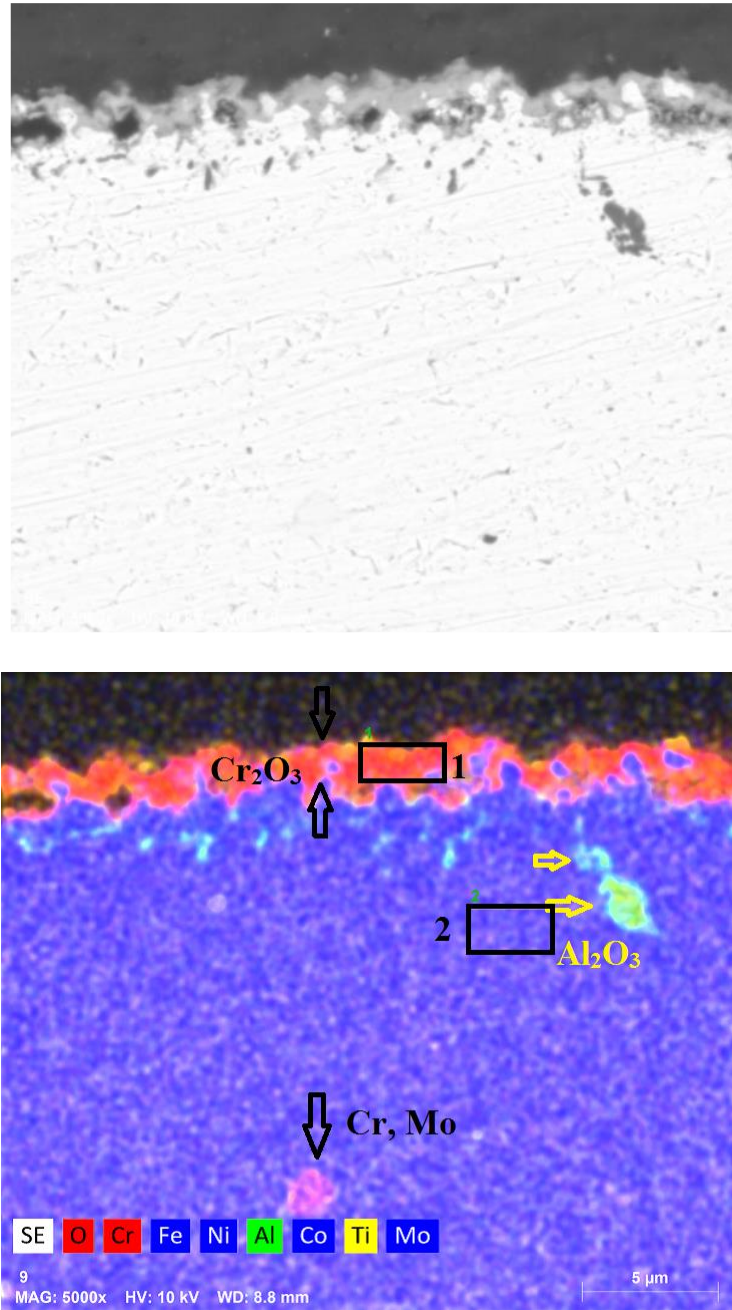
Figure 77. SEM images of the cross-section of the oxides after exposure to air at 1173 K.

Figure 78. The elemental maps in a cross sectional area of the oxide film at 1173 K
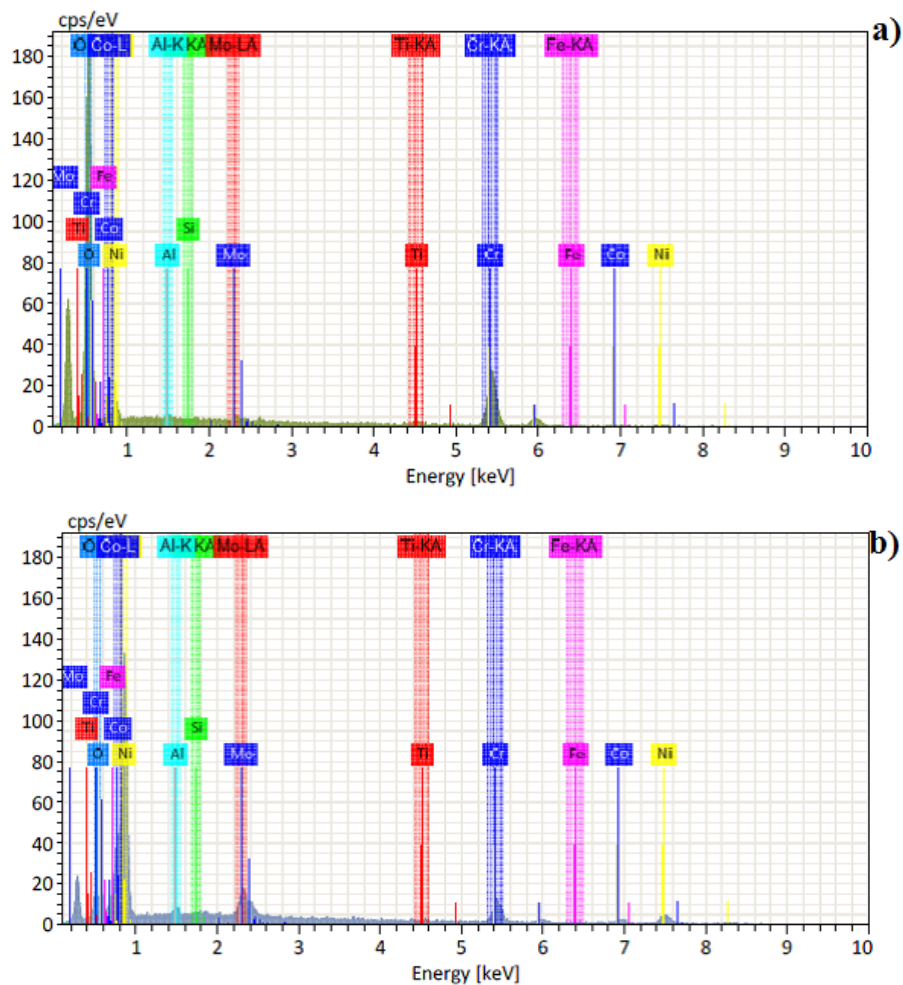
Figure 79. EDS graph at 1173 K a) Section 1 (Region 1) b) Section 2 (Region 2)

Table 40. Region 1 and Region 2 mass % and atomic % at 1173 K.

Element	Region 1 (section 1)		Region 2 (section 2)	
	Mass (%)	Atomic (%)	Mass (%)	Atomic (%)
Oxygen	24.82	62.03	0.33	1.56
Aluminum	0.18	0.27	0.56	1.58
Silicon	0.00	0.00	0.16	0.43
Titanium	1.26	1.05	0.06	0.09
Chromium	42.79	32.92	18.64	27.38
Iron	0.00	0.00	0.60	0.83
Cobalt	0.96	0.65	6.72	8.71
Nickel	3.77	2.57	41.17	53.57
Molybdenum	1.21	0.50	7.35	5.85
Sum	75.00	100.00	75.59	100.00

5.2.3.3 1273 K

At 1273 K, the SEM cross-section morphology micrograph reported the compositions of two regions. In general, cross section morphologies were observed to have an outer oxide layer and an inner layer with oxide protrusions, that is, internal oxidation was present. At 1273 K, as shown in Fig. 80 the first region (outer layer) mainly Cr and O with small amounts of Ti. The second region (inner layer) shows the presence of Al, Ni, and Cr. Surface morphologies are shown in Fig. 81 where double layers were formed in the cross section of the sample. The external layer (the top, or oxide layer) contained a Cr–oxide layer, while the internal layer contained large amounts of Ni. Also present was an area free of grain boundary carbides which were enriched aluminum, or a decarburized zone, just below the surface oxide layer. The surface oxide in air appeared relatively rough, as shown in Fig. 81.

The EDS analysis of the surface oxide and the microstructure are shown in Fig. 82 and the EDS analysis of the sample surface was performed as shown in Tables 41. The presence of chromium was noted at the external interface and nickel and aluminum were noted at the internal interface. It appears that aluminum is mainly located between the external and internal layer. At 1073 K, the surface oxide was mostly Cr rich oxide. Fig. 81 also shows an elemental map of a well-developed layer alloy/oxide interface. As shown in Fig. 82, different regions were analyzed by EDS-SEM analysis. Figure 82a shows Region 1 (outer layer) and Fig. 82b shows Region 2 (inner layer) EDS graph.
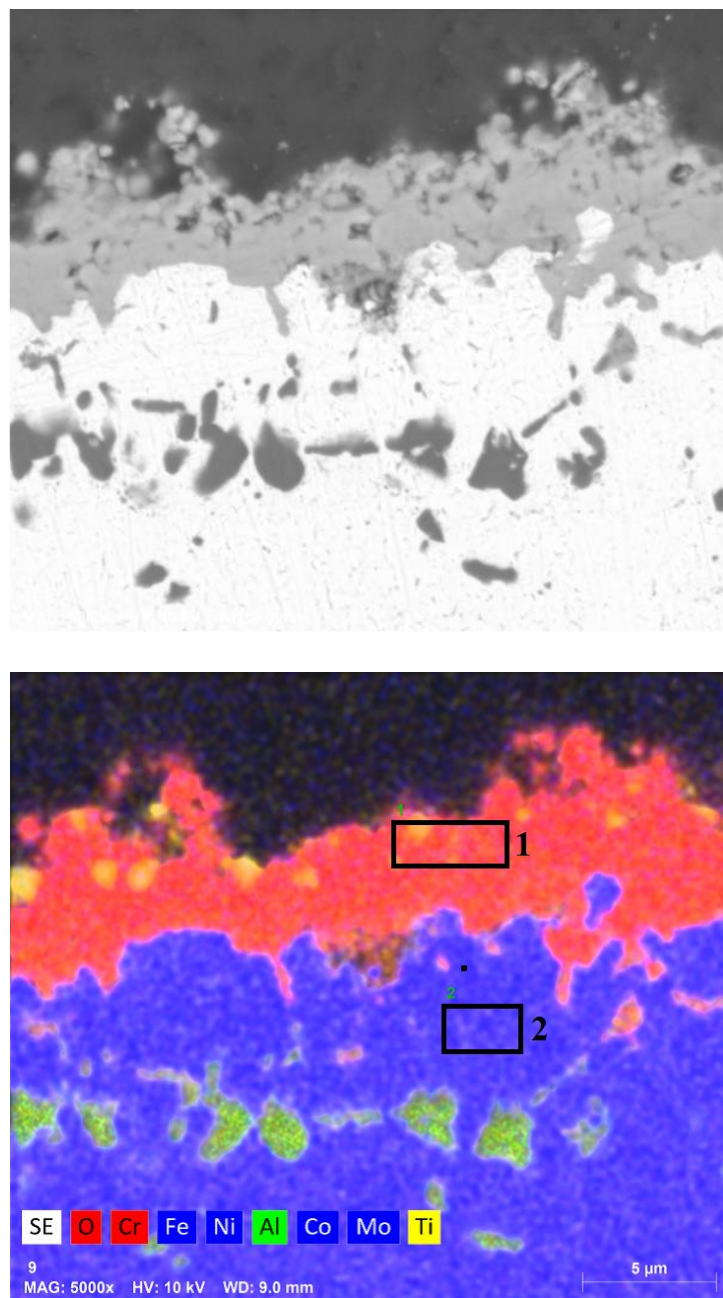
Figure 80. SEM images of the cross-section of the oxide after exposure to air at 1273 K.
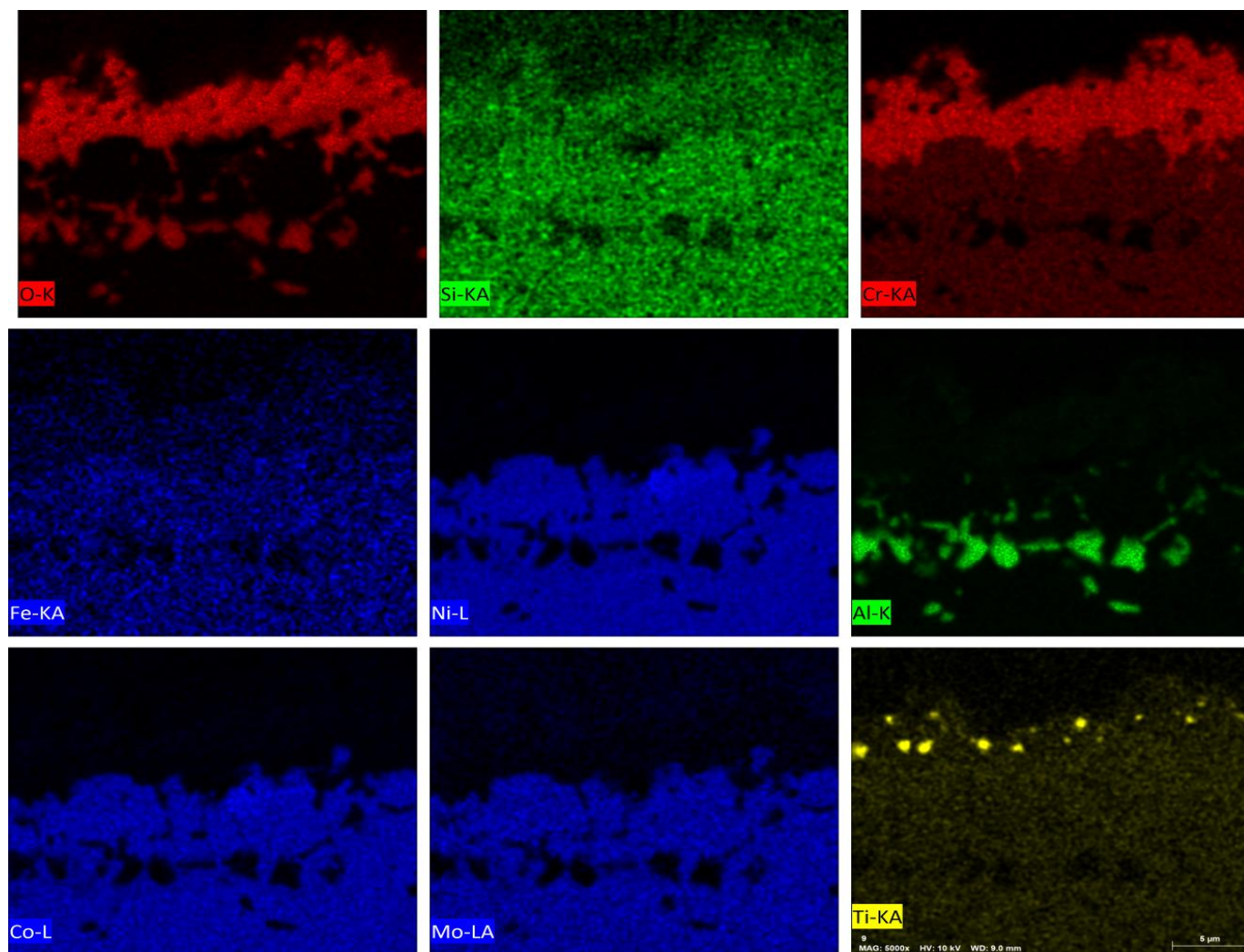
Figure 81. The elemental maps in a cross sectional area of the oxide film at 1273 K.
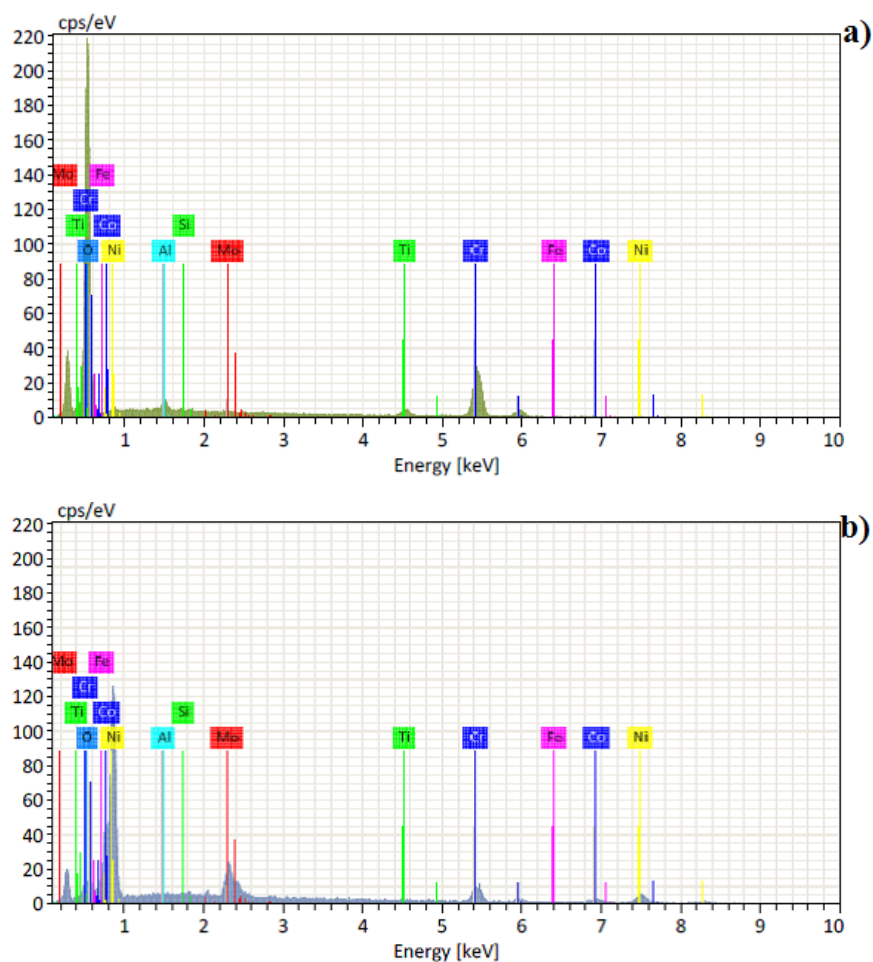
Figure 82. EDS graph at 1273 K a) Section 1 (Region 1) b) Section 2 (Region 2)

Table 41. Region 1 and Region 2 mass % and atomic % for of oxidized steel at 1273 K.

Element	Region 1 (section 1)		Region 2 (section 2)	
	Mass (%)	Atomic (%)	Mass (%)	Atomic (%)
Oxygen	24.23	64.18	0.67	3.44
Aluminum	0.35	0.55	0.17	0.51
Silicon	0.00	0.00	0.09	0.26
Titanium	2.38	2.10	0.30	0.51
Chromium	39.00	31.78	14.82	23.43
Iron	0.57	0.43	0.51	0.75
Cobalt	0.30	0.22	6.27	8.75
Nickel	0.91	0.66	39.10	54.75
Molybdenum	0.18	0.08	8.88	7.61
Sum	67.91	100.00	70.79	100.00

5.2.3.4. 1373 K

At 1373 K, EDS analysis of the sample surface was performed as shown in Table 42. SEM cross-section morphology micrograph reported the composition of two regions. In general, cross section morphologies were identified as having an outer oxide layer and an inner layer with inwardly protruding oxides, indicating internal oxidation was present. At 1373 K, shown in Fig. 83, the first region (outer layer) mainly Cr and O, also detected Ti. The second region (inner layer) shows the presence of Al, Ni, and Cr. Surface morphologies are shown in Fig. 83 where double layers were formed in the cross section of the sample. External layer (the top, or oxide layer) contained a Cr–oxide layer, while the internal layer contained large amounts of Ni. Also present was an enriched aluminum area, just below the surface oxide layer.

The EDS analysis of the surface oxide and the microstructure below are shown in Fig. 85. At 1373 K, the surface oxide was mostly Cr rich oxide. Fig. 84 also shows an elemental map of a well-developed layer alloy/oxide interface.

EDS analyses performed on the cross-section are given in Table 42. The presence of chromium was noted at the external interface and nickel and aluminum were noted at the internal interface. It appears that aluminum is mainly located between the external and internal layer.

Fig. 85 shows different regions analyzed by EDS-SEM Figure 85a shows Region 1 (outer layer) and Fig. 85b shows Region 2 (inner layer) EDS graph.
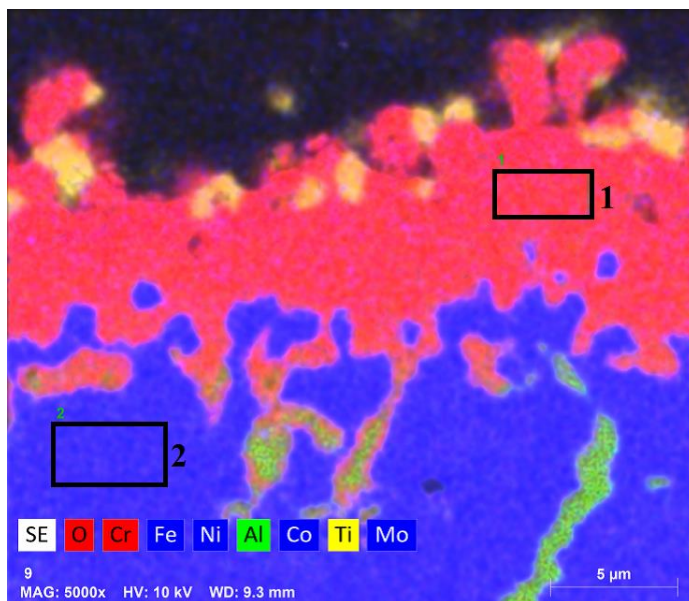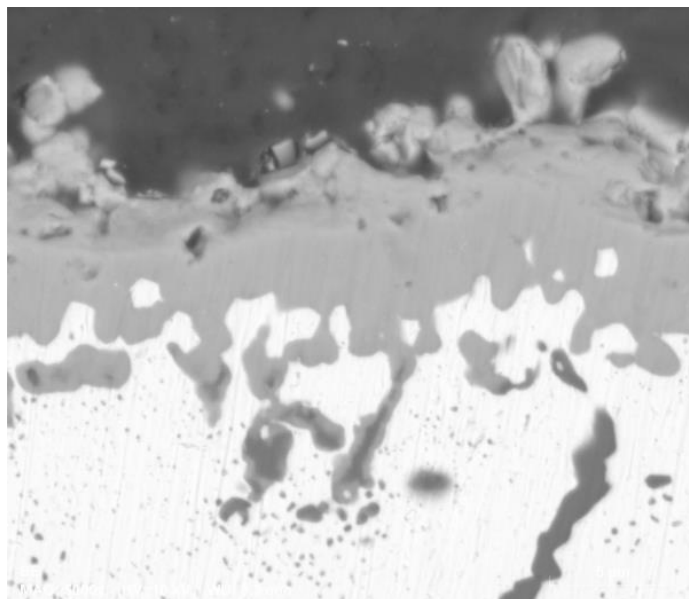
Figure 83. SEM images of the cross-section of the oxide after exposure to air at 1373 K.
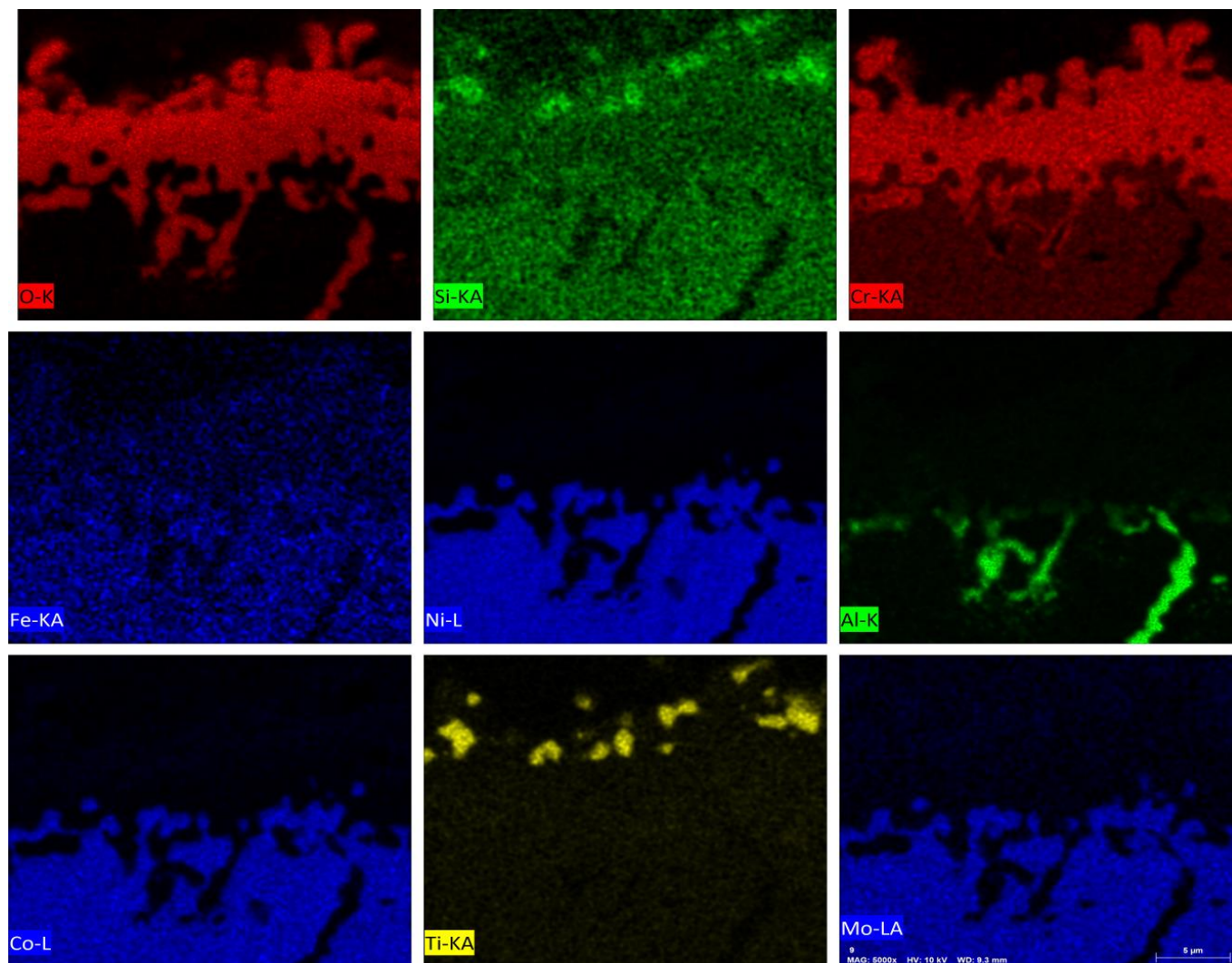
Figure 84. The elemental maps in a cross sectional area of the oxide film at 1373 K.
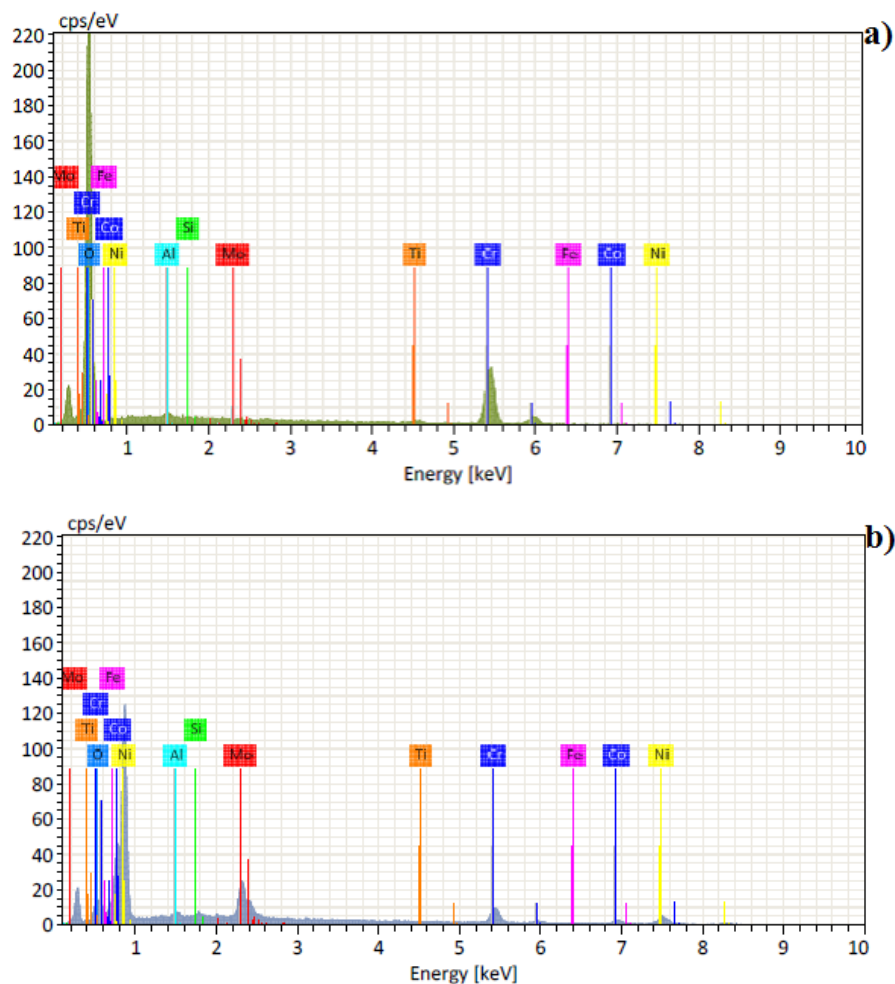
Figure 85. EDS graph at 1373 K a) Section 1 (Region 1) and b) Section 2 (Region 2)

Table 42. Region 1 and Region 2 mass % and atomic % at 1373 K.

Element	Region 1 (section 1) Mass (%)	Atomic (%)	Region 2 (section 2) Mass (%)	Atomic (%)
Oxygen	29.86	64.02	0.68	3.41
Aluminum	0.26	0.33	0.36	1.07
Silicon	0.15	0.18	0.11	0.32
Titanium	1.03	0.73	0.00	0.00
Chromium	52.47	34.62	14.68	22.56
Iron	0.00	0.00	1.19	1.70
Cobalt	0.21	0.12	6.76	9.16
Nickel	0.00	0.00	39.17	53.34
Molybdenum	0.00	0.00	10.12	8.43
Sum	83.97	100.00	73.06	100.00

5.2.3.5. 1473 K

At 1473 K, EDS analysis of the sample surface was performed as shown in Table 43. The SEM cross-section morphology micrograph reported the compositions of two regions. In general, cross section morphologies identified an outer oxide layer and an inner layer with inwardly protruded oxides, indicating the presence internal oxidation. At 1473 K, Fig. 86 shows the first region (outer layer) containing mainly Cr and O, with some Ti on outer edge. The second region (inner layer) shows the presence of Al, Ni, and Cr. Fig. 86 also shows surface morphology double layers formed in the cross section of the sample. The external layer (the top, or oxide layer) contained Cr –oxide layer, while the internal layer contained large amounts of Ni. The formation of voids within the oxides and breakdown of the surface oxide layers are evident in the Figure 86. The surface oxides were so unstable that some of them were about to be detached from the surface revealing the matrix below. Shown in Figs. 86 and 87 is the extensive formation of internal oxide below the unstable surface oxide layer. The composition and formation mechanism of the internal oxides also included aluminum oxides.

The EDS analysis of the surface oxide and the microstructure are shown in Fig. 88. At 1073 K, the surface oxide was mostly Cr rich oxide. Fig. 87 also shows an elemental map of a well-developed layer alloy/oxide interface.

EDS analyses performed on the cross-section are given in Table 43. The presence of chromium was noted at the external interface and nickel and aluminum were noted at the internal interface. It appears that the aluminum is mainly located between the external and internal layer.

119

As shown in Fig. 86 different regions were analyzed by EDS-SEM analysis.
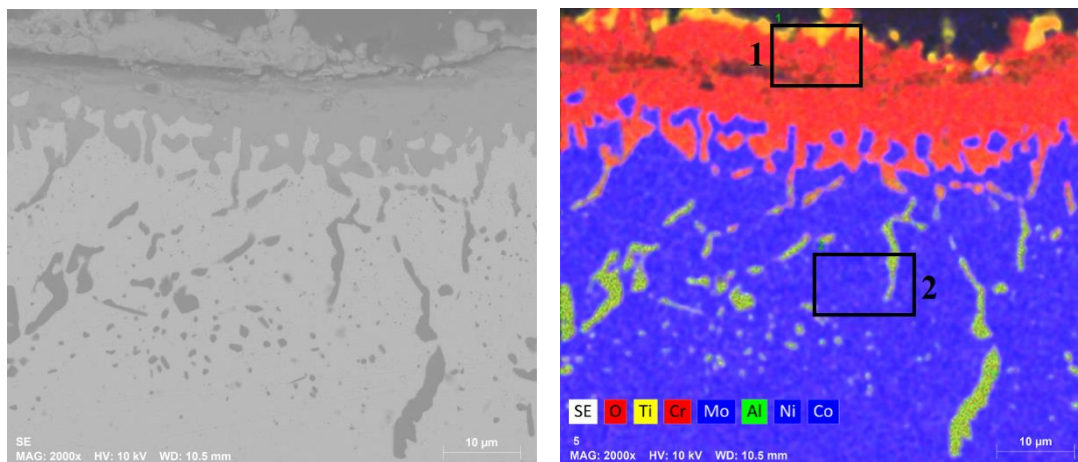
Figure 86. SEM images of the cross-section of the oxide after exposure to air at 1473 K.

The EDX analysis results of the surface oxide and the microstructure are shown in Fig. 88. Figure 88a shows Region 1 (outer layer) and Fig. 88b shows Region 2 (inner layer) EDS graph. The elemental mapping (Figure 87) was done for the specimens tested for at 1473 K. At 1473 K, the external oxide was mostly Cr-rich oxide when the exposure time was 24 h. Furthermore, Al was slightly enriched just below the external oxide layer, forming semi-continuous Al-oxides. The oxide was still predominantly Cr_2O_3, but a little more partitioning of Ti and Mo was observed. Clearly, Al-rich areas were spread throughout the external oxide after 24 h of oxidation. The Al-rich particles are thought to be Al-oxides.
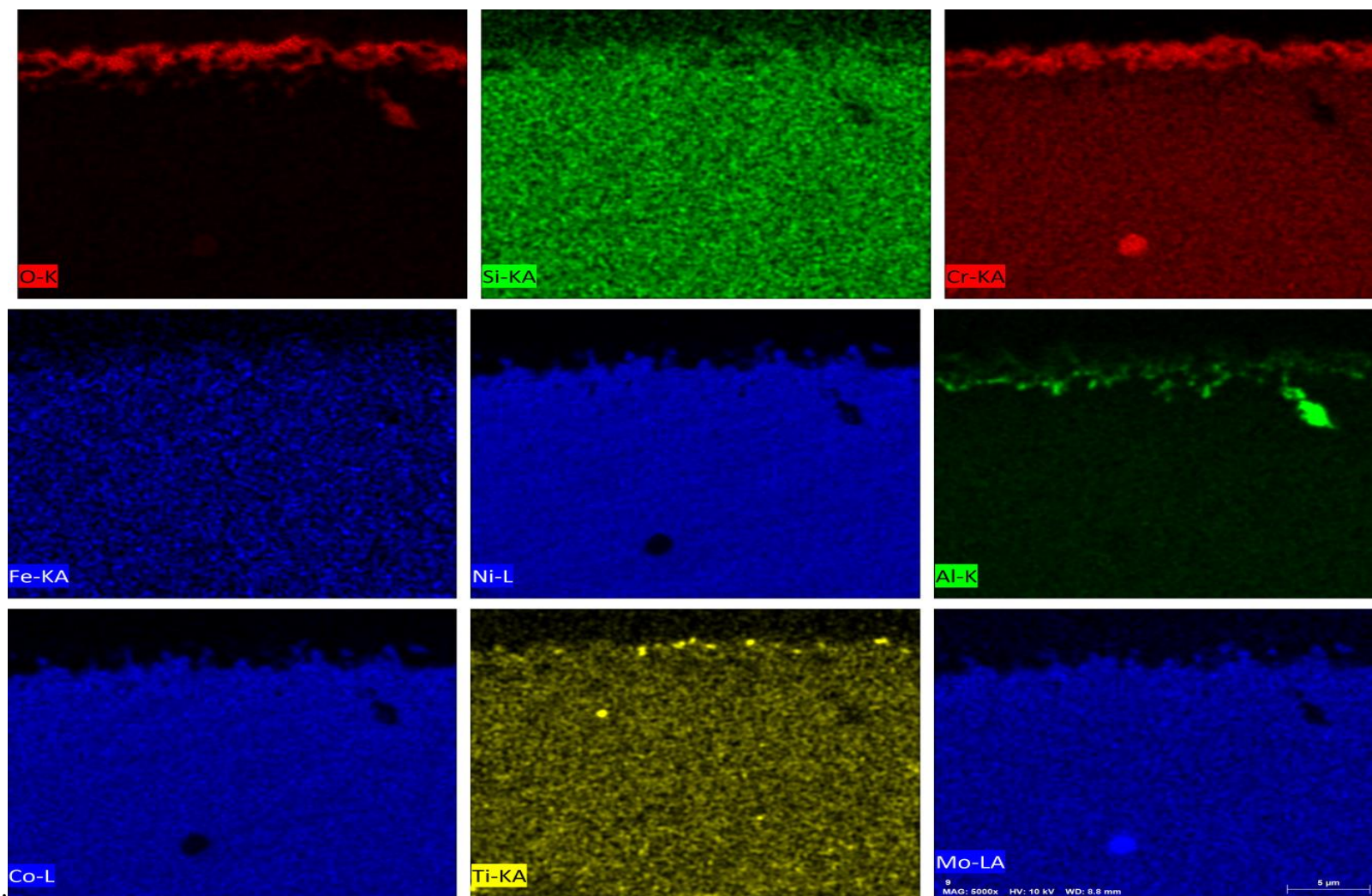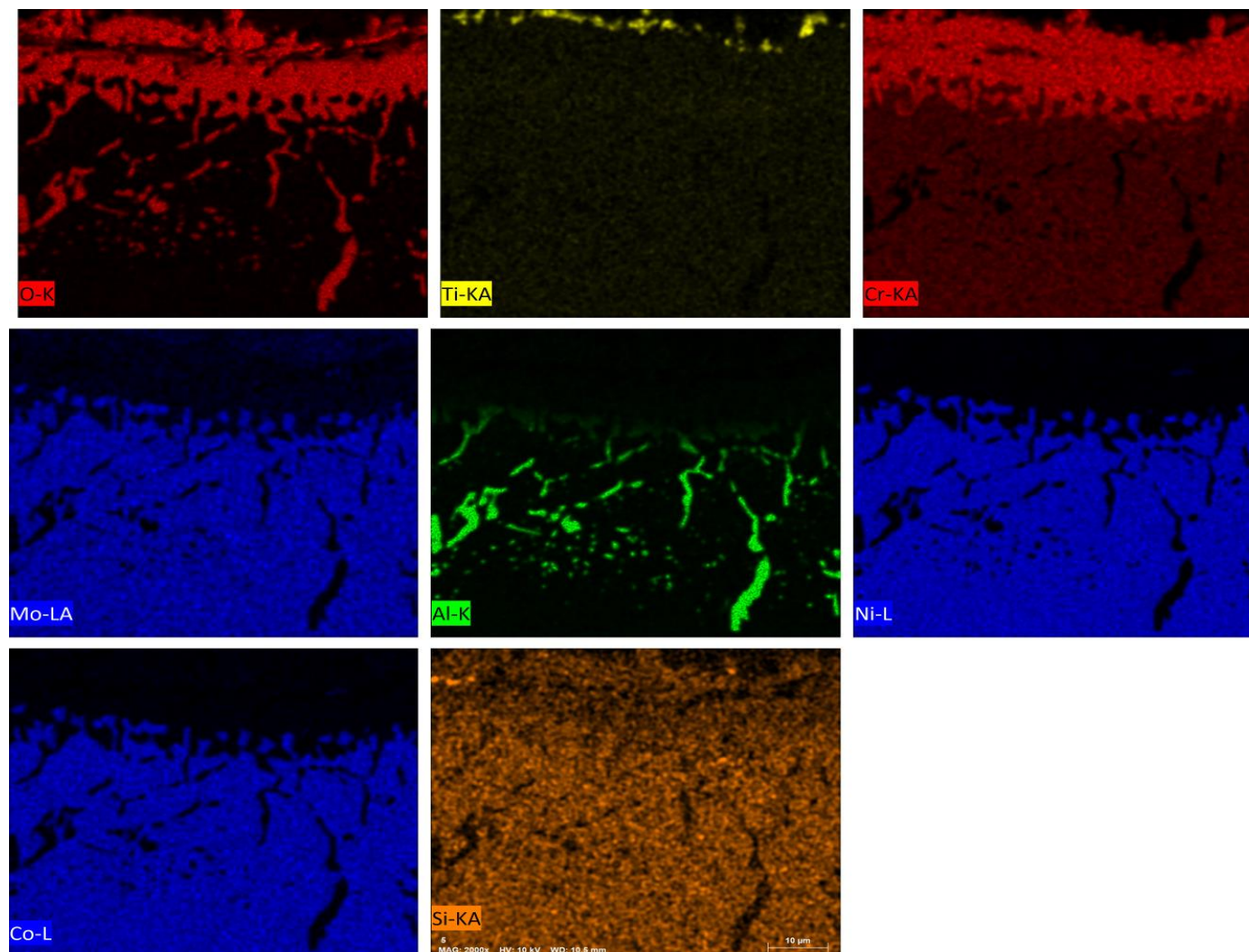
Figure 87. The elemental maps in a cross sectional area of the oxide film at 1473 K.
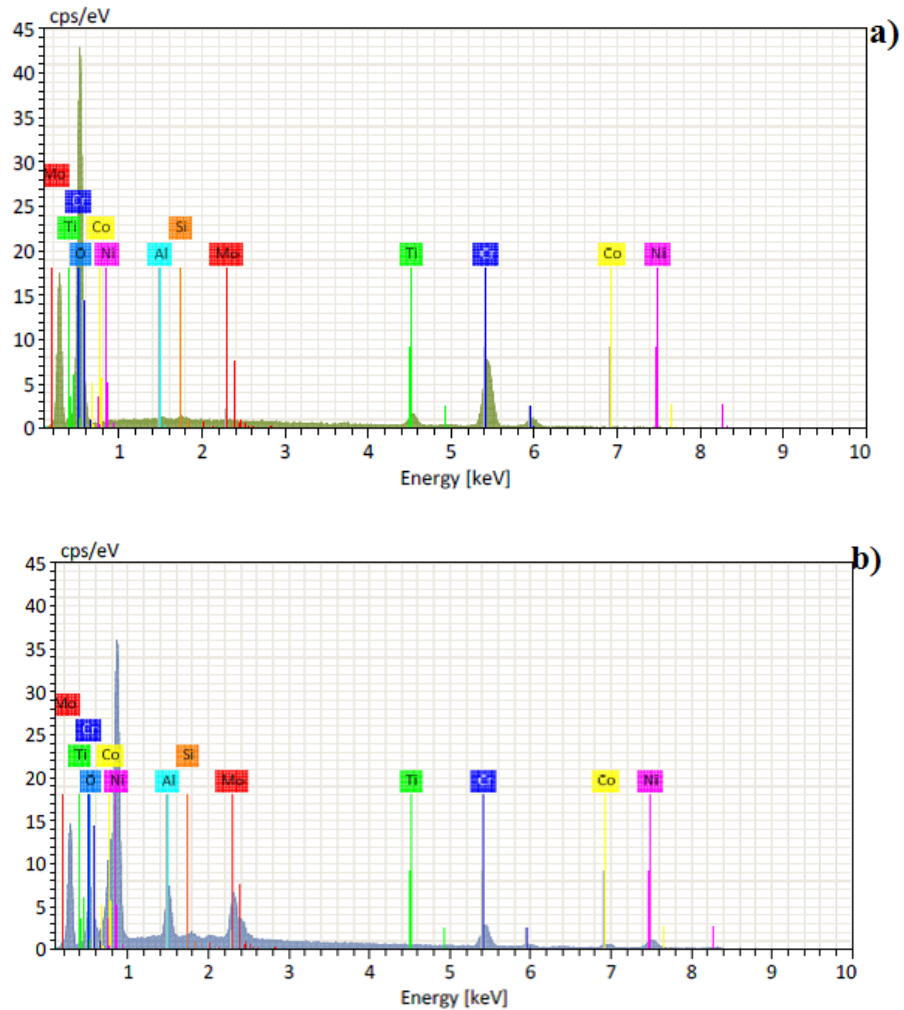
Figure 88. EDS graph at 1473 K a) Section 1 (Region 1) and b) Section 2 (Region 2)

Table 43. Region 1 and Region 2 mass % and atomic % at 1473 K.

Element	Region 1 (Section 1)		Region 2 (Section 2)	
	Mass (%)	Atomic (%)	Mass (%)	Atomic (%)
Oxygen	16.78	57.82	3.45	15.61
Aluminum	0.03	0.07	1.03	2.75
Silicon	0.23	0.45	0.00	0.00
Titanium	3.02	3.48	0.00	0.00
Chromium	35.51	37.65	15.08	20.99
Cobalt	0.27	0.25	6.47	7.94
Nickel	0.16	0.15	37.67	46.45
Molybdenum	0.22	0.13	8.30	6.26
Sum	56.23	100.00	72.00	100.00

122

5.2.4. Characterization of the Oxidized Layers with X-Ray Diffraction

The XRD results for the oxidized layers at 1073 K, 1173 K, 1273 K, 1373 K, and 1473 K are shown in Fig. 89. It clearly shows from the x-ray diffraction pattern of the air exposed sample that 1073 K and 1273 K are composed of Cr_2O_3 (JCPDS file No. 85-0730) and $Cr_{0.19}$ $Fe_{0.7}$ $Ni_{0.11}$ (JCPDS file No. 33-0397). And 1173 K is composed of Cr_2O_3 (JCPDS file No. 74-0326) and $Cr_{0.19}$ $Fe_{0.7}$ $Ni_{0.11}$ (JCPDS file No. 33-0397). $Cr_{0.19}$ $Fe_{0.7}$ $Ni_{0.11}$ appears to have had the strongest peak intensity among these oxides at 1073 K and 1173K, Cr_2O_3 had the strongest peaks intensity among these oxides at 1273 K.

At 1373 K, the scale formed is composed of Cr_2O_3 (JCPDS file No. 85-0730.

At 1373 K and 1473 K, as shown Fig. 89, XRD patterns were composed of Cr_2O_3 (JCPDS file No. 85-0730.
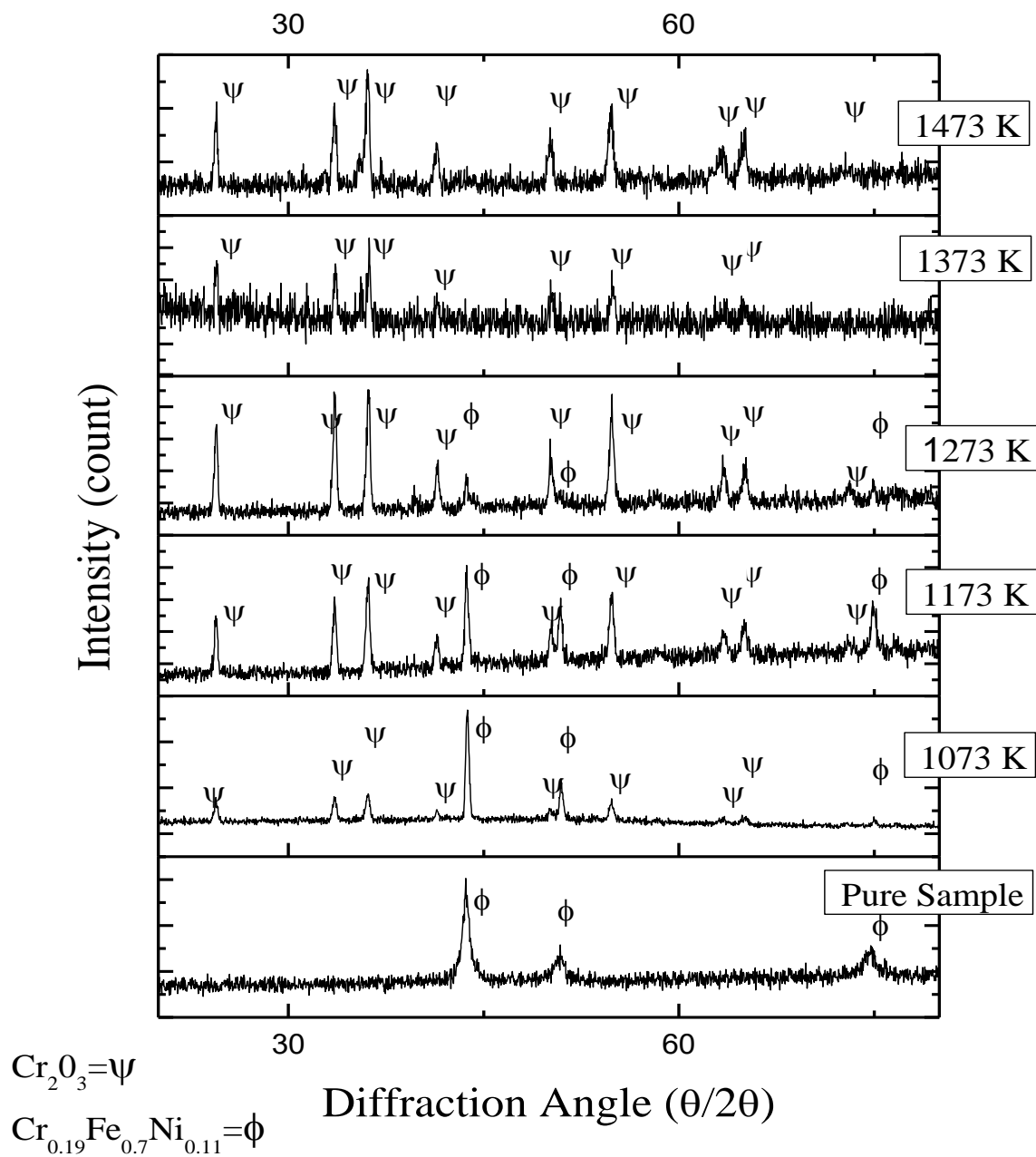
Figure 89. X-Ray diffraction of Alloy 617 pure sample and 1073 K to 1473 K samples.

$Cr_2O_3 = \psi$

$Cr_{0.19}Fe_{0.7}Ni_{0.11} = \phi$

5.3. Discussion

The weight gains and time with dependence temperature were shown in Fig. 53. As shown Fig. 54, the parabolic rate constant of alloy 617. In addition, maximum weight gains and activation energy was reported in present study. Different temperatures during oxidation process have been previously studied by different researchers [23,79,81,83–85,100]. It can be seen that the weight gains increased as the temperature increased. The weight gain change was observed at 1073 K but had no significant value, but after 1173 K, the gained weight was more predominant than at 1073 K; therefore, there was a critical temperature between 1073 K and 1173 K. Some studies have determined that this temperature is 1123 K[84]. The oxidation kinetics parabolic rate constant increased with increased temperatures; furthermore, the weight gain increased as the temperature increased. The reason for weight gain increase were mostly related to effect of oxides Cr, Al, and Ti, but after 1373 K, a change occurred, which mainly depended on oxidation of Ti. Some clarification of this argument is in [99], and our results agree with this reason. In addition, oxidation, spallation, carburization, decarburization have been given as reasons for weight gain during high temperature corrosion[101].

From Wagner theory and Tung[83], we understand that the high temperature parabolic oxidation rate signifies that the oxidation rate of the alloy is determined by the diffusion of ions migrating through a dense oxide. The parabolic rate are very close to the previously reported ones where the activation energy change is 205 kJ/mol[84], 240kJ/mol [102], 271kJ/mol [83], and 280kJ/ mol[103]. In the present study, the activation energy was 231.46 kJ/ mol for 1073 K to 1473 K, which is in good agreement with the activation energy reported herein.

According to SEM analysis, the formation of surface oxides and the penetration depth of internal oxide increased as the oxidation time increased.

At 1073 K, the nodular type structure and platelet were observed as shown in Figure 59. Figure 60 shows the EDS spectrum from the surface oxide scales, which indicates that the nodules and platelets oxides were mostly composed of Cr, Ni, and Mo. SEM cross section images observed three layers: The first outer layer mainly consisted of Cr-oxide (the surface layer); the second Al-oxide layer and inner carbide layer mainly consisted of Ni. On the outer surface, a Cr-rich (mainly Cr_2O_3) oxide layer was formed owing to Cr diffusion from the during the exposure time. Just below the Cr_2O_3 layer, an Al-rich (mainlyAl_2O_3) detached internal oxide layer was formed. The depletion of grain boundary carbides was caused by a reaction between the grain boundary carbides and oxygen provided by diffusion from the environment or the oxidation reaction of the surface oxide layers[104].

At 1173 K, the alloy surface was mostly covered with nodular shaped structures and grain boundaries ridges were formed as shown in Figure 62, where chromium rich oxide has grown on the Inconel 617 surface after temperature reached 1173 K. The oxide appears to be constituted by small nodules and seems to be titanium, aluminum, nickel, and molybdenum above the alloy grain boundaries, as shown in Table 31 and Table 32. Finally, Cr and Mo rich carbides were also observed in the alloy matrix. As shown Figure 77, the outer layer is predominantly made of Cr_2O_3; the inner layer is mostly made up of NiO. The SEM elemental maps in Figure 78 shows that outer-oxidation layer has Cr_2O_3, with Al content increased in inner layer.

The SEM element map in Figure 78, clearly shows that a relatively thick and continuous Cr_2O_3 layer lies beneath the Ni-containing layers. Oxide morphology is mostly a double layer consisting of an inner NiO layer and an outer Cr_2O_3 layer. One medium region of two regions was observed referred to as the Al_2O_3 region, as shown in Figure 77 and in the elemental maps of Figure 78.

At 1273 K, Figure 65 illustrates the surface oxidation of the Inconel alloy 617 surface. The comparison of 1073 K (Figure 59) and 1173 K (Figure 62) suggests that the nodules are more numerous at 1073 K. At 1273 K, the nodules were coalesced (Figure 65) in the bright-surface region where enriched chromium oxidation was detected. SEM cross section Figure 81 shows the surface morphology of the Cr_2O_3. At 1373 K, Figures 66 and 68, show a surface morphology where many nodules are stacked together.

Figure 83 and Table 42 show how oxidation exposure for 24 h at 1373 K resulted in further growth in oxide layers, internal oxidation, and a decarburized zone. Oxide layers were enriched with Cr oxide and united with aluminum grain boundaries. Elemental maps, as shown in Figure 84 showed aluminum and chromium layers in a cross section oxidation map.

At 1473 K, spallation of the oxide scale may also contribute to the formation of an oxide/alloy substrate after 24 h. The spallation of the scale was mainly caused by the outer TiO_2 layer, as shown in Figure 71 and Tables 37 and 38. Most of the TiO_2 layer was spalled due to the difference in the thermal expansion between inner Cr_2O_3 layer and outer TiO_2 layer.

As shown in Table 43, Ti ions were concentrated within the surface oxide layer after 24 h. From Sigler's oxidation tests using Ti-modified Fe-20 Cr alloys, a small amount of Ti (0.46 wt.%) increased the weight gain [99]. To obtain the composition near the oxides, elemental mapping was used. According to the elemental mapping analysis (Figure 85), the uniform surface oxide scale was identified as chromium (Cr_2O_3), and the discrete internal oxide was alumina (Al_2O_3) for 1073 K. Oxide content changed in chromium and aluminum regions with temperatures and the same temperatures-related changes affected Ti rich oxides.

The X-ray diffraction analyses carried out on the alloy 617 samples oxidized at 1073 K to 1473 K are clearly shown in Figure 89. The X-ray patterns indicate that the diffraction peaks for the underlying metal substrate were clearly marked in all samples, and peaks were strongly composed of Cr_2O_3. Peaks gradually increased with increasing temperature. Our results compare with different researchers[79,83,84] under similar conditions.

5.4. Conclusion

- Figures sequentially show the continuous growth of external oxide scales and grain boundary ridges with temperatures.

- The oxidation behavior of alloy 617 followed the parabolic oxidation kinetic rate law.

- The activation energy was 233.46 kJ/mol for 1073 K to 1473 K.

- At 1073 K, a thin external oxide layer was observed as a NiO-Cr_2O_3 double layer, with an external (top layer) of Cr_2O_3 and inner NiO layer, while, a continuous and

relatively irregular and inwardly protruded external oxide layer was observed. The external layer width depended on increasing temperatures from 1173 K to 1473 K. After 1173 K was reached, an Al_2O_3 sublayer appeared within the NiO-Cr_2O_3 layer.

- The oxide morphology and structure of alloy 617 were strongly affected by the environment.

- At 1473 K, the increasing mass gain was related with Ti oxidation, as shown in figures and tables.

- The oxidation depth increased as the temperature increased. Increasing oxidation temperatures attributed to the formation of pores, voids, and grain boundaries.

- The X-ray peaks were strongly composed of Cr_2O_3. Cr_2O_3 peaks, which gradually increased with increasing temperature.

CHAPTER 6. OXIDATION OF INCOLOY 800H ALLOY AT HIGH TEMPERATURES IN AIR

6.1. Introduction

A high-temperature nuclear reactor will require alloys to perform at temperatures greater than those existing in current nuclear power plants. Candidate materials such as nickel-iron-chromium based high temperature alloys and Incoloy 800H were exposed to air atmospheres and their corrosion was studied by a variety of analytical techniques. The tests were performed isothermally at temperatures between 1073 K and 1473 K (in steps of 100 K) for 24 hours in controlled air environments. The activation energy was found to be 266.8 kJ/mol for 1073 K to 1473 K. Results showed that the alloy was oxidized, approximately following a parabolic oxidation kinetic law with a parabolic rate constant calculated for each condition. Spallation is considered to occur as a result of oxidation after the temperature reaches 1373 K. At 1473 K, the increasing mass gain relates to Ti oxidation. As revealed by SEM cross section results, a three-layered external oxide scale was formed. A thermogravimetric analyzer (TGA), scanning electron microscopy (SEM)/energy dispersive X-ray spectroscopy (EDX or EDS), and X-Ray diffraction. were among the analytical techniques used.

Generation IV nuclear plants will operate at high temperatures and in high radiation fields. Metallic components will be exposed to high temperature and high radiation[105]. Therefore, the microstructural and mechanical properties of metallic components should be resistant to these conditions. Of the candidate alloy systems that could be considered for high temperature and high radiation applications, alloy 800H is

expected to play an important role as a structural component in Generation IV systems[22,106]. Alloy 800H has a composition of 31.6 wt% nickel and 20.4 wt% chromium. It has been shown that high Ni content (> 30 wt%) in austenitic steel improves material resistance to swelling under neutron irradiation at 400 °C (673 K) to a dose of 18.5 dpa [107]. The alloy also is expected to have good corrosion resistance with its high Cr content[105]. Incoloy 800H alloy is an austenitic high-strength solid-solution Fe–Ni–Cr super alloy, which was selected as a potential candidate for Generation IV nuclear plants due to its high resistance to high temperature oxidation and corrosion[2,108–112]. Incoloy 800H is being considered for use with such applications as intermediate heat exchanger(IHX), hot gas duct (HGD), steal generator and fuel cladding[113].

Oxidation resistance of austenitic alloys such as stainless steel or Incoloy is due largely to their high chromium content. When exposed to atmospheres with high oxidant levels these alloys quickly form a thin, compact, and adherent protective surface oxide film. This film is basically some modification of Cr_3O_3, and acts as a diffusion barrier to protect the alloy from further rapid oxidation[114,115]

To understand the oxidation behavior and the stability of oxides[116–118], there have been several studies on the high-temperature oxidation of alloys in air atmospheres [47,119–123], in supercritical water[121,124,125] and steam atmospheres[126,127]. Some studies investigated grain boundary characters[121,128–130].

The objectives of this work were to investigate the oxidation behavior of 800H alloy as it is exposed to different temperatures using various analytical techniques. We analyzed the oxidation/ corrosion effect of temperature on oxidation rate with thermogravimetric analysis (TGA), the oxide layer structure with scanning electron

microscopy/energy dispersive X-ray spectroscopy (SEM/EDS), and characterized the oxidation layer with X-ray diffraction (XRD).6.2. Results

6.2.1. Oxidation Kinetics

6.2.1.1. Oxidation data Incoloy 800H Alloy from TGA

Figure 90 shows the oxidation behavior of samples in the parabolic plot of weight gain versus exposure time at various temperatures in the range of 1073 K to 1473 K; the time of exposure is 24 hours at each temperature. Weight change of the samples was measured isothermally in the range of 1073 K to 1473 K in 100% air.
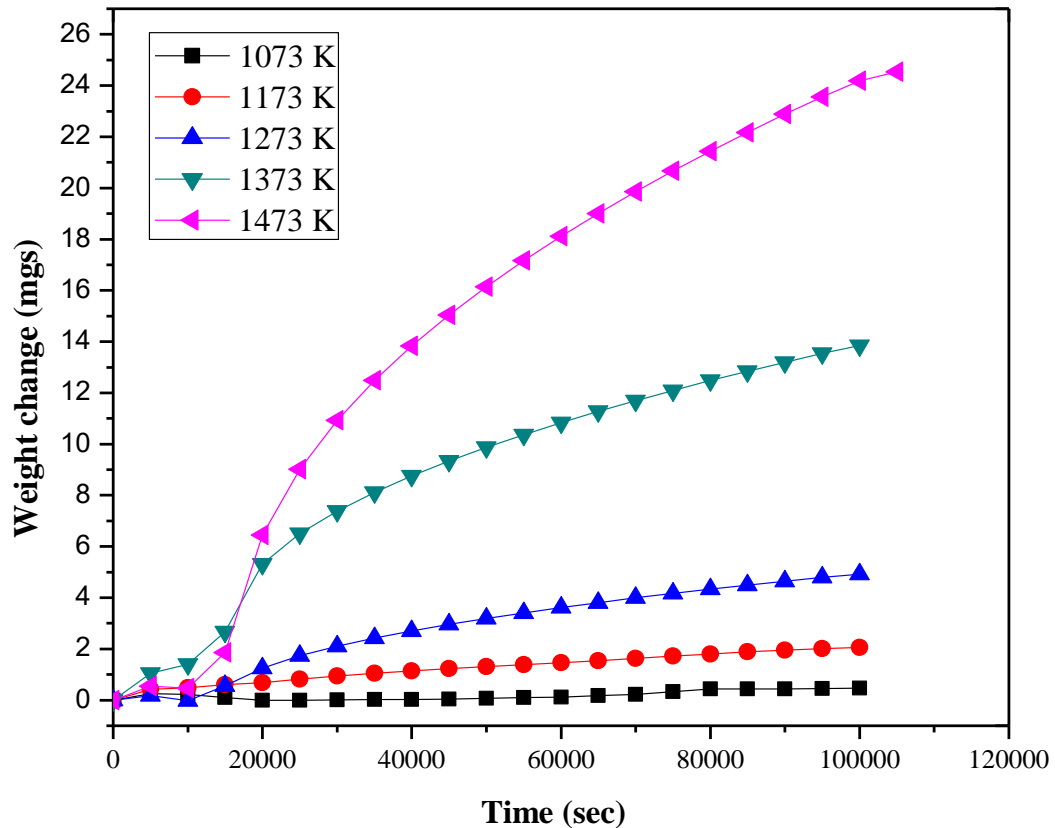
Figure 90. Oxidation of Incoloy 800H alloy in dry-medical grade air using TGA at 1073 K to 1473 K.

Table 44 displays total weight gain data from TGA. Weight gain was observed; mass gain increased with increasing temperature. The first 20000 seconds are required for the heating temperature interval; weight gains were variable during that period. Oxidation runs were performed twice to confirm the reliability and repeatability of the data.

Table 44. Total weight gains after 24-hour air exposure.

Temperature (K)	Weight Gain (mg)
1073	0.47
1173	2.05
1273	4.92
1373	13.85
1473	24.54

6.2.1.2. Oxidation Kinetics/ Rate Constant

Oxidation kinetics of Incoloy 800H were quantified through measurement of their mass gain per unit area ($\Delta m/a$) as a function of time at temperatures of 1073 K, 1173 K, 1273 K, 1373 K, and 1473 K in air by using thermogravimetric analysis (TGA). Plots of mass gain per unit area vs. time for the oxidation of Incoloy 800H at temperatures from 1073 K to 1473 K are illustrated in Figure 91.
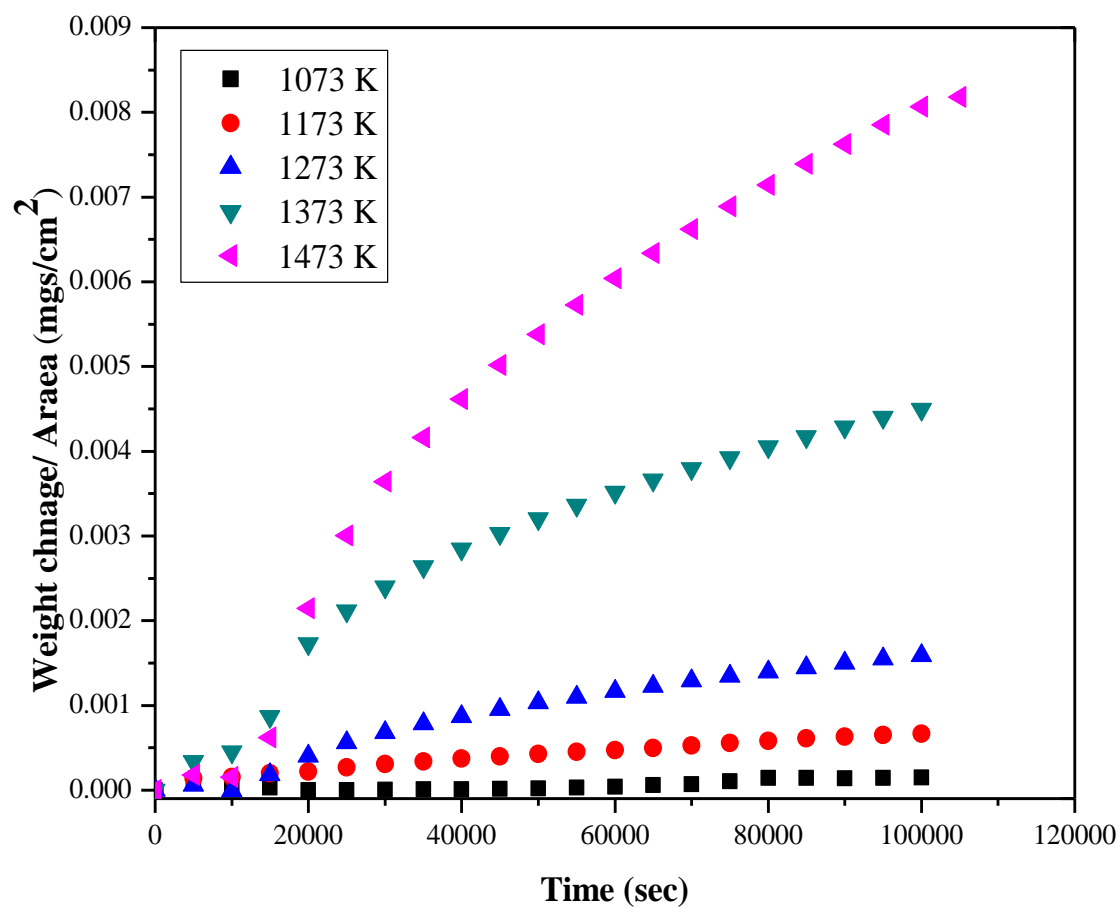
Figure 91. Oxidation kinetics for 800H plot of mass gain per unit area versus oxidation time for temperature in the range 1073 K–1473 K. (t = 0 refers to the time when the sample reached set temperature).

Figure 92 shows the oxidation kinetics of Incoloy 800H as obtained by our measurements.
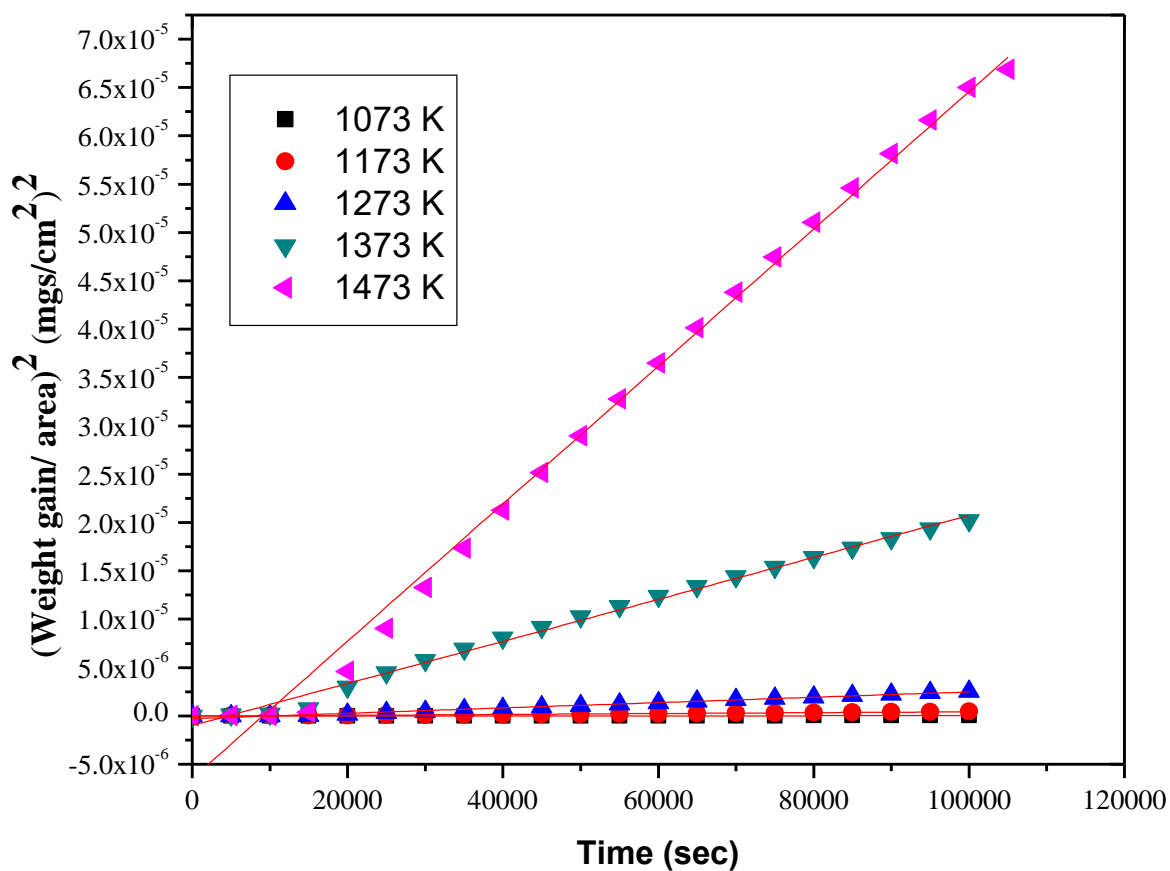
Figure 92. Oxidation kinetics for Incoloy 800H plot of (mass gain per unit area) 2 versus oxidation time for temperatures in the range 1073 K–1473 K. (t = 0 refers to the time when the sample reached set temperature).

As shown in Figure 92, the weight changes in the air conditions were nearly like those at 1073 K to 1473 K. The parabolic rate constants were identified by fitting oxidation data sets to linear lines, and the results are listed in Table 45.

Table 45. Experimental parabolic oxidation rate constant, kp of Incoloy 800H.

Temperature (K)	k value $(g^2 cm^{-4} sec^{-1})$
1073 K	2.1 x10^{-13}
1173 K	4.6x10^{-12}
1273 K	2.8x10^{-11}
1373 K	2.2x10^{-10}
1473 K	7.1x10^{-10}

6.2.1.3. Activation Energy of Incoloy 800H alloy

The graph in which log k is plotted against 1/T will have a slope of –Q in Figure 94. The activation energy of coating oxidation reaction Q for a parabolic rate of oxidation Incoloy 800H is 266.8 kJ/mol.
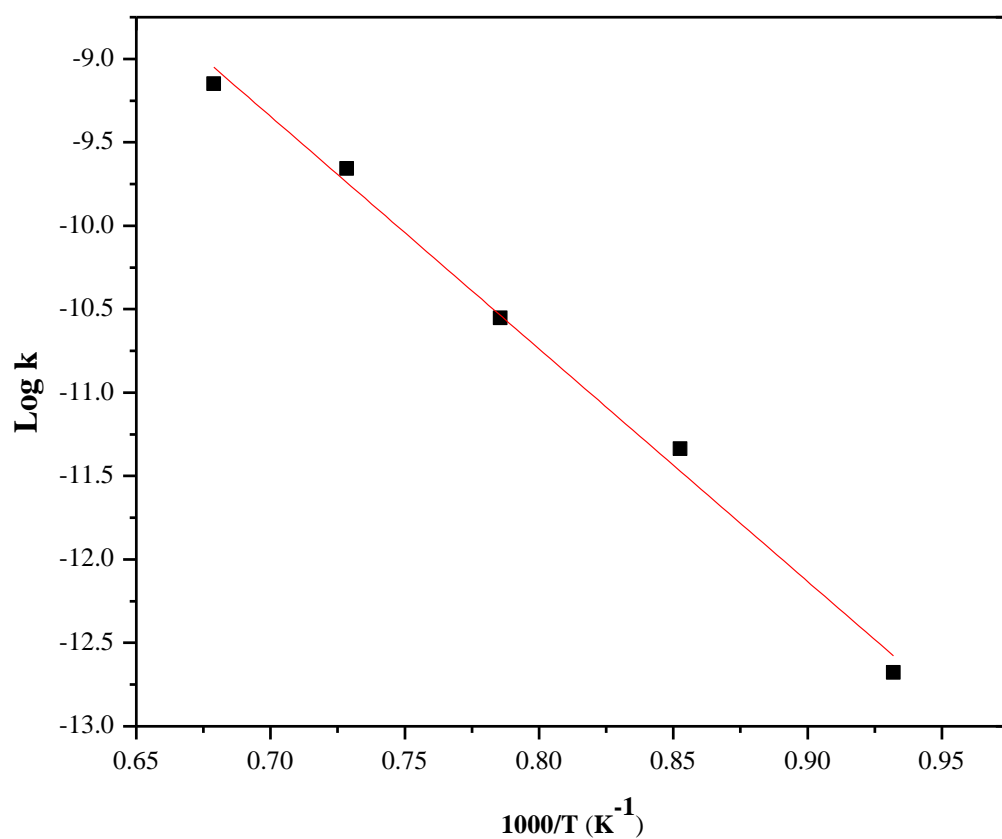
Figure 93. Arrhenius plot and exhibited activation energy for the Incoloy 800H alloy (1073K-1473 K).

6.2.2. Oxidation Microstructure (Surface Analysis) with Scanning electron microscopy/energy dispersive X-ray spectroscopy (SEM/EDS)

6.2.2.1. Room Temperature (Pure Sample)

The SEM images of Incoloy 800H alloy at room temperature from a pure sample are shown in Figure 94 and the corresponding EDS figures are shown in Figure 95. The scratches appear as the sample was re-grounded with 400 grit silicon-carbide paper.
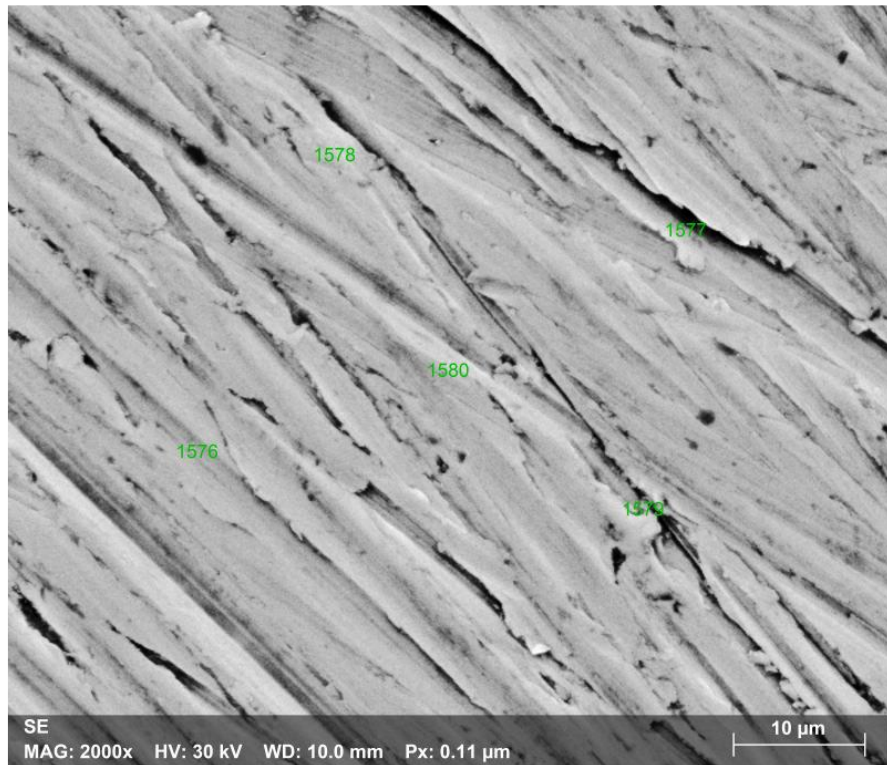
Figure 94. SEM surface morphology.
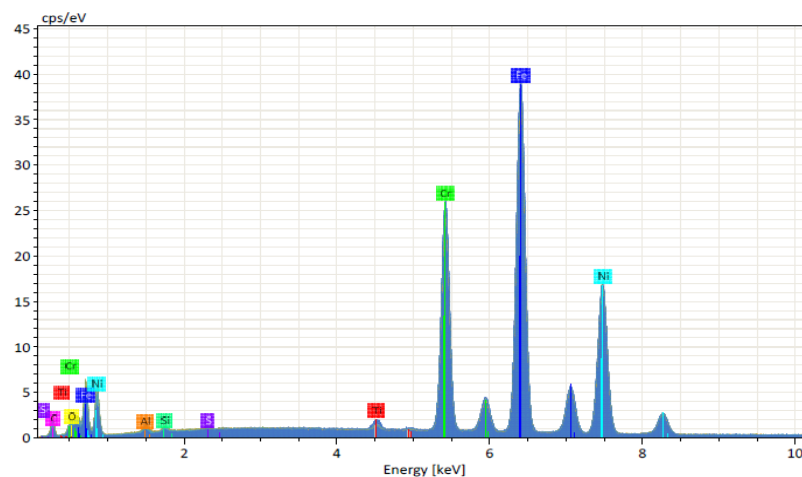
Figure 95. EDS graph for pure sample surface.

As shown in Table 46 the mean (absolute deviation) of atomic and mass percent of five different randomly selected regions were analyzed by EDS.

Table 46. Surface morphology mass and atomic percent analysis on the surface of Incoloy 800H alloy from a pure sample.

Element	C	O	Al	Si	S	Ti	Cr	Fe	Ni
Mass percent Mean (Absolute deviation)	7.76	1.33	0.77	0.31	0.08	0.31	18.7	42.8	28.0
Atomic percent Mean (Absolute deviation)	26.84	3.43	1.18	0.46	0.11	0.27	15.18	32.4	20.13

6.2.2.2. 1073 K
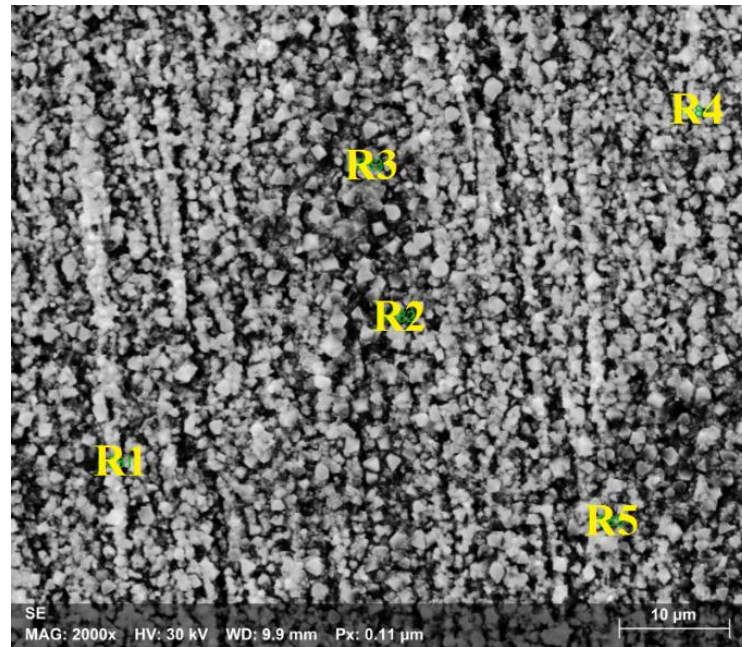
Figure 96. Surface morphology of Incoloy 800H at 1073 K.
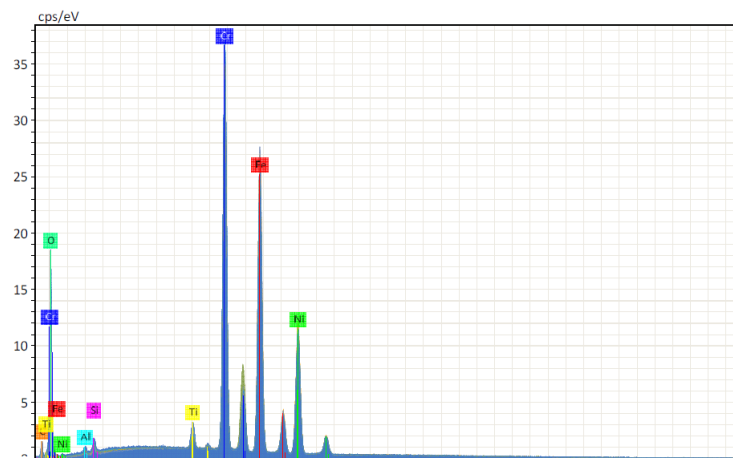
Figure 97. EDS spectrum of Incoloy 800H at 1073 K.

EDS analyses performed on the surface are given in Figure 97 and Tables 47 and 48. Table 47 shows that the sample is composed of mainly 18.82% Fe, 18.25% Cr, 39.48%

O, 10.98% C and 10.97% Ni by atomic percent. According to Table 48, the sample contains

30.00% Fe, 27.35% Cr, 18.60% O, and 18.50% Ni by mass percent.

Table 47. Surface morphology atomic percent analysis on five locations on the surface at

1073K.

Spectrum	C	O	Al	Si	Ti	Cr	Fe	Ni
R1	11.37	40.81	0.37	0.54	0.71	18.28	17.46	10.48
R2	10.91	43.16	0.31	0.55	0.43	17.38	17.25	10.00
R3	8.74	30.80	0.31	0.63	0.78	21.57	23.78	13.39
R4	10.42	35.47	0.41	0.64	0.74	19.08	20.73	12.52
R5	13.45	47.03	0.45	0.69	0.75	14.95	14.21	8.48
Mean	10.98	39.45	0.37	0.61	0.68	18.25	18.82	10.97

Table 48. Surface morphology mass percent analysis on five locations on the surface at

1073K

Spectrum	C	O	Al	Si	Ti	Cr	Fe	Ni
R1	4.03	19.27	0.30	0.45	1.00	28.04	28.77	18.14
R2	3.95	20.80	0.25	0.47	0.62	27.21	29.02	17.68
R3	2.69	12.65	0.22	0.45	0.95	28.78	34.09	20.17
R4	3.44	15.59	0.30	0.49	0.97	27.25	31.79	20.17
R5	5.30	24.68	0.40	0.64	1.17	25.48	26.02	16.32
Mean	3.88	18.60	0.30	0.45	0.94	27.35	30.00	18.50

SEM micrographs of these three samples are shown in Figure 98.
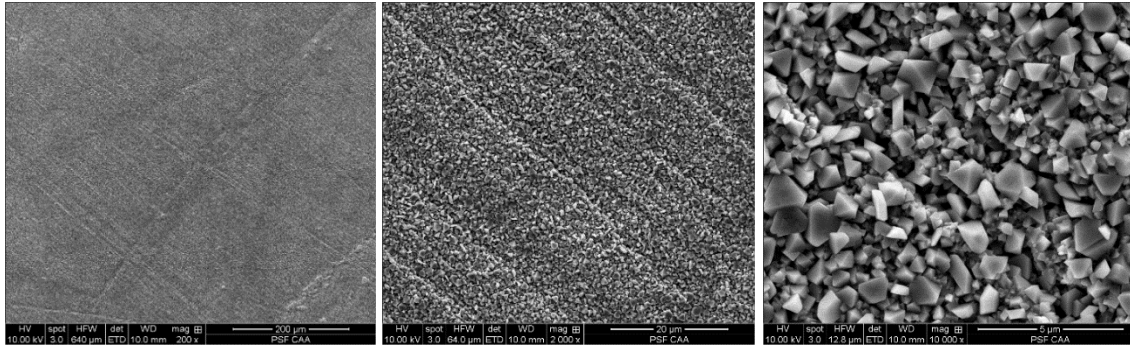
Figure 98. SEM images show surface morphology samples at 1073 K, at 300µm, 30µm and 5µm.

6.2.2.3. 1173K

Figure 99. Surface morphology of Incoloy 800H at 1173 K.

Figure 100. EDS spectrum of Incoloy 800H at 1173K.

EDS analyses performed on the surface are given in Figure 100 and Tables 49-50. Table 49 shows that the sample is composed of mainly 59.20% O, 20.49% Cr, and 11.31% C by atomic percent. According to Table 50, the sample contains 40.00% Cr, 36.00% O, and 10.70% Fe by mass percent.

Table 49. Surface morphology atomic percent analysis on five locations on the surface at 1173K.

Spectrum	C	O	Al	Si	Ti	Cr	Fe	Ni
R1	11.95	61.83	0.27	-	0.43	18.95	4.19	**2.38**
R2	9.83	54.44	0.25	-	0.99	27.15	4.65	**2.69**
R3	11.91	56.65	0.36	-	0.40	18.16	7.77	**4.76**
R4	9.99	60.66	0.27	-	0.48	18.81	6.18	**3.61**
R5	12.89	62.43	0.28	-	0.77	19.39	2.74	**1.50**
Mean	11.31	59.20	0.29	-	0.61	20.49	5.11	2.99

Table 50. Surface morphology mass percent analysis on five locations on the surface at 1173K.

Spectrum	C	O	Al	Si	Ti	Cr	Fe	Ni
R1	5.69	39.26	0.29	-	0.81	39.11	9.29	5.55
R2	4.11	30.33	0.24	-	1.64	49.16	9.04	5.49

143

R3	5.23	33.14	0.36	-	0.69	34.51	15.86	10.21
R4	4.52	36.54	0.27	-	0.86	36.83	13.00	7.98
R5	6.33	40.81	0.31	-	1.51	41.20	6.25	3.60
Mean	5.18	36.0	0.29	-	1.1	40.0	10.7	7.6
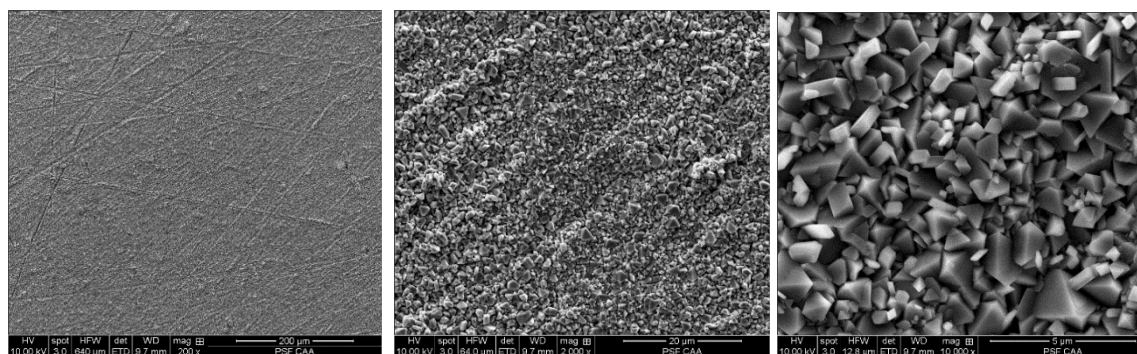
Figure 101. SEM images show surface morphology samples at 1173 K, at 300 µm, 30 µm and 5 µm.

SEM micrographs of these three samples are shown in Figure 101.

6.2.2.4. 1273 K
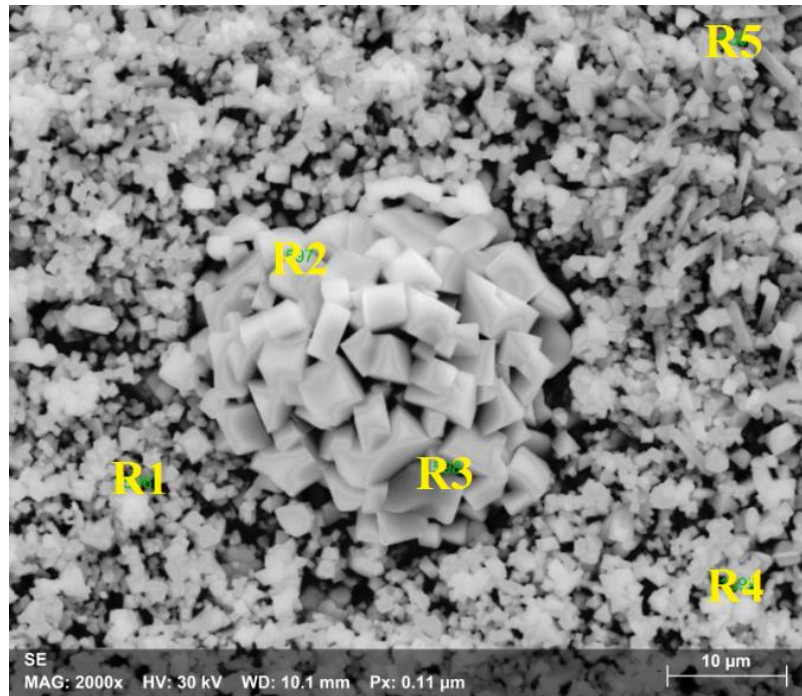
Figure 102. Surface morphology of Incoloy 800H at 1273 K and EDS spectrum.
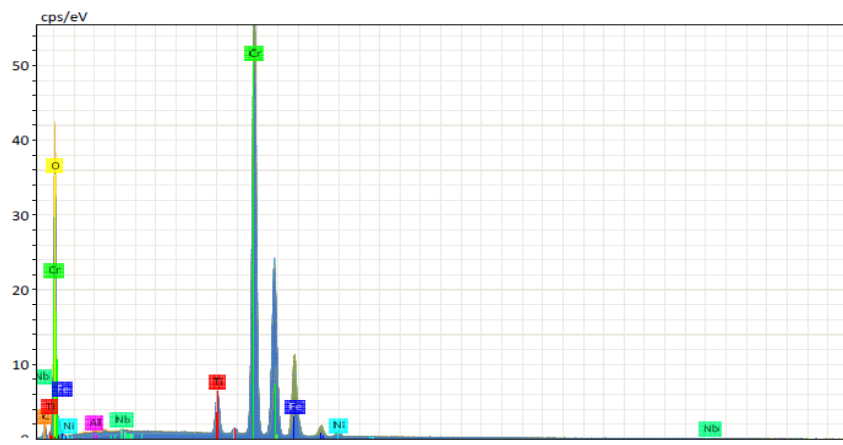
Figure 103. EDS spectrum of Incoloy 800H at 1273K.

EDS analyses performed on the surface are given in Figure 103 and Tables 51-52. Table 51 shows that the sample is composed of mainly 62.63% O, 23.12% Cr, and 9.25% C by atomic percent. According to Table 52, the sample contains 45.57% Cr, 39.83% O, and 8.88% Fe by mass percent.

Table 51. Surface morphology atomic percent analysis of five locations on surface at 1273 K.

Spectrum	C	O	Al	Si	Ti	Cr	Fe	Ni
R1	7.99	65.05	0.12	-	0.48	23.83	2.32	0.21
R2	10.19	63.06	0.08	-	0.74	19.85	5.57	0.52
R3	5.44	49.00	0.16	-	1.07	35.71	7.88	0.72
R4	13.27	67.80	0.10	-	0.62	16.58	1.49	0.15
R5	8.85	68.26	0.09	-	1.45	19.61	1.66	0.09
Mean	9.15	62.63	0.11	-	0.87	23.12	3.78	0.34

Table 52. Surface morphology mass percent analysis of five locations on surface at 1273 K.

Spectrum	C	O	Al	Si	Ti	Cr	Fe	Ni
R1	3.77	40.91	0.13	-	0.91	48.70	5.09	0.49
R2	4.81	39.68	0.08	-	1.39	40.60	12.23	1.19
R3	2.01	24.15	0.14	-	1.57	57.19	13.56	1.29
R4	7.15	48.64	0.12	-	1.32	38.65	3.73	0.40
R5	4.45	45.74	0.10	-	2.91	42.71	3.88	0.22
Mean	4.44	39.83	0.12	-	1.62	45.57	8.88	0.72

SEM micrographs of these three samples are shown in Figure 104.

Figure 104. SEM images show surface morphology samples at 1273 K, at 300 µm, 30 µm, and 5 µm.

6.2.2.5. 1373 K
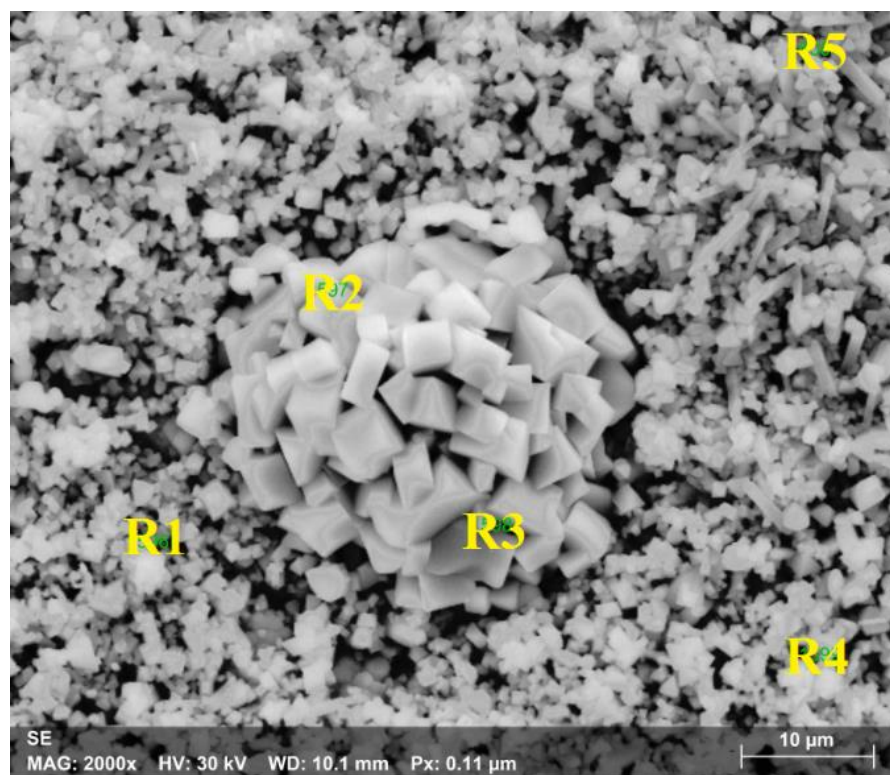
Figure 105. Surface morphology of Incoloy 800H at 1373 K.
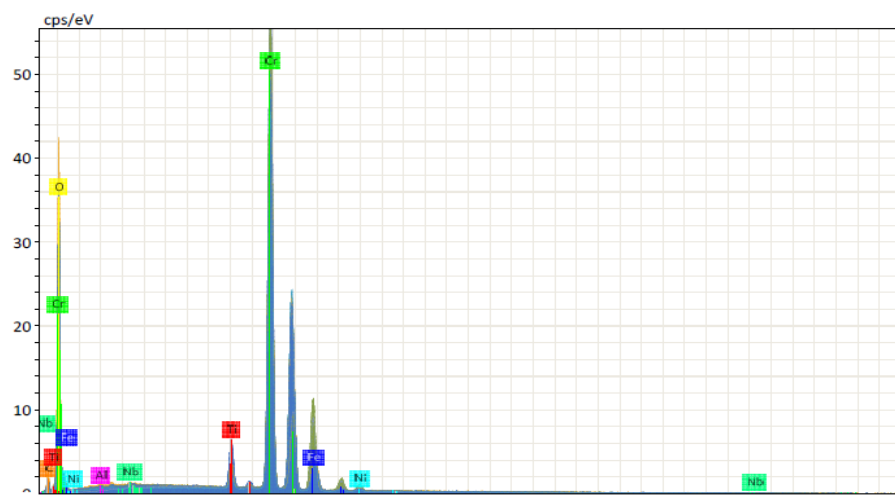
Figure 106. EDS spectrum of Incoloy 800H at 1373K.

Figure 106 and Tables 53 and 54 show EDS analyses performed on the surface wherein the sample is composed mainly of 62.63% O,23.12% Cr and 9.25% C by atomic percent. Table 54 shows the sample to contain 45.57% Cr, 39.83% O, and 8.88% Fe by mass percent.

Table 53. Surface morphology atomic percent analysis on five locations on the surface at 1373K.

Spectrum	C	O	Al	Si	Ti	Cr	Fe	Ni
R1	7.99	65.05	0.12	-	0.48	23.83	2.32	**0.21**
R2	10.19	63.06	0.08	-	0.74	19.85	5.57	**0.52**
R3	5.44	49.00	0.16	-	1.07	35.71	7.88	**0.72**
R4	13.27	67.80	0.10	-	0.62	16.58	1.49	**0.15**
R5	8.85	68.26	0.09	-	1.45	19.61	1.66	**0.09**
Mean	9.15	62.63	0.11	-	0.87	23.12	3.78	**0.34**

Table 54. Surface morphology mass percent analysis on five locations on the surface at 1373K.

Spectrum	C	O	Al	Si	Ti	Cr	Fe	Ni
R1	3.77	40.91	0.13	-	0.91	48.70	5.09	**0.49**
R2	4.81	39.68	0.08	-	1.39	40.60	12.23	**1.19**
R3	2.01	24.15	0.14	-	1.57	57.19	13.56	**1.29**

R4	7.15	48.64	0.12	-	1.32	38.65	3.73	**0.40**
R5	4.45	45.74	0.10	-	2.91	42.71	3.88	**0.22**
Mean	4.44	39.83	0.12	-	1.62	45.57	8.88	**0.72**

SEM micrographs of these three samples are shown in Figure 108.

Figure 107. SEM images show surface morphology samples at 1373 K, at 300 µm, 30
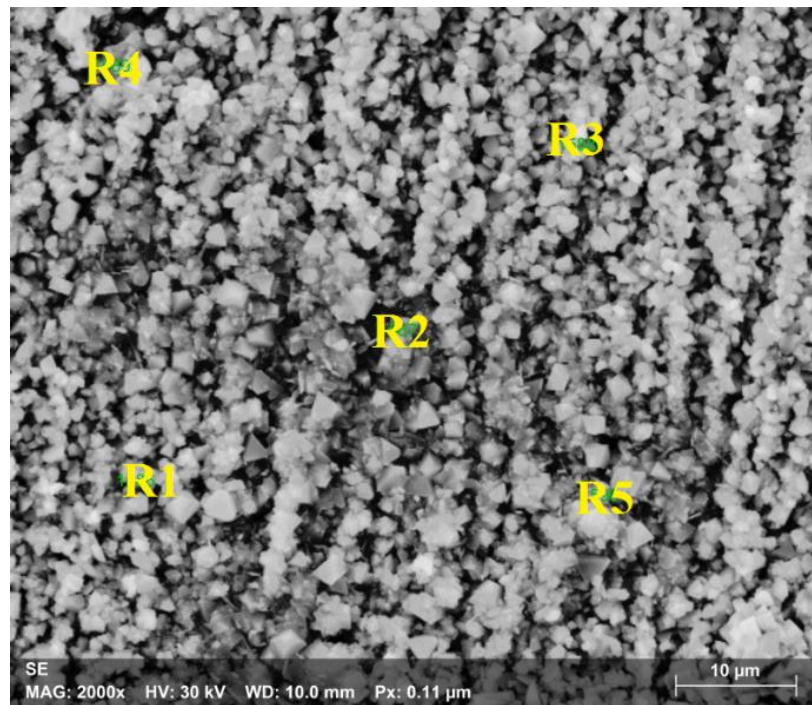
µm and 5 µm.

6.2.2.6. 1473

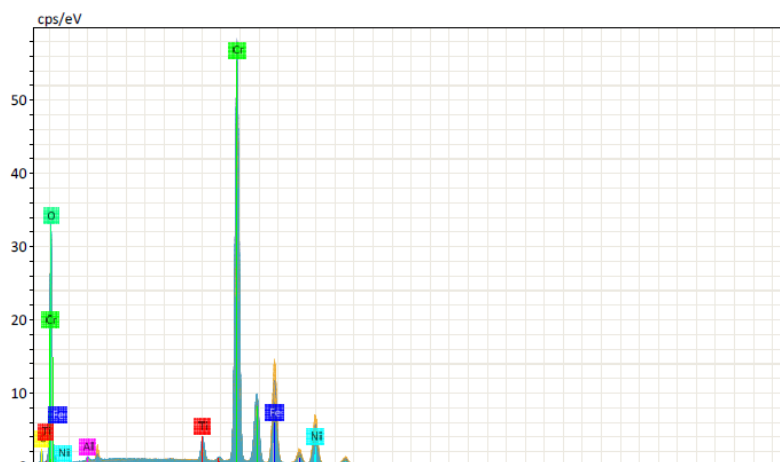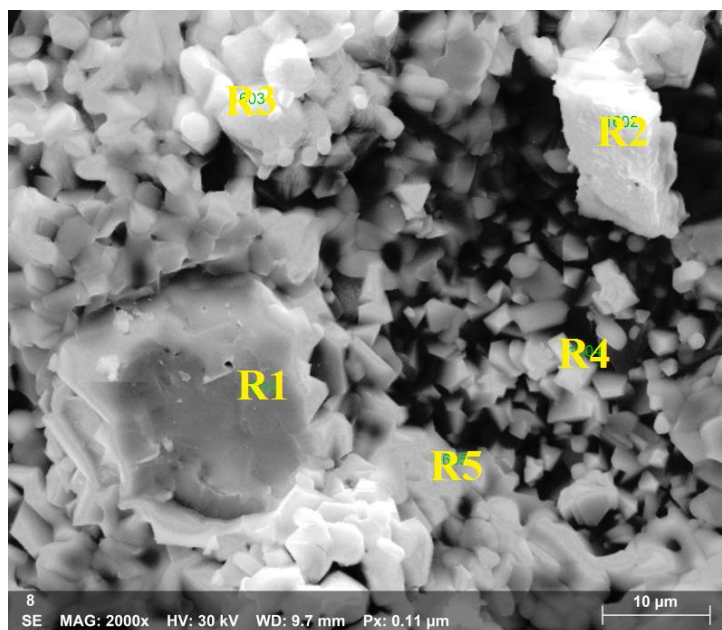Figure 108. Surface morphology of Incoloy 800H alloy at 1473 K.
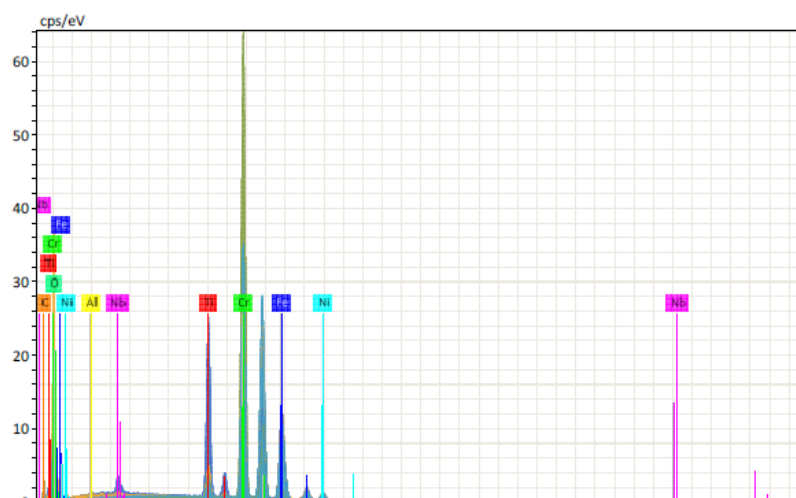
Figure 109. EDS spectrum of Incoloy 800H at 1473K.

EDS analyses performed on the surface are given in Figure 109 and Tables 55 and 56. Table 55 shows that the sample is composed mainly of 52.58% O, 26.01% Cr, and 10.99% C by atomic percent. According to Table 56, the sample contains 40.84% Cr, 32.87% O, and 14.72% Fe by mass percent.

Table 55. Surface morphology atomic percent analysis on five locations on the surface at 1473K.

Spectrum	C	O	Al	Si	Ti	Cr	Fe	Ni	Nb
R1	8.55	50.65	0.34	-	0.96	26.54	11.76	1.2	`-
R2	5.16	21.14	0.20	-	2.20	68.24	2.65	0.25	**0.16**
R3	10.77	59.38	0.26	-	1.27	17.38	10.05	0.88	-
R4	14.80	68.28	0.26	-	1.00	9.55	5.55	0.55	-
R5	15.65	63.43	0.17	-	5.92	8.33	5.53	0.30	**0.67**
Mean	10.99	52.58	0.25	-	2.27	26.01	7.11	0.64	**0.17**

Table 56. Surface morphology mass percent analysis on five locations on the surface at 1473K.

Spectrum	C	O	Al	Si	Ti	Cr	Fe	Ni	Nb
R1	3.34	26.35	0.30	-	1.50	44.87	21.36	2.29	-
R2	1.46	7.98	0.13	-	2.48	83.75	3.50	0.35	**0.34**
R3	4.85	35.66	0.22	-	2.29	33.92	21.07	1.95	-

150

R4	8.22	50.47	0.32	-	2.22	22.95	14.32	1.50	**-**
R5	8.13	43.89	0.20	-	12.26	18.72	13.36	0.76	**2.68**
Mean	5.2	32.87	0.24	-	4.15	40.84	14.72	1.37	**0.60**

SEM micrographs of these three samples are shown in Figure 110.
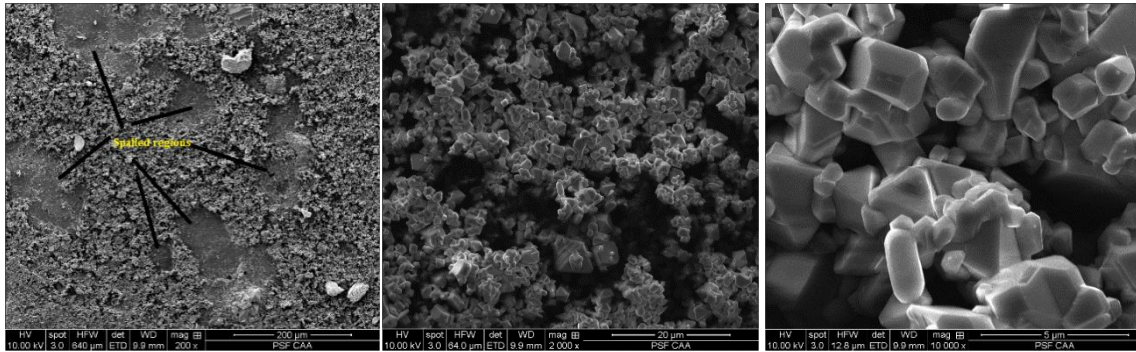
Figure 110. SEM images show surface morphology samples at 1473 K, at 300 µm, 30 µm and 5 µm.

On Figure 108, oxidation at 1473 K is much more aggressive than at previous oxidation condition temperatures; hence, spalling and oxidation areas, dark sides and shapes of grains have sharper angular nodules.

The surface morphology of oxidized samples indicated deposits over the surface as seen SEM surface analysis figures. Whereas some evidence of spallation of the external oxide surface was observed in the samples after 1373 K. (Figure 105.)

The effect of exposure temperatures (1073 K, 1173 K, 1273 K, 1373 K, and 1473 K) on the surface morphologies of the as-received samples are shown in Figures 98, 101, 104, 107, and 110, respectively. With the increase of exposure temperatures, the oxide scales on the as-received samples became relatively denser than the sparse oxide particles formed at 1073 K. In comparison, the as-received samples had more compact oxide scales

after 1073 K. This reveals a faceted structure and less compact outer layer with a smaller grain size. The scale is compact and adherent in nature, consisting of irregular size fine grains uniformly dispersed throughout the scale.

Figure 96 presents the surface morphology of the 800H alloy oxidized in air atmospheres at 1073 K. The results reveal that the oxide scales are uniform and dense. EDS analysis showed surface oxide crystals in Fe and Ni. Voids formed along the grain boundaries can be clearly seen in Figure 98 taken at higher magnification.

Figure 102 presents the surface morphology of the 800H alloy oxidized in air atmospheres at 1173 K. The results reveal that the oxide scales are uniform and dense. EDS analysis showed surface oxide crystals in Fe and Cr. After temperature exceeded 1173 K, the oxidation area and O content were twice as high as shown in Table 47-48.
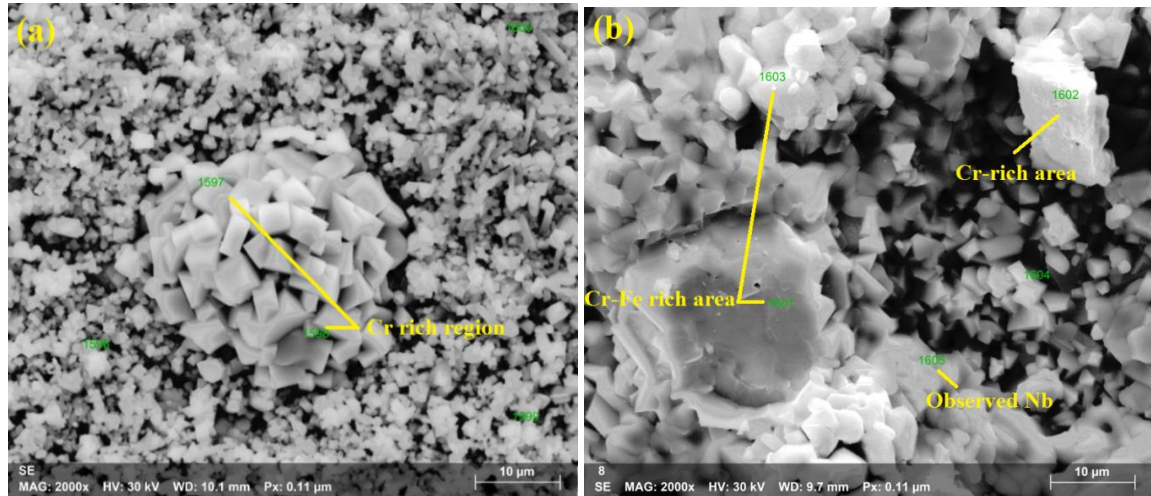
Figure 111. SEM images of surface morphology at (a) 1273 K and (b) 1473 K.

Figures 111 (a) and (b) present the SEM surface images of 800H alloy oxidized in air exposed at 1273 K and 1473 K, respectively. In Figure 111 (a), the results display that the largest grain areas are enriched Cr regions. In Figure 111 (b), the surface scale consists

of large and small grains. A large grain Cr-Fe rich region is shown in Figure 111 (b) as well as a bright white grain Cr rich region with 84% mass percent Cr content and an area with niobium (Nb) content.

Tables 52 and 54 show that the sample mass percentage of 800H alloy, at 1273 K and 1373 K are mainly Cr and O on the surface scale in comparison to all temperature conditions. These percentages are averages of the surface contents of five random regions and show that some elements increased and some decreased. Mainly Cr and O spectrums were increased and the largest points are at 1273 K and 1373 K as shown in Table 57 and Figures 102 and 105. Brightness grain boundaries and the titanium content grew with increased temperatures.

Table 57. Surface morphology mass percent average for five region analysis on the surface of alloy at 1073 K.

Spectrum	C	O	Al	Si	Ti	Cr	Fe	Ni
1073 K	3.88	18.6	0.3	0.45	0.94	27.4	30.0	18.5
1173 K	5.18	36.0	0.29	-	1.1	40.0	10.7	7.6
1273 K	4.44	39.83	0.12	-	1.62	45.57	8.88	0.72
1373 K	4.44	39.83	0.12	-	1.62	45.57	8.88	0.72
1473 K	5.2	32.87	0.24	-	4.15	40.84	14.72	1.37

6.2.3. Oxidation Microstructure (Cross-Section Analysis) with Scanning electron microscopy/energy dispersive X-ray spectroscopy (SEM/EDS)

6.2.3.1. 1073 K

At 1073 K, the SEM cross-section micrograph reported the compositions of two regions. The first region shown in Figure 112 is an internal layer made up mostly of Fe, Ni, C and Cr and O. The second region (external layer) focused on the white bright area

and this region showed the presence of Cr, C, O, and Fe. Surface morphologies are shown in Figure 110. Double layers were formed in the cross section of the sample. The external layer (top, or oxide layer) contained a Cr–oxide layer and the internal layer contained large amounts of Ni. Our results found that the oxide scale has small cracks as shown in Figure 112

The EDS analysis of the surface oxide and the microstructure below are shown in Figure 114. At 1073 K, the surface oxide was mostly Cr, Fe and C. Figure 113 also shows an elemental map of a well-developed layer of alloy/oxide interface. EDS analysis of the sample surface was performed as shown in Figure 114 and Table 58.

As shown in Figure 114 different regions were analyzed by EDS. Figure 114 (a) shows Region 1 (inner layer) and Figure 114 (b) shows Region 2 (outer layer) by EDS graph. Atomic and mass percentage on the cross-section are given in Table 58.

The thickness of the outer layer was measured and was found to be 850.0 nm.

Figure 112. SEM images of the cross-section of the oxide after exposure to air at 1073 K.

Figure 113. The elemental maps in a cross sectional area of the oxide film at 1073 K.

Figure 114. EDS graph at 1073 K (a) Region 1 (b) Region 2.

Table 58. Region 1 and Region 2 mass % and atomic % at 1073 K.

	Region 1		Region 2	
Element	Mass (%)	Atomic (%)	Mass (%)	Atomic (%)
Carbon	13.39	41.19	26.83	49.03
Oxygen	0.59	1.35	21.96	30.14
Aluminum	0.25	0.34	0.00	0.00
Silicon	0.26	0.34	0.08	0.06
Chlorine	0.04	0.05	0.30	0.19
Titanium	0.32	0.24	0.68	0.31
Chromium	19.44	13.81	22.94	9.68
Iron	40.64	26.89	21.43	8.43
Nickel	25.07	15.78	5.78	2.16
Sum	100.00	100.00	100.00	100.00

6.2.3.2. 1173 K

SEM images depict two regions as shown in Figure 115. At 1173 K, the first region mainly contains Fe, Ni, and Cr. The second region mainly consists of Cr, C, O, and Fe.

The results of EDS analyses performed on the cross-section are given in Tables 59 and Figure 117. Elements were detected by the SEM element map in Figure 116. The thickness of the outer layer was measured and was found to be 1.550 µm.

Figure 115. SEM images of the cross-section of the oxide after exposure to air at 1173 K.

Figure 116. The elemental maps in a cross sectional area of the oxide film at 1173 K.
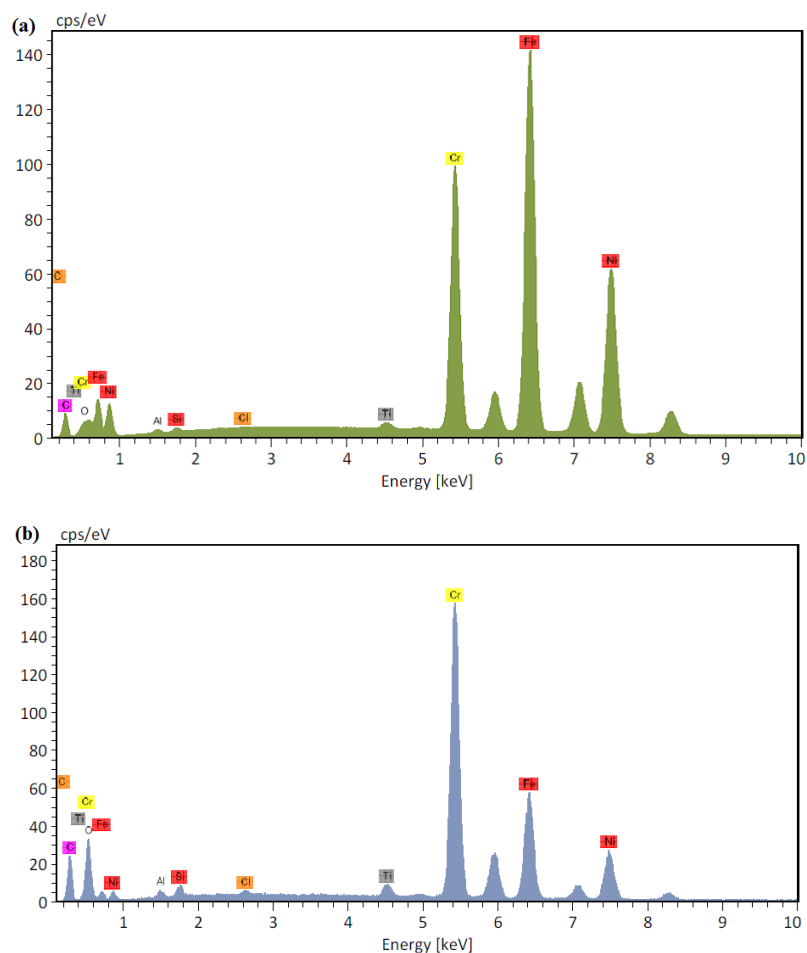
Figure 117. EDS graph at 1173 K (a) Region 1 (b) Region 2.

Table 59. Region 1 and Region 2 mass % and atomic % at 1173 K.

	Region 1		Region 2	
Element	**Mass (%)**	**Atomic (%)**	**Mass (%)**	**Atomic (%)**
Carbon	13.44	41.31	26.40	49.66
Oxygen	0.56	1.29	19.09	26.95
Aluminum	0.30	0.41	0.58	0.49
Silicon	0.26	0.34	0.73	0.58
Chlorine	0.04	0.05	0.20	0.13
Titanium	0.31	0.24	0.75	0.35
Chromium	18.96	13.46	28.81	12.52
Iron	40.52	26.79	14.81	5.99
Nickel	25.60	16.10	8.65	3.33
Sum	100.00	100.00	100.00	100.00

6.2.3.3. 1273 K

SEM images depict two regions as shown in Figure 118. At 1273K, the first region mainly contains Fe, Ni, and Cr. The second region mainly consists of Cr, C, O, and Fe.

The results of EDS analyses performed on the cross-section are given in Tables 60 and Figure 120. Elements were detected by the SEM element map in Figure 119.

The thickness of the outer layer was measured and was found to be 6.750 µm.
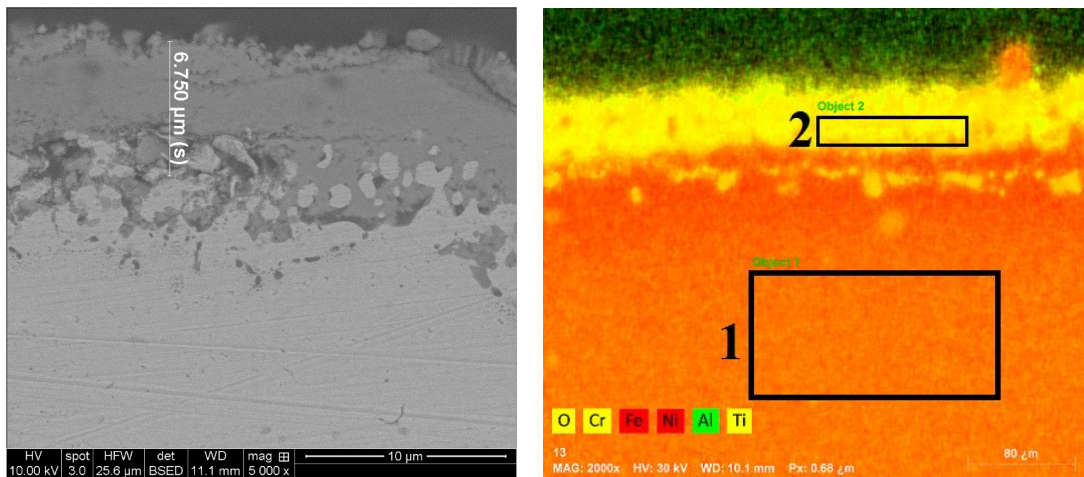
Figure 118. SEM images of the cross-section of the oxide after exposure to air at 1273 K.
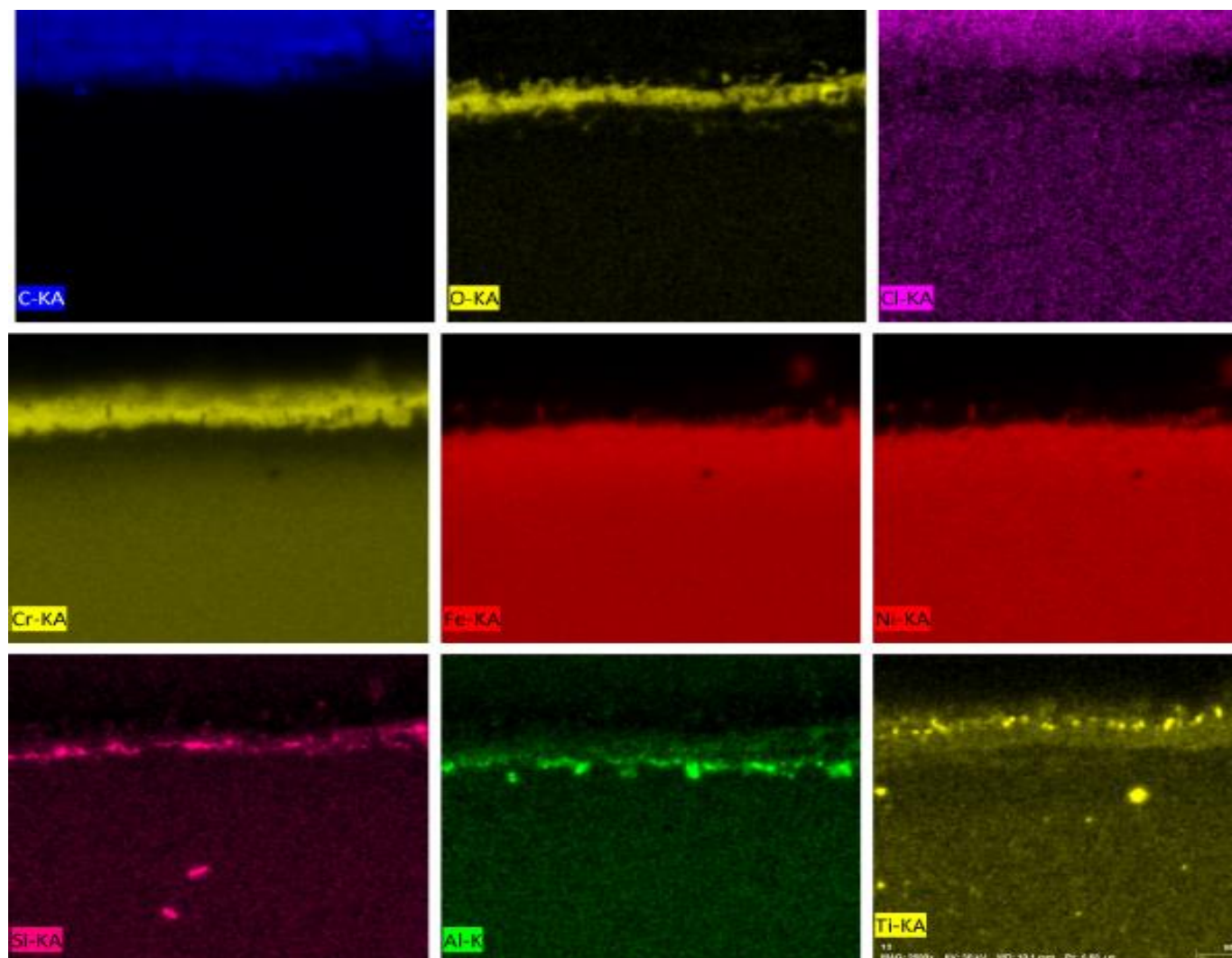
Figure 119. The elemental maps in a cross sectional area of the oxide film at 1273 K
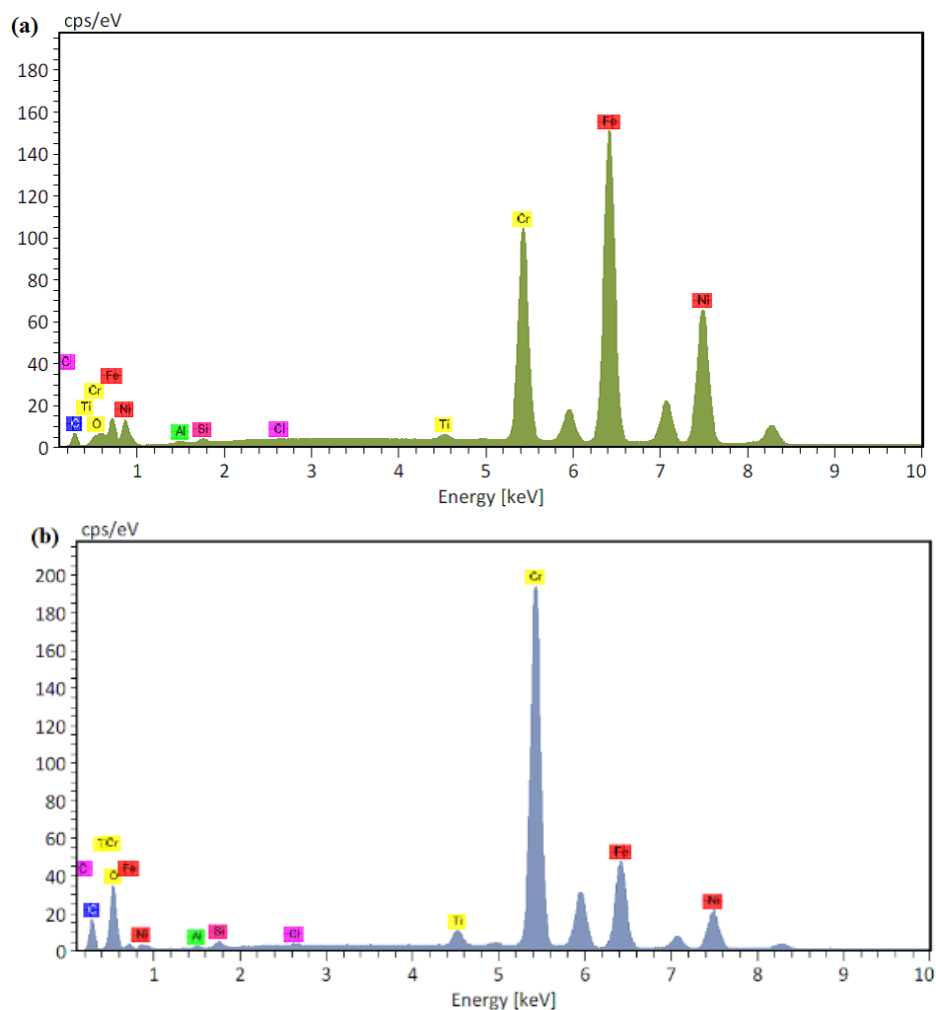
Figure 120. EDS graph at 1273 K (a) Region 1 and (b) Region 2.

Table 60. Region 1 and Region 2 mass % and atomic % at 1273 K.

	Region 1		Region 2	
Element	Mass (%)	Atomic (%)	Mass (%)	Atomic (%)
Carbon	9.93	33.37	19.31	40.65
Oxygen	0.48	1.22	18.88	29.84
Aluminum	0.29	0.44	0.17	0.16
Silicon	0.32	0.47	0.45	0.40
Chlorine	0.04	0.04	0.10	0.07
Titanium	0.32	0.27	1.01	0.54
Chromium	19.80	15.37	38.60	18.78
Iron	42.33	30.60	14.01	6.34
Nickel	26.49	18.22	7.46	3.21
Sum	100.00	100.00	100.00	100.00

6.2.3.4. 1373 K

SEM images depict two regions as shown in Figure 121. At 1373 K, the first region mainly contains Fe, Ni, and Cr. The second region mainly consists of Cr and O.

The results of EDS analyses performed on the cross-section are given in Tables 61 and Figure 123. Elements were detected by the SEM element map in Figure 122.
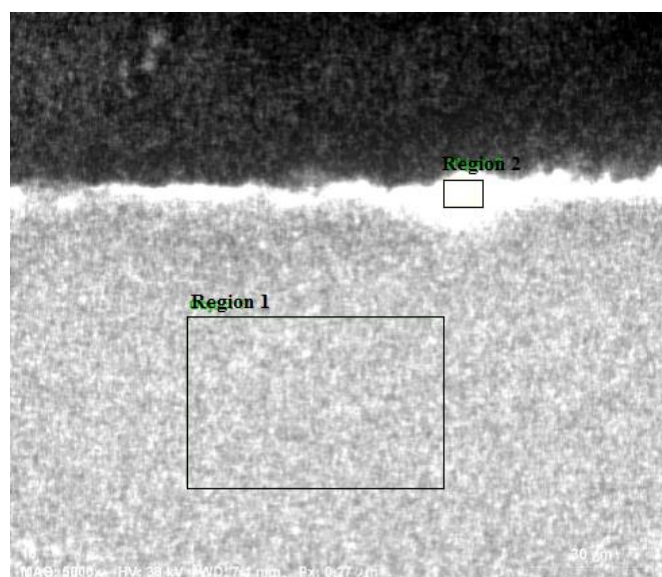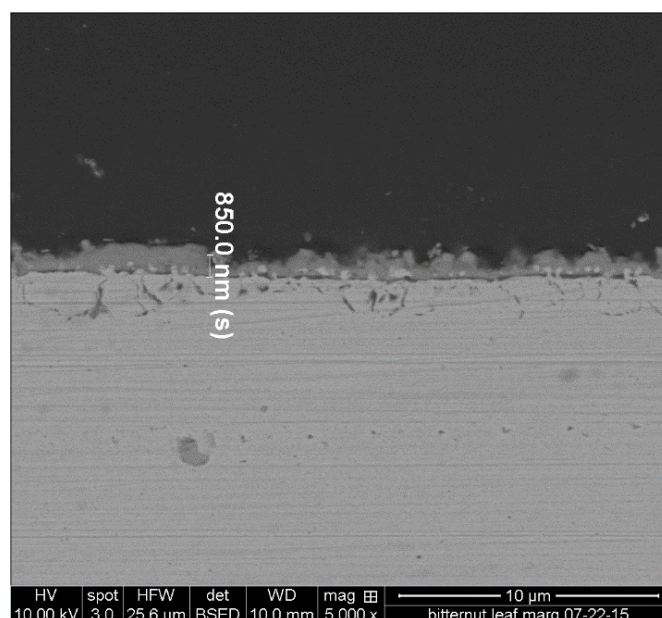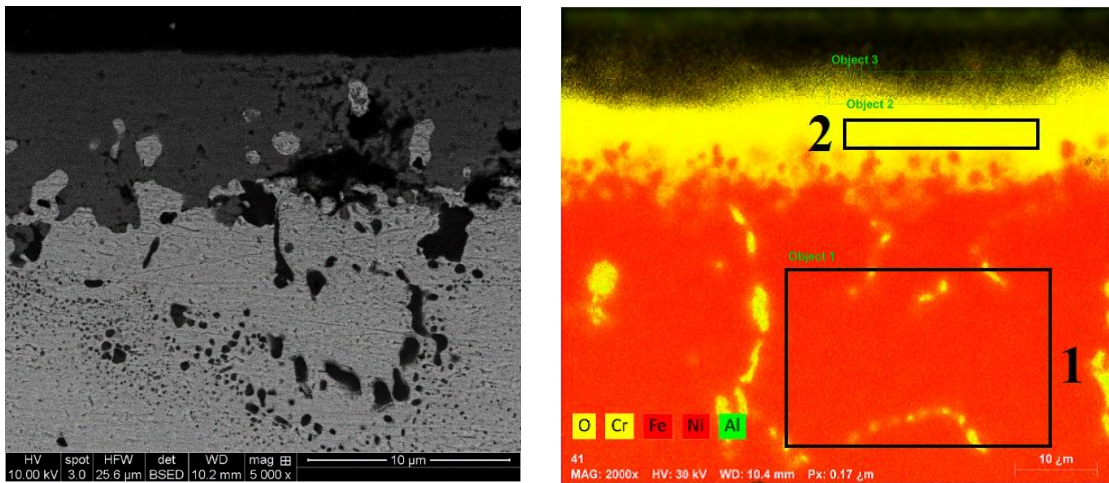

Figure 121. SEM images of the cross-section of the oxide after exposure to air at 1373 K.
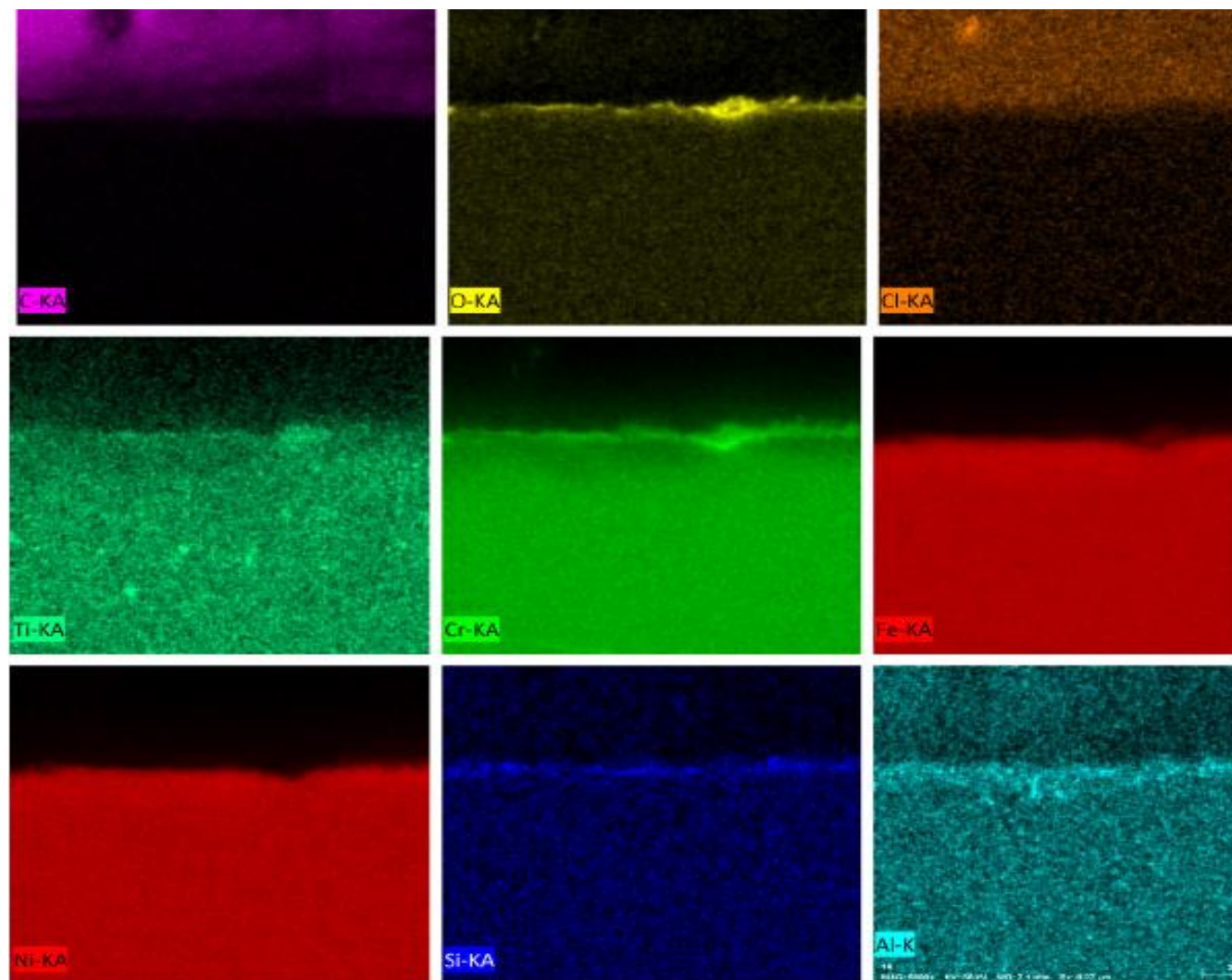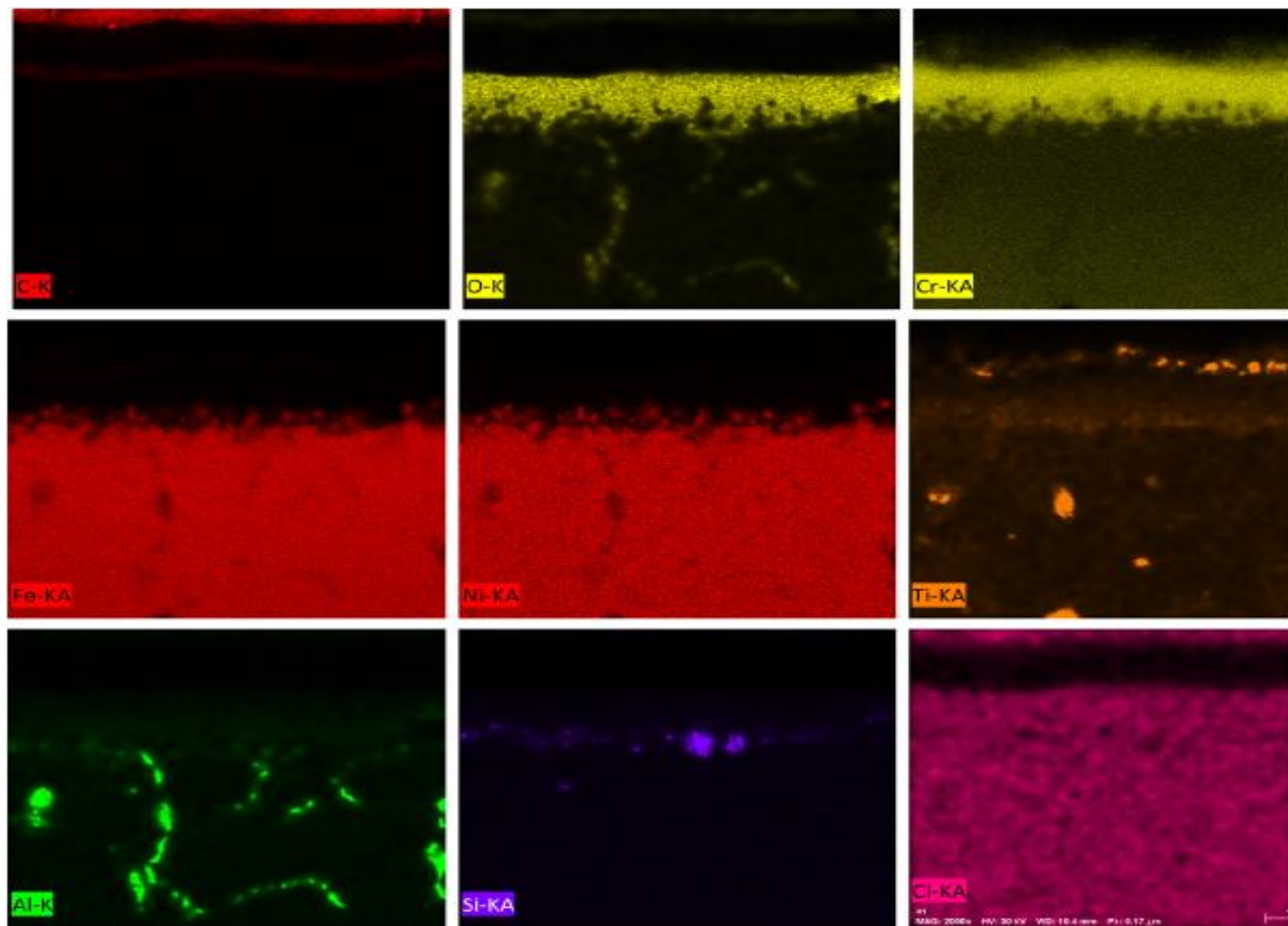
Figure 122. The elemental maps in a cross sectional area of the oxide film at 1373 K.
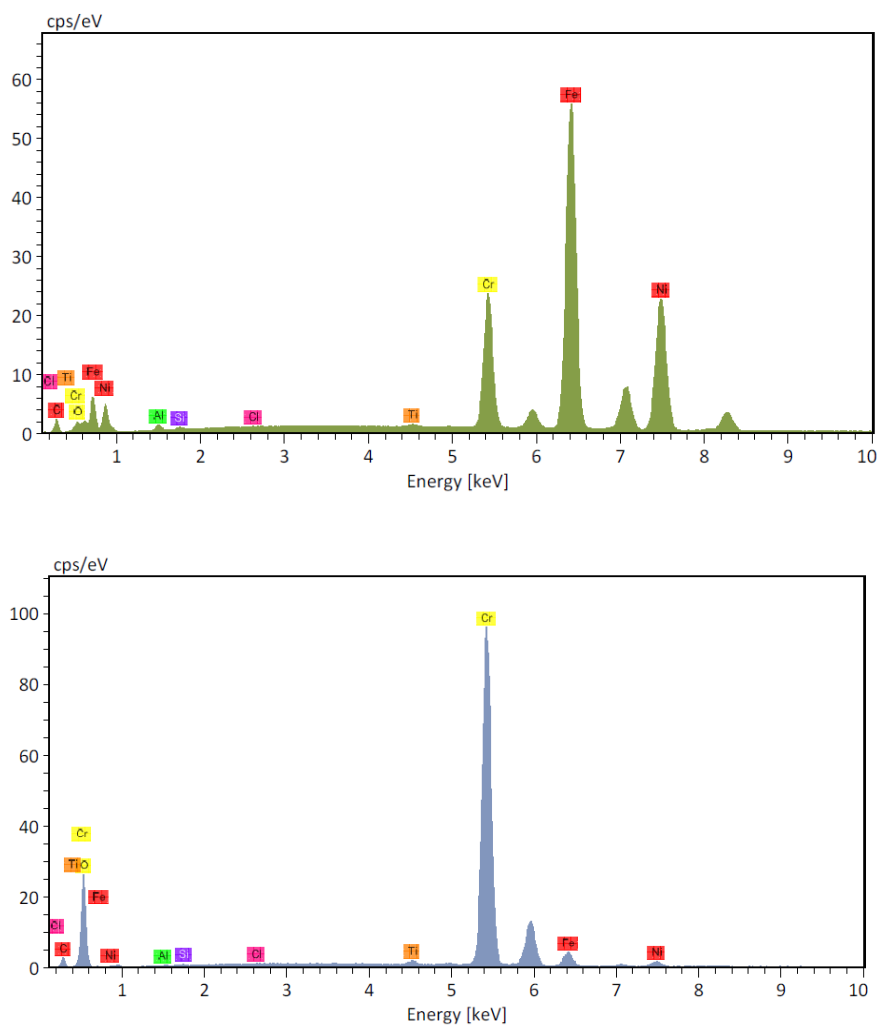
Figure 123. EDS graph at 1373 K (a) Region 1 (b) Region 2.

Table 61. Region 1 and Region 2 mass % and atomic % at 1373 K.

	Region 1		Region 2	
Element	Mass (%)	Atomic (%)	Mass (%)	Atomic (%)
Carbon	8.28	28.82	7.05	16.68
Oxygen	1.12	2.94	26.54	47.14
Aluminum	0.66	1.03	0.08	0.09
Silicon	0.20	0.30	0.12	0.12
Chlorine	0.02	0.03	0.02	0.01
Titanium	0.15	0.13	0.35	0.21
Chromium	13.14	10.57	60.32	32.97
Iron	47.30	35.43	3.87	1.97
Nickel	29.12	20.75	1.65	0.80
Sum	100.00	100.00	100.00	100.00

166

6.2.3.5. 1473 K

SEM images depict two regions as shown in Figure 124. At 1473 K, the first region mainly contains Fe, Ni, and Cr. The second region mainly consists of Cr and O.

The results of EDS analyses performed on the cross-section are given in Table 62 and Figure 126. Elements were detected by the SEM element map in Figure 125.

The thickness of the outer layer was measured and was found to be 10.15 µm. The thickness of the outer layer could be slightly increased as temperatures increased.
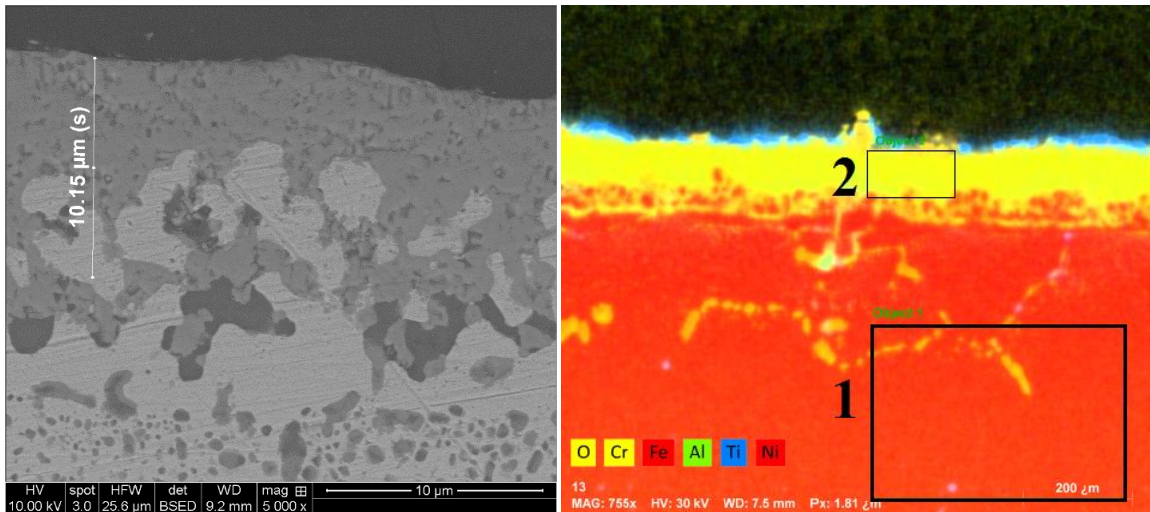
Figure 124. SEM images of the cross-section of the oxide after exposure to air at 1473 K.
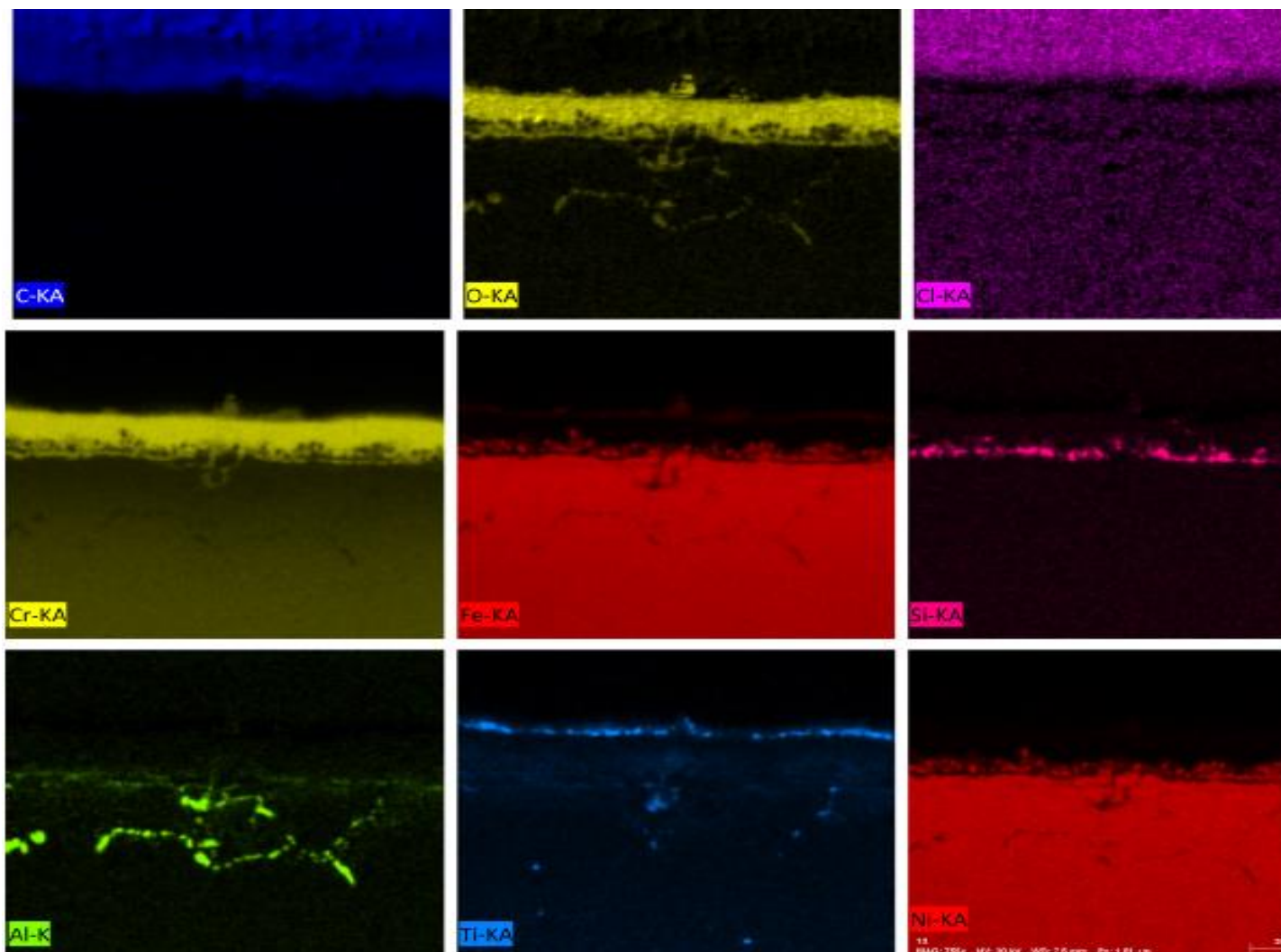
Figure 125. The elemental maps in a cross sectional area of the oxide film at 1473 K.
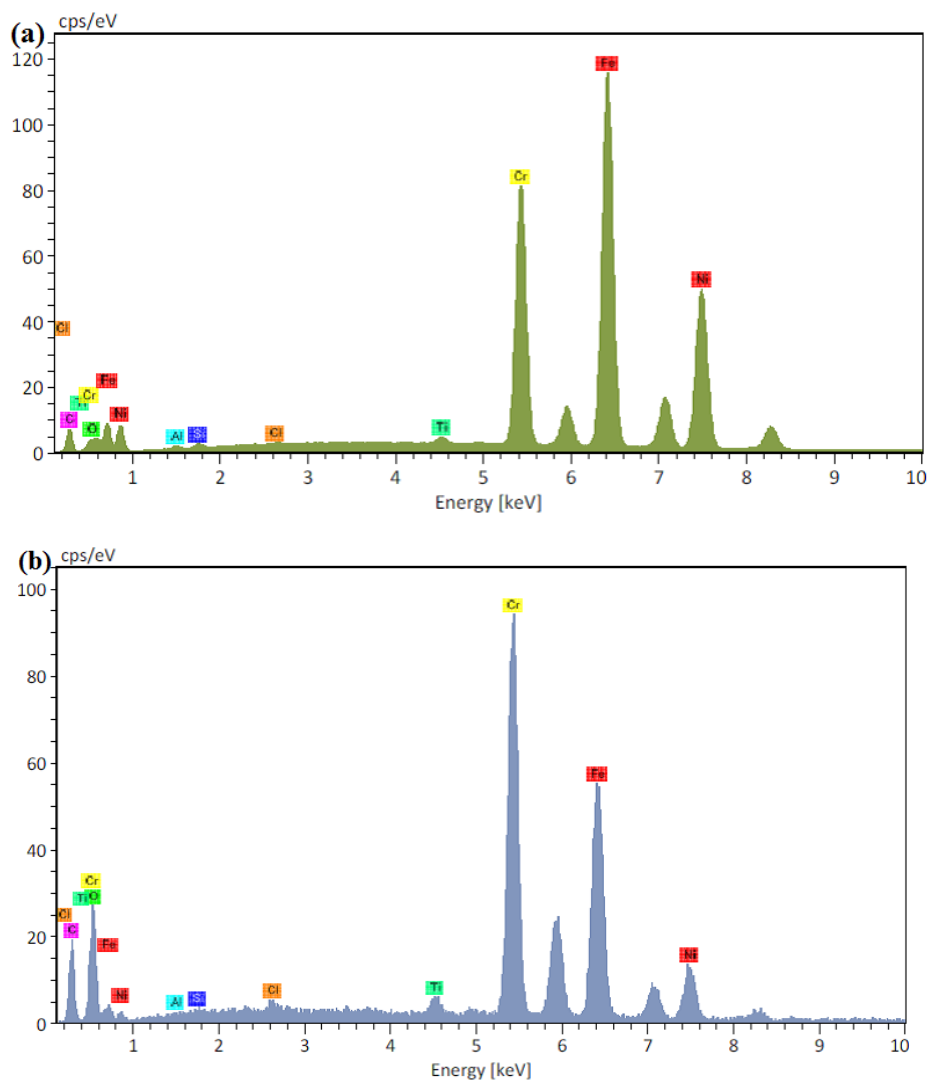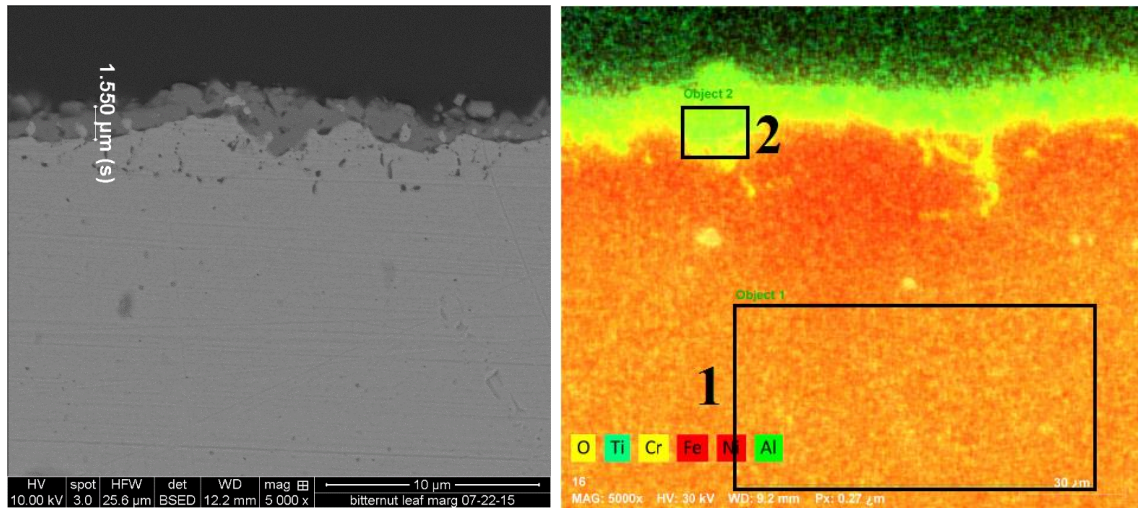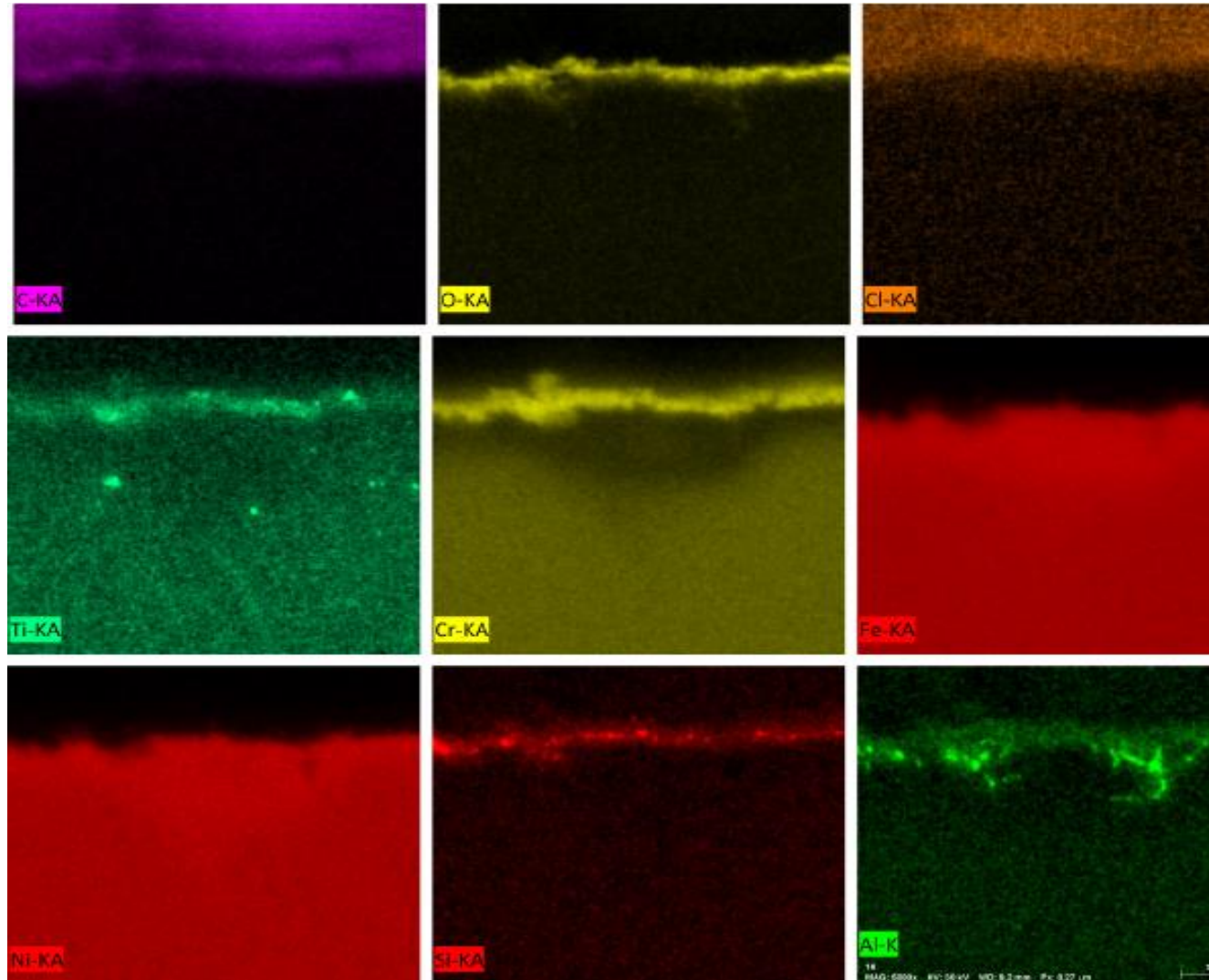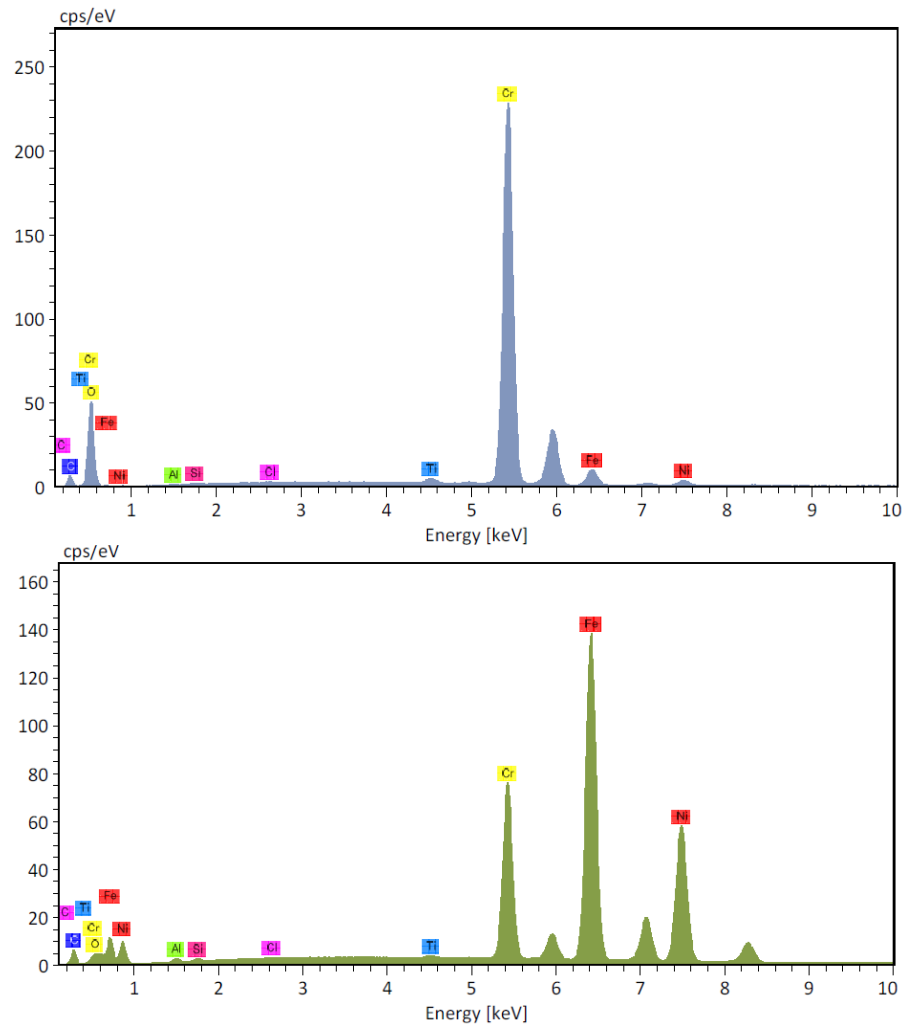
Figure 126. EDS graph at 1473 K (a) Region 1 and (b) Region 2.

Table 62. Region 1 and Region 2 mass % and atomic % at 1473 K.

Element	Region 1		Region 2	
	Mass (%)	Atomic (%)	Mass (%)	Atomic (%)
Carbon	11.09	35.96	9.25	20.96
Oxygen	0.91	2.23	26.85	45.68
Aluminum	0.45	0.65	0.05	0.05
Silicon	0.23	0.31	0.14	0.13
Chlorine	0.03	0.03	0.05	0.04
Titanium	0.11	0.09	0.41	0.23
Chromium	16.32	12.22	58.28	30.51
Iron	44.04	30.71	3.61	1.76
Nickel	26.82	17.79	1.36	0.63
Sum	100.00	100.00	100.00	100.00

169

6.2.4. Characterization of the oxidized Layer with X-Ray Diffraction

The XRD results for the oxidized layer at 1073 K, 1173 K, 1273 K, 1373 K, and 1473 K are shown in Figure 127. The x-ray diffraction pattern of the air exposed sample clearly shows that at 1073 K and 1173 K the oxides are composed of Cr_2O_3 (JCPDS file No. 74-0326), $Cr_{0.19} Fe_{0.7} Ni_{0.11}$ (JCPDS file No. 33-0397) and $Fe_{2.932} O_4$ (JCPDS file No. 86-1352). $Cr_{0.19} Fe_{0.7} Ni_{0.11}$ appears to have the strongest peak intensity among these oxides at 1073 K. Cr_2O_3 and $Cr_{0.19} Fe_{0.7} Ni_{0.11}$ have strongest peak intensity among these oxides at 1173 K.

At 1273 K, the scale formed is composed of Cr_2O_3 (JCPDS file No. 74-0326), $Cr_{0.19} Fe_{0.7} Ni_{0.11}$ (JCPDS file No. 33-0397), $Fe_{2.932} O_4$ (JCPDS file No. 86-1352), Fe_2O_3 (JCPDS file No. 84-0311) and Cr_2O_5 (JCPDS file No. 36-1329). These diffraction patterns show the strongest peaks of Cr_2O_3 and $Cr_{0.19} Fe_{0.7} Ni_{0.11}$.

At 1373 K and 1473 K, as shown in Figure 127, XRD patterns show the scale formed is composed of $Fe_{2.932} O_4$ (JCPDS file No. 86-1352), Fe_2O_3 (JCPDS file No. 84-0310 and 84-0311) and Cr_2O_5 (JCPDS file No. 36-1329). Of these diffraction patterns, the strongest peak is $Fe_{2.932} O_4$.
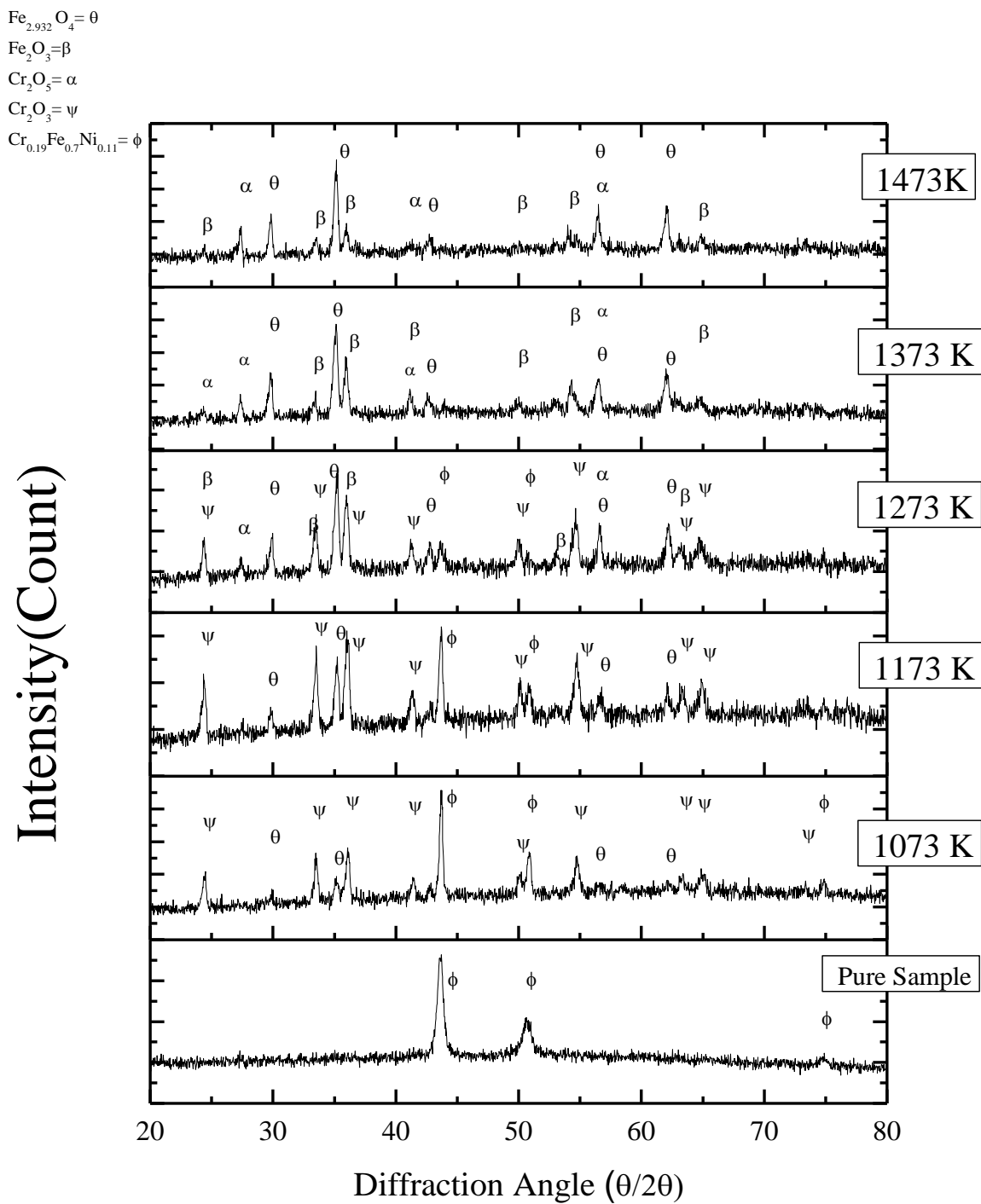
Figure 127. X-Ray diffraction of Incoloy 800H alloy pure sample and 1073 K to 1473 K samples.

171

6.3. Discussion

Weight gains and time with dependence on temperature were shown in Figure 90. Table 45 shows the parabolic rate constant of 800H alloy. In addition to maximum weight gains, activation energy was reported in the present study. Different temperatures affected the oxidation process, which was previously studied by different researchers[119]. High temperature oxidation behavior and oxidation kinetics are often reported in the literature for 800H alloy. This strongly agrees with results of previous studies[119]. It can be seen that weight gains increased as the temperature increased. The oxidation kinetics parabolic rate constant increased with temperatures. The gained weight was increased as temperatures increased; hence, the rising temperature was the reason for the weight gain increase. As reported by Betz[131], activation energy was determined to be 280 kJ/ mol. Thin oxide scales rich in Cr and Ti have been found to grow in a parabolic dependence with temperature. Oxidation rate constants have been correlated with temperature using an Arrhenius equation as shown in Figure 93.

At 1073 K to 1473 K SEM analysis, the formation of surface oxides and the penetration depths of internal oxide increased as the oxidation time increased. Oxide growth, which is initially non-uniform becomes more uniform during the course of the exposures. At 1073 and 1173 K, the surface SEM images results revealed that the oxide scale is uniform and dense. EDS analysis showed that the surface oxide crystals were enriched in Cr, Fe, and Ni. To illustrate the microstructure of the oxidized alloy, corresponding cross section morphology was investigated and displayed in the figure from Fig. 112. At 1073 K 850 nm and 1.550 µm oxide thickness can be clearly seen. The scale consists of two layers, a light grey-contrasted inner layer and a dark grey-contrasted

outer layer. EDS mapping results pointed out that the inner layer was rich in Cr, Fe and Ni, while the outer layer was rich in Fe, Cr and minor Ni, as shown in Figure 113. The two layers were confirmed to be Cr_2O_3, $Cr_{0.19}Fe_{0.7}Ni_{0.11}$ and $Fe_{2.932}O_4$, respectively, in combination with the XRD characterization. The oxide layer was found to be compact, dense and adherent to the surface of the specimens oxidized at temperatures ranging from 1073 K to 1173 K.

At 1273 K, as shown in Figure 105 the results display that the largest grain areas are enriched Cr regions. It was observed that Cr content increased in the external oxide layer with increasing temperature. Internal-oxidation precipitates of Al_2O_3 dissolved Cr and Fe just beneath the substrate were observed in cross section images especially after 1273 K. The oxide scale was non-uniform. EDS analysis showed that the surface oxide crystals were enriched in Cr and Fe. Also from elemental map images as shown in Figure 119, there was a stable SiO_2 layer and an unstable Al_2O_3 layer beneath the external Cr-rich oxide. XRD results confirm the oxidation layers' content at 1273 K, and the scale formed was composed of Cr_2O_3, $Cr_{0.19}Fe_{0.7}Ni_{0.11}$, $Fe_{2.932}O_4$, Fe_2O_3 and Cr_2O_5.

At 1373 K and 1473 K, spallation occurred as a result of oxidation. Whereas, some evidence of spallation of the external oxide surface was observed in the specimen exposed at 1373 K. Underneath the outer layer of oxide scale, particles with black contrast formed, particularly along grain boundaries of the matrix (see Figure 121). Elemental X-ray maps showed that these particles were enriched in Al, as presented in Figure 122. This contrast in composition of these internal oxides was characterized to be Al_2O_3, Al_2O_3 and occurred at a greater depth in the substrate alloy with increase temperatures. The large number of atomic and mass percentage of Ti confirms the

presence of a Ti-rich layer, which was associated with external oxidation along the grain boundaries at 1473 K. There was a stable SiO_2 layer and an unstable Al_2O_3 layer beneath the external Cr-rich oxide.

For the 800H alloy, which contains a small amount of Al as an alloying element, internal oxides, probably of Al_2O_3, were observed in the metal substrate underneath the external oxide scale. EDS microanalysis results of oxide layers formed in the specimens of the alloys exposed at different temperatures were presented in this dissertation. It was found that the analysis data are consistent with the determination of weight-gain for these alloys under the same condition[78].

6.4. Conclusion

- Figures sequentially show the continuous growth of external oxide scales and grain boundary ridges with increased temperatures.

- The oxidation behavior of Incoloy 800H alloy follows parabolic oxidation kinetic rate law. The activation energy is 266.8 kJ/mol for 1073 K to 1473 K.

- The oxide morphology and structure of Incoloy 800H alloy were strongly affected by their environment. Grain boundaries and microstructural defects affected specimens during high temperature oxidation.

- Spallation is considered to occur as a result of oxidation after 1373 K.

- At 1473 K, the increasing mass gain was related to Ti oxidation, as shown in Figure 122 and Table 62. At 1473 Niobium content was observed as shown in Figure 109 (b).

- The oxidation depth increased as the temperature increased. Increasing oxidation temperatures were attributed to the formation of pores, voids, and grain boundaries and were affected when exposed to high temperatures.

- Oxide growth, which is initially non-uniform, became more uniform during the course of exposure to higher temperatures.

REFERENCES

1. Chapin, D., Kiffer, S. & Nestell, J. The Very High Temperature Reactor: A Technical Summary. (2004).

2. Maloy, S. A. *et al. Status Report on Structural Materials for Advanced Nuclear Systems*. (2013). doi:10.2172/1097679

3. Petti, D., Crawford, D. & Chauvin, N. Fuels for Advanced Nuclear Energy Systems. *MRS Bull.* **34,** 40–45 (2009).

4. Natesan, K., Majumdar, S., Shankar, P. S. & Shah, V. N. Preliminary materials selection issues for the next generation nuclear plant reactor pressure vessel. *Nucl. Eng. Div. Argonne Natl. Lab.* (2006).

5. Barnard, C. J. & Hoiland, S. A. *Generation IV nuclear systems ten-years program plan*. **I,** (2007).

6. B. Riou, C. Escaravage, D. Hittner, D. P. No Title. in *Issues in Reactor Pressure Vessel* 10–22 (Proceedings of the 2nd international topical meeting on high temperature reactor technology, 2004).

7. Hussain, N. Oxidation behaviour of superalloys at elevated temperatures under different oxidizing atmosphere. (University of The Punjab, Pakistan, 2000).

8. Li, N. Oxidation behavior and residual stresses of AISI 430 alloy during in wet air. (L'UNIVERSITE PARIS-SUD, 2016).

9. Roberge, P. R. *Corrosion Engineering. Principles and Practice. Learning* (2008). doi:10.1036/0071482431

10. Roberge, P. R. & Pierre, R. *Handbook of Corrosion Engineering Library of Congress Cataloging-in-Publication Data*. (1999).

11. Fontana, M. G. *Corrosion Engineering*. (McGraw-Hill Book Company, 1985).

12. Swearingen, G. & Pugh, B. M. N. M. ; R. High Temperature Gas Reactors: Assessment of Applicable Codes and Standards. *Pacific Northwest Natl. Lab.* (2011).

13. AK Steel Corporation. Product Data Sheet: Stainless Steel 316/316L. 2 (2007).

14. Al-Mangour, B., Mongrain, R., Irissou, E. & Yue, S. Improving the strength and corrosion resistance of 316L stainless steel for biomedical applications using cold spray. *Surf. Coatings Technol.* **216,** 297–307 (2013).

15. Mylavarapu, S. K. Development of Compact Heat Exchangers for very high-temperature gas-cooled reactors. *Ohio State Univ.* (2008).

16. International, H. *Haynes 617 Alloy description:physical properties report*. (2008).

17. Metals, S. *INCOLOY alloy 800 report*. (2004).

18. Murty, K. L. & Charit, I. Structural materials for Gen-IV nuclear reactors: Challenges and opportunities. *J. Nucl. Mater.* **383,** 189–195 (2008).

19. McVay, K. L., Park, J.-H., Lee, S., Hassan, Y. a. & Anand, N. K. Preliminary tests of particle image velocimetry for the upper plenum of a scaled model of a very high temperature gas cooled reactor. *Prog. Nucl. Energy* **83,** 305–317 (2015).

20. Kim, D.-J., Jung, S. J., Mun, B. H., Kim, S. W. & Lim, Y. S. Parametric Study on the Tensile Properties of Ni-Based Alloy for a VHTR. *Metall. Mater. Trans. A* **46,** 47–57 (2015).

21. Yvon, P. & Carré, F. Structural materials challenges for advanced reactor systems. *J. Nucl. Mater.* (2009). doi:10.1016/j.jnucmat.2008.11.026

22. Natesan, K., Purohit, A. & Tam, S. W. *Materials Behavior in HTGR Environments*. (2003). doi:NUREG/CR-6824

23. Jang, C. *et al.* Oxidation behaviors of wrought nickel-based superalloys in various high temperature environments. *Trans. Nonferrous Met. Soc. China (English Ed.* **21,** 1524–1531 (2011).

24. De Carvalho, C. E. R., Da Costa, G. M., Cota, A. B. & Rossi, E. H. High temperature oxidation behavior of AISI 304 and AISI 430 stainless steels. *Mater. Res.* **9,** 393–397 (2006).

25. Jung, H., Ahn, T. & Mintz, T. *Corrosion of stainless steel type 316l in a seepage water dripping environment*. (2011).

26. Buscail, H., El Messki, S., Riffard, F., Perrier, S. & Issartel, C. Effect of pre-oxidation at 800 ??c on the pitting corrosion resistance of the AISI 316L stainless steel. *Oxid. Met.* **75,** 27–39 (2011).

27. Evans, H. E., Hilton, D. A., Holm, R. A. & Webster, S. J. Influence of silicon additions on the oxidation resistance of a stainless steel. *Oxid. Met.* **19,** 1–18

28. Li, B. & Gleeson, B. Effects of silicon on the oxidation behavior of Ni-base chromia-forming alloys. *Oxid. Met.* **65,** 101–122 (2006).

29. Riffard, F. *et al.* A New Interpretation of the Breakaway'' Oxidation Behaviour Observed at High Temperature on 304 Stainless Steel. *Mater. Sci. Forum* **461–464,** 175–182 (2004).

30. Saeki, I. *et al.* Growth process of protective oxides formed on type 293 and 329 stainless steels at 0162 k. *Corros. Sci.* **40,** 1295–1305 (1998).

31. Mendoza, H. & Angel, D. High temperature stability of a 316 austenitic stainless steel coated with CeO2 nanoparticles. (The University of Wisconsin Milwaukee, 2011).

32. Issartel, C. *et al.* Nitridation effect on the oxidation of a austenitic stainless steel AISI 304 at 900°C. *Appl. Surf. Sci.* **225,** 14–20 (2004).

33. Lopez, H. F., Mendoza, H. & Church, B. High-temperature oxidation resistance of

a nanoceria spray-coated 316l stainless steel under short-term air exposure. *Metall. Mater. Trans. A Phys. Metall. Mater. Sci.* **45,** 1362–1370 (2014).

34.   Cissé, S., Laffont, L., Tanguy, B., Lafont, M. C. & Andrieu, E. Effect of surface preparation on the corrosion of austenitic stainless steel 304L in high temperature steam and simulated PWR primary water. *Corros. Sci.* (2012). doi:10.1016/j.corsci.2011.12.007

35.   Bautista, A., Velasco, F. & Abenojar, J. Oxidation resitance of sintered stainless steels: Effect of yttria additions. *Corros. Sci.* **45,** 1343–1354 (2003).

36.   Cossio, M. L. T. *et al.* No Title No Title. *Uma ética para quantos?* **XXXIII,** 81–87 (2012).

37.   Issartel, C., Buscail, H., Nguyen, C. T. & Fleurentin, A. 330Cb alloy (Fe☐35Ni☐18Cr☐1Nb☐2Si) oxidation study between 800 and 1000 °C. *Mater. Corros.* **61,** 929–938 (2010).

38.   Reiser, J. R., DeVan, J. H. & Lawrence, E. J. Compatibility of molten salts with type 316 stainless steel and lithium. *J. Nucl. Mater.* **85,** 295–298 (1979).

39.   Peng, X., Yan, J., Zhou, Y. & Wang, F. Effect of grain refinement on the resistance of 304 stainless steel to breakaway oxidation in wet air. *Acta Mater.* **53,** 5079–5088 (2005).

40.   Merz, M. D. The oxidation resistance of fine-grained sputter-deposited 304 stainless steel. *Metall. Trans. A* **10,** 71–77

41.   Huntz, A. M. *et al.* Oxidation of AISI 304 and AISI 439 stainless steels. *Mater. Sci. Eng. A* **447,** 266–276 (2007).

42.   Tanabe, T. & Imoto, S. Surface oxidation of type 316 stainless steel. *Transactions of the Japan Institute of Metals* **20,** 507–515 (1979).

43.   Betz, G., Wehner, G. K., Toth, L. & Joshi, A. Composition-vs-depth profiles obtained with Auger electron spectroscopy of air-oxidized stainless-steel surfaces. *J. Appl. Phys.* **45,** 5312–5316 (1974).

44.   Li, D.-S., Qi-Xun, D., Cheng, X.-N., Rong-Rong, W. & Yan, H. High-Temperature Oxidation Resistance of Austenitic Stainless Steel Crl8NillCu3A13MnNb. *J. Iron Steel Res. Int.* **19,** 74–78 (2012).

45.   Gulbransen, E. A. & Andrew, K. F. Oxidation Studies on 304 Stainless Steel. *J. Electrochem. Soc.* **109,** 560–564 (1963).

46.   Ding, Y. Effects of elevated temperature exposure on the microstructural evolution of Ni(Cr)-Cr3C2 coated 304 stainless steel. (2009).

47.   Hussain, N., Shahid, K. A., Khan, I. H. & Rahman, S. Oxidation of High-Temperature Alloys (Superalloys) at Elevated Temperatures in Air : I. **41,** (1994).

48.   Kofstad, P., Rahmel, A., Rapp, R. A. & Douglas, D. L. International workshop on ``New Fundamentals of Scale Growth''. *Oxid. Met.* **32,** 125–166

49. Rundell, G. & McConnell, J. Oxidation resistance of eight heat-resistant alloys at 870{\textdegree}, 980{\textdegree}, 1095{\textdegree}, and 1150{\textdegree}C. *Oxid. Met.* **36,** 253–263

50. Sabioni, A. C. S. *et al.* About the role of chromium and oxygen ion diffusion on the growth mechanism of oxidation films of the AISI 304 austenitic stainless steel. *Oxid. Met.* **78,** 211–220 (2012).

51. Fátima, M. De, Claret, A., Sabioni, S., Huntz, A. & Hugo, É. High Temperature Oxidation Behavior of the AISI 430A and AISI 430E Stainless Steels in Ar / H 2 / H 2 O Atmosphere. *Mater. Res.* **11,** 227–232 (2008).

52. Sabioni, A., Huntz, A.-M., Conceição da Luz, E., Mantel, M. & Haut, C. Comparative study of high temperature oxidation behaviour in AISI 304 and AISI 439 stainless steels. *Mat. Res.* **6,** 179 (2003).

53. VÉLEZ, S. B. & A. Oxidation kinetics and mechanisms in HT-9 ferritic/martensitic stainless steel. (2005).

54. Uns, S. & Nr, S. W. Specification Sheet : Alloy 316 / 316L. 9–11 (2014).

55. Wolf, M. M. in 1–47 (2003).

56. AZO Materials. Stainless steel - high temperature resistance. 1–6 (2015).

57. Nikulin, I., Kaibyshev, R. & Skorobogatykh, V. High temperature properties of an austenitic stainless steel. *J. Phys. Conf. Ser.* **240,** 12071 (2010).

58. Was, G. S. *et al.* Corrosion and stress corrosion cracking in supercritical water. *J. Nucl. Mater.* **371,** 176–201 (2007).

59. Gao, X., Wu, X., Zhang, Z., Guan, H. & Han, E. hou. Characterization of oxide films grown on 316L stainless steel exposed to H2O2-containing supercritical water. *J. Supercrit. Fluids* (2007). doi:10.1016/j.supflu.2006.12.020

60. Badin, V., Diamanti, E., Forêt, P. & Darque-Ceretti, E. Water Vapor Oxidation of Ferritic 441 and Austenitic 316L Stainless Steels at 1100°C for Short Duration. *Procedia Mater. Sci.* **9,** 48–53 (2015).

61. Muthukumaran, V., Selladurai, V., Nandhakumar, S. & Senthilkumar, M. Corrosion and Hardness Behaviour of AISI 316L SS Implanted with Argon and Oxygen Ions Korózne a pevnostné vlastnosti AISI 316L SS pri implantácii iónmi argónu a kyslíka. 75–79

62. Moosa, A. A. Improving Oxidation Resistance of Stainless Steel (AISI 316L) by Pack Cementation. **25,** (2007).

63. Samuel, K. ., Mannan, S. . & Rodriguez, P. Serrated yielding in AISI 316 stainless steel. *Acta Metall.* **36,** 2323–2327 (1988).

64. Christopher, J. & Choudhary, B. K. Kinetics of Uniaxial Tensile Flow and Work Hardening Behavior of Type 316L(N) Austenitic Stainless Steel in the Framework of Two-Internal-Variable Approach. *Metall. Mater. Trans. A Phys. Metall. Mater.*

Sci. **46,** 674–687 (2014).

65. Choudhary, B. K., Samuel, E. I., Sainath, G., Christopher, J. & Mathew, M. D. Influence of Strain Rate and Temperature on Tensile Deformation and Fracture Behavior of Type 316L(N) Austenitic Stainless Steel. *Metall. Mater. Trans. A* **44,** 4979–4992 (2013).

66. P., L., B., B. & G., B. *Stainless Steels*. (1993).

67. Rameshwar Jha, C. W. H. and B. B. A. The Formation of Diffusion Coatings on some Low-Alloy Steels and their High Temperature Oxidation Behaviour: Part 1 Diffusion Coatings. **25,** 651–665 (2002).

68. Caplan, D. & Cohen, M. The Volatilization of Chromium Oxide. *J. Electrochem. Soc.* **108,** 438 (1961).

69. Cabet, C., Terlain, A., Lett, P., Guétaz, L. & Gentzbittel, J.-M. High temperature corrosion of structural materials under gas-cooled reactor helium. *Mater. Corros.* **57,** 147–153 (2006).

70. Proceedings, W., Falls, I. & States, U. S tructural Materials for Innovative Nuclear Systems. (2015).

71. Murty, K. L. & Charit, I. Structural materials for Gen-IV nuclear reactors: Challenges and opportunities. *J. Nucl. Mater.* (2008). doi:10.1016/j.jnucmat.2008.08.044

72. Giggins, C. S. & Pettit, F. S. Oxidation of Ni-Cr-Al Alloys Between 1000° and 1200°C. *J. Electrochem. Soc.* **118,** 1782 (1971).

73. Benz, J., Lillo, T. & Wright, R. *Aging of Alloy 617 at 650 and 750 ° C*. (2013).

74. Kim, D., Jang, C. & Ryu, W. S. Oxidation Characteristics and Oxide Layer Evolution of Alloy 617 and Haynes 230 at 900 {\textdegree}C and 1100 {\textdegree}C. *Oxid. Met.* **71,** 271–293 (2009).

75. Kewther, A., Hashmi, M. S. J. & Yilbas, B. S. Corrosion properties of inconel 617 alloy after heat treatment at elevated temperature. *J. Mater. Eng. Perform.* **10,** 108–113

76. Metals, S. *Product Data Sheet: INCONEL alloy 617*. *Special Metals Corporation* 1–12 (2005).

77. Sah, I., Kim, D., Lee, H. J. & Jang, C. Development and oxidation resistance evaluation of Al-rich surface layer on Alloy 617. *Surf. Coatings Technol.* **236,** 400–404 (2013).

78. Hussain, N., Shahid, K. A., Khan, I. H. & Rahman, S. Oxidation of high-temperature alloys (superalloys) at elevated temperatures in air. II. *Oxid. Met.* **43,** 363–378 (1995).

79. Kim, D., Jang, C. & Ryu, W. S. Oxidation characteristics and oxide layer evolution of Alloy 617 and Haynes 230 at 900 °c and 1100 °c. *Oxid. Met.* **71,** 271–

293 (2009).

80. Ohnami, M. & Inamura, R. Effect of Vacuum Environment on Creep Rupture Properties of Inconel 617 at 1000 C (Especially, Based of Crack Initiation and the Propagation). *Bull. JSME* **24,** 1530–1536 (1981).

81. Sharma, S. K., Ko, G. D., Li, F. X. & Kang, K. J. Oxidation and creep failure of alloy 617 foils at high temperature. *J. Nucl. Mater.* **378,** 144–152 (2008).

82. Sharma, S. K., Li, F. X., Ko, G. D. & Kang, K. J. Strengthening effect of Cr2O3 thermally grown on alloy 617 foils at high temperature. *J. Nucl. Mater.* **405,** 165–170 (2010).

83. Tung, H. M. & Stubbins, J. F. Incipient oxidation kinetics of alloy 617 and residual stress of the oxide scale formed in air at temperatures between 850 and 1000??C. *J. Nucl. Mater.* (2012). doi:10.1016/j.jnucmat.2012.01.015

84. Al-Hatab, K. A., Al-Bukhaiti, M. A. & Krupp, U. Cyclic oxidation kinetics and oxide scale morphologies developed on alloy 617. *Appl. Surf. Sci.* **318,** 275–279 (2014).

85. Jang, C., Lee, D. & Kim, D. Oxidation behaviour of an Alloy 617 in very high-temperature air and helium environments. *Int. J. Press. Vessel. Pip.* **85,** 368–377 (2008).

86. Mankins, W. L., Hosier, J. C. & Bassford, T. H. Microstructure and phase stability of INCONEL alloy 617. *Metall. Trans.* **5,** 2579–2590 (1974).

87. Ganesan, P., Smith, G. D. & Yates, D. H. Performance of Inconel Alloy 617 in Actual and Simulated Gas Turbine Environments. *Mater. Manuf. Process.* **10,** 925–938 (1995).

88. Chin, J., Johnson, W. R. & Chen, K. Compatibility of aluminide-coated Hastelloy X and Inconel 617 in a simulated gas-cooled reactor environment. *Thin Solid Films* **95,** 85–97 (1982).

89. Kim, D.-J., Lee, G.-G., Jeong, S. J., Kim, W. oo G. & Park, J. Y. Investigation on Material Degradation of Alloy 617 in High Temperature Impure Helium Coolant. *Nucl. Eng. Technol.* **43,** 429–436 (2011).

90. Lee, G. G. *et al.* Microstructural investigation of Alloy 617 creep-ruptured at high temperature in a helium environment. *J. Mater. Sci. Technol.* **29,** 1177–1183 (2013).

91. Bates, H. G. A. The Corrosion Behavior of High-Temperature Alloys During Exposure for Times up to 10,000h in Prototype Nuclear Process Helium at 700 to 900°C. *Nucl. Technol.* **66,** 415–428 (1984).

92. Christ, H.-J., Künecke, U., Meyer, K. & Sockel, H. G. Mechanisms of high-temperature corrosion in helium containing small amounts of impurities. II. Corrosion of the nickel-base alloy inconel 617. *Oxid. Met.* **30,** 27–51 (1988).

93. Christ, H.-J., Künecke, U., Meyer, K. & Sockel, H. G. High temperature corrosion of the nickel-based alloy Inconel 617 in helium containing small amounts of impurities. *Mater. Sci. Eng.* **87,** 161–168 (1987).

94. Jang, C., Lee, D. & Kim, D. Oxidation behaviour of an Alloy 617 in very high-temperature air and helium environments. *Int. J. Press. Vessel. Pip.* **85,** 368–377 (2008).

95. Cabet, C. *et al.* High temperature reactivity of two chromium-containing alloys in impure helium. *J. Nucl. Mater.* **375,** 173–184 (2008).

96. Cabet, C. & Rouillard, F. Corrosion of high temperature metallic materials in VHTR. *J. Nucl. Mater.* **392,** 235–242 (2009).

97. Cabet, C. & Rouillard, F. Corrosion Issues of High Temperature Reactor Structural Metallic Materials. *J. Eng. Gas Turbines Power* **131,** 62902 (2009).

98. Wright, R. N. *Summary of Studies of Aging and Environmental Effects on Inconel 617 and Haynes 230*. (2006). doi:10.2172/911722

99. Sigler, D. R. The oxidation behavior of Fe-20Cr alloy foils in a synthetic exhaust-gas atmosphere. *Oxid. Met.* **46,** 335–364

100. Kim, J. H. *et al.* The role of grain boundaries in the initial oxidation behavior of austenitic stainless steel containing alloyed Cu at 700??C for advanced thermal power plant applications. *Corros. Sci.* **96,** 52–66 (2015).

101. Kaczorowski, D. & Chapovaloff, J. Corrosion behaviour inconel 617 in VHTR environment. in *International Conference on Nuclear Engineering* 1–7 (2006).

102. Kofstad, P. & Lillerud, K. P. Chromium transport through Cr2O3 scales I. On lattice diffusion of chromium. *Oxid. Met.* **17,** 177–194

103. Sabioni, A. C. S., Lesage, B., Huntz, A. M., Pivin, J. C. & Monty, C. Self-diffusion in cr2o3 I. Chromium diffusion in single crystals. *Philos. Mag. A* **66,** 333–350 (1992).

104. Christ, H. J., Kuenecke, U., Meyer, K. & Sockel, H. G. High temperature corrosion of the nickel-based alloy Inconel 617 in helium containing small amounts of impurities. *Mater. Sci. Eng.* **87 p. 161-p.,** (1987).

105. Gan, J. Irradiated microstructure of alloy 800H. **351,** 223–227 (2006).

106. Laboratory, I. N. E. and E. *Next Generation Nuclear Plant Materials Research and Development Program Plan*. (2006).

107. F.A. Garner, N.H. Packan, A. S. K. scholar. in *Radition-Induced Changes in Microstructure: 13th International Symposium (part I)* 289 (1987).

108. W., R. & R., S. Status of alloy 800h in considerations for the gen IV nuclear energy systems. *J Press. Vessel Technol Trans ASME J. Press. Vessel Technol. Trans. ASME* **136,** (2014).

109. Swindeman, R. & (ORNL), O. R. N. L. Status of Alloy 800H in Considerations for the Gen IV Nuclear Energy Systems. *J. Press. Vessel Technol.* **136,** 54001 (2013).

110. Ashby, M. F. & Smidman, M. Materials for Nuclear Power Systems. *Granta Mater. Inspir. MFA* (2010).

111. Roy, A. K. & Virupaksha, V. Performance of alloy 800H for high-temperature heat exchanger applications. *Mater. Sci. Eng. A* **452–453,** 665–672 (2007).

112. DOE, U. S. A technology roadmap for generation IV nuclear energy systems. *Gener. IV Int. Forum* 1–97 (2002). doi:GIF-002-00

113. Mo, K. *et al.* Effect of orientation on plastic deformations of Alloy 617 for VHTR applications. *J. Nucl. Mater.* **443,** 366–377 (2013).

114. Michels, L. C. The effect of alloy depletion on the oxidation resistance of incoloy 800. *Journal of Nuclear Materials* **62,** 314–316 (1976).

115. Cabet, C. & Rouillard, F. Corrosion of high temperature metallic materials in VHTR. *J. Nucl. Mater.* (2009). doi:10.1016/j.jnucmat.2009.03.029

116. Langevoort, J. C., Hanekamp, L. J. & Gellings, P. J. On the kinetics of oxidation of austenitic stainless steels AISI 304 and incoloy 800H. *Appl. Surf. Sci.* **28,** 189–203 (1987).

117. Langewoort, J. C., SUtherland, I., Hanekamp, L. J. & Gellins, P. J. On the oxide formation on stainless steels AISI 304 and incoloy 800H investigated with xps. *Appl. Surf. Sci.* **28,** 167–179 (1987).

118. Polman, E. A., Fransen, T. & Gellings, P. J. High-Temperature Corrosion and Mechanical Properties of Protective Scales on Incoloy 800H : The Influence of Preoxidation and Ion Implantation. **33,** 135–155 (1990).

119. Chen, W. S., Kai, W., Tsay, L. W. & Kai, J. J. The oxidation behavior of three different zones of welded Incoloy 800H alloy. *Nucl. Eng. Des.* **272,** 92–98 (2014).

120. Khalid, F. A., Hussain, N. & Shahid, K. A. Microstructure and morphology of high temperature oxidation in superalloys. *Mater. Sci. Eng. A* **265,** 87–94 (1999).

121. Tan, L., Sridharan, K. & Allen, T. R. Microstructural Effects on the Corrosion Behavior of INCOLOY 800H. **298,** (2009).

122. Xu, H., Hocking, M. G. & Sidky, P. S. Sulfidation-Oxidation Behavior of Alloy 800H in SO2 - 02 and H2 - H2 S - C O - CO2 Atmospheres. **41,** (1994).

123. Gutirrez, A. & Damborenea, J. De. High-Temperature Oxidation Behavior of Laser-Surface-Alloyed Incoloy-800H with Al. **47,** 259–275 (1997).

124. Tan, L., Allen, T. R. & Yang, Y. Corrosion behavior of alloy 800H (Fe – 21Cr – 32Ni) in supercritical water. *Corros. Sci.* **53,** 703–711 (2011).

125. Choudhry, K. I., Mahboubi, S., Botton, G. A., Kish, J. R. & Svishchev, I. M. Corrosion of engineering materials in a supercritical water cooled reactor :

Characterization of oxide scales on Alloy 800H and stainless. *Corros. Sci.* **100,** 222–230 (2015).

126. Otsuka, N. & Fujikawa, H. Scaling of Austenitic Stainless Steels and Nickel-Based Alloys in High-Temperature Steam at 973K. *Corrosion* **47,** 240–248 (1991).

127. Yang, Z. *et al.* Materials at High Temperatures Oxidation behavior of a new Fe – Ni – Cr-based alloy in pure steam at 750 ° C Oxidation behavior of a new Fe – Ni – Cr-based alloy in pure steam at 750 ° C. **3409,** 0–6 (2016).

128. Akhiani, H., Nezakat, M., Sanayei, M. & Szpunar, J. The effect of thermo-mechanical processing on grain boundary character distribution in Incoloy 800H/HT. *Mater. Sci. Eng. A* **626,** 51–60 (2015).

129. Cao, Y. & Di, H. Grain boundary character distribution during the post-deformation recrystallization of Incoloy 800H at elevated temperature. *Mater. Lett.* **163,** 24–27 (2016).

130. Tan, L., Sridharan, K. & Allen, T. R. The effect of grain boundary engineering on the oxidation behavior of INCOLOY alloy 800H in supercritical water. **348,** 263–271 (2006).

131. Betz, W. *High Temperature Alloys for Gas Turbines and Other Applications, 1986: Proceedings of a Conference Held in Li{è}ge, Belgium, 6-9 October 1986.* (D. Reidel Publishing Company, 1986).

VITA

Hakan Us

Hakan Us was born in Kahramanmaras, Turkey in 1985. He attended Akdeniz University from 2004 to 2008 and received a Bachelor of Arts and Sciences degree in Physics in 2008. He earned his Master of Science degree in Nuclear engineering at the University of Missouri-Columbia, in July 2012. He plans to obtain his Ph.D. degree at the same university in December, 2016.